

# Nanostructured Surfaces, Coatings, and Films 2014

Guest Editors: Mengnan Qu, Jiamin Wu, Qi Wang, Yuanlie Yu,  
and Jinmei He





---

**Nanostructured Surfaces, Coatings,  
and Films 2014**

Journal of Nanomaterials

---

**Nanostructured Surfaces, Coatings,  
and Films 2014**

Guest Editors: Mengnan Qu, Jiamin Wu, Qi Wang,  
Yuanlie Yu, and Jinmei He



---

Copyright © 2015 Hindawi Publishing Corporation. All rights reserved.

This is a special issue published in "Journal of Nanomaterials." All articles are open access articles distributed under the Creative Commons Attribution License, which permits unrestricted use, distribution, and reproduction in any medium, provided the original work is properly cited.

## Editorial Board

- Domenico Acierno, Italy  
Katerina Aifantis, USA  
Sheikh Akbar, USA  
Nageh K. Allam, USA  
Margarida Amaral, Portugal  
Raul Arenal, Spain  
Ilaria Armentano, Italy  
Lavinia Balan, France  
Thierry Baron, France  
Andrew R. Barron, USA  
Hongbin Bei, USA  
Stefano Bellucci, Italy  
Enrico Bergamaschi, Italy  
D. Bhattacharyya, New Zealand  
G. Bongiovanni, Italy  
T. Borca-Tasciuc, USA  
Mohamed Bououdina, Bahrain  
Torsten Brezesinski, Germany  
C. Jeffrey Brinker, USA  
Christian Brosseau, France  
Yibing Cai, China  
Chuanbao Cao, China  
Victor M. Castaño, Mexico  
Albano Cavaleiro, Portugal  
Bhanu P. S. Chauhan, USA  
Wei Chen, China  
Yuan Chen, Singapore  
Tupei Chen, Singapore  
Shafiul Chowdhury, USA  
Kwang-Leong Choy, UK  
Jin-Ho Choy, Korea  
Yu-Lun Chueh, Taiwan  
E. Comini, Italy  
G. Compagnini, Italy  
David Cornu, France  
M. A. Correa-Duarte, Spain  
P. D. Cozzoli, Italy  
Majid Darroudi, Iran  
Shadi A. Dayeh, USA  
Luca Deseri, USA  
Yong Ding, USA  
Bin Dong, China  
Zehra Durmus, Turkey  
Joydeep Dutta, Oman  
Ali Eftekhari, USA  
Samy El-Shall, USA  
Farid El-Tantawy, Egypt  
Ovidiu Ersen, France  
Claude Estournès, France  
Andrea Falqui, Saudi Arabia  
Xiaosheng Fang, China  
Bo Feng, China  
Matteo Ferroni, Italy  
Wolfgang Fritzsche, Germany  
Alan Fuchs, USA  
Peng Gao, China  
Miguel A. Garcia, Spain  
Siddhartha Ghosh, Singapore  
P. K. Giri, India  
Russell E. Gorga, USA  
Jihua Gou, USA  
Jean M. Greneche, France  
Changzhi Gu, China  
Lin Guo, China  
John Zhanhu Guo, USA  
Smrati Gupta, Germany  
K. Hamad-Schifferli, USA  
Michael Harris, USA  
Jr-Hau He, Taiwan  
Nguyen D. Hoa, Vietnam  
Michael Z. Hu, USA  
Nay Ming Huang, Malaysia  
Qing Huang, China  
Shaoming Huang, China  
David Hui, USA  
Zafar Iqbal, USA  
B. Jeyadevan, Japan  
Xin Jiang, Germany  
Rakesh Joshi, Australia  
Myung-Hwa Jung, Korea  
Jeong-won Kang, Korea  
Hassan Karimi-Maleh, Iran  
A. Kelarakis, UK  
Alireza Khataee, Iran  
Ali K. Zak, Iran  
Dojin Kim, Korea  
Wonbaek Kim, Korea  
Philippe Knauth, France  
Ralph Krupke, Germany  
Christian Kübel, Germany  
Sushil Kumar, India  
Sanjeev Kumar, India  
Prashant Kumar, UK  
Subrata Kundu, India  
Michele Laus, Italy  
Eric Le Bourhis, France  
Burtrand Lee, USA  
Jun Li, Singapore  
Shijun Liao, China  
Meiyong Liao, Japan  
Silvia Licocchia, Italy  
Wei Lin, USA  
Jun Liu, USA  
Z. Lockman, Malaysia  
Songwei Lu, USA  
Jue Lu, USA  
Ed Ma, USA  
Malik Maaza, South Africa  
Lutz Mädler, Germany  
Gaurav Mago, USA  
Morteza Mahmoudi, Iran  
Mohammad A. Malik, UK  
D. Mangalaraj, India  
Sanjay R. Mathur, Germany  
Paulo C. Morais, Brazil  
Mahendra A. More, India  
Paul Munroe, Australia  
Jae-Min Myoung, Korea  
Rajesh R. Naik, USA  
Albert Nasibulin, Russia  
T. Natsuki, Japan  
Koichi Niihara, Japan  
Sherine Obare, USA  
Won-Chun Oh, Republic of Korea  
Atsuto Okamoto, Japan  
Abdelwahab Omri, Canada  
Ungyu Paik, Republic of Korea  
Edward A. Payzant, USA  
Ton Peijs, UK  
Oscar Perales-Pérez, Puerto Rico  
Wenxiu Que, China  
Peter Reiss, France  
Orlando Rojas, USA  
Marco Rossi, Italy  
Cengiz S. Ozkan, USA



---

Vladimir Šepelák, Germany  
Huaiyu Shao, Japan  
Prashant Sharma, USA  
Donglu Shi, USA  
Bhanu P. Singh, India  
S. Singh, USA  
V. Sivakov, Germany  
Yanlin Song, China  
Ashok Sood, USA  
M. Striccoli, Italy  
Jing Sun, China  
Xuping Sun, Saudi Arabia  
A. K. Sundramoorthy, USA  
S. Szunerits, France

Nyan-Hwa Tai, Taiwan  
Bo Tan, Canada  
Ion Tiginyanu, Moldova  
V. P. Tolstoy, Russia  
M. S. Toprak, Sweden  
Ramon Torrecillas, Spain  
Takuya Tsuzuki, Australia  
Tamer Uyar, Turkey  
Bala Vaidhyanathan, UK  
Luca Valentini, Italy  
Rajender S. Varma, USA  
A. Villaverde, Spain  
Ajayan Vinu, Australia  
Shiren Wang, USA

Yong Wang, USA  
Ruibing Wang, Macau  
Magnus Willander, Sweden  
Ping Xiao, UK  
Zhi Li Xiao, USA  
Yangchuan Xing, USA  
Doron Yadlovker, Israel  
Piaoping Yang, China  
Yoke K. Yap, USA  
Ramin Yousefi, Iran  
William W. Yu, USA  
Kui Yu, Canada  
Renyun Zhang, Sweden

## Contents

**Nanostructured Surfaces, Coatings, and Films 2014**, Mengnan Qu, Jiamin Wu, Qi Wang, Yuanlie Yu, and Jinmei He  
Volume 2015, Article ID 836096, 2 pages

**Structural and Magnetic Properties of Ni<sub>81</sub>Fe<sub>19</sub> Thin Film Grown on Si(001) Substrate via Single Graphene Layer**, Gui-fang Li, Shibin Liu, Shanglin Yang, and Yongqian Du  
Volume 2015, Article ID 575401, 5 pages

**Adsorption of Organic Dyes by TiO<sub>2</sub>@Yeast-Carbon Composite Microspheres and Their In Situ Regeneration Evaluation**, Zheng Pei, Zhang Kaiqiang, Dang Yu, Bai Bo, Guan Weisheng, and Suo Yourui  
Volume 2015, Article ID 498304, 13 pages

**Growth of Semimetals Bismuth and Antimony Films on Reactive Substrate**, Xiao Wang, Xiaoxing Wei, and Caixia Song  
Volume 2015, Article ID 581486, 5 pages

**A Low-Stress, Elastic, and Improved Hardness Hydrogenated Amorphous Carbon Film**, Qi Wang, Deyan He, and Junyan Zhang  
Volume 2015, Article ID 543631, 5 pages

**Glaze Icing on Superhydrophobic Coating Prepared by Nanoparticles Filling Combined with Etching Method for Insulators**, Chao Guo, Ruijin Liao, Yuan Yuan, Zhiping Zuo, and Aoyun Zhuang  
Volume 2015, Article ID 404071, 7 pages

**Study of Magnetization Reversal Process in FeCo/Ru/FeCo Exchange Coupled Synthetic Antiferromagnetic Multilayers**, Xi Liu, Shunji Ishio, and Hailin Ma  
Volume 2015, Article ID 452851, 5 pages

**The Photoluminescence Behaviors of a Novel Reddish Orange Emitting Phosphor CaIn<sub>2</sub>O<sub>4</sub>:Sm<sup>3+</sup> Codoped with Zn<sup>2+</sup> or Al<sup>3+</sup> Ions**, Jing Gou, Dongyang Zhang, Binxun Yu, Jing Wang, and Shengzhong Liu  
Volume 2015, Article ID 969724, 5 pages

**Synthesis and Electrochemical Performance of Graphene Wrapped Sn<sub>x</sub>Ti<sub>1-x</sub>O<sub>2</sub> Nanoparticles as an Anode Material for Li-Ion Batteries**, Xing Xin, Xufeng Zhou, Tao Shen, and Zhaoping Liu  
Volume 2015, Article ID 965061, 10 pages

**Superhydrophobic Polyimide via Ultraviolet Photooxidation: The Evolution of Surface Morphology and Hydrophobicity under Different Ultraviolet Intensities**, Hongyu Gu, Lixin Song, Jinlin Zhang, and Zhenyi Qi  
Volume 2015, Article ID 546384, 7 pages

**Surface Morphology and Growth of Anodic Titania Nanotubes Films: Photoelectrochemical Water Splitting Studies**, Chin Wei Lai  
Volume 2015, Article ID 820764, 7 pages

**Electrodeposition and Characterization of CuTe and Cu<sub>2</sub>Te Thin Films**, Wenya He, Hanzhi Zhang, Ye Zhang, Mengdi Liu, Xin Zhang, and Fengchun Yang  
Volume 2015, Article ID 240525, 5 pages

**Fabrication of Mechanical Durable Polysiloxane Superhydrophobic Materials**, Mengnan Qu, Jinmei He, Sun Zhe, Kanshe Li, Xiangrong Liu, and Chunxia Yu  
Volume 2015, Article ID 284685, 5 pages

**A Facile Strategy for the Functionalization of Boron Nitride Nanotubes with Pd Nanoparticles**, Yuanlie Yu, Hua Chen, and Yun Liu  
Volume 2015, Article ID 310214, 5 pages

**Fabrication and Evaluation of Polycaprolactone/Gelatin-Based Electrospun Nanofibers with Antibacterial Properties**, Lor Huai Chong, Mim Mim Lim, and Naznin Sultana  
Volume 2015, Article ID 970542, 8 pages

## Editorial

# Nanostructured Surfaces, Coatings, and Films 2014

Mengnan Qu,<sup>1</sup> Jiamin Wu,<sup>2</sup> Qi Wang,<sup>3</sup> Yuanlie Yu,<sup>4</sup> and Jinmei He<sup>1</sup>

<sup>1</sup>College of Chemistry and Chemical Engineering, Xi'an University of Science and Technology, Xi'an, China

<sup>2</sup>Department of Chemical and Petroleum Engineering, University of Pittsburgh, Pittsburgh, PA, USA

<sup>3</sup>Department of Physics, Lanzhou University, Lanzhou, China

<sup>4</sup>Advance Membranes and Porous Materials Center, King Abdullah University of Science and Technology, Jeddah, Saudi Arabia

Correspondence should be addressed to Mengnan Qu; [mnanqu@gmail.com](mailto:mnanqu@gmail.com)

Received 29 June 2015; Accepted 1 July 2015

Copyright © 2015 Mengnan Qu et al. This is an open access article distributed under the Creative Commons Attribution License, which permits unrestricted use, distribution, and reproduction in any medium, provided the original work is properly cited.

Nanotechnology makes it possible to intentionally modify the properties of surfaces and endow them with any desired function. Nanostructured surfaces, coatings, and films have represented important advances in control of wetting, adhesion, mechanical, thermal, magnetic, electrical, and optical properties and ability to direct cell behavior. A number of promising approaches to fabricate functional micro- and nanostructured surfaces, coatings, and films have been stimulated by opportunities to enhance the properties of surfaces and interfaces *via* the combination of surface structure, morphology, and physical and chemical properties. Such functional micro- and nanostructured surfaces, coatings, and films are playing an increasingly important part in a broad range of novel applications, such as energy, electronics, photonics, as well as sensor systems, advanced materials, and medical devices.

This special issue features articles that cover a wide range of recent progress in design, fabrication, and characterization of innovative nanostructured surfaces with the aim of improving their surface properties and functional performance, as well as new insights on physical principles underlying their properties and enormous potential applications. Highlighted below are important contributions from this special issue.

C. Song et al. address the growth of semimetal bismuth and antimony films on reactive substrate. The strategy presented is facile and cost effective, which may develop the design of functional thin films of metal or other inorganic materials.

B. Bo et al. present the study on the adsorption of organic dyes by TiO<sub>2</sub>@yeast-carbon composite microspheres and their *in situ* regeneration evaluation. The results will be useful for further research and practical applications of the novel TiO<sub>2</sub>@yeast composite in dye wastewater treatment.

R. Liao et al. report glaze icing on superhydrophobic coatings prepared by nanoparticles filling combined with etching method for insulators. The coated glass slides and glass insulators show excellent anti-icing performance at low temperature.

N. Sultana et al. fabricate the polycaprolactone/gelatin-based electrospun nanofibers and evaluate their antibacterial properties. The results confirm that the nanofibers are suitable for use in inhibiting bacterial infections and protecting the injured parts of both skin and tissues from contamination.

X. Liu et al. investigate the magnetization reversal process in FeCo/Ru/FeCo exchange coupled synthetic antiferromagnetic multilayers. The results show that the two magnetic layers have the same domain structure and the domain structures were reversed correspondingly when the applied field is smaller than the exchange coupling field.

Q. Wang et al. prepare a low-stress, elastic, and improved hardness hydrogenated amorphous carbon film. The results show that, at the hydrogen flow rate of 50 sccm, the deposited films have lower compressive stress, higher elastic recovery, and higher hardness, compared with the films deposited without hydrogen introduction.

H. Chen et al. describe a facile strategy for functionalization of boron nitride nanotubes with Pd nanoparticles.

The good catalytic activity of the Pd nanoparticles decorated boron nitride nanotubes to be a potential candidate in the application of electronic and catalysis fields.

Z. Qi et al. investigate the evolution of morphology and hydrophobicity of superhydrophobic polyimide surfaces under different ultraviolet intensities. This work will further promote the application of UV method in polyimide superhydrophobic materials.

F. Yang et al. address electrodeposition and characterization of CuTe and Cu<sub>2</sub>Te thin films. The results suggest that the epitaxial electrodeposition is an ideal method for deposition of compound semiconductor films for photoelectric applications.

J. He et al. fabricate mechanical durable polysiloxane superhydrophobic materials. The materials show stable superhydrophobicity after the surfaces undergo a long distance friction and its superhydrophobicity can be even slightly enhanced by the surface abrasion.

J. Gou et al. investigate the photoluminescence behaviors of the reddish orange emitting phosphor (CaIn<sub>2</sub>O<sub>4</sub>: Sm<sup>3+</sup> codoped with Zn<sup>2+</sup> or Al<sup>3+</sup> ions). The excellent luminescence properties demonstrate the potential application as new-style reddish orange phosphors on light emitting diode.

Z. Liu et al. synthesize graphene wrapped Sn<sub>x</sub>Ti<sub>1-x</sub>O<sub>2</sub> nanoparticles as anode materials and investigate their electrochemical performance. The results indicate that Sn<sub>x</sub>Ti<sub>1-x</sub>O<sub>2</sub> solid solutions can be used as anode materials for Li-ion batteries.

G. Li et al. investigate the structural and magnetic properties of the Ni<sub>81</sub>Fe<sub>19</sub> thin film grown on the Si substrate. The results confirm that Ni<sub>81</sub>Fe<sub>19</sub>/graphene heterostructure is a potential candidate for spin injection source into semiconductor channel.

C. W. Lai synthesizes the anodic TiO<sub>2</sub> films with different surface morphologies using electrochemical anodization technique. The anodic TiO<sub>2</sub> nanotubes generate a good photocurrent response of 1 mA/cm<sup>2</sup> with photoconversion efficiency of 2% in the photoelectrochemical water splitting studies.

As guest editors for this special issue, we hope that this special issue will not only provide the readers with accurate data, updated research, and important questions to be resolved, but also stimulate further developments in the field of nanostructured surfaces, coatings, and films.

## Acknowledgments

The editors gratefully thank the authors for their contributions to this special issue and the reviewers for their constructive comments.

*Mengnan Qu  
Jiamin Wu  
Qi Wang  
Yuanlie Yu  
Jinmei He*

## Research Article

# Structural and Magnetic Properties of Ni<sub>81</sub>Fe<sub>19</sub> Thin Film Grown on Si(001) Substrate via Single Graphene Layer

Gui-fang Li, Shibin Liu, Shanglin Yang, and Yongqian Du

*School of Electronics and Information, Northwestern Polytechnical University, 127 West Youyi Road, Xi'an, Shaanxi 710072, China*

Correspondence should be addressed to Gui-fang Li; [gfli@nwpu.edu.cn](mailto:gfli@nwpu.edu.cn)

Received 10 December 2014; Accepted 5 February 2015

Academic Editor: Yuanlie Yu

Copyright © 2015 Gui-fang Li et al. This is an open access article distributed under the Creative Commons Attribution License, which permits unrestricted use, distribution, and reproduction in any medium, provided the original work is properly cited.

We prepared magnetic thin films Ni<sub>81</sub>Fe<sub>19</sub> on single-crystal Si(001) substrates via single graphene layer through magnetron sputtering for Ni<sub>81</sub>Fe<sub>19</sub> and chemical vapor deposition for graphene. Structural investigation showed that crystal quality of Ni<sub>81</sub>Fe<sub>19</sub> thin films was significantly improved with insertion of graphene layer compared with that directly grown on Si(001) substrate. Furthermore, saturation magnetization of Ni<sub>81</sub>Fe<sub>19</sub>/graphene/Si(001) heterostructure increased to 477 emu/cm<sup>3</sup> with annealing temperature  $T_a = 400^\circ\text{C}$ , which is much higher than values of Ni<sub>81</sub>Fe<sub>19</sub>/Si(001) heterostructures with  $T_a$  ranging from 200°C to 400°C.

## 1. Introduction

Efficient and robust injection of spin polarized electrons into semiconductor channel and manipulating the injected spin electrons have been persistent problems for semiconductor-based spintronic devices [1–3]. Hanle effect curves from ferromagnetic metal into semiconductor channel by three-terminal geometry have been reported [4–7]; moreover, the spin valve signals from ferromagnetic metal into semiconductor channel were investigated by four-terminal geometry [8–10]; various insulator layers such as MgO, Al<sub>2</sub>O<sub>3</sub>, and SiO<sub>2</sub> were inserted between ferromagnetic metal and semiconductor to solve the conductance mismatch problem [11–14]. Although clear Hanle signals were obtained for three-terminal geometry in ferromagnetism/insulator/semiconductor system, the high contact resistance area products resulting from the insulator layer were a serious issue [15].

Graphene was a potential candidate for an insulator tunneling barrier because (1) it exhibited poor conductivity perpendicular to the plane although it is very conductive in plane [16] and (2) it is a highly uniform, defect-free, and thermally stable layer. Cobas et al. reported that clear magnetoresistance curves were obtained for graphene-based magnetic tunneling junctions in which graphene works as a tunneling barrier [17]. van't Erve et al. reported spin injection

from NiFe thin film into Si channel via graphene by three-terminal geometry [18]. However, the previous studies were restricted to the electrical properties of NiFe/graphene/Si heterostructures. The structural and magnetic properties of NiFe thin film grown on Si(001) substrate via graphene were rarely investigated.

Given this background, the purpose of the present study has been to fabricate Ni<sub>81</sub>Fe<sub>19</sub>/graphene heterostructures on Si(001) substrates and investigate their structural and magnetic properties. For this purpose, we prepared 50-nm thick Ni<sub>81</sub>Fe<sub>19</sub> thin films on Si(001) substrate via single graphene layer by magnetron sputtering with various annealing temperature,  $T_a$ . We also prepared 50-nm thick Ni<sub>81</sub>Fe<sub>19</sub> thin films directly grown on Si(001) substrates for comparison. The intensity of 111 peak and saturation magnetization significantly increased for Ni<sub>81</sub>Fe<sub>19</sub> thin films compared with that directly grown on Si(001) substrate with  $T_a = 400^\circ\text{C}$ , indicating the improvement of crystal structure. These results demonstrated that the structural and magnetic properties of Ni<sub>81</sub>Fe<sub>19</sub> thin film can be improved with insertion of graphene between ferromagnetic metal and semiconductor.

This paper is organized as follows. Section 2 describes materials and methods. Section 3 presents our experimental results regarding structural and magnetic properties of Ni<sub>81</sub>Fe<sub>19</sub>/graphene/Si(001) heterostructure and discussion. Section 4 summarizes our results and concludes.

## 2. Materials and Methods

Two kinds of layer structures were fabricated: firstly, (from the substrate side) graphene/ $\text{Ni}_{81}\text{Fe}_{19}$  (50 nm)/ $\text{AlO}_x$  (1 nm) on a Si(001) single-crystal substrate. Graphene was fabricated by chemical vapor deposition (CVD) on copper foil; then the copper foil was cut into the size of  $20 \times 20 \text{ mm}^2$ . Photoresist was coated on the surface of the graphene in order to assist the following wet-transfer process and add the copper foil into ferric trichloride to completely etch the copper. Then the photoresist-coated graphene was physically transferred on the Si(001) substrate which was cleaned by hydrofluoric acid solution and the photoresist was removed by acetone. Finally the sample was washed by deionized water. The prepared graphene/Si(001) substrate was installed in a high-vacuum chamber with base pressure of  $5.0 \times 10^{-4} \text{ Pa}$ ; the 50-nm thick  $\text{Ni}_{81}\text{Fe}_{19}$  thin films were deposited by magnetron sputtering at room temperature (RT) and then subsequently annealing *in situ* at temperature  $T_a = 400^\circ\text{C}$ . Secondly, we also fabricated 50-nm thick  $\text{Ni}_{81}\text{Fe}_{19}$  films directly grown on Si(001) at RT, which were annealed with  $T_a$  ranging from  $200^\circ\text{C}$  to  $400^\circ\text{C}$ .

We investigated the structural properties of the graphene through ALMEGA Dispersive Raman spectrometer (ALMEGA-TM) with a wavelength of 532 nm. The surface morphologies were observed using atomic force microscopy. The structural properties of  $\text{Ni}_{81}\text{Fe}_{19}$  thin films were investigated by X-ray diffraction (XRD)  $\theta$ - $2\theta$  scan. The magnetic properties of  $\text{Ni}_{81}\text{Fe}_{19}$  thin films were investigated through vibrating sample magnetometer (VersaLab, Quantum Design) at RT.

## 3. Results and Discussion

**3.1. Structural Properties of  $\text{Ni}_{81}\text{Fe}_{19}$ /Graphene/Si(001) Heterostructures.** Firstly, we describe the structural properties of  $\text{Ni}_{81}\text{Fe}_{19}$ /graphene/Si(001) heterostructure. Figure 1 shows the Raman spectra of graphene on single-crystal Si(001) substrate. The typical G and 2D peak were observed at shift of  $1596 \text{ cm}^{-1}$  and  $2685 \text{ cm}^{-1}$ , respectively. The peak intensity ratio of  $I_{2D}/I_G$  is about 1.6; the higher peak intensity ratio for 2D peak compared with that of G peak indicated the graphene was single layer. Furthermore, the full width at half maximum (FWHM) of 2D peak was about  $21 \text{ cm}^{-1}$ , which is very close to the  $25 \text{ cm}^{-1}$  for the perfect single graphene layer. Although D peak was observed at shift of  $1352 \text{ cm}^{-1}$  which is related to the defect in the graphene layer, the peak intensity ratio  $I_D/I_G \approx 0.06$  which is appreciably low, indicating the prepared graphene was almost defect-free [19].

Figure 2 shows the surface morphologies of  $\text{Ni}_{81}\text{Fe}_{19}$  thin film on Si(001) substrate via single graphene layer by atomic force microscopy (AFM) measurements, the 50-nm thick  $\text{Ni}_{81}\text{Fe}_{19}$  thin film had sufficiently flat surface morphologies with root mean square (rms) roughness of 0.47 nm, the  $\text{Ni}_{81}\text{Fe}_{19}$  film was deposited at RT and subsequently annealed at  $400^\circ\text{C}$  on Si(001) substrate via graphene layer. This rms value was almost similar to that  $\text{Ni}_{81}\text{Fe}_{19}$  thin film directly

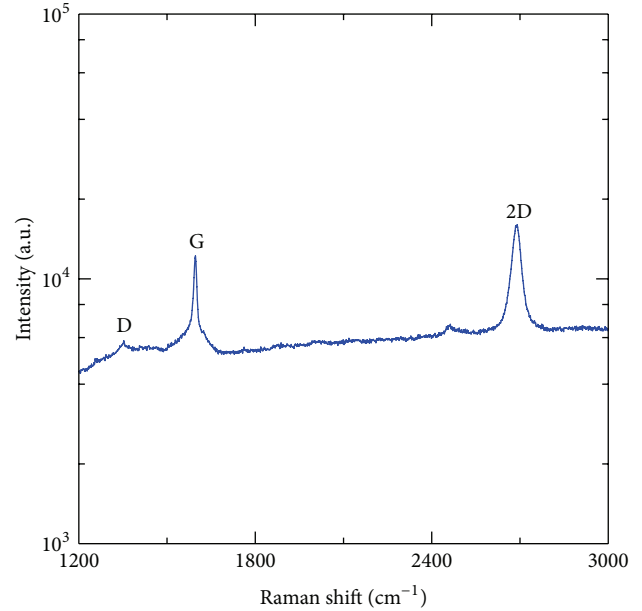


FIGURE 1: The Raman spectra of graphene on single-crystal Si(001) substrate.

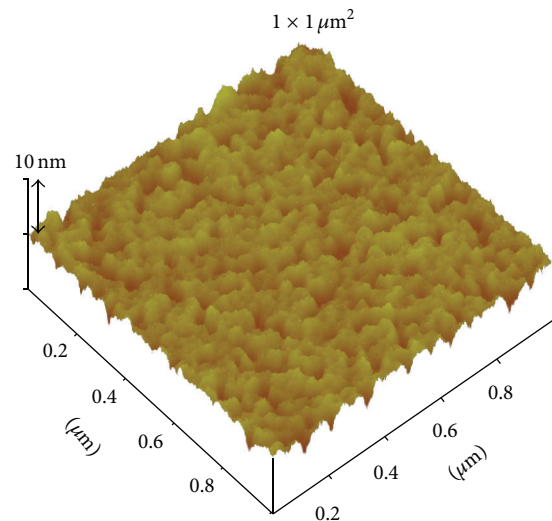


FIGURE 2: Three-dimensional AFM image ( $1 \times 1 \mu\text{m}^2$ ) of the surface topography of 50-nm thick  $\text{Ni}_{81}\text{Fe}_{19}$  thin film on Si(001) substrate via single graphene annealed at  $400^\circ\text{C}$ .

grown on MgO-buffered MgO substrate with value of 0.31 nm at annealing temperature  $T_a$  of  $400^\circ\text{C}$ .

Figure 3 shows X-ray diffraction patterns of 50-nm thick  $\text{Ni}_{81}\text{Fe}_{19}$  films grown on Si(001) substrate via single graphene layer with annealing temperature of  $400^\circ\text{C}$ . The X-ray diffraction patterns of 50-nm thick  $\text{Ni}_{81}\text{Fe}_{19}$  films directly grown on Si(001) were also shown for comparison, in which the  $\text{Ni}_{81}\text{Fe}_{19}$  films were as-deposited and postdeposition annealed at temperature ranging from  $200^\circ\text{C}$  to  $300^\circ\text{C}$ . No appreciable peak was observed for the as-deposited  $\text{Ni}_{81}\text{Fe}_{19}$  films, indicating that it was amorphous film. With increasing

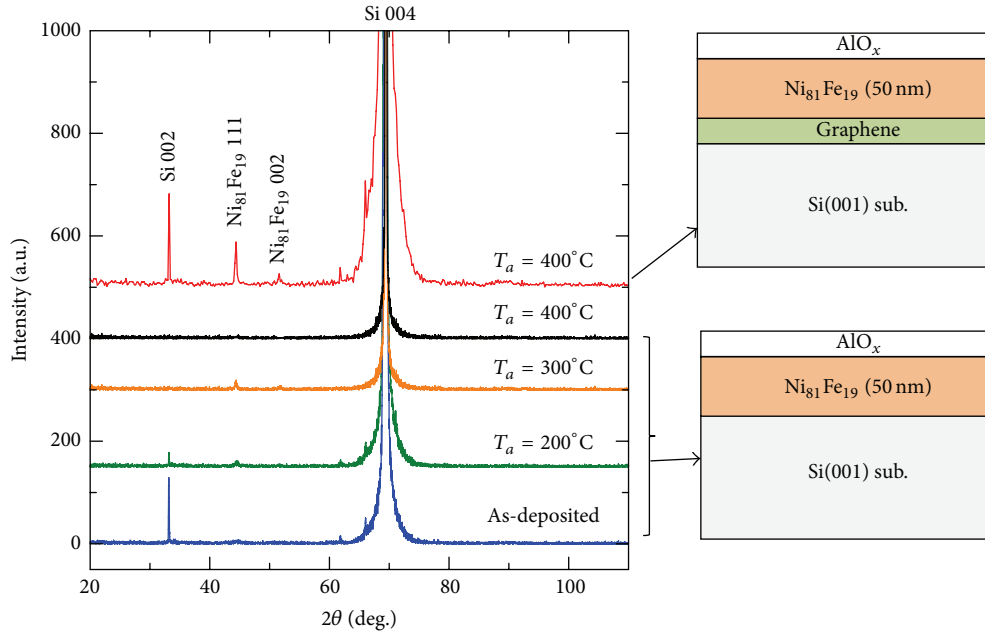


FIGURE 3: X-ray diffraction patterns of 50-nm thick  $\text{Ni}_{81}\text{Fe}_{19}$  films grown on Si(001) substrate with various annealing temperature  $T_a$ , in which one set of curves indicate the  $\text{Ni}_{81}\text{Fe}_{19}/\text{Si}(001)$  heterostructures with  $T_a$  ranging from 200°C to 300°C and as-deposited  $\text{Ni}_{81}\text{Fe}_{19}$  films, the other set of curve indicate the  $\text{Ni}_{81}\text{Fe}_{19}/\text{graphene}/\text{Si}(001)$  heterostructure with  $T_a = 400^\circ\text{C}$ .

the annealing temperature, the 111 peak of  $\text{Ni}_{81}\text{Fe}_{19}$  films appeared for  $T_a$  up to 200°C. In this sense, the crystal structure of the as-deposited  $\text{Ni}_{81}\text{Fe}_{19}$  films was improved by the annealing. With continuous increasing the  $T_a$  to 300°C, 002 peak of  $\text{Ni}_{81}\text{Fe}_{19}$  films was obtained and the intensity of 111 peak slightly increased compared with that for  $T_a = 200^\circ\text{C}$ ; however, the 002 peak of single-crystalline silicon substrate disappeared with  $T_a = 300^\circ\text{C}$ , which was possibly due to the interdiffusion between  $\text{Ni}_{81}\text{Fe}_{19}$  films and Si at relatively high annealing temperature. In order to confirm the supposition, the annealing temperature was increased up to 400°C. No appreciable 111 and 002 peaks of  $\text{Ni}_{81}\text{Fe}_{19}$  films and 002 peak of silicon substrate were observed. The graphene was inserted between  $\text{Ni}_{81}\text{Fe}_{19}$  films and Si(001) substrate as shown in Figure 3; the intensity of 111 and 002 peaks was significantly increased with  $T_a = 400^\circ\text{C}$  and the interdiffusion between  $\text{Ni}_{81}\text{Fe}_{19}$  films and Si(001) substrate was prevented; the crystal structure of  $\text{Ni}_{81}\text{Fe}_{19}$  films was significantly improved by inserting graphene layer. Furthermore, the XRD patterns show that the heterostructure is composed of face centered cubic (fcc) structure, which is consistent with the fact that fcc structure is dominant in high Ni content  $\text{Ni}_{81}\text{Fe}_{19}$  film [20].

**3.2. Magnetic Properties of 50-nm Thick  $\text{Ni}_{81}\text{Fe}_{19}$  Thin Films Grown on Si(001) Substrate via Single Graphene Layer.** Next, we describe the magnetic properties of  $\text{Ni}_{81}\text{Fe}_{19}$  thin films grown on Si(001) via graphene layer and that directly grown on Si(001) substrate. Figure 4(a) shows the magnetic hysteresis ( $M$ - $H$ ) curves of  $\text{Ni}_{81}\text{Fe}_{19}$  thin films at 300 K. The  $M$ - $H$  curve with  $T_a = 400^\circ\text{C}$  was that  $\text{Ni}_{81}\text{Fe}_{19}$  thin film grew on Si(001) substrate via graphene layer; the other two curves were those  $\text{Ni}_{81}\text{Fe}_{19}$  thin films directly grown on Si(001)

substrates. The magnetic field ( $H$ ) was applied in the plane of the film along [100] direction of silicon substrate. The saturation magnetization ( $M_s$ ) was 310  $\text{emu}/\text{cm}^3$  for  $\text{Ni}_{81}\text{Fe}_{19}$  thin films deposited at RT without annealing; the  $M_s$  slightly increased to 350  $\text{emu}/\text{cm}^3$  with  $T_a = 300^\circ\text{C}$ . The obtained  $M_s$  values were close to those  $\text{Ni}_{81}\text{Fe}_{19}$  thin films grown on Ta and Ti substrate [21]. With increasing  $T_a$  up to 400°C, no appreciable  $M$ - $H$  curve was observed for  $\text{Ni}_{81}\text{Fe}_{19}/\text{Si}(001)$  heterostructure, which was due to the nonnegligible interdiffusion between  $\text{Ni}_{81}\text{Fe}_{19}$  thin film and Si(001) substrate. However, with insertion of the graphene between  $\text{Ni}_{81}\text{Fe}_{19}$  films and Si(001) substrate, the  $M_s$  significantly increased up to 477  $\text{emu}/\text{cm}^3$  for  $T_a = 400^\circ\text{C}$ , indicating that the magnetic properties of  $\text{Ni}_{81}\text{Fe}_{19}$  thin film significantly improved.

Figure 4(b) shows the coercive force ( $H_c$ ) for  $\text{Ni}_{81}\text{Fe}_{19}$  thin film as a function of  $T_a$ . The  $H_c$  values at 300 K decreased with increasing  $T_a$  from  $H_c = 10$  Oe for the as-deposited film to  $H_c = 3$  Oe for  $T_a = 400^\circ\text{C}$ . The decrease in  $H_c$  with increasing  $T_a$  was probably induced by a decrease in the pinning center density for the magnetic domain motion with increasing  $T_a$  up to 400°C [22].

## 4. Conclusion

We prepared  $\text{Ni}_{81}\text{Fe}_{19}$  thin films grown on Si(001) substrate via graphene layer. First, the Raman spectra showed that the graphene was single layer and almost defect-free. Second, the X-ray pattern of  $\text{Ni}_{81}\text{Fe}_{19}/\text{graphene}/\text{Si}(001)$  heterostructure confirmed that the crystal quality of  $\text{Ni}_{81}\text{Fe}_{19}$  thin films significantly increased with insertion of graphene single layer. Third, sufficiently flat surface morphologies were obtained for  $\text{Ni}_{81}\text{Fe}_{19}$  thin films grown on Si(001) via graphene layer.

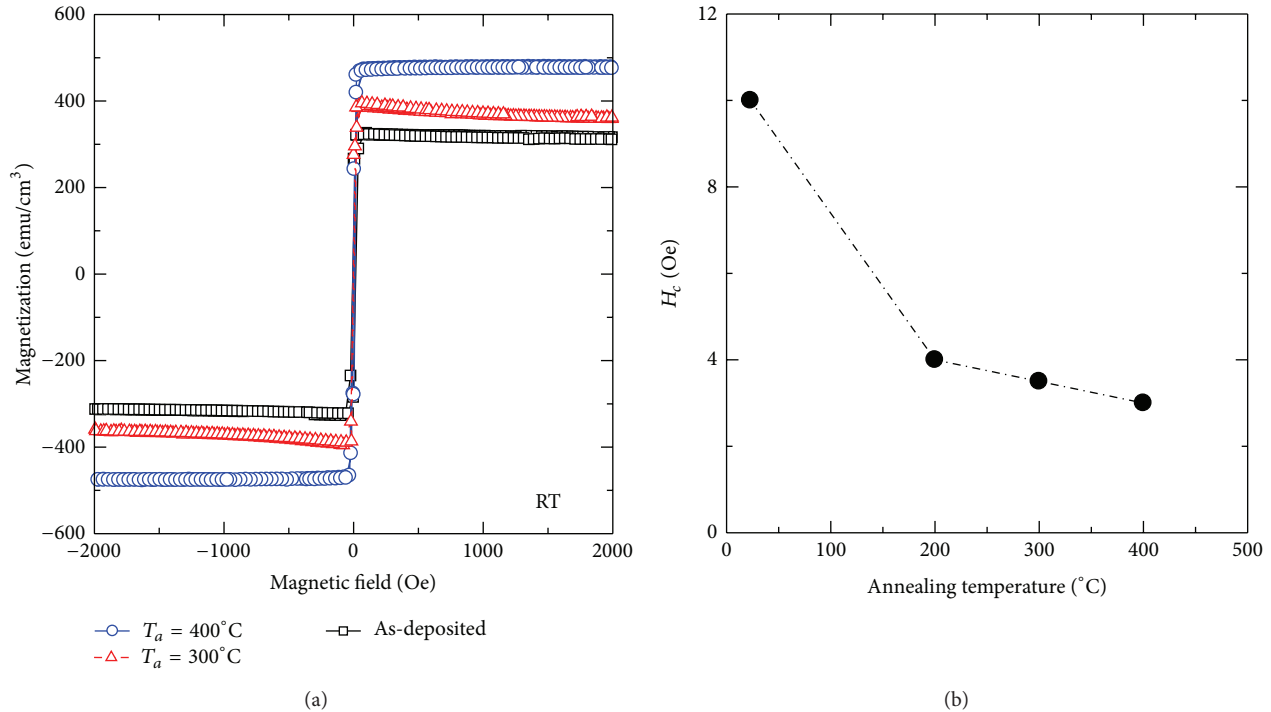


FIGURE 4: (a) Typical magnetic hysteresis curves for  $\text{Ni}_{81}\text{Fe}_{19}/\text{graphene}/\text{Si}(001)$  and  $\text{Ni}_{81}\text{Fe}_{19}/\text{Si}(001)$  heterostructures at 300 K with various  $T_a$ , where  $H$  was applied in the plane of the film along the  $[100]_{\text{Si}}$  direction. (b) The coercive force ( $H_c$ ) for  $\text{Ni}_{81}\text{Fe}_{19}$  thin film as a function of  $T_a$ .

Fourth, relatively higher saturation magnetization values at 300 K were obtained for  $\text{Ni}_{81}\text{Fe}_{19}$  thin films grown on Si(001) via graphene layer. These results confirmed that  $\text{Ni}_{81}\text{Fe}_{19}/\text{graphene}$  heterostructure is a potential candidate for spin injection source for spin injection into semiconductor channel.

## Conflict of Interests

The authors declare that there is no conflict of interests regarding the publication of this paper.

## Acknowledgment

This work was partly supported by The Fundamental Research Funds for the Central Universities (Grant no. 3102014JCQ01059), China.

## References

- [1] X. Lou, C. Adelman, S. A. Crooker et al., "Electrical detection of spin transport in lateral ferromagnet-semiconductor devices," *Nature Physics*, vol. 3, no. 3, pp. 197–202, 2007.
- [2] S. P. Dash, S. Sharma, R. S. Patel, M. P. De Jong, and R. Jansen, "Electrical creation of spin polarization in silicon at room temperature," *Nature*, vol. 462, no. 7272, pp. 491–494, 2009.
- [3] M. Tran, H. Jaffrès, C. Deranlot et al., "Role of  $\delta$ -hole-doped interfaces at ohmic contacts to organic semiconductors," *Physical Review Letter*, vol. 102, no. 3, Article ID 036601, 2009.
- [4] K.-R. Jeon, B.-C. Min, I.-J. Shin et al., "Electrical spin accumulation with improved bias voltage dependence in a crystalline CoFe/MgO/Si system," *Applied Physics Letters*, vol. 98, no. 26, Article ID 262102, 2011.
- [5] H. Saito, S. Watanabe, Y. Mineno et al., "Electrical creation of spin accumulation in  $p$ -type germanium," *Solid State Communications*, vol. 151, no. 17, pp. 1159–1161, 2011.
- [6] A. Jain, L. Louahadj, J. Peiro et al., "Electrical spin injection and detection at  $\text{Al}_2\text{O}_3/n$ -type germanium interface using three terminal geometry," *Applied Physics Letters*, vol. 99, no. 16, Article ID 162102, 2011.
- [7] I. A. Fischer, L.-T. Chang, C. Sürgers et al., "Hanle-effect measurements of spin injection from  $\text{Mn}_5\text{Ge}_3\text{C}_{0.8}/\text{Al}_2\text{O}_3$ -contacts into degenerately doped Ge channels on Si," *Applied Physics Letters*, vol. 105, no. 22, Article ID 222408, 2014.
- [8] O. M. J. van't Erve, A. T. Hanbicki, M. Holub et al., "Electrical injection and detection of spin-polarized carriers in silicon in a lateral transport geometry," *Applied Physics Letters*, vol. 91, no. 21, Article ID 212109, 2007.
- [9] T. Sasaki, T. Oikawa, T. Suzuki, M. Shiraishi, Y. Suzuki, and K. Noguchi, "Temperature dependence of spin diffusion length in silicon by Hanle-type spin precession," *Applied Physics Letters*, vol. 96, no. 12, Article ID 122101, 2010.
- [10] Y. Zhou, W. Han, L.-T. Chang et al., "Electrical spin injection and transport in germanium," *Physical Review B*, vol. 84, no. 12, Article ID 125323, 2011.
- [11] G. Schmidt, D. Ferrand, L. W. Molenkamp, A. T. Filip, and B. J. van Wees, "Fundamental obstacle for electrical spin injection from a ferromagnetic metal into a diffusive semiconductor," *Physical Review B: Condensed Matter and Materials Physics*, vol. 62, no. 8, pp. R4790–R4793, 2000.

- [12] E. I. Rashba, "Theory of electrical spin injection: tunnel contacts as a solution of the conductivity mismatch problem," *Physical Review B: Condensed Matter and Materials Physics*, vol. 62, no. 24, Article ID R16267, pp. R16267–R16270, 2000.
- [13] G.-F. Li, T. Taira, K.-I. Matsuda, M. Arita, T. Uemura, and M. Yamamoto, "Epitaxial growth of Heusler alloy  $\text{Co}_2\text{MnSi}/\text{MgO}$  heterostructures on Ge(001) substrates," *Applied Physics Letters*, vol. 98, no. 26, Article ID 262505, 2011.
- [14] G.-F. Li, T. Taira, H.-X. Liu, K.-Z. Matsuda, T. Uemura, and M. Yamamoto, "Fabrication of fully epitaxial CoFe/MgO/CoFe magnetic tunnel junctions on Ge(001) substrates via a MgO interlayer," *Japanese Journal of Applied Physics*, vol. 51, no. 9, Article ID 093003, 2012.
- [15] T. Uemura, K. Kondo, J. Fujisawa, K.-I. Matsuda, and M. Yamamoto, "Critical effect of spin-dependent transport in a tunnel barrier on enhanced Hanle-type signals observed in three-terminal geometry," *Applied Physics Letters*, vol. 101, no. 13, Article ID 132411, 2012.
- [16] K. S. Krishnan and N. Ganguli, "Large anisotropy of the electrical conductivity of graphite," *Nature*, vol. 144, no. 3650, p. 667, 1939.
- [17] E. Cobas, A. L. Friedman, O. M. J. van't Erve, J. T. Robinson, and B. T. Jonker, "Graphene as a tunnel barrier: graphene-based magnetic tunnel junctions," *Nano Letters*, vol. 12, no. 6, pp. 3000–3004, 2012.
- [18] O. M. J. van't Erve, A. L. Friedman, E. Cobas, C. H. Li, J. T. Robinson, and B. T. Jonker, "Low-resistance spin injection into silicon using graphene tunnel barriers," *Nature Nanotechnology*, vol. 7, no. 11, pp. 737–742, 2012.
- [19] G. Wang, M. Zhang, Y. Zhu et al., "Direct growth of graphene film on germanium substrate," *Scientific Reports*, vol. 3, article 2465, 2013.
- [20] B. Liu, R. Huang, J. Wang et al., "Mössbauer investigation of Fe-Ni fine particles," *Journal of Applied Physics*, vol. 85, no. 2, pp. 1010–1013, 1999.
- [21] S. Yang, S. Liu, B. Guo, W. Feng, and X. Hou, "Comparison of soft magnetic properties of  $\text{Ni}_{81}\text{Fe}_{19}$  film with different substrates used for microfluxgate," *Micro & Nano Letters*, vol. 8, no. 10, pp. 602–605, 2013.
- [22] E. C. Stoner and E. P. Wohlfarth, "A mechanism of magnetic hysteresis in heterogenous alloys," *Philosophical Transactions of the Royal Society A*, vol. 240, p. 599, 1948.

## Research Article

# Adsorption of Organic Dyes by TiO<sub>2</sub>@Yeast-Carbon Composite Microspheres and Their In Situ Regeneration Evaluation

Zheng Pei,<sup>1</sup> Zhang Kaiqiang,<sup>1</sup> Dang Yu,<sup>1</sup> Bai Bo,<sup>2</sup> Guan Weisheng,<sup>1</sup> and Suo Yourui<sup>2</sup>

<sup>1</sup>College of Environmental Science and Engineering, Chang'an University, Xi'an 710054, China

<sup>2</sup>Northwest Plateau Institute of Biology, Chinese Academy of Sciences, Xining 810001, China

Correspondence should be addressed to Bai Bo; [baibochina@163.com](mailto:baibochina@163.com)

Received 21 July 2014; Revised 9 September 2014; Accepted 1 October 2014

Academic Editor: Jinmei He

Copyright © 2015 Zheng Pei et al. This is an open access article distributed under the Creative Commons Attribution License, which permits unrestricted use, distribution, and reproduction in any medium, provided the original work is properly cited.

TiO<sub>2</sub>@yeast-carbon microspheres with raspberry-like morphology were fabricated based on the pyrolysis method. The obtained products were characterized by field emission scanning electron microscopy (FE-SEM), energy dispersive spectrometry (EDS), and X-ray diffraction (XRD). Effects of initial dye concentration and contact time on adsorption capacity of TiO<sub>2</sub>@yeast-carbon for cationic dye methylene blue (MB) and anionic dye congo red (CR) were investigated. Experimental data were described by Langmuir, Freundlich, Temkin, and Koble-Corrigan isotherm models, respectively. It was found that the equilibrium data of MB adsorption were best represented by Koble-Corrigan, and CR adsorption was best described by both Freundlich and Koble-Corrigan isotherm models. The kinetic data of MB and CR adsorption fitted pseudo-second-order kinetic model well. The results demonstrated that TiO<sub>2</sub>@yeast-carbon microspheres achieved favorable removal for the cationic MB in comparison with that for the anionic CR. In addition, regeneration experimental results showed that TiO<sub>2</sub>@yeast-carbon exhibited good recycling stability, reusability, and in situ renewability, suggesting that the as-prepared TiO<sub>2</sub>@yeast-carbon might be used as the potential low cost alternative for recalcitrant dye removal from industrial wastewater. One possible mechanism for regenerating dye-loaded TiO<sub>2</sub>@yeast in situ was also proposed.

## 1. Introduction

Organic dyes are widely and frequently used in various industries as textile, printing, petroleum, paper, and rubber [1, 2]. During the manufacturing and dyeing process, a substantial amount of dyestuff is lost into water, which poses a great threat to the environment. Typically, the presence of these toxic organic compounds reduces light penetration into water, affects photosynthesis of aquatic lives, impedes the growth of microbes, creates toxicity to fish, accumulates in the food chain, and even travels long distance, causing harm not only to the place where they are produced and used but also globally [3]. Moreover, most of the organic dyes are recalcitrant and difficult to degrade because of their complex and stable aromatic molecular structure [4]. Hence, the removal or degradation of organic dyes from water bodies has become a major environmental problem. Till now, some physical or chemical strategies have been

attempted to remove dye contaminants from water, including adsorption [5], advanced oxidation process (AOP) [6], membrane filtration [7], ozonation [8], and coagulation-flocculation [9]. Among the above-mentioned technologies, adsorption has been proven to be one of the most efficient and reliable methods for removing dyes from aqueous solution because of its flexibility, high efficiency, ease of operation, simplicity of design, and insensitivity to toxic pollutants [10]. A wide variety of low cost and easily available materials, such as bentonite [11], fly ash [12], clay [13], active carbon [14], and agriculture wastes [15, 16], have been exploited for the removal of dyes from aqueous solutions.

Yeast-carbon is a porous and amorphous solid carbon material, which is derived mainly from baker's yeast. For example, Nacco and Aquarone [17] firstly reported the fabrication of yeast-carbon by carbonizing yeast cells in gas-heated muffle. The prepared yeast-carbon exhibited larger surface area. Guan et al. [18] synthesized amphiphilic porous

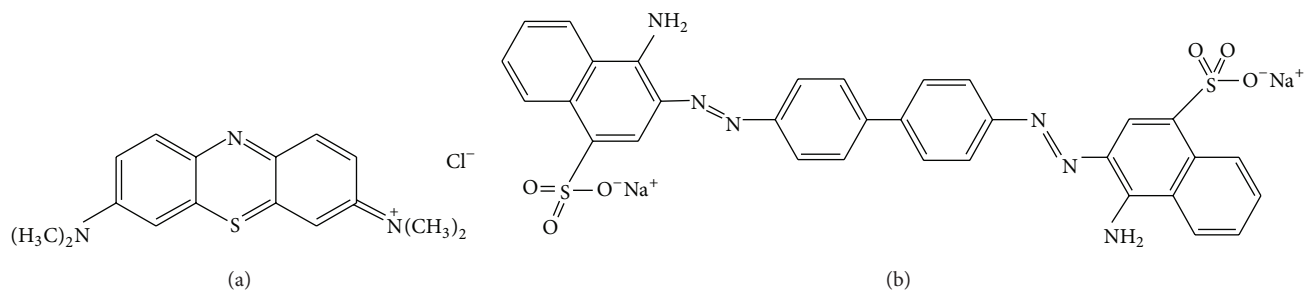


FIGURE 1: The structures of dyes: (a) MB and (b) CR.

hollow carbonaceous spheres via mild hydrothermal treatment of yeast cells and further pyrolyzing. The obtained carbon spheres displayed effective sorption of phenol from water. In comparison with the great successes in the yeast-carbon synthesis, the practical application of yeast-carbon as adsorbent in wastewater treatment has still been limited because the adsorbent could get saturated easily in the adsorption process, which requires extra regeneration or complete replacement [4]. More recently,  $\text{TiO}_2$  has become a hot topic mainly for its excellent photocatalytic performance [19]. The integration of adsorption and  $\text{TiO}_2$  photocatalysis seems to offer a good solution to overcome the shortcoming of extra regeneration or complete replacement from the traditional adsorption process. In such a synergetic process, the rich pore structure of adsorbents might promote the transfer and adsorption of organic dyes, while the  $\text{TiO}_2$  could destroy dyes by photocatalytic oxidation, thus regenerating the adsorbent in situ [20].

In the previous work, we fabricated the novel  $\text{TiO}_2$ @yeast-carbon microsphere with raspberry-like morphology based on the pyrolysis method [21]. In the present work, as a continual job, the prepared hybrid raspberry-like  $\text{TiO}_2$ @yeast-carbon microspheres were further used as adsorbents for removal of two typical organic dyes (Methylene blue and Congo red) from aqueous solution. The adsorption equilibrium isotherms and kinetics was fully conducted. Moreover, in situ regeneration of the adsorbents was investigated, and one possible mechanism for regenerating dye-loaded  $\text{TiO}_2$ @yeast in situ was also proposed.

## 2. Materials and Methods

**2.1. Materials.** The powdered yeast was provided by Angel Yeast Co.  $\text{TiO}_2$  with the primary particle size at 20–30 nm was from Degussa and was used without further purification. Absolute ethanol and double-distilled water were used throughout all the experimental procedures. Methylene blue (MB) and Congo red (CR) were purchased from Xi'an Chemical Agent Company and were used as pollutants in the present work. Analytic grade sodium hydroxide (NaOH) and sulfuric acid ( $\text{H}_2\text{SO}_4$ ) were purchased from Xi'an Chemical Agent Company.

**2.2. Synthesis of  $\text{TiO}_2$ @Yeast-Carbon Microspheres.** In a typical synthesis procedure, 0.1 g of  $\text{TiO}_2$  was dissolved in 200 mL

of distilled water, using ultrasonic vibration for 10 min, and the pH value was adjusted to approximately 9–10 by adding dropwise sodium hydroxide (1.0 mol/L). Then, the dispersion was stirred in magnetic stirrers for 30 min to facilitate particle deaggregation. In a separate vessel, 1.25 g yeast powder was washed with distilled water and absolute ethanol for three times, respectively. Subsequently, the yeast was dispersed in 200 mL of distilled water and magnetically stirred vigorously for 30 min, and the pH value was adjusted to approximately 3 with sulfuric acid (1.0 mol/L). After that, the above  $\text{TiO}_2$  and yeast cells were gathered by centrifugation from their own suspensions and redispersed in 200 mL of distilled water, respectively. Thereafter,  $\text{TiO}_2$  and yeast suspensions were slowly mixed with continuously magnetic stirring for 1.5 h at room temperature and left for 3.0 h without further stirring in order to ensure the formation of  $\text{TiO}_2$ @yeast particles. The mixture was collected by centrifugation, washed with distilled water and absolute ethanol for three times, and then desiccated at 353 K for 1.0 h. Finally, the dried  $\text{TiO}_2$ @yeast particles were calcined at 573 K in a nitrogen pipe furnace for 1.0 h and cooled to room temperature. After that,  $\text{TiO}_2$ @yeast-carbon hybrid microspheres were obtained. For comparison, the yeast-carbon was prepared by similar method without adding  $\text{TiO}_2$ .

**2.3. Characterization.** Surface structure and morphology of samples were observed by using Philip XL-30 field emission scanning electron microscope (FE-SEM). Detailed composition characterization was carried out with energy-dispersive spectroscopy (EDS) analysis. X-ray diffraction (XRD) patterns were conducted on X. Pert Pro diffractometer using  $\text{Cu K}\alpha$  radiation ( $\lambda = 0.15418$  nm) at a scanning rate of  $10^\circ/\text{min}$ .

**2.4. Dye Solution Preparation.** Methylene blue and Congo red were cationic and anionic dyes, respectively, and were used as model pollutants to study the adsorption properties of  $\text{TiO}_2$ @yeast-carbon microspheres. The structures of both dyes are shown in Figure 1. Stock MB and CR solutions (1.0 g/L) were prepared by dissolving 1 g of MB or CR in 1 L of double distilled water, respectively. Experimental solutions of desired concentration were obtained by further dilution.

**2.5. Analysis of Organic Dyes.** The samples were separated from the solution at set intervals with centrifugation at 3000 rpm for 5 min and were returned to the reaction system

immediately after each analysis. The concentrations of MB and CR in the supernatant solution were determined using a double beam UV/visible spectrophotometer (UV-752, Shanghai) at 666.4 nm and 499.0 nm, respectively. Calibration curve was found to be very reproducible and linear over the concentration range used in this work.

**2.6. Batch Adsorption Experiments.** Adsorption studies were carried by adding 0.25 g TiO<sub>2</sub>@yeast-carbon microspheres and 100 mL MB or CR solution of certain concentration into a set of flasks followed by stirring in magnetic stirrers at room temperature without adjusting the solution pH. The flasks were wrapped in aluminum foil to prevent photolysis. After desired adsorption time, 5 mL sample supernatant was taken out to analyze the residual concentration of MB or CR. In all sets of experiments, each test was conducted in duplicates, and the mean value was recorded. The amount of adsorbed dye per gram TiO<sub>2</sub>@yeast-carbon hybrid microspheres at equilibrium ( $q_e$ , mg/g) and at time  $t$  ( $q_t$ , mg/g) was calculated by the following equation:

$$\begin{aligned} q_e &= \frac{(C_0 - C_e)V}{m}, \\ q_t &= \frac{(C_0 - C_t)V}{m}, \end{aligned} \quad (1)$$

where  $C_0$ ,  $C_e$ , and  $C_t$  (mg/g) are concentrations of dye at initial, equilibrium, and time  $t$ , respectively.  $V$  (L) is the volume of the dye solution, and  $m$  (g) is the mass of adsorbent.

**2.7. In Situ Regeneration of TiO<sub>2</sub>@Yeast-Carbon Microspheres.** In order to evaluate the reusability and renewability of the TiO<sub>2</sub>@yeast-carbon, MB was chosen as the model pollutant. The procedure is as follows: an amount of 0.14 g of prepared TiO<sub>2</sub>@yeast-carbon was suspended in a MB solution (100 mL) with an initial concentration of 2 mg/L in a beaker. The solution was magnetically stirred in dark for about 2.5 h to ensure the establishment of an adsorption-desorption equilibrium. Then, the mixed suspensions were irradiated under a UV lamp (Philips TL 8W/08F8T5/BLB; 0.0155 m bulb diameter, 0.26 m bulb length, and 1.2 W UVA output) located directly above the flasks at a distance of 6 cm from the surface of the solution. The aqueous samples were taken out at a regular interval time and analyzed until a second equilibrium was achieved, which meant that a cycle was over. At the end of each run, the dye-loaded TiO<sub>2</sub>@yeast-carbon microspheres were collected by centrifugation, washed thoroughly, and dried to be reused in the next cycle. Another cycle of sorption-regeneration was repeated in the same manner as mentioned above. All of the experiments were performed in triplicate at room temperature. The removal rate ( $\eta$ , %) of MB was calculated by the following equation:

$$\eta = \frac{(C_0 - C_e)}{C_0} \times 100\%. \quad (2)$$

### 3. Results and Discussion

**3.1. Characterization.** Figure 2(a) is the SEM images of yeast-carbon. It reveals that the yeast-carbon had smooth surface morphology and uniform size (length =  $3.5 \pm 0.4 \mu\text{m}$ ; width =  $2.3 \pm 0.5 \mu\text{m}$ ). Figure 2(b) depicts an image of the TiO<sub>2</sub>@yeast which is the precursor of TiO<sub>2</sub>@yeast-carbon. The size of TiO<sub>2</sub>@yeast (length =  $3.7 \pm 0.4 \mu\text{m}$ ; width =  $2.6 \pm 0.5 \mu\text{m}$ ) increased compared with the yeast-carbon in Figure 2(a), which may be assigned to the attachment of TiO<sub>2</sub> particles. Figure 2(c) presents an overall image of the TiO<sub>2</sub>@yeast-carbon hybrid microspheres. The micrograph in Figure 2(c) indicates that the particles inherited the general shape and good dispersity of the precursor in Figure 2(b). Figures 2(d) and 2(e) expresses the TiO<sub>2</sub>@yeast-carbon spheres in different magnifications. The TiO<sub>2</sub>@yeast-carbon in Figure 2(d) exhibits a typical raspberry-like structure since the TiO<sub>2</sub> nanoparticles were randomly decorated on the surface of carbon microspheres. Figure 2(f) displays the detailed information of the outer appearance of the TiO<sub>2</sub>@yeast-carbon microspheres under a higher magnification. It can be clearly seen that the surfaces of the microspheres were coated with small TiO<sub>2</sub> particles, whereas some residual bare areas still remained. These residual bare regions were of great benefit to the adsorption of dye molecules in aqueous solution.

Additionally, the unique raspberry-like structure of TiO<sub>2</sub>@yeast-carbon is further confirmed from the EDS analysis. In the insert image in Figure 2(a), C, O, Zn, P, and Pt elements can be observed. C, O, and P result from the yeast cells, Zn element comes from the yeast cells activation agent ZnCl<sub>2</sub>, and Pt is assumed to be due to the metal spraying before SEM studies. C, O, P, and Ti elements are observed in the insert image in Figure 2(d). C, O, and P elements also derive from the yeast, and the Ti element detected indicates that TiO<sub>2</sub> has been already successfully coated on the yeast carbon.

XRD patterns of TiO<sub>2</sub>, yeast, yeast-carbon, and TiO<sub>2</sub>@yeast-carbon are shown in Figure 3. Diffraction peaks at around 20° in Figures 3(a) and 3(b) indicate the formation of amorphous species. Figure 3(c) illustrates an XRD pattern of TiO<sub>2</sub>@yeast-carbon. The broad peak at 20° is mainly caused by the amorphous structure of yeast-carbon. Moreover, the remaining diffraction peaks are in good agreement with TiO<sub>2</sub> in Figure 3(d) and no other diffraction peaks can be detected within the investigated range. Figure 3(d) exhibits the XRD pattern of the original components of TiO<sub>2</sub> nanoparticles (P25 TiO<sub>2</sub>: 78% anatase-type TiO<sub>2</sub> and 22% rutile-type TiO<sub>2</sub>). The observed sharper diffraction peaks at 25°, 37.9°, 48.2°, 54.8°, and 63.0° are consistent with diffraction peaks of anatase-type TiO<sub>2</sub> (JCPDS. number: 21-1272) [22], and the other diffraction peaks centering at 69.0°, 70.3°, and 75.0° correspond well with the reflections of rutile-type TiO<sub>2</sub> (JCPDS. number: 21-1276) [23].

**3.2. Adsorption Capacity of MB and CR on TiO<sub>2</sub>@Yeast-Carbon.** Figure 4 describes the measured isotherms for MB and CR on the TiO<sub>2</sub>@yeast-carbon samples at the same initial dye concentration. From Figure 4,  $Q_t$  for MB and CR

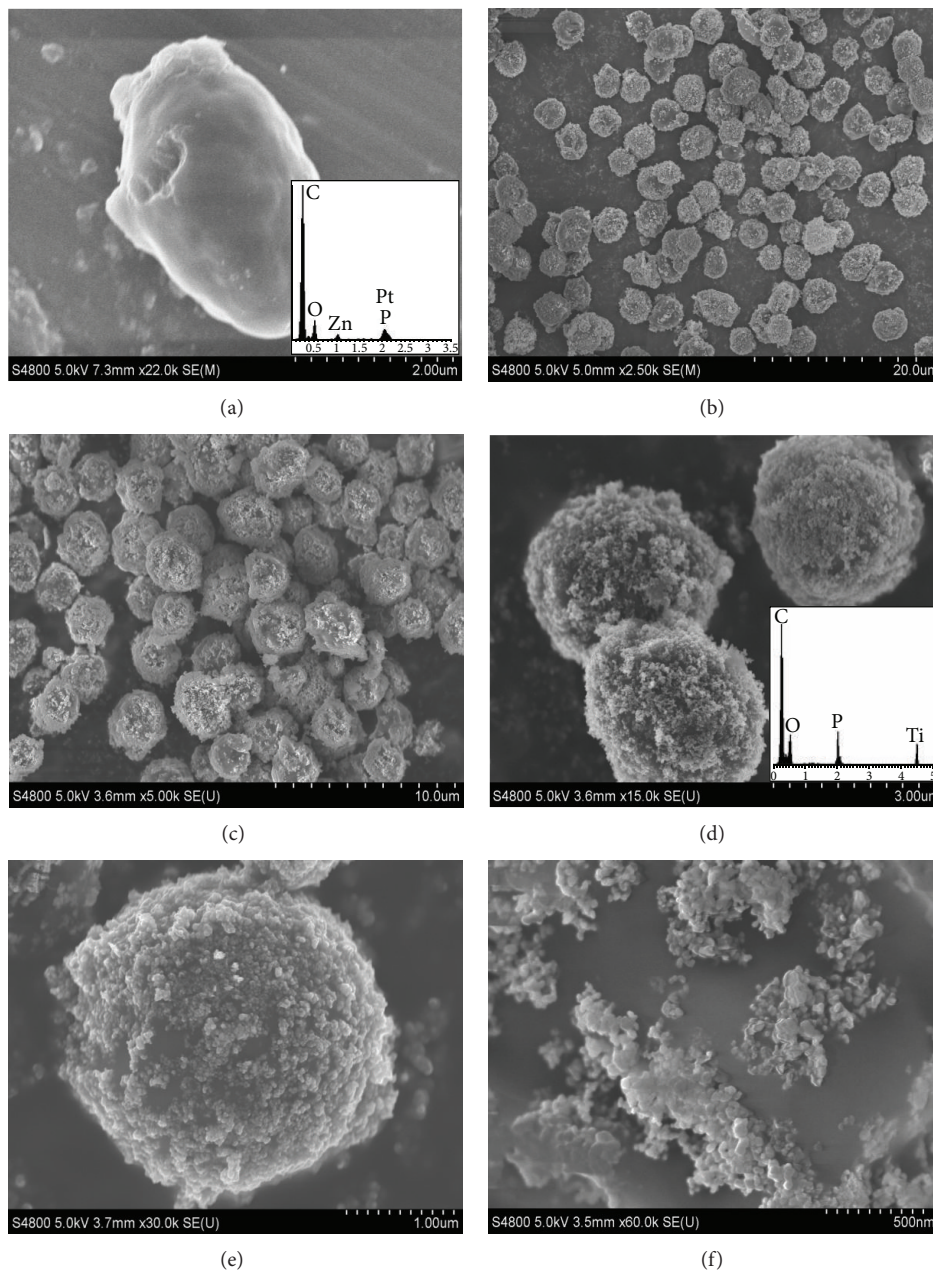


FIGURE 2: FE-SEM images of (a) the yeast-carbon, (b) general observation of the raspberry-like  $\text{TiO}_2$ @yeast precursor, (c) the overall view of the raspberry-like  $\text{TiO}_2$ @yeast-carbon microspheres, (d-e) the selected raspberry-like  $\text{TiO}_2$ @yeast-carbon microspheres, and (f) typical raspberry-like  $\text{TiO}_2$ @yeast-carbon microspheres observed under high magnifications.

increased dramatically during the initial time. Then, MB and CR adsorption reached equilibrium at the time of about 80 and 130 min, respectively, which was similar to observations of Hameed et al. [24]. As shown in Figure 4, two adsorption stages existed obviously: a very rapid initial adsorption over a few minutes, followed by a longer period of much slower uptake. The rapid uptake at the initial contact time could be ascribed to the fact that there were plenty of available adsorption active sites on the surface of  $\text{TiO}_2$ @yeast-carbon, while the slow rate of dye adsorption was probably due to the repulsive forces between the dye molecules in the solution

and on the surface of the  $\text{TiO}_2$ @yeast-carbon [25]. It can also be seen from Figure 4 that the adsorption capacity of cationic dye MB by  $\text{TiO}_2$ @yeast-carbon was significantly higher than that of anionic dye CR, as manifested by the approximately 3-fold higher adsorption capacity of the CR, which could be assigned to the negatively charged surface of the adsorbent [21, 26]. Moreover, because the CR possesses more polar atoms (N and S), the interaction between CR and  $\text{TiO}_2$ @yeast-carbon may be stronger than that between MB and  $\text{TiO}_2$ @yeast-carbon. This may induce a collapse in the pore structure of  $\text{TiO}_2$ @yeast-carbon and then create a

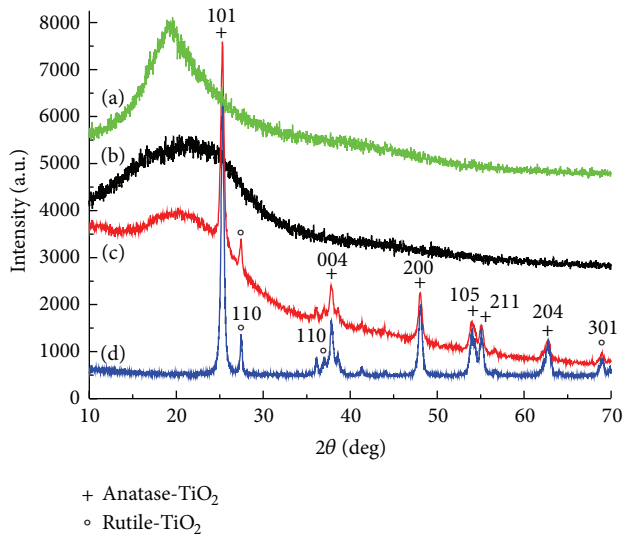


FIGURE 3: XRD patterns for (a) the premier yeast; (b) the prepared yeast-carbon; (c)  $\text{TiO}_2$ @yeast-carbon; (d) the pure  $\text{TiO}_2$ .

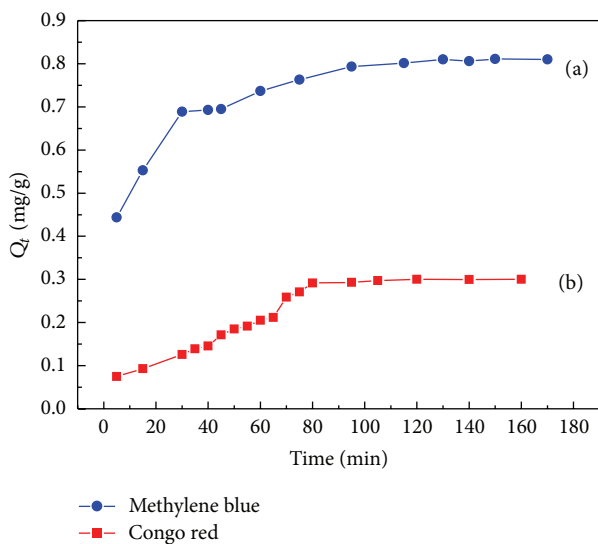


FIGURE 4: Adsorption isotherms for MB: (a) and CR: (b) on  $\text{TiO}_2$ @yeast-carbon.

sharp decrease in the adsorption capacity. It is noteworthy that the adsorption capacity of MB on  $\text{TiO}_2$ @yeast-carbon is similar to that of Basic Green 5 measured by Juang et al. [27]. According to the adsorption results above, it is experimentally demonstrated that  $\text{TiO}_2$ @yeast-carbon may be a good adsorbent for the removal of MB even if no chemical modification is taken.

The favorable removal of cationic MB in comparison with the anionic CR by  $\text{TiO}_2$ @yeast-carbon adsorbent can be further verified by changing of initial dye concentration. Figure 5 illustrates the influence of dye concentration on adsorption capacity of  $\text{TiO}_2$ @yeast-carbon nanocomposite for MB and CR. As shown in Figure 5, the adsorption capacity for MB and CR augmented with the increase of dye concentration, which

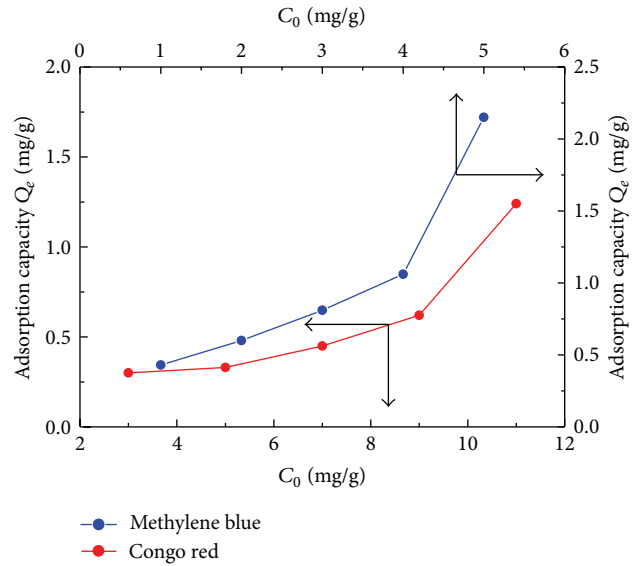


FIGURE 5: Influence of adsorbate concentration on adsorption capacity of  $\text{TiO}_2$ @yeast-carbon nanocomposite for MB and CR.

could be explained by the elevated concentration gradient between the bulk solution and the surface of the  $\text{TiO}_2$ @yeast-carbon [25]. As presented in Figure 5, the adsorption of MB on  $\text{TiO}_2$ @yeast-carbon showed higher capacity than CR within the investigated concentration. However, the adsorption capacity for MB or CR is sure to reach a constant if the dye concentration exceeds continuously because a certain amount of  $\text{TiO}_2$ @yeast-carbon could only provide limited active adsorption sites.

**3.3. Adsorption Isotherms.** Adsorption isotherm models are important to investigate how adsorbates interact with adsorbents [28] and are widely used to describe the adsorption progress [10]. Langmuir, Freundlich, Temkin, and Koble-Corrigan isotherm models were used to fit the equilibrium data obtained from the study of MB and CR adsorption onto  $\text{TiO}_2$ @yeast-carbon at initial concentrations of 1.0~5.0 mg/L and 3.0~11.0 mg/L, respectively.

Langmuir isotherm assumes monolayer adsorption onto a surface containing a finite number of adsorption sites of uniform strategies of adsorption with no transmigration of the adsorbate in the plane of surface [10, 29]. The nonlinear Langmuir equation is given as

$$Q_e = \frac{Q_m K_L C_e}{1 + K_L C_e}, \quad (3)$$

where  $Q_e$  is the amount of dye adsorbed per unit mass of the hybrid microspheres at equilibrium (mg/g),  $C_e$  is the equilibrium concentration of the adsorbate (mg/L),  $Q_m$  is the theoretical maximum adsorption capacity (mg/g), and  $K_L$  is the Langmuir adsorption constant reflecting the tendency of adsorption (L/mg).

To predict whether the adsorption process is favorable or unfavorable, equilibrium parameter  $R_L$ , a dimensionless constant separation factor, is defined by Weber and Chakravorti as the following equation [30]:

$$R_L = \frac{1}{1 + K_L C_{0,m}}, \quad (4)$$

where  $C_{0,m}$  is the highest initial dye concentration (mg/L); the value of  $R_L$  indicates the type of isotherm to be either favorable ( $0 < R_L < 1$ ), unfavorable ( $R_L > 1$ ), irreversible ( $R_L = 0$ ), or linear ( $R_L = 1$ ).

The Freundlich model is an empirical theory based on adsorption on heterogeneous surface with nonuniform distribution of adsorption energy and affinities through a multilayer adsorption [31]. The nonlinear Freundlich equation is expressed as follows [32]:

$$Q_e = K_F C_e^{1/n}, \quad (5)$$

where  $K_F$  is the Freundlich isotherm constant related to the sorption capacity and represents the strength of the adsorptive bond ( $\text{mg} \cdot \text{g}^{-1} (\text{L} \cdot \text{mg}^{-1})^{1/n}$ ). The constant  $1/n$  gives an indication of how favorable the adsorption process is, and a value between 0.1 and 1.0 represents a favorable adsorption [33].

Moreover, Temkin isotherm takes the adsorbate-adsorbent interactions into account based on the assumptions that the heat of adsorption of all the molecules in the layer decreases linearly with coverage due to adsorbent-adsorbate interactions and that the adsorption is characterized by a uniform distribution of binding energies, up to some maximum binding energy [34, 35]. The Temkin isotherm has generally been applied as

$$Q_e = A \cdot \ln(B \cdot C_e), \quad (6)$$

where  $A = RT/b$  and  $b$  is J/mol,  $T$  (K) is the absolute temperature,  $R$  (8.314 J/mol·K) is the universal gas constant, and  $B$  (L/mol) is the equilibrium binding constant corresponding to the maximum binding energy, respectively.

Koble-Corrigan (K-C) isotherm model is an empirical three-parameter model which combines both Langmuir and Freundlich isotherm models for representing equilibrium adsorption data and is given by (7) as follows [36]:

$$Q_e = \frac{A_{KC} \cdot C_e^\beta}{1 + B_{KC} C_e^\beta}, \quad (7)$$

where  $A_{KC}$ ,  $B_{KC}$ , and  $\beta$  are Koble-Corrigan isotherm constants. When  $\beta = 1$ , the equation reduces to Langmuir equation; if  $B_{KC} \cdot C_e^\beta \ll 1$ , the equation becomes Freundlich equation. If  $B_{KC} \cdot C_e^\beta \gg 1$ , the adsorbate quantity per unit weight of adsorbent at equilibrium remains to be a constant of  $A_{KC}/B_{KC}$  [37].

A comparison of the adsorption experimental isotherms of MB onto the  $\text{TiO}_2$ @yeast-carbon and theoretical plots of the Langmuir, Freundlich, Temkin, and Koble-Corrigan isotherm models was shown in Figure 6. Correlation coefficients and constants of the models were given in Table 1.

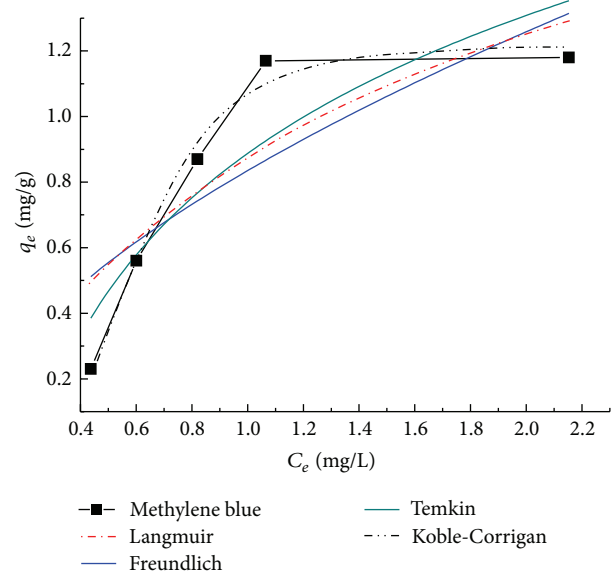


FIGURE 6: Comparison of Langmuir, Freundlich, Temkin, and Koble-Corrigan isotherm models for MB adsorption onto  $\text{TiO}_2$ @yeast-carbon composites (adsorbent = 0.014 g; solution volume = 100 mL; pH = 6; contact time = 1.5 h; temperature = 298 K; and concentration of MB = 1.0, 2.0, 3.0, 4.0, and 5.0 mg/L, resp.).

TABLE 1: Isotherm constants for the adsorption of MB and CR onto  $\text{TiO}_2$ @yeast-carbon.

Adsorption isotherm models	Constants	MB	CR
Langmuir isotherm	$Q_m$ (mg/g)	2.20	1.62
	$K_L$ (l/mg)	0.65	0.57
	$R^2$	0.6745	0.9128
	$R^L$	0.2346	0.2597
Freundlich isotherm	$1/n$	0.630	0.655
	$K_F$ $[(\text{mg/g})(\text{mg}^{-1})^{1/n}]$	0.840	0.033
Temkin isotherm	$R^2$	0.5832	0.9920
	$A$	0.607	0.500
	$B$	4.314	0.510
Koble-Corrigan isotherm	$R^2$	0.7517	0.9134
	$A_{KC}$	8.63	0.03
	$B_{KC}$	7.08	5.22
	$\beta$	4.20	1.54
	$R^2$	0.9745	0.9883

As can be seen from Figure 6, Koble-Corrigan isotherm plot was very close to the experimental data plot. Besides, it was observed in Table 1 that the value of  $R^2$  of Koble-Corrigan model ( $R^2 > 0.97$ ) was higher than those of Temkin, Langmuir, and Freundlich isotherm models, showing that Koble-Corrigan model was most suitable for the MB adsorption than the other models. This indicated that a combination of heterogeneous and homogeneous uptakes occurred in MB uptake by the synthesized  $\text{TiO}_2$ @yeast-carbon. Meanwhile,

TABLE 2: Isotherm models for adsorption of MB and CR on various adsorbents.

Adsorbent	Dyes	Adsorption isotherm	Reference
Activated carbon/cobalt ferrite/alginate	MB	Langmuir, Freundlich	Ai et al. [40]
Bamboo-based activated carbon	MB	Langmuir	Hameed et al. [24]
TiO <sub>2</sub> @yeast	MB	Langmuir	Chen and Bai [33]
Graphene	MB	Langmuir	Liu et al. [41]
Perlite	MB	Langmuir	Doğan et al. [42]
Garlic peel	MB	Freundlich	Hameed and Ahmad [43]
TiO <sub>2</sub> @yeast-carbon	MB	Koble-Corrigan	This study
Bagasse fly ash and activated carbon	CR	Redlich-Peterson	Mall et al. [34]
Kaolin	CR	Langmuir	Vimonses et al. [2]
Bentonite zeolite	CR	Freundlich	Vimonses et al. [2]
Activated carbon prepared from coir pith	CR	Langmuir, Freundlich	Namasivayam and Kavitha [44]
Chitosan/montmorillonite nanocomposite	CR	Langmuir	L. Wang and A. Wang [45]
TiO <sub>2</sub> @yeast-carbon	CR	Freundlich, Koble-Corrigan	This study

comparing the coefficients of determination of the Langmuir and Freundlich models, we could infer that homogeneous uptake was the main mechanism of the MB adsorption process [38]. Moreover, the value of  $R_L$  from the Langmuir isotherm was between 0 and 1, the Freundlich constant  $1/n$  was smaller than 1, and the value  $\beta$  in Koble-Corrigan model is over 1, indicating that the adsorption of MB onto TiO<sub>2</sub>@yeast-carbon was a favorable adsorption process.

Figure 7 typically showed the adsorption isotherms of CR onto the TiO<sub>2</sub>@yeast-carbon. The parameters of the isotherm equations were summarized in Table 1. It was shown in Figure 7 that both Koble-Corrigan and Freundlich models are suitable for CR adsorption process. From Figure 7, the low deviation between the calculated behavior and experimental plot had been observed. This fitting result can be explained by the presence of competition between adsorbate molecules for the adsorption sites on the surface [36]. The higher value of  $R^2$  in Table 1 from Freundlich model than Koble-Corrigan model implied that Freundlich model fitted the most exactly. In contrast, the  $R_L$  value obtained from the Langmuir model, the Freundlich constant ( $1/n$ ), and the value  $\beta$  from Koble-Corrigan model exhibited the same tendency as those for MB adsorption above, representing that the adsorption of CR on the TiO<sub>2</sub>@yeast-carbon was favorable.

The above analyses showed that the Koble-Corrigan model yields a better fit of MB than the other models. CR adsorption on the TiO<sub>2</sub>@yeast-carbon microspheres conforms well to Freundlich and Koble-Corrigan models. Namely, the Koble-Corrigan model fitted both MB and CR adsorption well. In addition, constants of  $A_{KC}$  and  $B_{KC}$  from Koble-Corrigan model are indicators of adsorption capacity and affinity of the adsorbent [36]. The values of Koble-Corrigan constant  $A_{KC}$  were 8.63 and 0.03 and those of  $B_{KC}$  were 7.08 and 5.22 for MB and CR, respectively. The greater  $A_{KC}$  and  $B_{KC}$  values for MB indicated higher MB adsorption capacity, affinity, and intensity compared to CR adsorption onto TiO<sub>2</sub>@yeast-carbon microspheres. This phenomenon was in accordance with the result illustrated in Figure 4, which may be attributed to the different active functional groups in MB and CR molecules [39], revealing that the

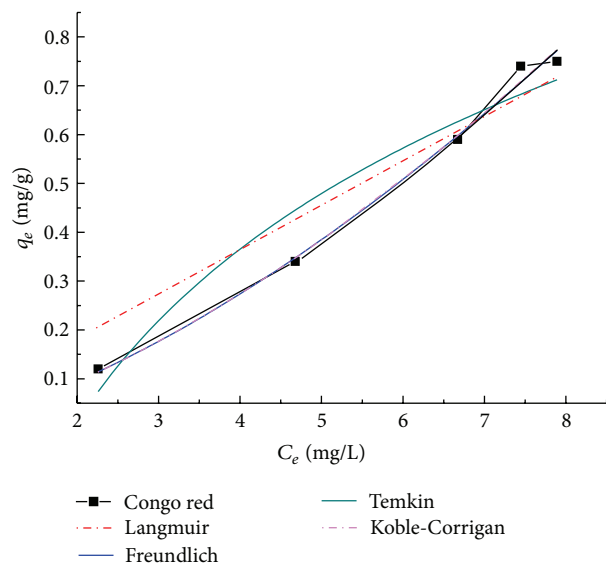


FIGURE 7: Comparison of Langmuir, Freundlich, Temkin, and K-C isotherm models for CR adsorption onto TiO<sub>2</sub>@yeast-carbon composites (adsorbent = 0.014 g; solution volume = 100 mL; pH = 6; contact time = 1.5 h; temperature = 298 K; and concentration of CR = 3.0, 5.0, 7.0, 9.0, and 11.0 mg/L, resp.).

TiO<sub>2</sub>@yeast-carbon microspheres can be served as a promising adsorptive material for MB.

Since adsorption isotherm is basically important to describe how adsorbates interact with adsorbents, some researchers had also investigated the best fitted isotherm models for the adsorption of MB and CR onto several adsorbents in aqueous solutions [2, 24, 33, 34, 40–45]. The results were listed in Table 2, and the TiO<sub>2</sub>@yeast-carbon studied in this work represented different adsorption behaviors.

**3.4. Adsorption Kinetics.** To investigate the adsorption mechanism, such as mass transfer and chemical reaction, the MB and CR adsorption data were analyzed using the pseudo-first-order and pseudo-second-order models, respectively. The

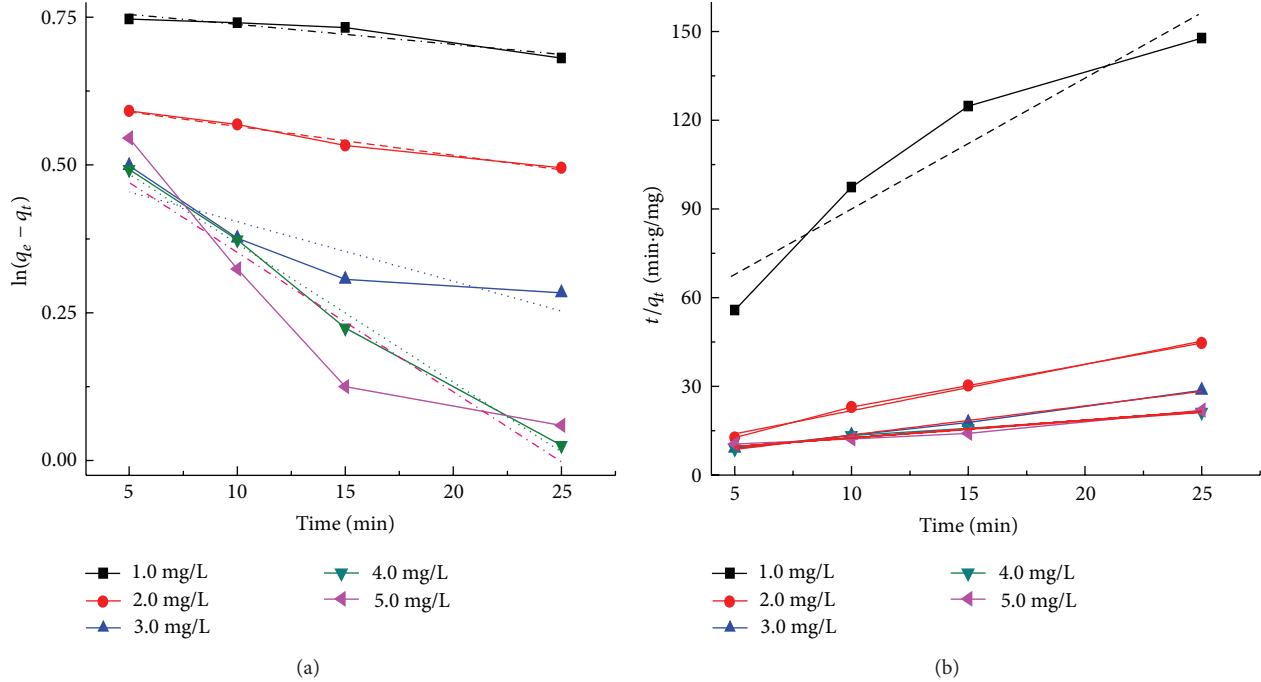


FIGURE 8: Pseudo-first-order (a) and pseudo-second-order (b) adsorption kinetics for adsorption of MB onto  $\text{TiO}_2$ @yeast-carbon at different initial concentrations ( $\text{TiO}_2$ @yeast-carbon dosage = 0.14 g/L; pH = 6.0; temperature = 298 K; and concentration of MB = 1.0, 2.0, 3.0, 4.0, and 5.0 mg/L, resp.).

pseudo-first-order kinetic model was described by Lagergren and the pseudo-second-order kinetic model was based on the assumption that the rate limiting step of the adsorption process was chemical sorption [25]. The pseudo-first-order equation can be expressed as [46]

$$\ln(Q_e - Q_t) = \ln Q_e - k_1 \cdot t, \quad (8)$$

where  $Q_e$  (mg/g) and  $Q_t$  (mg/g) are the amounts of dye adsorbed onto the composites at equilibrium and at time  $t$ , respectively. The rate constant  $k_1$  ( $\text{min}^{-1}$ ) of the pseudo-first-order model was calculated from the plots of  $\ln(Q_e - Q_t)$  versus  $t$ .

The pseudo-second-order equation can be described in the following equation [28]:

$$\frac{t}{Q_t} = \frac{1}{(k_2 \cdot Q_e^2)} + \frac{t}{Q_e}, \quad (9)$$

where  $k_2$  ( $\text{g} \cdot \text{mg}^{-1} \cdot \text{min}^{-1}$ ) is the adsorption rate constant of the pseudo-second-order equation and can be obtained from the linear plots of  $t/Q_t$  against  $t$ .

Besides, the applicability of both kinetic models was tested through the sum of error squares (SSE, %), which was given as follows [47]:

$$\text{SSE} (\%) = \sqrt{\frac{\sum (Q_{e,\text{exp}} - Q_{e,\text{cal}})^2}{N}}, \quad (10)$$

where  $N$  is the number of data points. The higher the correlation coefficient ( $R^2$ ) and the lower the values of SSE,

the better the goodness of fit will be. Table 3 also listed the calculated SSE results for MB and CR adsorption onto  $\text{TiO}_2$ @yeast-carbon at different initial concentrations.

Figure 8 exhibits the plots of the pseudo-first-order and pseudo-second-order kinetics of MB adsorption on  $\text{TiO}_2$ @yeast-carbon at different initial concentrations. The adsorption rate constants, correlation coefficient, and SSE values were calculated and summarized in Table 2. It was observed from Table 2 that the experimental  $Q_e$  values ( $Q_{e,\text{exp}}$ ) did not agree with the calculated ones ( $Q_{e,\text{cal}}$ ) although the correlation coefficient values for the pseudo-first-order at some concentrations were higher than 0.85. As a result, the sorption of MB on the  $\text{TiO}_2$ @yeast-carbon did not follow pseudo-first-order in all cases. It was also obvious that the correlation coefficient  $R^2$  was found to range from 0.936 to 0.994 for the pseudo-second-order kinetic model, which were higher than those for the pseudo-second-order model, and the experimental  $Q_e$  values ( $Q_{e,\text{exp}}$ ) were closer with the theoretical calculated values ( $Q_{e,\text{cal}}$ ) compared to the pseudo-first-order model. Furthermore, SSE values for the pseudo-second-order model were lower than those for the pseudo-second-order model. All the illustrations mentioned above indicated that the adsorption of MB onto  $\text{TiO}_2$ @yeast-carbon followed the pseudo-second-order kinetic model, and the chemical sorption might be involved in the adsorption process. Moreover, the rate constant ( $k_2$ ) decreased with the increase of the initial MB concentrations, which was due to the striking hindrance of higher concentrations of MB [40].

Figure 9 presents the plots of the pseudo-first-order and pseudo-second-order kinetics of CR adsorption on

TABLE 3: Kinetic adsorption parameters of different initial concentration of MB and CR.

$C_0$ (mg/L)	$Q_{e,exp}$ (mg/g)	$k_1$ ( $\text{min}^{-1}$ )	Pseudo-first-order			Pseudo-second-order			
			$Q_{e,cal}$ (mg/g)	$R^2$	SSE (%)	$k_2$ (g/mg·min)	$Q_{e,cal}$ (mg/g)	$R^2$	SSE (%)
MB									
1.0	0.43	$3.4 \times 10^{-3}$	2.16	0.868	0.87	0.426	0.39	0.961	0.10
2.0	0.60	$4.9 \times 10^{-3}$	1.65	0.912	1.01	0.404	0.63	0.989	0.08
3.0	0.81	$1.0 \times 10^{-2}$	1.82	0.683	0.42	0.260	1.01	0.994	0.02
4.0	1.06	$2.4 \times 10^{-2}$	1.79	0.953	0.38	0.055	1.16	0.976	0.24
5.0	2.15	$2.0 \times 10^{-2}$	1.84	0.767	0.18	0.049	2.14	0.936	0.32
CR									
3.0	0.29	$9.6 \times 10^{-2}$	1.67	0.960	0.69	0.270	0.30	0.981	0.04
9.0	0.62	$8.5 \times 10^{-2}$	1.25	0.903	0.32	0.052	0.64	0.989	0.11
11.0	1.24	$11.0 \times 10^{-2}$	3.75	0.941	1.25	0.040	1.33	0.994	0.01

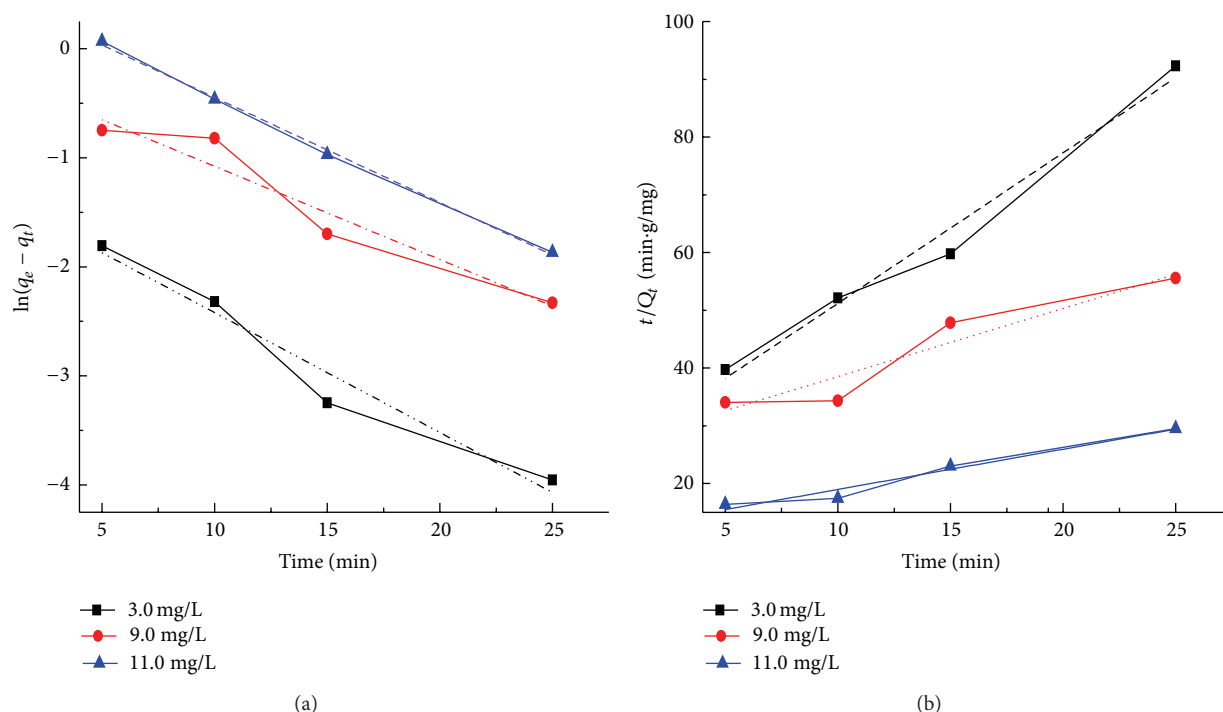


FIGURE 9: Pseudo-first-order (a) and pseudo-second-order (b) adsorption kinetics for adsorption of CR onto  $\text{TiO}_2$ @yeast-carbon at different initial concentrations ( $\text{TiO}_2$ @yeast-carbon dosage = 0.14 g/L; pH = 6.0; temperature = 298 K; and concentration of MB = 3.0, 9.0, and 11.0 mg/L, resp.).

$\text{TiO}_2$ @yeast-carbon at different initial concentrations. The adsorption rate constants, correlation coefficient, and SSE values are also given in Table 3. The results presented an ideal fit to the pseudo-second-order kinetics for all concentrations with the higher correlation coefficient ( $R^2 > 0.98$ ) and lower SSE values. A good agreement with this model was confirmed by the similar values of calculated adsorption capacity at equilibrium ( $Q_{e,cal}$ ) and experimental ones ( $Q_{e,exp}$ ) for all concentrations. The best fit to the pseudo-second-order kinetics model indicates that the adsorption mechanism depends on the adsorbate and adsorbent, and the rate controlling step might be chemical sorption involving valence forces through exchange or sharing of electrons [2]. The rate

constant ( $k_2$ ) also decreased with the increase of the initial CR concentrations, owing to that the higher probability of collisions among CR molecules would decrease the sorption rate [28]. Similar kinetic results have also been reported for the CR adsorption onto bagasse fly ash [34], activated carbon from coir [44], and chitosan/montmorillonite [45].

**3.5. Regeneration of Dye Loaded  $\text{TiO}_2$ @Yeast-Carbon Microspheres.** No matter if adsorption is carried out in static or dynamical forms, it will gradually reach equilibrium if more contaminated water was treated or more adsorption cycles were conducted without regeneration [48]. So the removal of

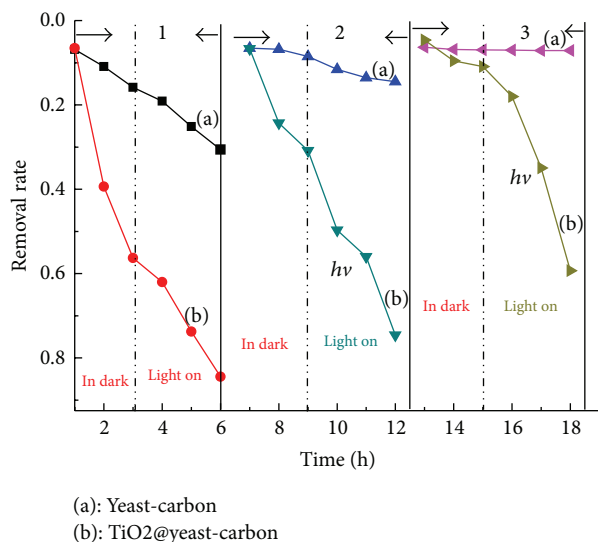


FIGURE 10: The circulation experiment of TiO<sub>2</sub>@yeast-carbon composite microspheres.

adsorbed pollutants and the regeneration study of saturated composite were completely necessary. Hence, experiments were performed to evaluate the lifetime and reusing efficiency of prepared composite in removing MB (Figure 10).

For the dark adsorption section in the first cycle, near absorption-desorption equilibrium was established during the 3.0 h dark phase before the irradiation of the dyes solutions. It can also be seen from Figure 10 that strengthening trend occurs for the adsorption capacities of TiO<sub>2</sub>@yeast-carbon microsphere when TiO<sub>2</sub> nanoparticles were attached onto the yeast-carbon. This enhanced effect of adsorption might be ascribed to the integration of yeast-carbon and TiO<sub>2</sub> nanoparticles, which creates more adsorption sites for MB. The dark adsorption results show that TiO<sub>2</sub>@yeast-carbon microsphere have faster adsorption kinetics due to their larger vacant surface area compared to the naked yeast-carbon. This phenomenon can be further affirmed by the pseudo-first-order kinetic data in Table 4. As can be seen, the kinetic rate constant in dark ( $k_{\text{dark}}$ ) for TiO<sub>2</sub>@yeast-carbon is  $5.5 \times 10^{-3}$ , which is almost 4.2 times of that for the yeast-carbon. The higher  $k_{\text{dark}}$  gave clear evidence that TiO<sub>2</sub>@yeast-carbon exhibited higher adsorption rate than yeast-carbon. Thereafter, the experiments for the removal of MB compound from aqueous solution were continued for about 3 h under UV light irradiation. Figure 10 shows that in the first cycle approximately 30% of MB was removed from the aqueous solution by adsorption on the naked yeast-carbon. In the presence of the raspberry-like TiO<sub>2</sub>@yeast-carbon microspheres and under UV irradiation, nearly 85% of MB molecule disappearance was accomplished.

These results suggest that the prepared TiO<sub>2</sub>@yeast-carbon composites are effective for the removal of MB from aqueous solutions. The integration of adsorption by the yeast-carbon with photocatalysis by the TiO<sub>2</sub> nanoparticles attached on the yeast-carbon surface showed a combined function in the removal of the MB molecule. Specifically,

yeast-carbon can increase the photodegradation rate by progressively allowing an increased concentration of MB to come in contact with the TiO<sub>2</sub> nanoparticles through means of adsorption. TiO<sub>2</sub> nanoparticles on the surface of yeast-carbon can be activated to generate hydroxyl free radicals, which can decompose most of the MB molecules and keep the adsorption sites unsaturated. In return, the simultaneous adsorption of the MB molecules onto the renewed areas of the yeast-carbon provides a continuous supply of substrate to the TiO<sub>2</sub> nanoparticles [49]. Thus, the adsorption performance of the yeast-carbon and the photocatalytic property of the attached TiO<sub>2</sub> have been integrated as a novel property for the raspberry-like TiO<sub>2</sub>@yeast-carbon composites.

It was also observed in Figure 10 that, after three times reuses, the MB removal by yeast-carbon apparently dropped from 30.6% to 7.0%. It could be attributed to the fact that the removal of MB in aqueous solution by yeast-carbon mostly relied on adsorption, which fully depended on the absorption sites. Hereby, the bare active sites on yeast-carbon were covered by MB molecules adsorbed in the last cycle, which gave explanation for the rapid loss of MB removal. However, the TiO<sub>2</sub>@yeast-carbon still achieved desired removal efficiency for MB with slight decrease from 84.4% to 59.3% even though it had been reused for three times; that is, after 3 successive cycles under UV light irradiation, the removal rate of MB by TiO<sub>2</sub>@yeast-carbon was still 70% of that for the first cycling run. These phenomena give evidence that TiO<sub>2</sub>@yeast-carbon nanocomposites exhibited excellent photocatalytic stability and regeneration efficiency.

The outstanding regeneration ability of TiO<sub>2</sub>@yeast-carbon in comparison with the yeast-carbon could be further affirmed by contrasting the pseudo-first-order kinetic rate constants  $k_{\text{dark}}$  (in dark) and  $k_{\text{light}}$  (light on) in Table 4. As can be seen, the  $k_{\text{dark}}$  for TiO<sub>2</sub>@yeast-carbon during three cycle times are  $5.5 \times 10^{-3}$ ,  $4.2 \times 10^{-3}$ , and  $9.0 \times 10^{-3}$ , respectively, which were almost 4.2, 15.0, and 10.1 times those for the yeast-carbon. The higher  $k_{\text{dark}}$  means that TiO<sub>2</sub>@yeast-carbon regenerated by UV light illumination exhibited higher adsorption rate than yeast-carbon. Besides, irradiation of yeast-carbon after dark adsorption equilibrium had resulted in smaller  $k_{\text{light}}$  ( $1.22 \times 10^{-3}$ ,  $5.7 \times 10^{-4}$ , and  $1.7 \times 10^{-5}$ ) compared to TiO<sub>2</sub>@yeast-carbon under UV light, showing that the attachment of TiO<sub>2</sub> nanoparticles on the surface of yeast-carbon had a great significant influence on the removal rate of MB and implied that in situ regeneration of the MB-loaded TiO<sub>2</sub>@yeast-carbon had already occurred.

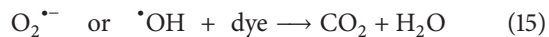
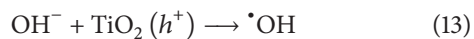
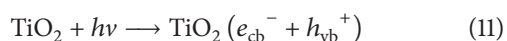
### 3.6. In Situ Regenerating Mechanism for TiO<sub>2</sub>@Yeast-Carbon.

Based on the results above, a synergistic effect might be one possible mechanism for in situ regenerating dye-loaded TiO<sub>2</sub>@yeast-carbon. The synergistic effect works by integrating the adsorption of the yeast-carbon with the photocatalysis of the TiO<sub>2</sub> nanoparticles attached on the yeast-carbon surface. More specifically, based on the bare areas on the surface of yeast-carbon and TiO<sub>2</sub>, dye molecules were adsorbed onto the TiO<sub>2</sub>@yeast-carbon through means of adsorption. Then, the adsorption sites are keeping unsaturated by illuminating the whole system. Because the irradiation of TiO<sub>2</sub> particles

TABLE 4: Kinetic constant (g/mg·min)  $k_{\text{dark}}$  (in dark),  $k_{\text{light}}$  (light on), and Adj.  $R$ -Square  $R^2$  for removing MB.

	Cycle 1		Cycle 2		Cycle 3	
	Yeast-carbon	TiO <sub>2</sub> @yeast-carbon	Yeast-carbon	TiO <sub>2</sub> @yeast-carbon	yeast-carbon	TiO <sub>2</sub> @yeast-carbon
$k_{\text{dark}}$	$1.3 \times 10^{-3}$	$5.5 \times 10^{-3}$	$2.8 \times 10^{-4}$	$4.2 \times 10^{-3}$	$8.9 \times 10^{-5}$	$9.0 \times 10^{-4}$
$R^2$	0.980	0.838	0.834	0.870	0.866	0.904
$k_{\text{light}}$	$1.22 \times 10^{-3}$	$6.03 \times 10^{-3}$	$5.7 \times 10^{-4}$	$5.57 \times 10^{-3}$	$1.7 \times 10^{-5}$	$5.44 \times 10^{-3}$
$R^2$	0.992	0.917	0.946	0.968	0.894	0.946

on the yeast-carbon with photons of energy ( $h\nu$ ) equal to or higher than those of band gap results in the excitation of electrons from the valence band (vb) to the conduction band (cb) of the particle, which can produce the electrons ( $e_{\text{cb}}^-$ ) in the conduction band and the holes ( $h_{\text{vb}}^+$ ) at the valence band edge of the TiO<sub>2</sub> (11) [50]. The electrons and holes can migrate to the particle surface of TiO<sub>2</sub>, where the  $h_{\text{vb}}^+$  can react with the adsorbed O<sub>2</sub>, surrounded water molecules, and surface hydroxide group, respectively, to generate the highly reactive hydroxyl radicals ( $\cdot\text{OH}$ ) ((12) and (13)) and superoxide ions O<sub>2</sub><sup>-</sup> (14). The resulted  $\cdot\text{OH}$  and O<sub>2</sub><sup>-</sup> are known to be very powerful and indiscriminately oxidizing agents and can oxidize the organic compounds adsorbed onto or very close to the TiO<sub>2</sub> surface during the photocatalytic process, resulting in degradation of dye into small units like carbon dioxide and water (15):



Simultaneously, the renewed adsorption sites provide a durative supply of MB molecule for TiO<sub>2</sub> particle. Then, the activity of TiO<sub>2</sub>@yeast-carbon was successfully recovered after in situ regeneration. The recovered adsorbent could be used for the next adsorption and catalytic reaction cycle. All in all, the combination of both adsorption and heterogeneous catalysis could be regarded as cleaner, greener, favored, and promising technology for removing dye from water. An optimal amount of TiO<sub>2</sub> coverage should exist since the coverage rate of the attached TiO<sub>2</sub> nanoparticles onto the yeast-carbon surface in the TiO<sub>2</sub>@yeast-carbon composite is an important factor for the control of removing dyes. This aspect is currently under investigation.

## 4. Conclusions

In conclusion, TiO<sub>2</sub>@yeast-carbon with raspberry-like structure was successfully prepared based on pyrolysis method and was characterized by FE-SEM, EDS, and XRD. The synthetic TiO<sub>2</sub>@yeast-carbon was used as adsorbent to remove MB and CR from aqueous solutions, respectively. FE-SEM images displayed that TiO<sub>2</sub>@yeast-carbon microspheres have rough

surface morphology and uniform diameter with good dispersity. EDS showed that TiO<sub>2</sub> has been already successfully coated on the yeast carbon. The adsorption results showed that TiO<sub>2</sub>@yeast-carbon microspheres achieved favorable removal of cationic MB in comparison with the anionic CR. Equilibrium data for MB adsorption were best described by the Koble-Corrigan isotherm model. The adsorption of CR onto TiO<sub>2</sub>@yeast-carbon showed best agreement with both Freundlich and Koble-Corrigan models. Kinetic data indicated that the adsorption of both MB and CR onto TiO<sub>2</sub>@yeast-carbon microspheres obeyed pseudo-second-order kinetic model well. Moreover, regeneration experiments showed that TiO<sub>2</sub>@yeast-carbon composites exhibited excellent recycling stability, reusability, and renewable ability. One possible mechanism for regenerating dye-loaded TiO<sub>2</sub>@yeast in situ was also proposed. This paper may be useful for further research and practical applications of the novel TiO<sub>2</sub>@yeast composite in dye wastewater treatment.

## Conflict of Interests

The authors declare that there is no conflict of interests regarding the publication of this paper.

## Acknowledgments

This work was financially supported by the National Natural Science Foundation of China (no. 21176031), Fundamental Research Funds for the Central Universities (no. 2013G2291015), and National Undergraduate Training Programs for Innovation and Entrepreneurship of Chang'an University (no. 201410710059).

## References

- [1] M. Saquib, M. Abu Tariq, M. M. Haque, and M. Muneer, "Photocatalytic degradation of disperse blue 1 using UV/TiO<sub>2</sub>/H<sub>2</sub>O<sub>2</sub> process," *Journal of Environmental Management*, vol. 88, no. 2, pp. 300–306, 2008.
- [2] V. Vimonses, S. Lei, B. Jin, C. W. K. Chow, and C. Saint, "Kinetic study and equilibrium isotherm analysis of Congo Red adsorption by clay materials," *Chemical Engineering Journal*, vol. 148, no. 2-3, pp. 354–364, 2009.
- [3] A. Roy, S. Chakraborty, S. P. Kundu, B. Adhikari, and S. B. Majumder, "Adsorption of anionic-azo dye from aqueous solution by lignocellulose-biomass jute fiber: equilibrium, kinetics, and thermodynamics study," *Industrial and Engineering Chemistry Research*, vol. 51, no. 37, pp. 12095–12106, 2012.

- [4] N. M. Mahmoodi, "Binary catalyst system dye degradation using photocatalysis," *Fibers and Polymers*, vol. 15, no. 2, pp. 273–280, 2014.
- [5] V. S. Mane and P. V. V. Babu, "Studies on the adsorption of Brilliant Green dye from aqueous solution onto low-cost NaOH treated saw dust," *Desalination*, vol. 273, no. 2-3, pp. 321–329, 2011.
- [6] S. Hisaindee, M. A. Meetani, and M. A. Rauf, "Application of LC-MS to the analysis of advanced oxidation process (AOP) degradation of dye products and reaction mechanisms," *TrAC Trends in Analytical Chemistry*, vol. 49, pp. 31–44, 2013.
- [7] J. Wu, M. A. Eiteman, and S. E. Law, "Evaluation of membrane filtration and ozonation processes for treatment of reactive-dye wastewater," *Journal of Environmental Engineering*, vol. 124, no. 3, pp. 272–277, 1998.
- [8] K. Turhan, I. Durukan, S. A. Ozturkcan, and Z. Turgut, "Decolorization of textile basic dye in aqueous solution by ozone," *Dyes and Pigments*, vol. 92, no. 3, pp. 897–901, 2012.
- [9] S. S. Moghaddam, M. R. A. Moghaddam, and M. Arami, "Coagulation/flocculation process for dye removal using sludge from water treatment plant: optimization through response surface methodology," *Journal of Hazardous Materials*, vol. 175, no. 1–3, pp. 651–657, 2010.
- [10] L. Wang, J. Zhang, R. Zhao, C. Li, Y. Li, and C. Zhang, "Adsorption of basic dyes on activated carbon prepared from *Polygonum orientale* Linn: equilibrium, kinetic and thermodynamic studies," *Desalination*, vol. 254, no. 1–3, pp. 68–74, 2010.
- [11] Q. H. Hu, S. Z. Qiao, F. Haghseresht, M. A. Wilson, and G. Q. Lu, "Adsorption study for removal of basic red dye using bentonite," *Industrial & Engineering Chemistry Research*, vol. 45, no. 2, pp. 733–738, 2006.
- [12] D. Sun, X. Zhang, Y. Wu, and X. Liu, "Adsorption of anionic dyes from aqueous solution on fly ash," *Journal of Hazardous Materials*, vol. 181, no. 1–3, pp. 335–342, 2010.
- [13] G. K. Sarma, S. SenGupta, and K. G. Bhattacharyya, "Methylene blue adsorption on natural and modified clays," *Separation Science and Technology*, vol. 46, no. 10, pp. 1602–1614, 2011.
- [14] A. A. Ahmad, A. Idris, and B. H. Hameed, "Organic dye adsorption on activated carbon derived from solid waste," *Desalination and Water Treatment*, vol. 51, no. 13–15, pp. 2554–2563, 2013.
- [15] M. Jayarajan, R. Arunachalam, and G. Annadurai, "Agricultural wastes of Jackfruit peel nano-porous adsorbent for removal of Rhodamine dye," *Asian Journal of Applied Sciences*, vol. 4, no. 3, pp. 263–270, 2011.
- [16] D. Uçar and B. Armağan, "The removal of reactive black 5 from aqueous solutions by cotton seed shell," *Water Environment Research*, vol. 84, no. 4, pp. 323–327, 2012.
- [17] R. Nacco and E. Aquarone, "Preparation of active carbon from yeast," *Carbon*, vol. 16, no. 1, pp. 31–34, 1978.
- [18] Z. Guan, L. Liu, L. He, and S. Yang, "Amphiphilic hollow carbonaceous microspheres for the sorption of phenol from water," *Journal of Hazardous Materials*, vol. 196, pp. 270–277, 2011.
- [19] W. Jiang, J. A. Joens, D. D. Dionysiou, and K. E. O'Shea, "Optimization of photocatalytic performance of TiO<sub>2</sub> coated glass microspheres using response surface methodology and the application for degradation of dimethyl phthalate," *Journal of Photochemistry and Photobiology A: Chemistry*, vol. 262, pp. 7–13, 2013.
- [20] J. Matos, A. Garcia, T. Cordero, J.-M. Chovelon, and C. Ferronato, "Eco-friendly TiO<sub>2</sub>-AC photocatalyst for the selective photooxidation of 4-chlorophenol," *Catalysis Letters*, vol. 130, no. 3-4, pp. 568–574, 2009.
- [21] D. Yu, B. Bo, and H. Yunhua, "Fabrication of TiO<sub>2</sub>@yeast-carbon hybrid composites with the raspberry-like structure and their synergistic adsorption-photocatalysis performance," *Journal of Nanomaterials*, vol. 2013, Article ID 851417, 8 pages, 2013.
- [22] M. Liu, L. Piao, W. Lu et al., "Flower-like TiO<sub>2</sub> nanostructures with exposed 001 facets: facile synthesis and enhanced photocatalysis," *Nanoscale*, vol. 2, no. 7, pp. 1115–1117, 2010.
- [23] S. Feng, J. Yang, M. Liu et al., "Hydrothermal growth of double-layer TiO<sub>2</sub> nanostructure film for quantum dot sensitized solar cells," *Thin Solid Films*, vol. 520, no. 7, pp. 2745–2749, 2012.
- [24] B. H. Hameed, A. T. M. Din, and A. L. Ahmad, "Adsorption of methylene blue onto bamboo-based activated carbon: kinetics and equilibrium studies," *Journal of Hazardous Materials*, vol. 141, no. 3, pp. 819–825, 2007.
- [25] Y.-P. Chang, C.-L. Ren, J.-C. Qu, and X.-G. Chen, "Preparation and characterization of Fe<sub>3</sub>O<sub>4</sub>/graphene nanocomposite and investigation of its adsorption performance for aniline and *p*-chloroaniline," *Applied Surface Science*, vol. 261, pp. 504–509, 2012.
- [26] J. Rivera-Utrilla, I. Bautista-Toledo, M. A. Ferro-García, and C. Moreno-Castilla, "Activated carbon surface modifications by adsorption of bacteria and their effect on aqueous lead adsorption," *Journal of Chemical Technology and Biotechnology*, vol. 76, no. 12, pp. 1209–1215, 2001.
- [27] L. C. Juang, C. C. Wang, and C. K. Lee, "Adsorption of basic dyes onto MCM-41," *Chemosphere*, vol. 64, no. 11, pp. 1920–1928, 2006.
- [28] H.-X. Ou, Y.-J. Song, Q. Wang et al., "Adsorption of lead(II) by silica/cell composites from aqueous solution: kinetic, equilibrium, and thermodynamics studies," *Water Environment Research*, vol. 85, no. 2, pp. 184–191, 2013.
- [29] I. Langmuir, "The adsorption of gases on plane surfaces of glass, mica and platinum," *The Journal of the American Chemical Society*, vol. 40, no. 9, pp. 1361–1403, 1918.
- [30] T. W. Weber and R. K. Chakravorti, "Pore and solid diffusion models for fixed-bed adsorbers," *AIChE Journal*, vol. 20, no. 2, pp. 228–238, 1974.
- [31] L. Huang, Y. Sun, W. Wang, Q. Yue, and T. Yang, "Comparative study on characterization of activated carbons prepared by microwave and conventional heating methods and application in removal of oxytetracycline (OTC)," *Chemical Engineering Journal*, vol. 171, no. 3, pp. 1446–1453, 2011.
- [32] H. M. F. Freundlich, "Über die adsorption in losungen," *Zeitschrift Für Physikalische Chemie. International Journal of Research in Physical Chemistry and Chemical Physics A*, vol. 57, pp. 385–470, 1906.
- [33] L. Chen and B. Bai, "Equilibrium, kinetic, thermodynamic, and in situ regeneration studies about methylene blue adsorption by the raspberry-like TiO<sub>2</sub>@yeast microspheres," *Industrial and Engineering Chemistry Research*, vol. 52, no. 44, pp. 15568–15577, 2013.
- [34] I. D. Mall, V. C. Srivastava, N. K. Agarwal, and I. M. Mishra, "Removal of congo red from aqueous solution by bagasse fly ash and activated carbon: kinetic study and equilibrium isotherm analyses," *Chemosphere*, vol. 61, no. 4, pp. 492–501, 2005.

- [35] M. I. Tempkin and V. Pyzhev, "Kinetics of ammonia synthesis on promoted iron catalysts," *Acta Physicochim (URSS)*, vol. 12, no. 3, pp. 217–222, 1940.
- [36] P. Wu, W. Wu, S. Li et al., "Removal of  $\text{Cd}^{2+}$  from aqueous solution by adsorption using Fe-montmorillonite," *Journal of Hazardous Materials*, vol. 169, no. 1–3, pp. 824–830, 2009.
- [37] W. Jiang, M. Pelaez, D. D. Dionysiou, M. H. Entezari, D. Tsoutsou, and K. O'Shea, "Chromium(VI) removal by maghemite nanoparticles," *Chemical Engineering Journal*, vol. 222, pp. 527–533, 2013.
- [38] M. Zhang, H. Zhang, D. Xu et al., "Removal of ammonium from aqueous solutions using zeolite synthesized from fly ash by a fusion method," *Desalination*, vol. 271, no. 1–3, pp. 111–121, 2011.
- [39] M. Hamidpour, M. Kalbasi, M. Afyuni, and H. Shariatmadari, "Kinetic and isothermal studies of cadmium sorption onto bentonite and zeolite," *International Agrophysics*, vol. 24, no. 3, pp. 253–259, 2010.
- [40] L. Ai, M. Li, and L. Li, "Adsorption of methylene blue from aqueous solution with activated carbon/cobalt ferrite/alginate composite beads: kinetics, isotherms, and thermodynamics," *Journal of Chemical & Engineering Data*, vol. 56, no. 8, pp. 3475–3483, 2011.
- [41] T. Liu, Y. Li, Q. Du et al., "Adsorption of methylene blue from aqueous solution by graphene," *Colloids and Surfaces B: Biointerfaces*, vol. 90, no. 1, pp. 197–203, 2012.
- [42] M. Doğan, M. Alkan, and Y. Onganer, "Adsorption of methylene blue from aqueous solution onto perlite," *Water, Air, and Soil Pollution*, vol. 120, no. 3–4, pp. 229–248, 2000.
- [43] B. H. Hameed and A. A. Ahmad, "Batch adsorption of methylene blue from aqueous solution by garlic peel, an agricultural waste biomass," *Journal of Hazardous Materials*, vol. 164, no. 2–3, pp. 870–875, 2009.
- [44] C. Namasivayam and D. Kavitha, "Removal of Congo Red from water by adsorption onto activated carbon prepared from coir pith, an agricultural solid waste," *Dyes and Pigments*, vol. 54, no. 1, pp. 47–58, 2002.
- [45] L. Wang and A. Wang, "Adsorption characteristics of Congo red onto the chitosan/montmorillonite nanocomposite," *Journal of Hazardous Materials*, vol. 147, no. 3, pp. 979–985, 2007.
- [46] S. A. Idris, K. M. Alotaibi, T. A. Peshkur, P. Anderson, M. Morris, and L. T. Gibson, "Adsorption kinetic study: effect of adsorbent pore size distribution on the rate of Cr (VI) uptake," *Microporous and Mesoporous Materials*, vol. 165, pp. 99–105, 2013.
- [47] W. Guan, J. Pan, H. Ou et al., "Removal of strontium(II) ions by potassium tetratitanate whisker and sodium trititanate whisker from aqueous solution: equilibrium, kinetics and thermodynamics," *Chemical Engineering Journal*, vol. 167, no. 1, pp. 215–222, 2011.
- [48] L. F. Liu, P. H. Zhang, and F. L. Yang, "Adsorptive removal of 2,4-DCP from water by fresh or regenerated chitosan/ACF/ $\text{TiO}_2$  membrane," *Separation and Purification Technology*, vol. 70, no. 3, pp. 354–361, 2010.
- [49] B. Bai, N. Quici, Z. Li, and G. L. Puma, "Novel one step fabrication of raspberry-like  $\text{TiO}_2$ @yeast hybrid microspheres via electrostatic-interaction-driven self-assembled heterocoagulation for environmental applications," *Chemical Engineering Journal*, vol. 170, no. 2–3, pp. 451–456, 2011.
- [50] V. K. Gupta, R. Jain, A. Mittal, M. Mathur, and S. Sikarwar, "Photochemical degradation of the hazardous dye Safranin-T using  $\text{TiO}_2$  catalyst," *Journal of Colloid and Interface Science*, vol. 309, no. 2, pp. 464–469, 2007.

## Research Article

# Growth of Semimetals Bismuth and Antimony Films on Reactive Substrate

Xiao Wang,<sup>1</sup> Xiaoxing Wei,<sup>2</sup> and Caixia Song<sup>2</sup>

<sup>1</sup>State Key Laboratory of Marine Coatings, Marine Chemical Research Institute Co. Ltd., Qingdao 266071, China

<sup>2</sup>College of Chemistry and Molecular Engineering, Qingdao University of Science & Technology, Qingdao 266042, China

Correspondence should be addressed to Caixia Song; [songcaixia@qingdaonews.com](mailto:songcaixia@qingdaonews.com)

Received 7 July 2014; Accepted 23 August 2014

Academic Editor: Yuanlie Yu

Copyright © 2015 Xiao Wang et al. This is an open access article distributed under the Creative Commons Attribution License, which permits unrestricted use, distribution, and reproduction in any medium, provided the original work is properly cited.

Semimetal Bi and Sb thin films with novel hierarchical structures were synthesized on zinc substrate via a hydrothermal method. X-ray diffraction (XRD) analysis confirmed the formation of pure semimetals Bi and Sb. Scanning electron microscopy images showed that Bi films constructed with microtube arrays and hierarchical microspheres can be obtained selectively by altering the concentration of  $\text{Bi}^{3+}$  ions. The synthesized Sb films were constructed with bowl-shaped particles. The growth process of these semimetal architectures was briefly discussed.

## 1. Introduction

In recent years, shape controlled synthesis of metal materials in the nano-/microdimensions has been one of the important topics because these materials generally exhibit many size-, shape-, and structure-dependent properties. In particular, semimetal bismuth has attracted great attention because of its low carrier density, small effective mass, and large mean-free path, making it an interesting system for studying quantum confinement effects [1, 2]. In addition, nanostructured bismuth could exhibit even more interesting electronic and thermoelectric properties [3, 4]. Stimulated by these interesting properties, a number of different methods have been developed to prepare various bismuth nanostructures. Single crystal filaments of bismuth with diameters in the micron range have been prepared by Glocker and Skove [5]. Bi nanowires and nanorods were prepared by high pressure injection of the liquid metal or vapor phase of bismuth into the channels of porous anodic alumina template [6, 7]. Bismuth nanowires have also been electrodeposited into nanometer-sized pores of polymer [8] or nanoporous anodic alumina [9, 10]. Solution chemical methods have also been explored for the synthesis of Bi nanowires and nanotubes [11–13]. Wang et al. reported the synthesis of Bi

nanoplates, nanorods, and nanoribbons from the precursor  $\text{Bi}[\text{N}(\text{SiMe}_3)_2]_3$  [14]. Bismuth nanoparticles have been prepared in reverse micelles [15], by thermolysis [16], and through solution reduction [17–19]. Schulz et al. prepared Bi pseudocubes by thermal decomposition of a metal organic precursor [20]. The crystal structure of semimetal Sb is similar to that of Bi, but the effective mass components of the electron ellipsoids in Sb are much larger than those in Bi. Clear optical switching of Sb thin films was observed under microscopic measurement [21]. Sb nanowires have been prepared similarly by vapor deposition [22], pulsed electrodeposition techniques [23], and solvothermal method [24]. Recently, Liu et al. prepared 3D nanostructured antimony in  $\text{SbCl}_3$ - $(n\text{-Bu})_4\text{NBF}_4$ -DMSO solution [25].

Although several reports have been concerned with solution chemistry synthesis of semimetal bismuth and antimony nanocrystals, the synthesis of Bi tubular arrays and flower-shaped crystals and Sb nanobowls, to the best of our knowledge, has not been reported in the literature. Previously, we reported the synthesis of ZnO nanorod arrays on zinc substrate via hydrothermal method [26]. Herein we extend this hydrothermal method to the synthesis of semimetal bismuth and antimony films with hierarchical structures.

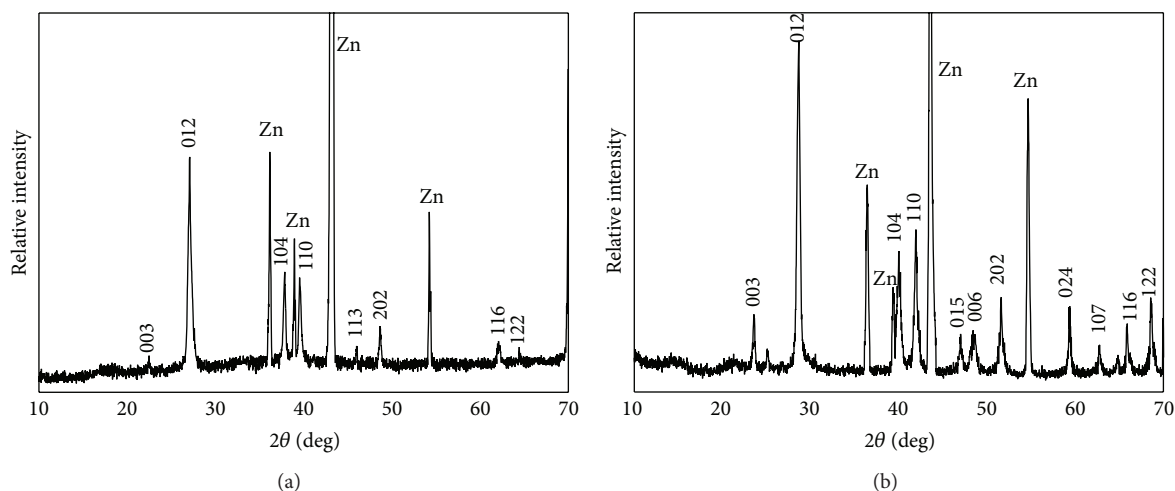


FIGURE 1: XRD patterns of Bi ((a) 120°C, 10 h, 4.6 mmol/L of  $\text{Bi}^{3+}$ ) and Sb ((b) 150°C, 24 h, 2.8 mmol/L of  $\text{Sb}^{3+}$ ).

## 2. Experimental Materials and Methods

Fresh zinc foils (15 mm × 15 mm) with a purity of 99.9% were used as both a reagent and a substrate for the direct growth of bismuth microtube arrays. In a typical process, analytically pure  $\text{BiCl}_3$  and poly-(vinylpyrrolidone) (PVP, M.W. 10000) were dispersed in deionized water under vigorous stirring; then the pH value was adjusted to 7.0 by addition of diluted aqueous NaOH. The mixture was transferred into a Teflon-lined stainless steel autoclave up to 85% of its capacity. The zinc foils were carefully washed with absolute alcohol and deionized water by ultrasound. After the zinc substrate was dipped into the solution, the autoclave was sealed and put into an oven. The reaction was conducted at 120°C for 10 h. After that, the zinc foils were taken out and rinsed with deionized water and alcohol. Bowl-shaped antimony nanostructures were prepared in the same way, just replacing  $\text{BiCl}_3$  with  $\text{SbCl}_3$ .

The as-prepared products on the substrate were directly subjected to characterizations by scanning electron microscopy (SEM) and powder X-ray diffraction (XRD). The XRD patterns were recorded by employing a Philips X'pert X-ray diffractometer with Cu K-Alpha radiation ( $\lambda = 0.154187$  nm). SEM images were obtained on a JSM-6700F field emission scanning electron microscope.

## 3. Results and Discussion

Figure 1 shows XRD pattern of the as-prepared bismuth and antimony samples. As shown in Figure 1(a), all the major peaks are labeled and can be attributed to rhombcentered bismuth metal according to the standard JCPDS diffraction file (cards number 5–519), except those marked with Zn coming from the zinc substrate. The calculated lattice parameters ( $a = 0.454$  nm and  $c = 1.184$  nm) are consistent with those reported in the JCPDS diffraction file, while XRD pattern in Figure 1(b) confirms the formation of rhombcentered metal antimony (JCPDS cards number 35–732), accompanied by

those strong peaks marked with Zn coming from the zinc substrate.

The morphology of the as-prepared bismuth sample was examined by SEM. Figure 2(a) shows SEM image of the zinc foil. It can be seen that zinc foil has a relatively smooth surface. After being treated in 4.6 mmol/L of  $\text{Bi}^{3+}$ , the entire surface of the zinc substrate is covered by a film of rod-like structures based on the SEM observation in Figure 2(b). It can be clearly seen from SEM image that only rod-like features are observed for the sample, which are quasi-aligned in a dense array. A higher magnification SEM image of bismuth rod arrays is shown in Figure 2(c). It can be clearly seen that the individual bismuth rod has a diameter in range of 300~1000 nm and length of more than 10  $\mu\text{m}$  growing radially on zinc substrate. Some open-ended tubes are also observed in Figure 2(c). Close examination of the top tips of the bismuth rods reveals that most of the rod-like structures are in fact bismuth tubes (Figure 2(d)). The average diameter of the open-ended tubes is ~600 nm, with hollow centers typically measured to be ~200 nm in diameter. Careful observation reveals that the walls of the tubes are constructed with large amount of flexible sheet-like tiny species in nanoscale.

The influence of the concentration of  $\text{Bi}^{3+}$  on the structures of the films has been investigated. When the synthesis was carried out in higher concentration of  $\text{Bi}^{3+}$  (5.8 mmol/L), a large amount of spherical bismuth microstructures, instead of Bi tubular crystals, was produced (Figure 3(a)). Although most of the microspheres appear to be separate particles, some of them are partially fused together to form larger microsphere aggregates. The exterior surfaces of the microspheres are not smooth but contain extensively growing sheet-like structures. To further examine the surface structure of these microspheres, a high magnification SEM image was obtained and is shown in the inset of Figure 3(a). The microspheres are randomly grown from seemingly flexible nanosheets that can be bent and connected with each other. The thickness of these nanosheets mostly ranges between 80 and 120 nm, whereas the size of the spherical structure is around 3  $\mu\text{m}$ . When the concentration of  $\text{Bi}^{3+}$  was further

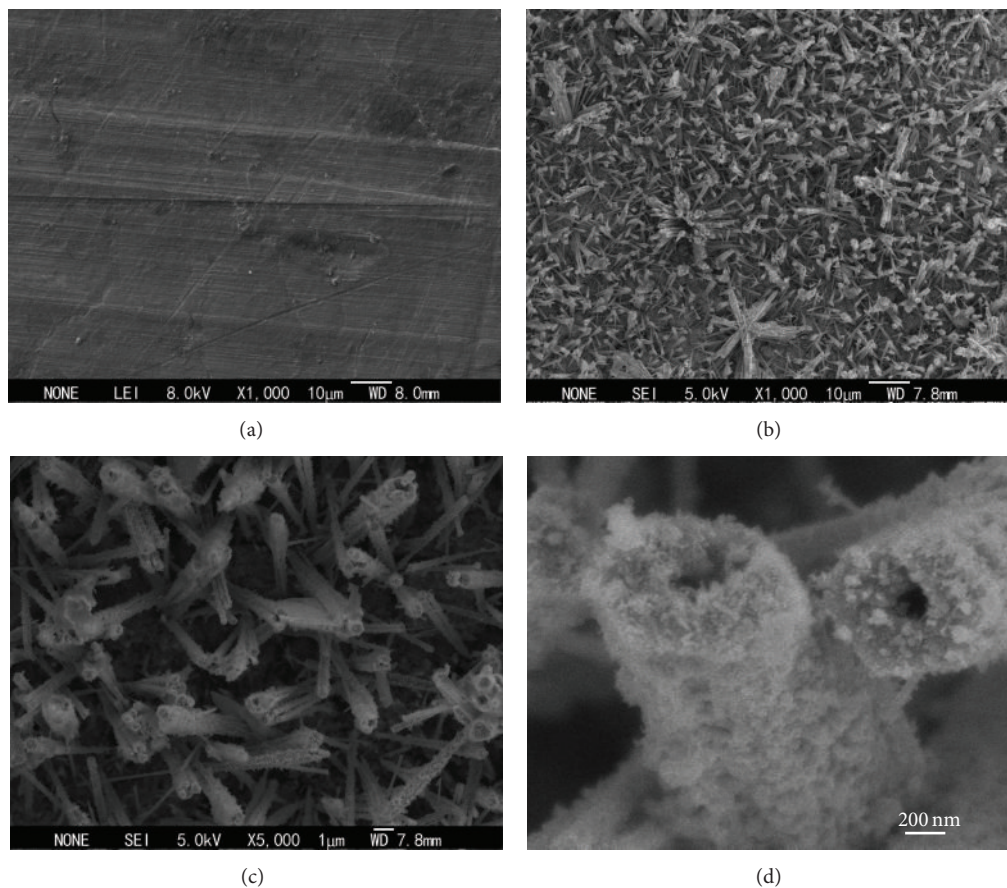


FIGURE 2: SEM images of zinc substrate (a) and Bi microtube arrays ((b)–(d) 120°C, 10 h, 4.6 mmol/L of  $\text{Bi}^{3+}$ ).

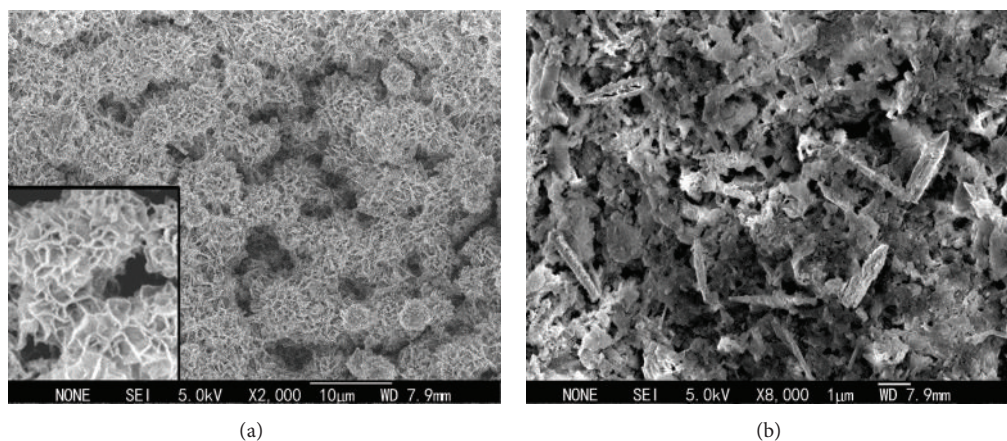
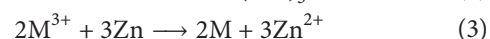


FIGURE 3: SEM images of Bi (a) flower-shaped crystal and (b) sheet-like structures. Inset of (a) shows magnified image of the spheres.

increased to 7.0 mmol/L, SEM image shown in Figure 3(b) revealed that the film was constructed with randomly stacked sheet-like structures with irregular shapes.

The formation of bismuth nanotubes in aqueous hydrazine system has been thought to be the result of the rolling of its pseudolayered structure [11]. As for the growth of tubular structures on substrate, the nuclei patterns on the substrates were deduced to be the mechanism for the formation of tube architectures. It has been reported that

ring-like patterned nuclei agglomeration results in the growth of tubular structures [27]. In the present study, the hydrothermal reaction of bismuth crystals can be explained as follows:



(M = Bi, Sb).

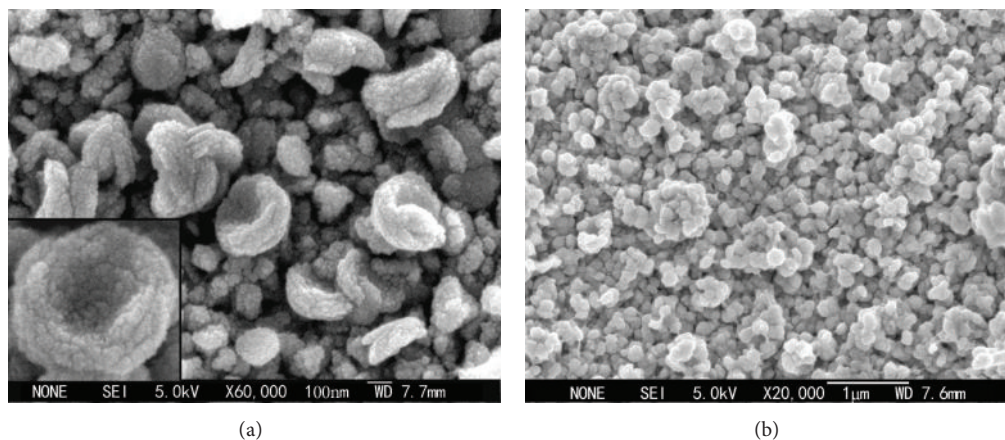


FIGURE 4: SEM images of Sb films prepared at 150°C for 24 h with (a) 2.8 and (b) 4.8 mmol/L of  $\text{Sb}^{3+}$ . Inset of (a): a magnified image of one bowl.

$\text{Bi}^{3+}$  ions have higher reaction activity with metal Zn; thus it is necessary to reduce the concentration of  $\text{Bi}^{3+}$  ions by adjusting the pH values. And then  $\text{BiCl}_3$  hydrolyzed into  $\text{BiOCl}$  and/or  $\text{Bi(OH)}_3$ . Controlled release of  $\text{Bi}^{3+}$  ions in reactions (1) and (2) was suitable for the reduction of  $\text{Bi}^{3+}$  into Bi nuclei. And the in situ formed Bi nuclei or nanoparticles may serve as seeds for the continuous epitaxial growth of Bi nuclei into tubular structures on the surface of zinc foil, which is similar to those tubular structures resulting from ring-like patterned nuclei agglomeration [27]. Along with the growth of Bi tubes, secondary nucleation may take place on their surface, which leads to the branched growth of sheet-like species on the tubes surface and thickening the walls of the tubes, whereas at higher concentration of  $\text{Bi}^{3+}$  ions with higher reaction velocity, the nucleation and crystal growth occur at a faster rate. As a result, nanosheets related Bi nanostructures were formed which might be contributed to the pseudolayered nature of metal bismuth.

It is known that antimony has a pseudolayered arsenic structure similar to that of rhombohedral bismuth. By extending this method to the preparation of antimony, however, bowl-shaped aggregates of Sb nanoparticles were obtained (150°C, 2.8 mmol/L  $\text{Sb}^{3+}$ ). Figure 4(a) shows the SEM image of the antimony film. It clearly reveals that zinc substrate was covered with Sb nano- or microparticles. Most of the particles exhibit bowl-shaped morphologies and display size in the range of 100–500 nm and wall thickness of about 80 nm. Higher magnification SEM image of an individual Sb nanobowl in the inset of Figure 4(a) reveals that the Sb nanobowl was constructed with even smaller Sb nanoparticles of 10–20 nm in diameters. Control experimental results show that the concentrations of  $\text{Sb}^{3+}$  have much influence on the structure of the films. If the reaction was conducted at higher concentration of  $\text{Sb}^{3+}$  (4.8 mmol/L), SEM image in Figure 4(b) reveals that the thin film is also constructed with nanoparticles and their aggregates, exhibiting irregular spherical shapes and wide size distributions.

More experimental results showed that the as-prepared products were sensitive to the initial pH value of

the suspension. If initial pH value was higher than 8, ZnO can be detected in the samples, while at lower initial pH values, such as a value lower than 6.0, the reaction activity between zinc and  $\text{Bi}^{3+}$  ( $\text{Sb}^{3+}$ ) ions was higher; as a result, irregularly aggregated nanostructures were obtained. When the hydrothermal reaction was conducted with initial pH value of 7.0, desired samples were obtained and the pH value slightly decreased to the range of 5.0–6.0. Additional experiments aimed at elucidating different growth mechanisms for metal Bi and Sb are in progress in our laboratory.

#### 4. Conclusion

In summary, a convenient hydrothermal route has been developed to prepare microtube arrays and hierarchical microspheres of metal Bi and bowl-shaped particles of metal Sb. The morphologies of Bi and Sb metal crystalline films were mainly controlled by the concentrations of metal ions and the initial pH values of the suspension. Extensive studies on different growth mechanisms for metals Bi and Sb are needed. The preparation strategy presented here is facile and cost-effective, which may open new avenues for the design of functional thin films of metal or other inorganic materials.

#### Conflict of Interests

The authors declare that there is no conflict of interests regarding the publication of this paper.

#### Acknowledgments

This work was financially supported by the Natural Science Foundation of Shandong Province (ZR2011EMM007, ZR2013BM002) and the Natural Science Found of Qingdao (12-1-4-3-(13)-jch).

## References

- [1] T. E. Huber, M. J. Graf, C. A. Foss Jr., and P. Constant, "Processing and characterization of high-conductance bismuth wire array composites," *Journal of Materials Research*, vol. 15, no. 8, pp. 1816–1821, 2000.
- [2] Y. W. Wang, J. S. Kim, G. H. Kim, and K. S. Kim, "Quantum size effects in the volume plasmon excitation of bismuth nanoparticles investigated by electron energy loss spectroscopy," *Applied Physics Letters*, vol. 88, no. 14, Article ID 143106, 2006.
- [3] E. Condrea and A. Nicorici, "Quantum size effect in the resistivity of bismuth nanowires," *Solid State Communications*, vol. 150, no. 1-2, pp. 118–121, 2010.
- [4] H. Zhang, J. S. Son, J. Jang et al., " $\text{Bi}_{1-x}\text{Sb}_x$  alloy nanocrystals: colloidal synthesis, charge transport, and thermoelectric properties," *ACS Nano*, vol. 7, no. 11, pp. 10296–10306, 2013.
- [5] D. A. Glocker and M. J. Skove, "Field effect and magnetoresistance in small bismuth wires," *Physical Review B*, vol. 15, no. 2, pp. 608–616, 1977.
- [6] Z. Zhang, D. Gekhtman, M. S. Dresselhaus, and J. Y. Ying, "Processing and characterization of single-crystalline ultrafine bismuth nanowires," *Chemistry of Materials*, vol. 11, no. 7, pp. 1659–1665, 1999.
- [7] J. Reppert, R. Rao, M. Skove et al., "Laser-assisted synthesis and optical properties of bismuth nanorods," *Chemical Physics Letters*, vol. 442, no. 4–6, pp. 334–338, 2007.
- [8] K. Liu, C. L. Chien, and P. C. Searson, "Finite-size effects in bismuth nanowires," *Physical Review B: Condensed Matter and Materials Physics*, vol. 58, no. 22, Article ID R14681, 1998.
- [9] Y. Peng, D. H. Qin, R. J. Zhou, and H. L. Li, "Bismuth quantum-wires arrays fabricated by electrodeposition in nanoporous anodic aluminum oxide and its structural properties," *Materials Science and Engineering B: Solid-State Materials for Advanced Technology*, vol. 77, no. 3, pp. 246–249, 2000.
- [10] Y. Zhu, X. Dou, X. Huang, A. Li, and G. Li, "Thermal properties of Bi nanowire arrays with different orientations and diameters," *The Journal of Physical Chemistry B*, vol. 110, no. 51, pp. 26189–26193, 2006.
- [11] Y. Li, J. Wang, Z. Deng et al., "Bismuth nanotubes: A rational low-temperature synthetic route," *Journal of the American Chemical Society*, vol. 123, no. 40, pp. 9904–9905, 2001.
- [12] J. Wang, X. Wang, Q. Peng, and Y. Li, "Synthesis and characterization of bismuth single-crystalline nanowires and nanospheres," *Inorganic Chemistry*, vol. 43, no. 23, pp. 7552–7556, 2004.
- [13] B. Yang, C. Li, H. Hu, X. Yang, Q. Li, and Y. Qian, "A room-temperature route to bismuth nanotube arrays," *European Journal of Inorganic Chemistry*, vol. 2003, no. 20, pp. 3699–3702, 2003.
- [14] F. Wang, R. Tang, H. Yu, P. C. Gibbons, and W. E. Buhro, "Size- and shape-controlled synthesis of bismuth nanoparticles," *Chemistry of Materials*, vol. 20, no. 11, pp. 3656–3662, 2008.
- [15] E. E. Foos, R. M. Stroud, A. D. Berry, A. W. Snow, and J. P. Armistead, "Synthesis of nanocrystalline bismuth in reverse micelles," *Journal of the American Chemical Society*, vol. 122, no. 29, pp. 7114–7115, 2000.
- [16] Z. Wang, C. Jiang, R. Huang, H. Peng, and X. Tang, "Investigation of optical and photocatalytic properties of bismuth nanospheres prepared by a facile thermolysis method," *The Journal of Physical Chemistry C*, vol. 118, no. 2, pp. 1155–1160, 2014.
- [17] D. Ma, J. Zhao, R. Chu et al., "Novel synthesis and characterization of bismuth nano/microcrystals with sodium hypophosphite as reductant," *Advanced Powder Technology*, vol. 24, no. 1, pp. 79–85, 2013.
- [18] W. Z. Wang, B. Poudel, Y. Ma, and Z. F. Ren, "Shape control of single crystalline bismuth nanostructures," *The Journal of Physical Chemistry B*, vol. 110, no. 51, pp. 25702–25706, 2006.
- [19] Y. W. Wang, B. H. Hong, and K. S. Kim, "Size control of semimetal bismuth nanoparticles and the UV - Visible and ER absorption spectra," *Journal of Physical Chemistry B*, vol. 109, no. 15, pp. 7067–7072, 2005.
- [20] S. Schulz, S. Heimann, C. Wölper, and W. Assenmacher, "Synthesis of bismuth pseudocubes by thermal decomposition of  $\text{Bi}_2\text{Et}_4$ ," *Chemistry of Materials*, vol. 24, no. 11, pp. 2032–2039, 2012.
- [21] T. Fukaya, J. Tominaga, T. Nakano, and N. Atoda, "Optical switching property of a light-induced pinhole in antimony thin film," *Applied Physics Letters*, vol. 75, no. 20, pp. 3114–3116, 1999.
- [22] J. Heremans, C. M. Thrush, Y.-M. Lin, S. B. Cronin, and M. S. Dresselhaus, "Transport properties of antimony nanowires," *Physical Review B*, vol. 63, no. 8, Article ID 085406, 2001.
- [23] Y. Zhang, G. Li, Y. Wu, B. Zhang, W. Song, and L. Zhang, "Antimony nanowire arrays fabricated by pulsed electrodeposition in anodic alumina membranes," *Advanced Materials*, vol. 14, no. 17, pp. 1227–1230, 2002.
- [24] Y. W. Wang, B. H. Hong, J. Y. Lee, J.-S. Kim, G. H. Kim, and K. S. Kim, "Antimony nanowires self-assembled from Sb nanoparticles," *Journal of Physical Chemistry B*, vol. 108, no. 43, pp. 16723–16726, 2004.
- [25] P. Liu, K. Zhong, C. Liang et al., "Self-assembly of three-dimensional nanostructured antimony," *Chemistry of Materials*, vol. 20, no. 24, pp. 7532–7538, 2008.
- [26] D. Wang and C. Song, "Controllable synthesis of ZnO nanorod and prism arrays in a large area," *The Journal of Physical Chemistry B*, vol. 109, no. 26, pp. 12697–12700, 2005.
- [27] S. Sharma and M. K. Sunkara, "Direct synthesis of gallium oxide tubes, nanowires, and nanopaintbrushes," *Journal of the American Chemical Society*, vol. 124, no. 41, pp. 12288–12293, 2002.

## Research Article

# A Low-Stress, Elastic, and Improved Hardness Hydrogenated Amorphous Carbon Film

Qi Wang,<sup>1</sup> Deyan He,<sup>1</sup> and Junyan Zhang<sup>2</sup>

<sup>1</sup>School of Physics, Lanzhou University, Lanzhou 730000, China

<sup>2</sup>State Key Laboratory of Solid Lubrication, Lanzhou Institute of Chemical Physics, Chinese Academy of Sciences, Lanzhou 730000, China

Correspondence should be addressed to Qi Wang; wangqi77@lzu.edu.cn

Received 6 October 2014; Accepted 2 December 2014

Academic Editor: Yuanlie Yu

Copyright © 2015 Qi Wang et al. This is an open access article distributed under the Creative Commons Attribution License, which permits unrestricted use, distribution, and reproduction in any medium, provided the original work is properly cited.

The evolution of hydrogenated amorphous carbon films with fullerene-like microstructure was investigated with a different proportion of hydrogen supply in deposition. The results showed at hydrogen flow rate of 50 sccm, the deposited films showed a lower compressive stress (lower 48.6%), higher elastic recovery (higher 19.6%, near elastic recovery rate 90%), and higher hardness (higher 7.4%) compared with the films deposited without hydrogen introduction. Structural analysis showed that the films with relatively high  $sp^2$  content and low bonded hydrogen content possessed high hardness, elastic recovery rate, and low compressive stress. It was attributed to the curved graphite microstructure, which can form three-dimensional covalently bonded network.

## 1. Introduction

Hydrogenated amorphous carbon films with fullerene-like microstructure have attracted increasing attention due to their extraordinary properties of high mechanical hardness and low friction coefficient [1–4]. It can be as a protective coating in tooling components, such as knives, drill bits, dies, and molds, and as a coating on hard-disk platters and hard-disk read heads. Until now, hydrogenated amorphous carbon films with fullerene-like microstructure had been synthesized by our group and other groups with different techniques including dc pulse plasma chemical vapor deposition (CVD), magnetron sputtering (MS), ECR CVD, and ICP CVD [1–8].

In this paper, hydrogenated carbon films were deposited with dc pulse plasma CVD system. The as-deposited carbon films could be considered as nanocomposite thin films with fullerene-like microstructure in the diamond-like carbon (DLC) matrix based on our previous results [1, 2]. In order to study the evolution of structure and properties of films, a different content of  $H_2$  was introduced to the mixture of methane and hydrogen as feedstock. The deposition pressure was kept constant. The result discloses the close relationship between  $sp^2$  content, bonded hydrogen content and

hardness, elastic recovery rate, and compressive stress. The film deposited at hydrogen flow rate 20 and 50 sccm showed higher hardness and elastic and lower compressive stress.

## 2. Experiments

Hydrogenated amorphous carbon films were prepared on Si (100) substrates at different flux ratio of methane to hydrogen in the mixture which was about 1:0, 1:1, 1:2, 1:5, and 1:10 by dc-pulse plasma CVD technique. The flux of methane was kept constantly at 10.3 sccm. The deposition pressure was kept at 13 Pa. After deposition, optical profilometry, X-ray photoelectron spectra (XPS), reflection Fourier transform infrared (FTIR) spectra, and high-resolution transmission electron microscopy (HRTEM) were applied to probe the microstructure. Nanoindentation was applied to assess mechanical properties of the films.

## 3. Results and Discussion

Figure 1(a) shows the thickness and compressive stress of hydrogenated amorphous carbon films deposited with dc pulse plasma CVD versus  $H_2$  flow rate. The film thickness

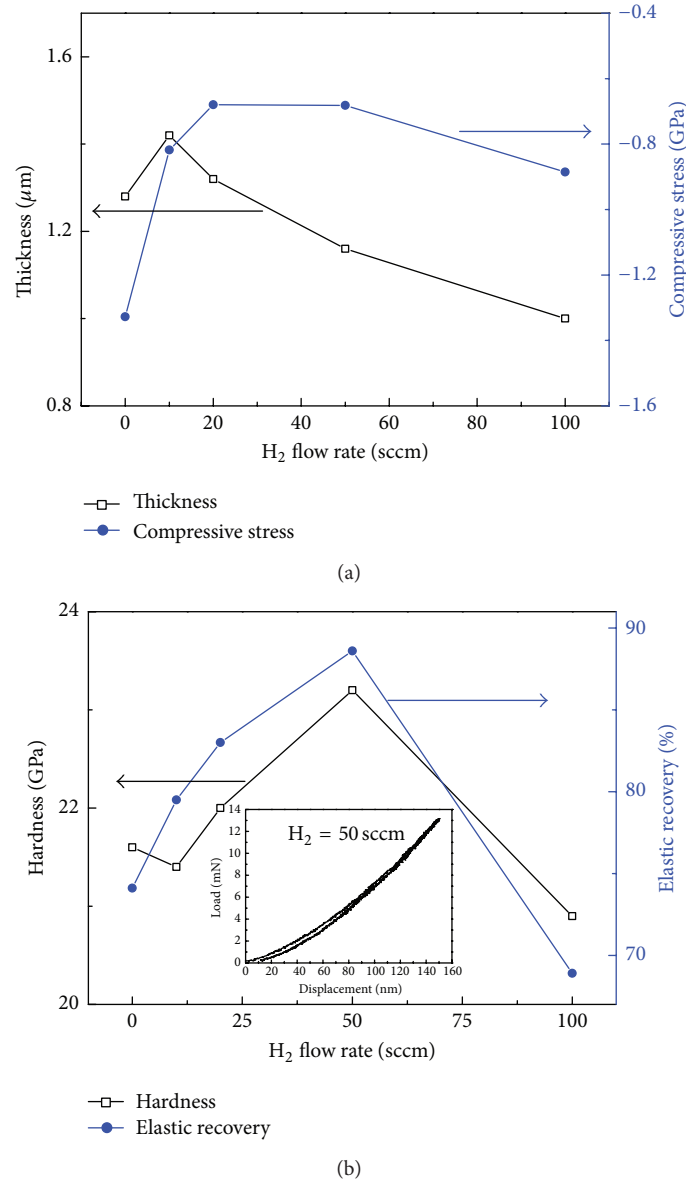


FIGURE 1: (a) Thickness and compressive stress of the as-deposited hydrogenated amorphous carbon films versus H<sub>2</sub> flow rate; (b) hardness and elastic recovery  $R$  of the as-deposited hydrogenated amorphous carbon films versus H<sub>2</sub> flow rate.

values were measured by surface profilometer. The compressive stress values were calculated by Stoney's equation with curvature radii that were measured by optical profilometry. It is obvious that the compressive stress value decreased quickly when H<sub>2</sub> was introduced into the mixture gas as feedstock. The values for the films deposited at H<sub>2</sub> 20 and 50 sccm are lower (~48.6%) than the film deposited without H<sub>2</sub> introduction. Generally, for amorphous carbon films, the decrease of compressive stress is corresponding to the structure transform of sp<sup>3</sup>-bonded atoms to sp<sup>2</sup>-bonded atoms.

Figure 1(b) exhibited the mechanical properties of the hydrogenated amorphous carbon films versus the H<sub>2</sub> flow rate. In our experiment, in order to minimise the effect of substrate, the maximum indentation depth was kept at 1/7 of the film thickness. Five replicate indentations were made

for each film sample. The elastic recovery  $R$  was defined as  $R = (d_{\max} - d_{\text{res}})/d_{\max}$ , where  $d_{\max}$  and  $d_{\text{res}}$  were the maximum displacement at the maximum load and the residual displacement after unloading, respectively [9]. This is a clear indication of plastic deformation regime. For the films deposited using dc-pulse plasma CVD versus the H<sub>2</sub> flow rate, the mechanical properties increased at the beginning, as shown in Figure 1(b). When the H<sub>2</sub> flow rate increased to 50 sccm, the hardness of the film was as high as ~23.2 GPa, 7.4% higher compared to ~21.6 GPa for the film deposited without H<sub>2</sub> introduction, and the elastic recovery  $R$  was as high as ~88.6%, 19.6% higher compared to ~74.1% for the film deposited without H<sub>2</sub> introduction. When the H<sub>2</sub> flow rate increased to 100 sccm, there was a sharp decrease for hardness and elastic recovery. The values were decreased to ~20.9 GPa

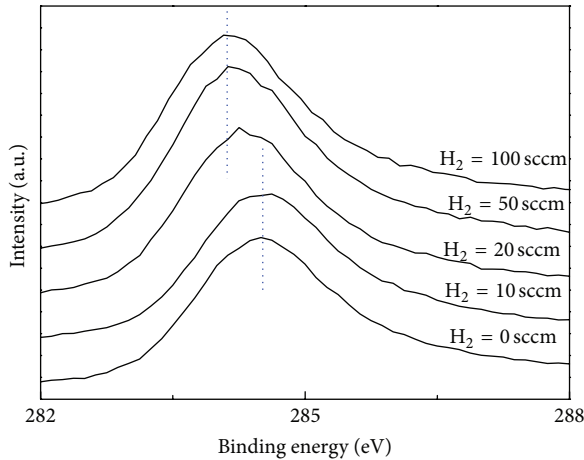


FIGURE 2: XPS spectra of as-deposited hydrogenated amorphous carbon films versus  $H_2$  flow rate.

and  $\sim 68.9\%$ , respectively. In order to reveal the reason of the transform and the origin of lower stress, higher hardness, and elastic recovery  $R$ , it is necessary to perform the films' structure probing to reveal the structure factor.

Figure 2 shows the C1s core level XPS spectra of hydrogenated amorphous carbon films versus different  $H_2$  flow rates. In this paper, Au thin film about 0.2 nm was deposited on the test surfaces so as to minimize the charging effect in the XPS analysis. The C1s peak can be decomposed into two peaks:  $sp^2$  and  $sp^3$ . The one around 284.3 eV corresponded to  $sp^2$  carbon atoms, and that around 285.2 eV corresponded to  $sp^3$  carbon atoms [10]. The C1s binding energy position of the film deposited without  $H_2$  introduction is  $\sim 284.6$  eV. As the  $H_2$  flow rate increased, except at the  $H_2$  flow rate of 10 sccm, a clear chemical shift to lower binding energy showed at  $H_2$  flow rate of 20, 50, and 100 sccm. We concluded that the  $sp^2$  carbon structure increased with the increased  $H_2$  flow rate. It was likely that excess  $H_2$  flow rate increased the impact of ion etching and impingement and led to the structure transformation from  $sp^3$  to  $sp^2$ . In particular, the binding energy positions of C1s at the  $H_2$  flow rate of 50 and 100 sccm are very close to the binding energy of C1s for pure graphite, 284.3 eV [11]. Combined with the data of stress, hardness, and elastic recovery  $R$ , the reason for the improved properties of the film deposited at  $H_2$  flow rate of 20 and 50 sccm should be the increased  $sp^2$  structure. It mainly existed in the form of fullerene-like curved graphite structure. The increased binding energy level at  $H_2$  flow rate of 10 sccm is due to the defects (dangling bonds) in the films that were ended or occupied by H atoms when  $H_2$  was introduced, which prompted the formation of  $sp^3$  structure.

In order to get a better understanding of the bonding structure of all the samples, reflection FTIR spectra were invoked to determine the C–H bonding configuration. The bonded hydrogen content in films can be applied as a probe to detect the structural environment of the attached carbon atoms due to the localized nature of the C–H vibration. FTIR spectrum was widely used in this sense to characterize the

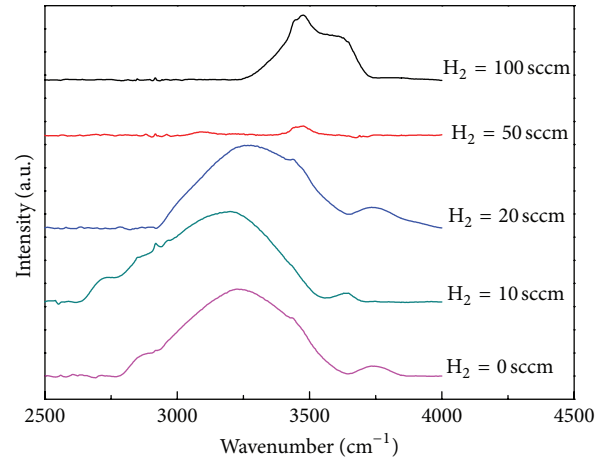


FIGURE 3: Reflection IR spectra of as-deposited hydrogenated amorphous carbon films versus  $H_2$  flow rate.

C–H bonding in hydrogenated carbon films. It is known that the FTIR intensity of amorphous carbon films is relevant to the hydrogen incorporation.

Generally, the peaks in the range of 2800–3300  $cm^{-1}$  are attributed to the different stretching vibrations of C–H bonds. The C–H stretching modes can break down into three regions, the  $sp^1 \equiv C-H$  modes centre on 3300  $cm^{-1}$ , the  $sp^2 =CH_n$  modes lie from 2975 to 3085  $cm^{-1}$ , and  $sp^3 -C-H_n$  modes lie from 2850 to 2955  $cm^{-1}$  [12]. Figure 3 shows the reflection FTIR spectra of as-deposited hydrogenated amorphous carbon films versus the  $H_2$  flow rate. For the film deposited without  $H_2$  introduction, the peak was broad, and it can conclude  $sp^3 -C-H_n$ ,  $sp^2 =CH_n$ , and  $sp^1 \equiv C-H$  complexes. However, by carefully examining the peaks, it is also found that there is a clear chemical shift to high wavenumber at  $H_2$  flow rate of 20, 50, and 100 sccm, and the peak intensity at the flow rate of 50 sccm decreased sharply, indicating a reduction of bonded hydrogen in carbon films. At the  $H_2$  flow rate of 10 sccm, since the defects (dangling bonds) in the films probably could be ended or occupied completely by H ions generated by methane and  $H_2$ , which prompt the formation of  $sp^3$  structure, the peak position has a little shift to lower wavenumber. The analysis of increased  $sp^3$  content is consistent with that provided by XPS. When  $H_2$  content further increased, impact of ion etching and impingement increased, and  $sp^3 -C-H_n$  changed into  $sp^2 =CH_n$  and  $sp^1 \equiv C-H$ . As the  $H_2$  flow rate was increased to 50 sccm, mounts of C–H bonding were destroyed;  $-H$  easily combined each other to form  $H_2$  and led to a loss of hydrogen content in the as-deposited film. It is obvious that the structure was gradually turned into  $sp^2$ . When  $H_2$  flow rate increased further, impact of ion etching and impingement was strong and led to porous structure in film. We suggest that this is the reason for the absorption peak of  $H_2O$  at a wavenumber of 3400–3700  $cm^{-1}$  for the film deposited at  $H_2$  flow rate of 100 sccm. Combined with XPS spectra, the reason of the improved properties of the film deposited at  $H_2$  flow rate of 20 and 50 sccm should be the

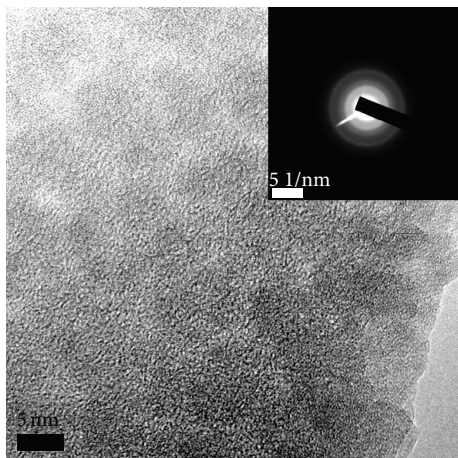


FIGURE 4: TEM images of as-deposited hydrogenated amorphous carbon films versus  $H_2$  flow rate of 50 sccm. The scale bar represents 5 nm.

increased  $sp^2$  structure that mainly existed in the form of fullerene-like curved graphite structure, and the reason for poor properties of the film deposited at  $H_2$  flow rate of 100 sccm should be the porous structure of the film formed in deposition process.

Figure 4 shows the HRTEM image of the hydrogenated amorphous carbon film deposited at  $H_2$  flow rate of 50 sccm by dc pulse plasma CVD, displaying amorphous structure. There is no obvious ordered fullerene-like curved graphite structure. The corresponding SAED pattern indicates the amorphous structure of the film and displays three corresponding measures of spacing of 1.15, 2.00, and 3.50 Å. The two rings at 1.15 and 2.00 Å coincide with those observed for amorphous carbon structure, whereas the ring at 3.50 Å matches well the interplane spacing of hexagonal basal planes of graphite (0002) [13]. The appearance of a broad feature at 3.50 Å indicates the presence of defective graphitic planes and confirms the formation of fullerene-like structure in as-deposited films. However, the fullerene-like features in our HRTEM image are not so clear compared to the other reports [2, 14]. The reason is mainly from the too large thickness for HRTEM samples. Meanwhile, the HRTEM image can be seen from our previous reports. Combined with XPS and FTIR spectra results, it was reasonably concluded that the improved mechanical properties were corresponding to increased curved graphite (fullerene-like) structure. We speculated the reason why there was no obvious curved graphite structure that was from the impact of ion etching and impingement and led to a poor order of the structure.

It was obvious that the improvement of mechanical property versus  $H_2$  flow rate was due to the change of microstructure. It was much different from conventional hydrogenated amorphous carbon films, in which the mechanical properties decreased as  $sp^2$  bonding structure increased; in other words, a high concentration of  $sp^2$  graphitic bonds indicates soft film. Recently, the nanostructure of the films may also play dominant role in determining the mechanical properties of amorphous carbon films [1, 2]. This thought is supported

by the recent report that the mechanical properties of DLC films probably are not only dominated by  $sp^3$  fraction but also the degree of the  $sp^2$  bonding arrangement. In this paper, combined with XPS results, according to our and other researchers' reports, fullerene-like microstructure in the hydrogenated carbon matrix could be considered as the structure factor for the lower compressive stress, high hardness, and high elasticity. The film can possess lower stress, higher hardness, and higher elasticity by adjusting  $sp^2$  content and bonded hydrogen content.

#### 4. Conclusion

In summary, the evolution of structure and mechanical properties of the hydrogenated amorphous carbon films with fullerene-like microstructure was investigated. The results showed that at hydrogen flow rate of 50 sccm, the deposited hydrogenated amorphous carbon films exhibited lower compressive stress (lower 48.6%), higher elastic recovery (higher 19.6%, near elastic recovery rate 90%), and higher hardness (higher 7.4%) compared with the films deposited without hydrogen introduction. Structural analysis showed that the film with relatively high  $sp^2$  content and low bonded hydrogen content possessed high hardness, elastic recovery rate, and low compressive stress. It was attributed to the curved grapheme microstructure, which can form three-dimensional covalently bonded network. Meanwhile, when excess  $H_2$  was introduced, impact of ion etching and impingement was strong and led to porous structure in film.

#### Conflict of Interests

The authors declare that there is no conflict of interests regarding the publication of this paper.

#### Acknowledgment

The project was financially supported by the Ph.D. Programs Foundation of Ministry of Education of China with Grant no. 20100211120017.

#### References

- [1] Q. Wang, C. B. Wang, Z. Wang, J. Y. Zhang, and D. He, "Fullerene nanostructure-induced excellent mechanical properties in hydrogenated amorphous carbon," *Applied Physics Letters*, vol. 91, no. 14, Article ID 141902, 2007.
- [2] C. B. Wang, S. R. Yang, Q. Wang, Z. Wang, and J. Y. Zhang, "Super-low friction and super-elastic hydrogenated carbon films originated from a unique fullerene-like nanostructure," *Nanotechnology*, vol. 19, no. 22, Article ID 225709, 2008.
- [3] Z. Wang and J. Zhang, "Deposition of hard elastic hydrogenated fullerenelike carbon films," *Journal of Applied Physics*, vol. 109, no. 10, Article ID 103303, 4 pages, 2011.
- [4] J. G. Buijnsters, M. Camero, R. Gago, A. R. Landa-Canovas, C. Gómez-Aleixandre, and I. Jiménez, "Direct spectroscopic evidence of self-formed C60 inclusions in fullerenelike hydrogenated carbon films," *Applied Physics Letters*, vol. 92, no. 14, Article ID 141920, 2008.

- [5] J. G. Buijnsters, R. Gago, I. Jiménez, M. Camero, F. Agulló-Rueda, and C. Gómez-Aleixandre, "Hydrogen quantification in hydrogenated amorphous carbon films by infrared, Raman, and x-ray absorption near edge spectroscopies," *Journal of Applied Physics*, vol. 105, no. 9, Article ID 093510, 2009.
- [6] P. Wang, X. Wang, B. Zhang, and W. M. Liu, "Structural, mechanical and tribological behavior of fullerene-like carbon film," *Thin Solid Films*, vol. 518, no. 21, pp. 5938–5943, 2010.
- [7] L. Ji, H. Li, F. Zhao, W. L. Quan, J. M. Chen, and H. D. Zhou, "Effects of pulse bias duty cycle on fullerene-like nanostructure and mechanical properties of hydrogenated carbon films prepared by plasma enhanced chemical vapor deposition method," *Journal of Applied Physics*, vol. 105, no. 10, Article ID 106113, 2009.
- [8] J. Robertson, "Diamond-like amorphous carbon," *Materials Science & Engineering: R: Reports*, vol. 37, no. 4–6, pp. 129–281, 2002.
- [9] M. A. Tamor and W. C. Vassell, "Raman 'fingerprinting' of amorphous carbon films," *Journal of Applied Physics*, vol. 76, no. 6, pp. 3823–3830, 1994.
- [10] F. Tuinstra and J. L. Koenig, "Raman spectrum of graphite," *Journal of Chemical Physics*, vol. 53, no. 3, pp. 1126–1130, 1970.
- [11] G. Abrasonis, R. Gago, M. Vinnichenko, U. Kreissig, A. Kolitsch, and W. Möller, "Sixfold ring clustering in  $sp^2$ -dominated carbon and carbon nitride thin films: a Raman spectroscopy study," *Physical Review B*, vol. 73, no. 12, Article ID 125427, 2006.
- [12] A. C. Ferrari and J. Robertson, "Interpretation of Raman spectra of disordered and amorphous carbon," *Physical Review B—Condensed Matter and Materials Physics*, vol. 61, no. 20, pp. 14095–14107, 2000.
- [13] J. Díaz, G. Paolicelli, S. Ferrer, and F. Comin, "Separation of the  $sp^3$  and  $sp^2$  components in the C1s photoemission spectra of amorphous carbon films," *Physical Review B: Condensed Matter and Materials Physics*, vol. 54, no. 11, pp. 8064–8069, 1996.
- [14] W. T. Zheng, H. Sjöström, I. Ivanov et al., "Reactive magnetron sputter deposited  $CN_x$ : effects of  $N_2$  pressure and growth temperature on film composition, bonding, and microstructure," *Journal of Vacuum Science & Technology A: Vacuum, Surfaces and Films*, vol. 14, no. 5, pp. 2696–2701, 1996.

## Research Article

# Glaze Icing on Superhydrophobic Coating Prepared by Nanoparticles Filling Combined with Etching Method for Insulators

Chao Guo,<sup>1</sup> Ruijin Liao,<sup>1</sup> Yuan Yuan,<sup>2</sup> Zhiping Zuo,<sup>1</sup> and Aoyun Zhuang<sup>1</sup>

<sup>1</sup>State Key Laboratory of Power Transmission Equipment & System Security and New Technology, Chongqing University, Chongqing 400044, China

<sup>2</sup>College of Materials Science and Engineering, Chongqing University, Chongqing 400044, China

Correspondence should be addressed to Ruijin Liao; [rjliao@cqu.edu.cn](mailto:rjliao@cqu.edu.cn)

Received 5 September 2014; Accepted 18 November 2014

Academic Editor: Jiamin Wu

Copyright © 2015 Chao Guo et al. This is an open access article distributed under the Creative Commons Attribution License, which permits unrestricted use, distribution, and reproduction in any medium, provided the original work is properly cited.

Icing on insulators may cause flashover or even blackout accidents in the power transmission system. However, there are few anti-icing techniques for insulators which consume energy or manpower. Considering the water repelling property, the superhydrophobic surface is introduced for anti-icing of insulators. Among the icing forms, the glaze icing owns the highest density, strongest adhesion, and greatest risk to the power transmission system but lacks researches on superhydrophobic surface. In this paper, superhydrophobic surfaces with contact angle of  $166.4^\circ$ , contact angle hysteresis of  $0.9^\circ$ , and sliding angle of less than  $1^\circ$  are prepared by nanoparticle filling combined with etching method. The coated glass slide and glass insulator showed excellent anti-icing performance in the glaze icing test at  $-5^\circ\text{C}$ . The superhydrophobicity and anti-icing property of the coatings benefit from the low surface energy and hierarchical rough structure containing micron scale pits and nanoscale coraloid bulges supported by scanning electron microscopy (SEM), atomic force microscopy (AFM), and X-ray photoelectron spectroscopy (XPS) characterization.

## 1. Introduction

Icing is a global problem causing tremendous economic losses, equipment failures, and casualties. In 2008, the icing in southern China resulted in outage of 36740 power transmission lines and 1743 substations with 2 billion dollars of direct economic loss [1]. The icing accumulation on insulators and transmission lines caused line breakage, conductor galloping, falling down of transmission tower, and insulator flashover, further leading to power blackout. Techniques for anti-icing and deicing of transmission lines have been well developed like current deicing [2], deicing robot [3], ferromagnetic wires [4], and electromagnetic-impulsive deicing [5]. However, these methods consume a lot of energy and cannot be applied on insulators whose anti-icing and deicing techniques are very limited. Liao et al. [6] introduced the semiconducting RTV silicone coating on insulators to generate Joule heat to reduce the ice formation which however still costs energy and

accelerates the aging of the coating. The superhydrophobic surface is an efficient anti-icing method as its water repelling property proved by many researches [7–9]. However, they mainly considered the frost formation or icing of static water drops on superhydrophobic surfaces [10, 11]. As an important icing form, the glaze icing is most dangerous to the power transmission system because of its high density and adhesion whose accumulation on superhydrophobic surfaces lacks attention. There are three kinds of insulators in the power transmission system which are the glass insulator, the ceramic insulator, and the composite insulator. The glass insulator is widely utilized in the State Grid of China with a ratio of 23.9% up to 2007. Therefore, the glass slides and glass insulators were chosen as the coating substrates.

There are many methods to fabricate superhydrophobic surfaces like sol-gel [12], physical vapor deposition [13], chemical vapor deposition [14], lithography [15], and phase separation [16]. However, most methods are expensive and

complicated which are not suitable for industry application on insulators. In the previous research, the application of silica, calcium carbonate, fluorosilicone resin, and epoxy in superhydrophobic surfaces have been explored while the combination of nanoparticles filling and etching methods seems rare. For instance, Zhang et al. fabricated superhydrophobic surface with a mixture of nano- and micro-sized calcium carbonate ( $\text{CaCO}_3$ ) suspensions [17]. Hydrophobic surfaces were prepared on epoxy coating surfaces by using fluorosilicone copolymer and  $\text{SiO}_2$  nanoparticles [18]. In this paper, a facile approach combining the nanoparticle filling and the etching method to fabricate superhydrophobic coating is proposed. The wettability, surface morphology, and chemical construction of the coatings are characterized. In particular, the glaze icing properties of coatings on glass slides and glass insulators are investigated in the artificial climate chamber.

## 2. Experimental

**2.1. Preparation.** The glass slides were ultrasonically cleaned in absolute ethanol and distilled water and then dried before used as substrates. The fluoroalkylsilane (2 mL, G502,  $\text{C}_{14}\text{F}_{12}\text{H}_{20}\text{SiO}_3$ , >95%), distilled water (4 g) and ethanol (200 mL) were added into a flask. The mixed solution was stirred at 240 r/min and  $60^\circ\text{C}$  for 30 min before nanometer calcium carbonate (10 g, 30–60 nm) was added. 150 mL of upper clear liquid was removed after 15 minutes' standing. Then nanosilica particles (10 g, 15–25 nm, Henan Wangwu Technology Co., Ltd.) and ethyl acetate (90 mL) were added into the solution and stirred for another 30 min. Finally 130 g of solution containing nanometer calcium carbonate (10 g) and nanosilica particles (10 g) was obtained. The as-prepared nanoparticles were filled in polymers consisted of fluorosilicon resin (FSI, fluorinated organosilicon resin with contact angle of  $110^\circ$ , Ark Chemicals Industry Co. Ltd) and epoxy resin (E-51). Three coatings were fabricated by adjusting the contents of nanoparticles (20%, 33%, and 49%). The mass ratio among nano- $\text{CaCO}_3$ , nano- $\text{SiO}_2$ , FSI, E-51, curing agent, and solvent was 1:1:6:1.2:1:11 for the coating with nanoparticle content of 20%. The mixed solution was dispersed by electromagnetic stirring and ultrasonic agitation before spray coating. The spraying distance between the nozzle and the substrates was 25 cm and the air pressure was held at 0.4 MPa. The nozzle was fixed and the substrates moved with a speed of 2 cm/s. The substrates were sprayed for 4 times and then dried at  $130^\circ\text{C}$  for 30 min. The coatings were then immersed into acetic acid for 10 s and then put into abundant distilled water for etching. Finally, these samples were dried at  $130^\circ\text{C}$  for 30 min before characterization. The glass insulators (FC70/146, Huayu HV Insulator Co. Ltd.) were treated in the same way as the glass slides.

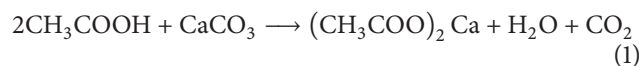
**2.2. Characterization.** The wettability of the samples was evaluated using an optical contact angle meter (Drop Meter A-200, MAIST Vision Inspection & Measurement Co., Ltd.). The contact angle was observed by placing a  $5\ \mu\text{L}$  droplet on the sample and five measurements were made for each

sample. The contact angle hysteresis was measured by method of adding and decreasing the volume of the droplet. The surface morphologies of the samples were observed with the field emission scanning electron microscope (FESEM, S-4800, Hitachi Ltd., Japan). The surface topography of the samples was obtained by atomic force microscope (AFM-IPC-208B, Chongqing University) using a tungsten probe (force constant = 0.06 N/m) operating in tapping mode in air at ambient conditions. The composition of the sample was analyzed using X-ray photoelectron spectrometry (XPS, Thermo escalab 250Xi, Thermo Fisher Scientific Inc., MA, USA) with  $\text{Al K}\alpha$  X-ray source. The glaze icing experiment was conducted in the artificial climate chamber with temperature of  $-5^\circ\text{C}$  and relative humidity of  $79 \pm 10\%$ . The rain was generated through a nozzle by pumping water of  $3.8\text{--}5^\circ\text{C}$  with volume median diameter of about  $100\ \mu\text{m}$ . The glass slides were set vertically facing the rain drops while the glass insulators were hanged.

## 3. Results and Discussion

The morphologies of the coatings before and after etching with particle content of 33% are presented in Figure 1. The surface is rather like that of moon with many ringlike pits or craters whose sizes range from 1 to  $20\ \mu\text{m}$  in Figures 1(a) and 1(d). Observed in the nanoscale of Figures 1(c) and 1(f), the edges of the pits consist of nanometer coralloid bulges due to the addition of nanoparticles. This hierarchical rough structure is generated by the fast evaporation of the solvent when spraying. The mixture of resins (including fluorosilicone resin and epoxy resin), nanoparticles (including  $\text{SiO}_2$  and  $\text{CaCO}_3$ ), ethyl acetate, and ethyl alcohol is sprayed onto the glass with high speed leading to the fast evaporation of solvent, increase of the viscosity, and inhomogeneous distribution of the mixture. The bigger pits and smaller coralloid bulges are formed after the solidification of resins. However, the coatings before and after etching show little difference in the SEM images which need more accurate topological information.

The topological information of the surfaces is given in Figure 2. The coating after etching has rougher surface as the height difference between the peak and valley (1404 nm),  $R_a$  (at  $y = 3200\ \text{nm}$ ), and  $S_a$  are all bigger. This may be caused by the etching of  $\text{CaCO}_3$  as shown in (1). The  $\text{CaCO}_3$  particles were reacted with acetic acid making the pits deeper and the surface rougher leading to the improvement of wettability. Consider



The XPS spectra of the coatings are illustrated in Figure 3. After etching, the peaks of Ca 2s and Ca 2p almost disappear proving the reaction of  $\text{CaCO}_3$  with acetic acid. The increase of peaks of Si 2s, Si 2p, O 1s, and F 1s may be caused by increase of content of resins and nanosilica as the etching of  $\text{CaCO}_3$ . From Figure 4, the presence of  $-\text{CF}_2$  on the surface from the fluorosilicone resin can be confirmed indicating the low surface energy of the coating.

The wettability of the samples is given in Figure 5. The coatings showed excellent superhydrophobicity and achieved

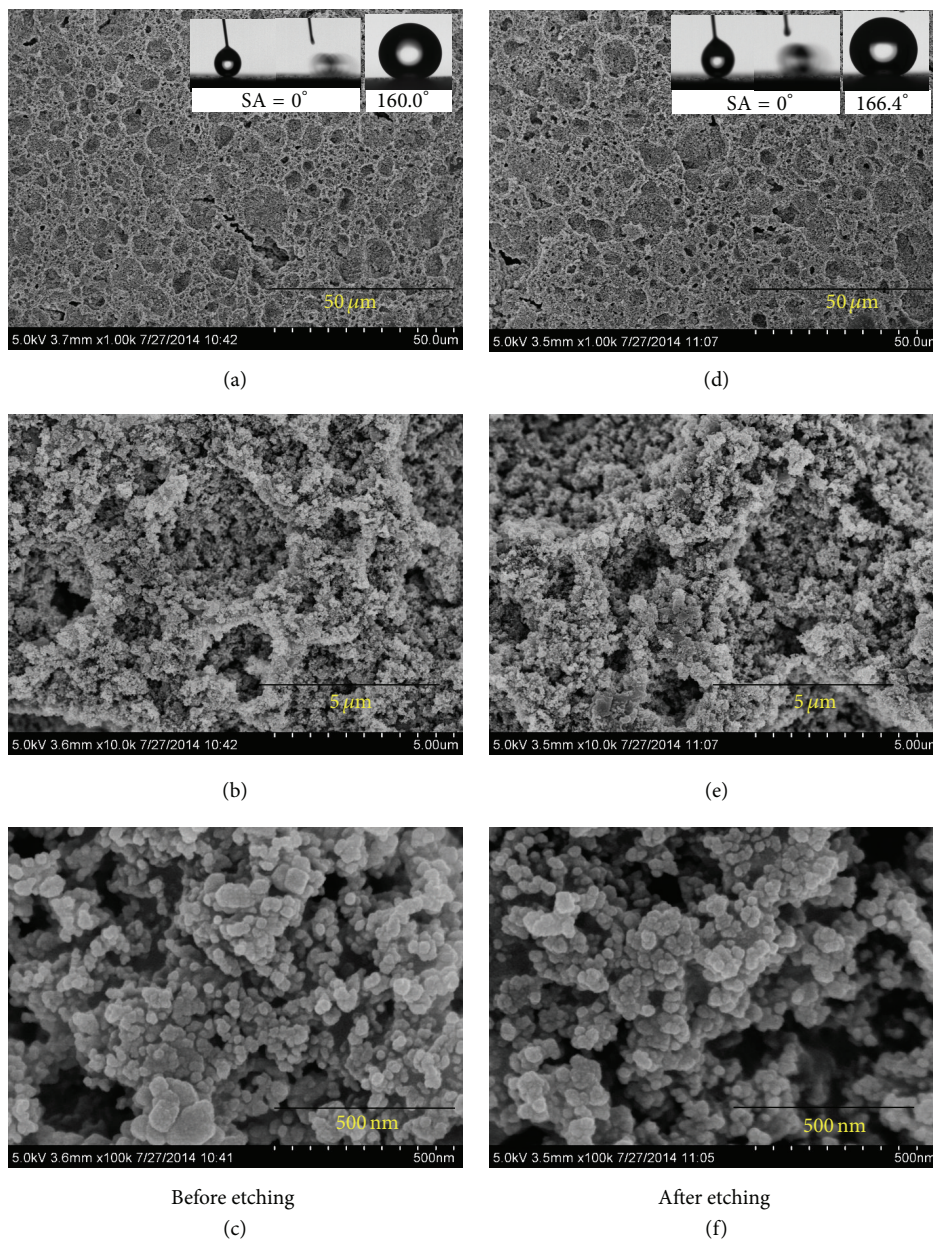


FIGURE 1: SEM images of coatings before (a)–(c) and after etching (d)–(f) with particle content of 33%. The insets show the optical images of sliding angle and contact angle testing.

improvement after etching. The contact angle increases from  $159^\circ$  up to  $165^\circ$  with the increase of nanoparticles content before etching. However, coatings with smaller percentage of nanoparticles get bigger contact angles after etching. All the samples show sliding angle (SA) of less than  $1^\circ$  illustrated by the insets of Figure 1 in which the water drops slide off the horizontal surface in few seconds. The contact angle hystereses of coatings decrease after etching and the lowest contact angle hysteresis is achieved by coatings with particle content of 33%. As the dynamic wettability is more important in anti-icing and etched surface shows better superhydrophobicity, etched coatings with particle content of 33% are chosen for glaze icing test and characterization.

The superhydrophobic property of the coating is due to the special rough structure and chemical composition of the surface [19]. The high contact angle is caused by the surface tension of water and air retained at the interface between water and the micro-/nanohierarchical structure. The low contact angle hysteresis and low sliding angle benefit from the rough structure and low surface energy. The friction of the water drop with the surface affects the sliding angle and contact angle hysteresis when the water drop starts to slide and is sliding, respectively. For the superhydrophobic surface in this paper, the friction of the water drop with the surface is small because the contact area and the adhesive force between them are small.

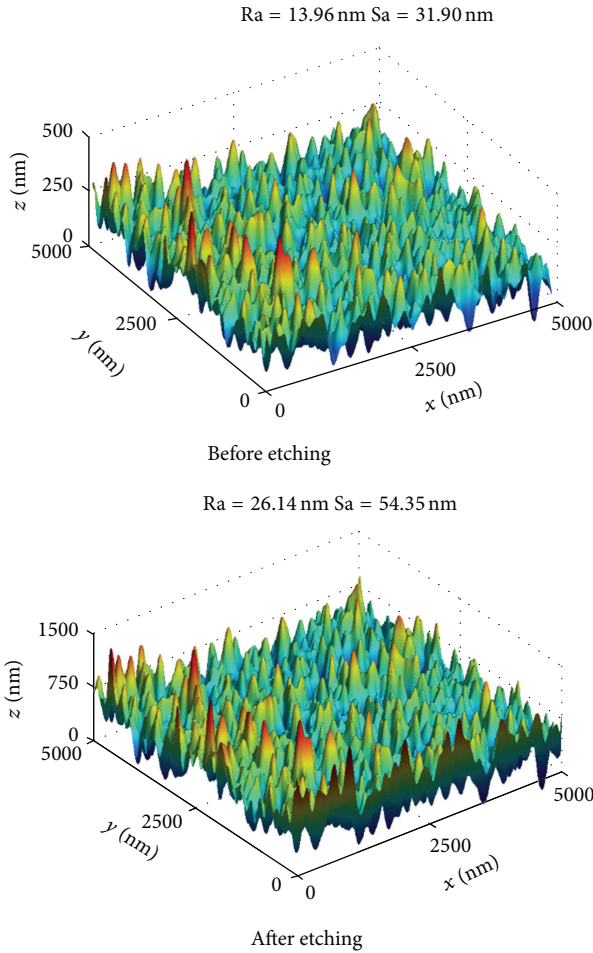


FIGURE 2: AFM images of coatings before and after etching with particle content of 33%.

The schematic diagram and results of glaze icing test are shown in Figure 6. After 60 min of glaze icing, only 20% of the coated sample was covered with separated ice caused by the hydrophilic edge of the glass slide. On the contrary, the uncoated glass slide was covered fully by thick and transparent ice. This anti-icing property can be interpreted by the excellent superhydrophobicity of the coating. The hierarchical rough structure is beneficial to the repelling of freezing rain on the surface. As the diameter of freezing rain falls in certain range, smaller drops can be repelled by nanometer pillars and collide with each other to become bigger drops which can be repelled by micrometer-scale pits [20]. Fortunately, bigger water drops are difficult to lose their internal energy and become ice because they have relative less contact area with the surface and the cold air. High contact angle of  $166.4^\circ$  indicates small contact area of the water drop with the surface. Meanwhile, low slide angle of less than  $1^\circ$  and contact angle hysteresis of  $0.9^\circ$  leads to the fast sliding of water drops on the surface which reduces the contact time of water drops with the surface. Therefore, reduced contact area and contact time of the water drops with the surface decrease the probability of heterogeneous nucleation of water and the

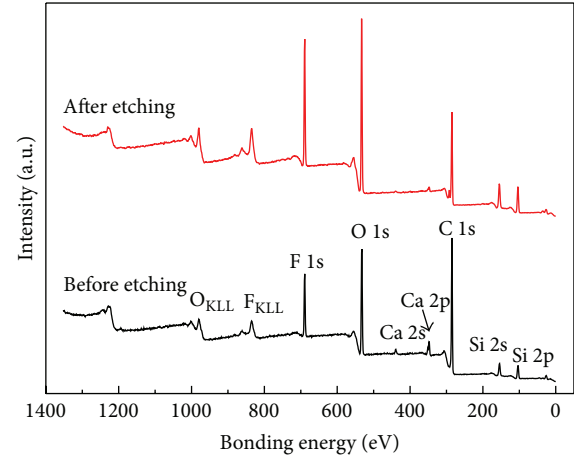


FIGURE 3: XPS images of coatings before and after etching with particle content of 33%.

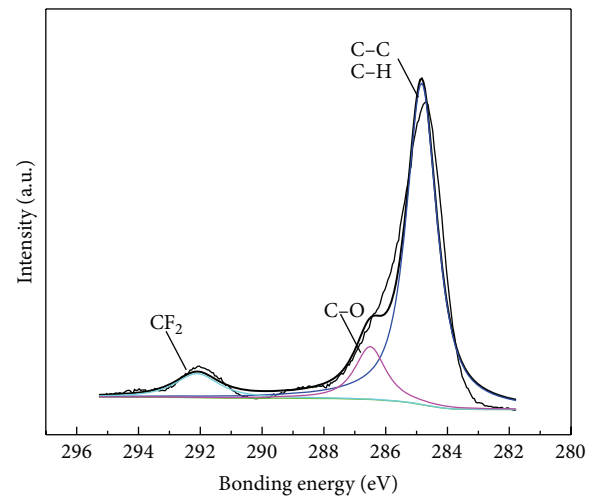


FIGURE 4: High resolution XPS of C 1s of coatings after etching with particle content of 33%.

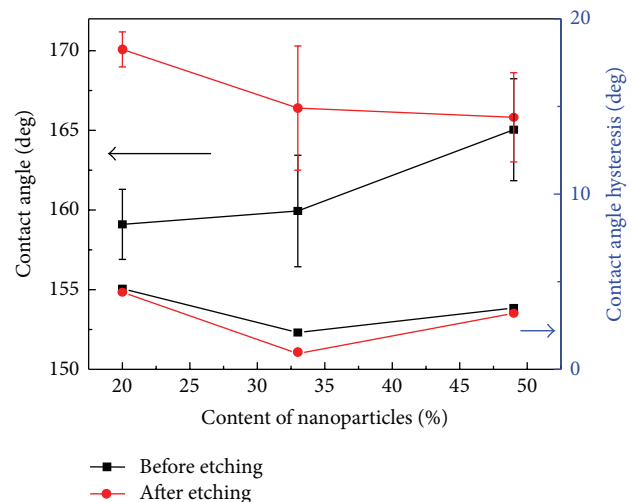


FIGURE 5: Wettability of samples before and after etching varying with the content of nanoparticles.

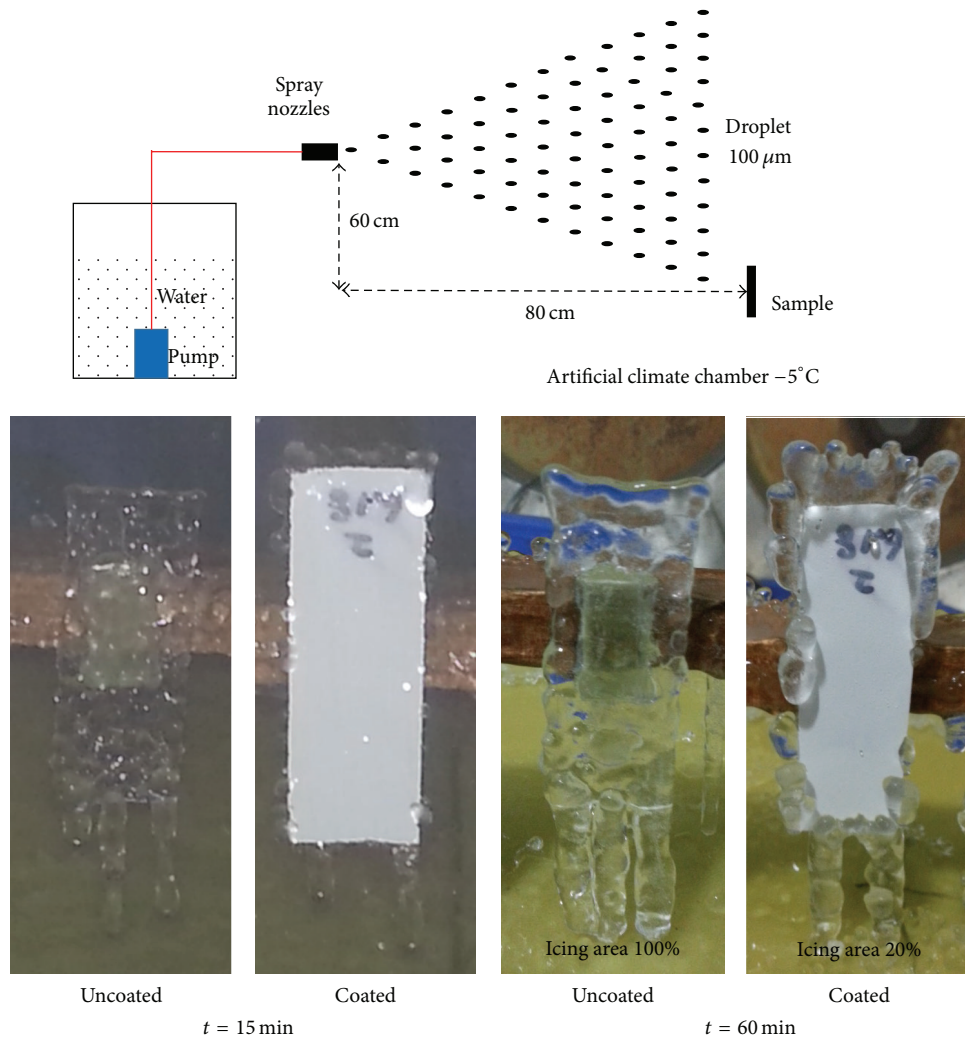


FIGURE 6: The schematic diagram of glaze icing test and glaze icing results of coated and uncoated glass slides at  $t = 15$  min and 60 min (particle content = 33%).

rate of heat transmission between the two phases of solid and liquid.

Similar results were received in the glaze icing test as shown in Figure 7. At the beginning of the test ( $t = 5$  min), the coated insulator had few separated water drops and ice particles as the water drops could bounce and slide off the insulator surface. At the end of the glaze icing test, only partial surface of the coated insulator was covered with separated ice particles and some unfrozen water drops. On the contrary, the uncoated and hydrophilic insulator was covered with thick ice which reduced the surface resistance and may lead to insulator flashover and power blackout in the power transmission system [21]. The anti-icing performance of the insulator is worse than the vertically placed glass slide as the tilting angle of the insulator surface is only about  $15^\circ$  and the diameter is 255 mm which is rather larger than the size of the glass slides (25 mm \* 75 mm). The contact time of the water drops with the coating is increased as the tilting

angle is smaller and the distance is longer which leads to the increase of probability of heterogeneous nucleation and rate of heat transmission. In general, the superhydrophobic coating shows great potential in anti-icing of insulators in power transmission system.

#### 4. Conclusions

Superhydrophobic coatings with contact angle of  $166.4^\circ$ , contact angle hysteresis of  $0.9^\circ$ , and sliding angle of less than  $1^\circ$  are fabricated by nanoparticle filling combined with etching method when the particle content is 33%. This coating on glass slide showed excellent anti-icing property with only 20% of surface area covered by glaze ice. Similarly, few parts of the coated insulator were covered with separated ice and unfrozen water drops. On the contrary, the uncoated glass slides and insulators were fully covered with thick ice. The excellent superhydrophobicity and anti-icing property



FIGURE 7: The glaze icing results of coated and uncoated glass insulators at  $t = 5$  min and 60 min (particle content = 33%).

are due to the hierarchical rough structure and low surface energy proved by the SEM, AFM, and XPS characterization.

### Conflict of Interests

The authors declare that there is no conflict of interests regarding the publication of this paper.

### Acknowledgments

This work is financially supported by the General Program of Natural Science Foundation of China (51377177) and Natural Science Foundation Project of CQ CSTC (cstcjjA50007).

### References

- [1] X. Wang, J. Hu, B. Wu, L. Du, and C. Sun, "Study on edge extraction methods for image-based icing on-line monitoring on overhead transmission lines," in *Proceedings of the International Conference on High Voltage Engineering and Application (ICHVE '08)*, pp. 661–665, Chongqing, China, November 2008.
- [2] M. Huneault, C. Langheit, R. St-Arnaud, J. Benny, J. Audet, and J.-C. Richard, "A dynamic programming methodology to develop de-icing strategies during ice storms by channeling load currents in transmission networks," *IEEE Transactions on Power Delivery*, vol. 20, no. 2, pp. 1604–1610, 2005.
- [3] J. Zhao, R. Guo, L. Cao, and F. Zhang, "Improvement of lineROver: a mobile robot for de-icing of transmission lines," in *Proceedings of the 1st International Conference on Applied Robotics for the Power Industry (CARPI '10)*, pp. 1–4, Montreal, Canada, October 2010.
- [4] M. Yasui, K. Maekawa, Y. Naganuma et al., "Removal of icy snow accumulation on the transmission line by applying LC-spiral rod," *Fujikura Technical Review*, vol. 16, pp. 26–33, 1987.
- [5] M. Farzaneh, C. Volat, and A. Leblond, *Anti-Icing and De-Icing Techniques for Overhead Lines*, Springer, New York, NY, USA, 2008.
- [6] W. Liao, Z. Jia, Z. Guan et al., "Reducing ice accumulation on insulators by applying semiconducting RTV silicone coating," *IEEE Transactions on Dielectrics and Electrical Insulation*, vol. 14, no. 6, pp. 1446–1454, 2007.
- [7] C. Antonini, M. Innocenti, T. Horn, M. Marengo, and A. Amirfazli, "Understanding the effect of superhydrophobic coatings on energy reduction in anti-icing systems," *Cold Regions Science and Technology*, vol. 67, no. 1-2, pp. 58–67, 2011.
- [8] L. Mishchenko, B. Hatton, V. Bahadur, J. A. Taylor, T. Krupenkin, and J. Aizenberg, "Design of ice-free nanostructured surfaces based on repulsion of impacting water droplets," *ACS Nano*, vol. 4, no. 12, pp. 7699–7707, 2010.
- [9] L. Ge, G. Ding, H. Wang, J. Yao, P. Cheng, and Y. Wang, "Anti-icing property of superhydrophobic octadecyltrichlorosilane film and its ice adhesion strength," *Journal of Nanomaterials*, vol. 2013, Article ID 278936, 3 pages, 2013.
- [10] J. B. Boreyko and C. P. Collier, "Delayed frost growth on jumping-drop superhydrophobic surfaces," *ACS Nano*, vol. 7, no. 2, pp. 1618–1627, 2013.
- [11] J. Yang and W. Li, "Preparation of superhydrophobic surfaces on Al substrates and the anti-icing behavior," *Journal of Alloys and Compounds*, vol. 576, pp. 215–219, 2013.
- [12] K. Tadanaga, J. Morinaga, A. Matsuda, and T. Minami, "Superhydrophobic-superhydrophilic micro patterning on flowerlike alumina coating film by the sol-gel method," *Chemistry of Materials*, vol. 12, no. 3, pp. 590–592, 2000.

- [13] C. Becker, J. Petersen, G. Mertz, D. Ruch, and A. Dinia, "High superhydrophobicity achieved on poly(ethylene terephthalate) by innovative laser-assisted magnetron sputtering," *The Journal of Physical Chemistry C*, vol. 115, no. 21, pp. 10675–10681, 2011.
- [14] Y. Wu, M. Kouno, N. Saito, F. Andrei Nae, Y. Inoue, and O. Takai, "Patterned hydrophobic-hydrophilic templates made from microwave-plasma enhanced chemical vapor deposited thin films," *Thin Solid Films*, vol. 515, no. 9, pp. 4203–4208, 2007.
- [15] J. Y. Shiu, C. W. Kuo, P. Chen, and C. Y. Mou, "Fabrication of tunable superhydrophobic surfaces by nanosphere lithography," *Chemistry of Materials*, vol. 16, no. 4, pp. 561–564, 2004.
- [16] A. Nakajima, K. Abe, K. Hashimoto, and T. Watanabe, "Preparation of hard super-hydrophobic films with visible light transmission," *Thin Solid Films*, vol. 376, no. 1-2, pp. 140–143, 2000.
- [17] H. Zhang, X. Zeng, Y. Gao, F. Shi, P. Zhang, and J.-F. Chen, "A facile method to prepare superhydrophobic coatings by calcium carbonate," *Industrial and Engineering Chemistry Research*, vol. 50, no. 6, pp. 3089–3094, 2011.
- [18] R. Karmouch and G. G. Ross, "Superhydrophobic wind turbine blade surfaces obtained by a simple deposition of silica nanoparticles embedded in epoxy," *Applied Surface Science*, vol. 257, no. 3, pp. 665–669, 2010.
- [19] R. Blossey, "Self-cleaning surfaces—Virtual realities," *Nature Materials*, vol. 2, no. 5, pp. 301–306, 2003.
- [20] J. B. Boreyko and C.-H. Chen, "Self-propelled jumping drops on superhydrophobic surfaces," *Physics of Fluids*, vol. 22, no. 9, Article ID 091110, 2010.
- [21] M. Farzaneh and J. Kiernicki, "Flashover problems caused by ice build-up on insulators," *IEEE Electrical Insulation Magazine*, vol. 11, no. 2, pp. 5–17, 1995.

## Research Article

# Study of Magnetization Reversal Process in FeCo/Ru/FeCo Exchange Coupled Synthetic Antiferromagnetic Multilayers

Xi Liu,<sup>1</sup> Shunji Ishio,<sup>2</sup> and Hailin Ma<sup>1</sup>

<sup>1</sup>Key Laboratory of Ministry of Education on Opto-Electronic Technology and Intelligent Control, Lanzhou Jiaotong University, Lanzhou, Gansu 730070, China

<sup>2</sup>Department of Materials Science and Engineering, Akita University, Tegata Gakuen-machi, Akita 010-8502, Japan

Correspondence should be addressed to Xi Liu; liuxi@mail.lzjtu.cn

Received 13 September 2014; Revised 24 November 2014; Accepted 8 December 2014

Academic Editor: Jiamin Wu

Copyright © 2015 Xi Liu et al. This is an open access article distributed under the Creative Commons Attribution License, which permits unrestricted use, distribution, and reproduction in any medium, provided the original work is properly cited.

FeCo/Ru/FeCo exchange coupled synthetic antiferromagnetic multilayers were prepared with two sputtering modes. One is continuous sputtering mode, and the other mode is layer-by-layer sputtering mode. The former mode implies that substrate faced the target and film growth process was continuous when FeCo layers were sputtering, whereas the latter implies that substrate was rotating with the mask at a speed of 5 rpm when FeCo layers were sputtering. It was found that the exchange coupling field  $H_{ex}$  of sample sputtered by layer-by-layer mode was higher than the one sputtered by continuous mode. Domain structures were measured with applying varied in-plane magnetic fields along the easy axis in order to study the magnetization reversal process. We found it is a domain wall move process. When the applied field is smaller than  $H_{ex}$ , both the two magnetic layers have domain structure and the domain structure of the two layers is reversed correspondingly. When the applied field is varying in the range of  $-H_{ex}$  to  $H_{ex}$ , the domain wall of the two layers moves correspondingly at the same time.

## 1. Introduction

Synthetic antiferromagnetic (SAF) multilayer [1] is comprised of two ferromagnetic layers separated by a nonmagnetic metallic spacer layer in which the ferromagnetic layers are coupled through antiferromagnetic interlayer exchange. Such interlayer coupling is subject to the thickness of the nonmagnetic layer [2] and is highly sensitive to structural defects [3]. In an ideal situation with proper thickness of nonmagnetic layer and low structural defects, no remanence can be observed in easy axis and the total magnetization becomes zero when the applied magnetic field is smaller than exchange coupling field  $H_{ex}$ . In recent years, there have been many studies on SAF multilayers, as it shows great promise as soft underlayers for perpendicular recording media [4, 5], high moment write head material [6], and high frequency application [7]. But the reversal process in FeCo/Ru/FeCo SAF multilayers has not been studied yet. It is not known if the reversal process is a domain wall move process or moment coherent rotation process.

In this present study, FeCo/Ru/FeCo SAF layers were prepared under two different FeCo sputtering modes which significantly changed the surface intermixing, so different exchange coupling fields  $H_{ex}$  were measured. MFM measurements with different applying in-plane magnetic fields in the easy axis were done to study the reversal process in FeCo/Ru/FeCo multilayers.

## 2. Experiment

SAF multilayers Ru/FeCo(10 nm)/Ru( $d_{Ru}$  nm)/FeCo(10 nm)/Ru were prepared on SiO<sub>2</sub> substrate by using DC magnetron sputtering with a Fe<sub>70</sub>Co<sub>30</sub> target and a Ru target. The base pressure was lower than  $3 \times 10^{-5}$  Pa. A magnetic field around 100 Oe was applied along the substrate surface during deposition for inducing in-plane magnetic anisotropy in the films. Ru layers are deposited with power of 15 W, Ar-gas pressure of 0.5 Pa, and substrate rotating speed of 5 rpm. The thickness of Ru interlayer  $d_{Ru}$  varied from 0.60 nm to 1.20 nm. All samples used a Ru seed layer (2 nm) and a Ru

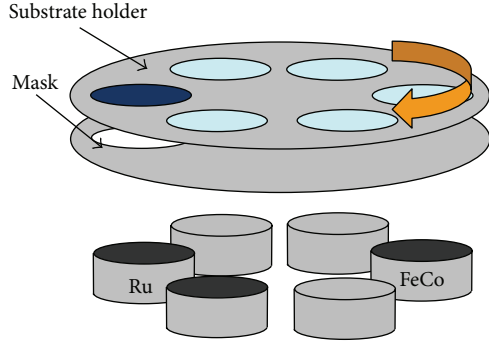


FIGURE 1: Schematic diagram of sputter system.

TABLE 1: Deposition conditions of two series samples.

	Power	Ar pressure	Rotating speed	Sputtering rate
Series A	10.0 W	0.2 Pa	No rotation	0.10 nm/sec
Series B	17.8 W	0.2 Pa	5 rpm	0.25 nm/rot

capping layer (3 nm). The multilayers were prepared in a multilayer sputtering system and the schematic diagram is shown in Figure 1. We prepared two series samples, and the conditions are given in Table 1. FeCo layer of series A was prepared with a continuous sputtering mode: substrates were not rotating and facing FeCo target through the hole in the mask during deposition. FeCo layer of series B was prepared with a layer-by-layer sputtering mode: substrates and the mask were rotating at the same speed.

Magnetic properties were measured by a vibrating sample magnetometer (VSM). The domain structure was measured by a magnetic force microscopy (MFM) applying different in-plane magnetic fields along easy-axis. A FePt tip was adopted and measurement conditions were vibrating the amplitude of the tip of 15 nm for morphology measurement and 3 nm for phase measurement with scan height of about 10 nm and constant  $Q$  factor of about 6000. Before being measured, FePt tip was magnetized by VSM along the pinpoint direction.

### 3. Results and Discussions

Upon investigation of the relationship between the exchange coupling field  $H_{ex}$  and the thickness of Ru interlayer  $d_{Ru}$  in SAF films, it was found that the  $H_{ex}$  of SAF coupled structures is related to  $d_{Ru}$ . As shown in Figure 2, with the increase of  $d_{Ru}$ , the  $H_{ex}$  of series B samples increases and reaches a maximum value when  $d_{Ru} = 0.90$  nm, and when  $d_{Ru}$  increases further ( $d_{Ru} > 0.90$  nm),  $H_{ex}$  decreases drastically. We also found that the  $H_{ex}$  of series A samples had the same results: the  $H_{ex}$  value got maximum when  $d_{Ru} = 0.90$  nm but the value of series B samples was much larger than series A samples. Figures 3(a) and 3(b) show the  $M$ - $H$  of two series samples with  $d_{Ru} = 0.90$  nm. It was shown that the exchange coupling field  $H_{ex}$  of series B sample is higher than series A sample: about 185 Oe for series B sample and about 80 Oe for series A sample. Figures 3(c) and 3(d) show two series samples without Ru spacer layer. It was shown that

the induced anisotropy field  $H_k$  of series B sample is higher than series A sample. This result agrees with the SAF layers' result, because the effective anisotropy field  $H_k$  relates to the exchange coupling field  $H_{ex}$  in SAF sandwich films [7]. It is well known that the interlayer coupling of samples grown by MBE is larger than that grown by sputtering, because of the larger surface intermixing in the sputtered samples due to the substrate bombardment by neutral atoms. This gives rise to random component in the atom distribution near the interface and to a destructive interference of the scattered electronic waves, so the coupling is frustrated [8, 9]. We think the growth process of series B samples is similar to MBE process, and it can effectively decrease the bombardment by neutral atoms compared with the growth process of series A samples. So we can conclude that the layer-by-layer growth mode can decrease the surface intermixing and get laser induced anisotropy field  $H_k$  and exchange coupling field  $H_{ex}$ .

In order to study the reversal process of SAF multilayers, we measured MFM images applying varied in-plane magnetic field along easy-axis. From the MFM measurement we found the surface of the two series samples is very flat and the average roughness is less than 0.1 nm. Figure 4 shows the MFM images of series B sample with  $d_{Ru} = 0.90$  nm measured with different in-plane magnetic field. The magnetic field applied along the easy-axis direction and ranged from 1500 Oe to  $-1500$  Oe. Because of the multilayer structure, we can just measure domain structure of upper FeCo layer. But we can deduce the bottom layer's domain structure according to magnetic properties of exchange coupled SAF multilayers. Figure 4(a) shows MFM images measured when the as-deposited sample had not been applied magnetic field, we can see clear domain structure. Figure 4(b) shows MFM images measured with 1500 Oe in-plane magnetic field, and we cannot see very clear domain wall structure, which means magnetization is saturated and almost all magnetic moments array along the applied field. From Figure 4(c) it can be seen when applied magnetic field decreases to 1000 Oe, many small reverse domains appear. Figure 4(f) is measured when the applied in-plane magnetic field decreases from 1500 Oe to 200 Oe. From Figures 4(c)–4(f), it can be seen those small reversed magnetic domains grow bigger and the domain wall moves with change of the applied in-plane magnetic field. Figures 4(g)–4(l) were measured with the applied in-plane magnetic field range from 150 Oe to  $-200$  Oe. From  $M$ - $H$  loop we can get the total magnetization of film are zero when the applied magnetic field are smaller than the exchange coupling field  $H_{ex}$ . But we can see clearly domain wall structure, so we can deduce that the bottom FeCo layer has the same domain structure as the upper layer, but the magnetization direction is reverse correspondingly. From marked parts in Figures 4(g)–4(l) we can see the domain wall moves process, so we can deduce that the domain wall of the two layers moves correspondingly at the same time. Figures 4(m)–4(p) show the MFM images measured when the applied magnetic field ranges from  $-300$  Oe to  $-1500$  Oe, we can see the positive domain becomes smaller and disappears. So, we can conclude that the reversal process in SAF multilayers is a domain wall move process, and the domain wall in both upper layer and bottom layer moves

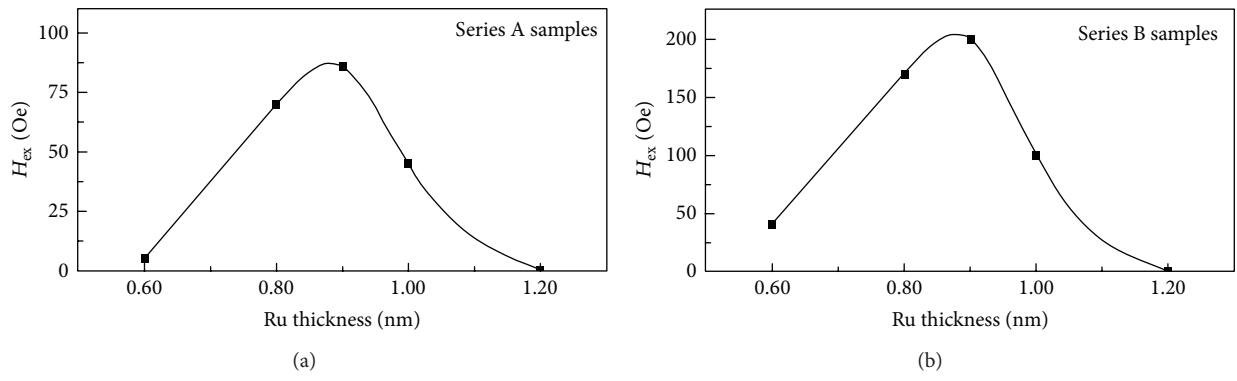


FIGURE 2: Dependence of  $H_{ex}$  of series A and B samples on  $d_{Ru}$ .

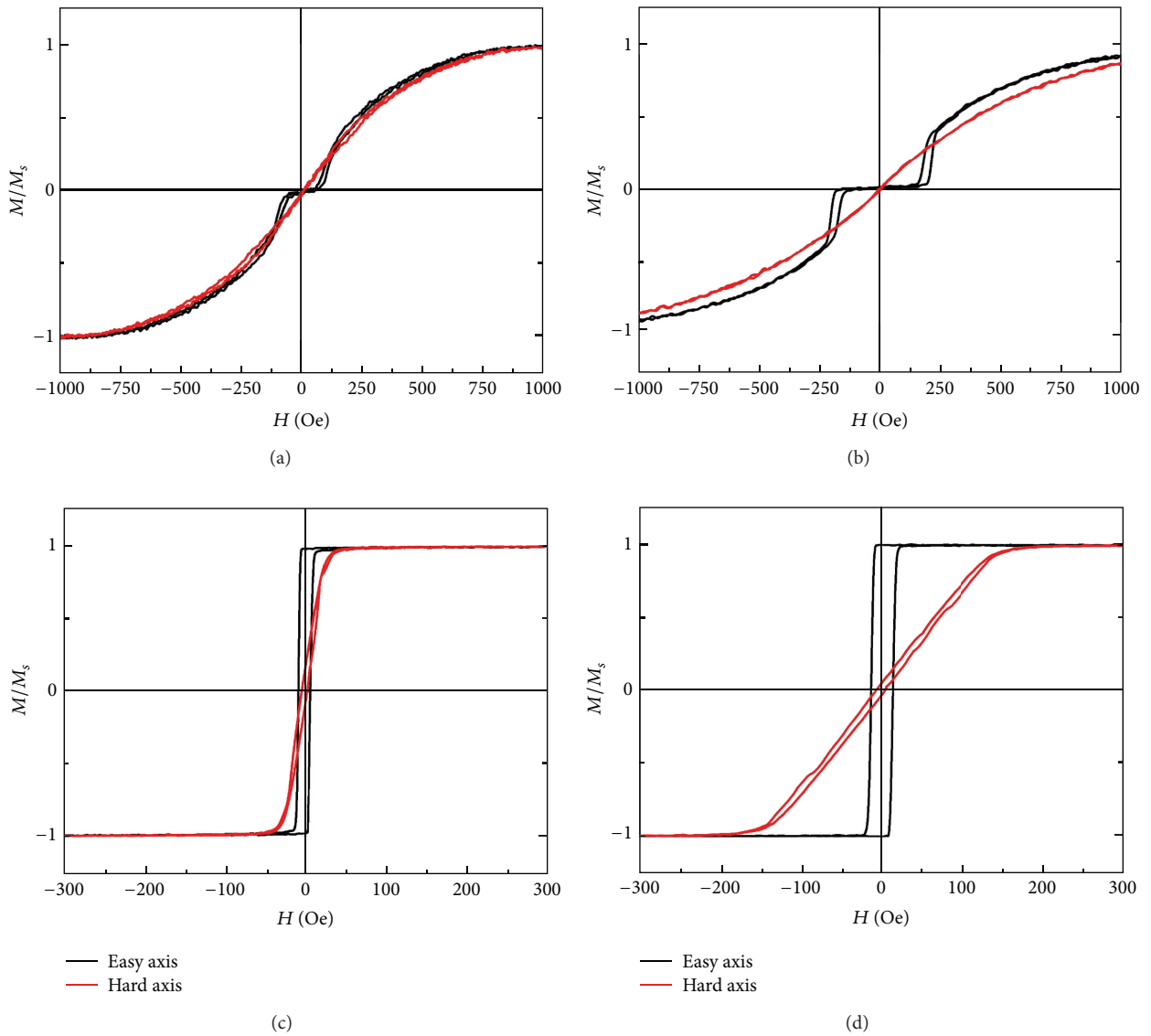


FIGURE 3:  $M-H$  loop of (a) series A sample with  $d_{Ru} = 0.90$  nm, (b) series B sample with  $d_{Ru} = 0.90$  nm, (c) series A sample without Ru spacer layer, (d) series B sample without Ru spacer layer.

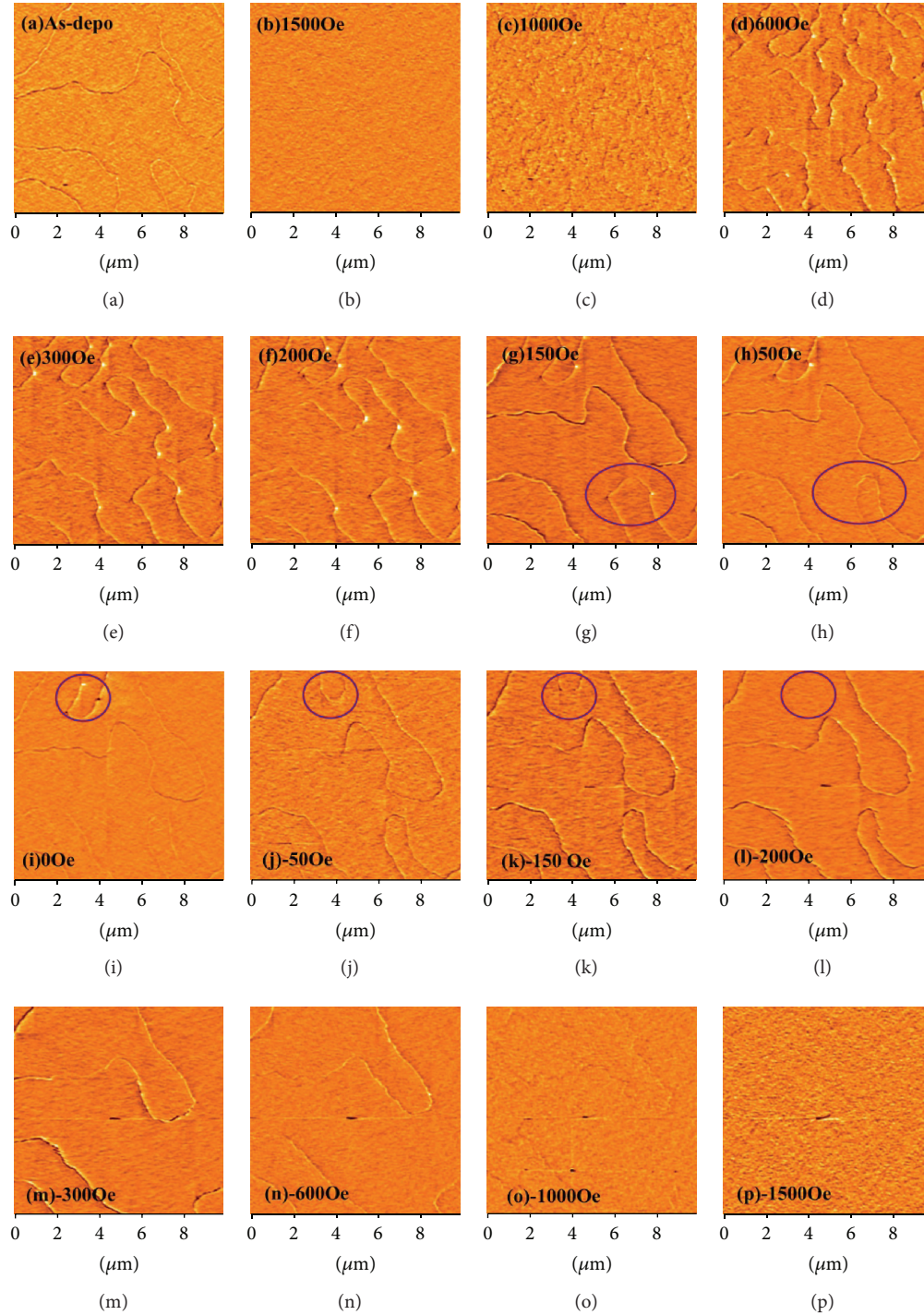


FIGURE 4: MFM images of FeCo(10 nm)/Ru(0.90 nm)/FeCo(10 nm) prepared with layer-by-layer mode measured with in-plane magnetic field range from 1500 Oe to  $-1500$  Oe.

with the varying in-plane magnetic fields; when the in-plane magnetic field is smaller than exchange coupling field  $H_{ex}$ , the domain structure in the two layers is the same but the magnetization direction is reverse correspondingly, and the domain wall in the two layers moves correspondingly at the same time.

#### 4. Conclusion

Synthetic antiferromagnetic multilayers Ru/FeCo(10 nm)/Ru( $d_{Ru}$  nm)/FeCo(10 nm)/Ru were prepared with two FeCo sputtering mode: continuous mode and layer-by-layer mode. The exchange coupling field  $H_{ex}$  of SAF film deposited by

layer-by-layer mode is higher than samples deposited by continuous mode because of decrease of surface intermixing due to the substrate bombardment by neutral atoms. The magnetization reversal process is a domain wall move process. When the applied field was smaller than  $H_{ex}$ , both the two magnetic layers have same domain structure and the domain structure of the two layers was reverse correspondingly. It is also found that the domain wall of the two magnetic layers move correspondingly at the same time when the applied field is smaller than  $H_{ex}$  and changing.

## Conflict of Interests

The authors declare that there is no conflict of interests regarding the publication of this paper.

## Acknowledgment

This study was supported by the Science Foundation for Young Scholars of Lanzhou Jiaotong University (Grant no. 2013036).

## References

- [1] P. Grünberg, R. Schreiber, Y. Pang, U. Walz, M. B. Brodsky, and H. Sowers, "Layered magnetic structures: evidence for antiferromagnetic coupling of Fe layers across Cr interlayers," *Physical Review Letters*, vol. 57, no. 19, pp. 2442–2445, 1986.
- [2] S. S. P. Parkin, N. More, and K. P. Roche, "Oscillations in exchange coupling and magnetoresistance in metallic superlattice structures: Co/Ru, Co/Cr, and Fe/Cr," *Physical Review Letters*, vol. 64, no. 19, pp. 2304–2307, 1990.
- [3] C. H. Marrows, B. J. Hickey, M. Herrmann et al., "Damage caused to interlayer coupling of magnetic multilayers by residual gases," *Physical Review B—Condensed Matter and Materials Physics*, vol. 61, article 4131, 2000.
- [4] Y. Kawato, M. Futamo, and K. Nakamoto, "Perpendicular magnetic recording medium and magnetic storage apparatus," U.S. Patent no. 20020028356 A1, (2002).
- [5] S. C. Byeon, A. Misra, and W. D. Doyle, "Synthetic antiferromagnetic soft underlayers for perpendicular recording media," *IEEE Transactions on Magnetics*, vol. 40, no. 4, pp. 2386–2388, 2004.
- [6] Y. Chen, K. Sin, H. Jiang et al., "High moment materials and fabrication processes for shielded perpendicular write head beyond 200 Gb/in<sup>2</sup>," *IEEE Transactions on Magnetics*, vol. 43, no. 2, pp. 609–614, 2007.
- [7] L. Zhang, W. Zhang, X. Liu et al., "High frequency characteristics of synthetic antiferromagnetic coupling FeCoN sandwich films," *IEEE Transactions on Magnetics*, vol. 47, no. 10, pp. 3932–3934, 2011.
- [8] P. Bruno and C. Chappert, "Ruderman-Kittel theory of oscillatory interlayer exchange coupling," *Physical Review B*, vol. 46, no. 1, pp. 261–270, 1992.
- [9] Y. Wang, P. M. Levy, and J. L. Fry, "Interlayer magnetic coupling in Fe/Cr multilayered structures," *Physical Review Letters*, vol. 65, no. 21, pp. 2732–2735, 1990.

## Research Article

# The Photoluminescence Behaviors of a Novel Reddish Orange Emitting Phosphor $\text{CaIn}_2\text{O}_4:\text{Sm}^{3+}$ Codoped with $\text{Zn}^{2+}$ or $\text{Al}^{3+}$ Ions

Jing Gou,<sup>1</sup> Dongyang Zhang,<sup>1</sup> Binxun Yu,<sup>2</sup> Jing Wang,<sup>1</sup> and Shengzhong Liu<sup>1</sup>

<sup>1</sup>School of Materials Science and Engineering, Shaanxi Normal University, Key Laboratory of Applied Surface and Colloid Chemistry of Ministry of Education, Xi'an 710119, China

<sup>2</sup>School of Chemistry and Chemical Engineering, Shaanxi Normal University, Xi'an 710119, China

Correspondence should be addressed to Jing Gou; [goujing@snnu.edu.cn](mailto:goujing@snnu.edu.cn)

Received 1 December 2014; Revised 26 December 2014; Accepted 29 December 2014

Academic Editor: Yuanlie Yu

Copyright © 2015 Jing Gou et al. This is an open access article distributed under the Creative Commons Attribution License, which permits unrestricted use, distribution, and reproduction in any medium, provided the original work is properly cited.

A novel reddish orange phosphor  $\text{CaIn}_2\text{O}_4:\text{Sm}^{3+}$  codoped with  $\text{Zn}^{2+}$  or  $\text{Al}^{3+}$  ions was prepared by solid state reaction and their luminescence properties were investigated under near ultraviolet excitation. The strategy of  $\text{Zn}^{2+}$  or  $\text{Al}^{3+}$  ions codoping was used with the aim to improve the luminescence properties of  $\text{CaIn}_2\text{O}_4:\text{Sm}^{3+}$ , but the concrete effects of the two ions is different. The introduction of  $\text{Zn}^{2+}$  ions can produce  $\text{Zn}_{\text{In}}$  defects that favor charge balance in  $\text{CaIn}_2\text{O}_4:\text{Sm}^{3+}$  to facilitate its photoluminescence. The effect of  $\text{Al}^{3+}$  ions codoping can effectively transfer energy from charge-transfer absorption band to characteristic transition of  $\text{Sm}^{3+}$  ions, utilizing more energy from host absorption for the photoluminescence of  $\text{Sm}^{3+}$  ions. Based on these mechanisms, the luminescence intensity of  $\text{CaIn}_2\text{O}_4:0.6\%\text{Sm}^{3+}$  was enhanced to 1.59 times and 1.51 times when codoping amount of  $\text{Zn}^{2+}$  and  $\text{Al}^{3+}$  ions reached 0.6%. However, the chromaticity coordinates of  $\text{CaIn}_2\text{O}_4:0.6\%\text{Sm}^{3+}$  almost did not have any changes after  $\text{Zn}^{2+}$  ions or  $\text{Al}^{3+}$  ions codoping; those are still located at reddish orange region. The excellent luminescence properties of  $\text{CaIn}_2\text{O}_4:0.6\%\text{Sm}^{3+}, 0.6\%\text{Zn}^{2+}$  and  $\text{CaIn}_2\text{O}_4:0.6\%\text{Sm}^{3+}, 0.6\%\text{Al}^{3+}$  demonstrate that they both have potential application value as new-style reddish orange phosphors on light-emitting diode.

## 1. Introduction

White light-emitting diodes (WLEDs), with the advantages of long lifetime, less energy consumption, and environment friendly characteristics, are thought to be the most important solid state light sources for substituting the widely used incandescent lamps and fluorescent lamps [1–5]. But it still needs to overstep many technological obstructions. It is well known that WLEDs can be realized by combing a single near ultraviolet (NUV, 370–410 nm) light-emitting diodes (LEDs) chip with tricolor phosphors or combining a simple blue LEDs chip with yellow phosphor [6]. With the development of semiconductor technology, NUV-LEDs chips can offer a higher efficient solid state light. Thus the corresponding phosphors which can be efficiently excited by NUV urgently needed to be explored, but the red phosphor excited by

NUV light is rare at present. In last decade, many scientists have been devoted to the red phosphors doped by  $\text{Eu}^{3+}$  and  $\text{Eu}^{2+}$  [7–9]. However, commercial red phosphors (e.g.,  $\text{Y}_2\text{O}_2\text{S}:\text{Eu}^{3+}$ ,  $\text{CaS}:\text{Eu}^{2+}$ , and  $\text{SrS}:\text{Eu}^{2+}$ ) do not have enough absorption in the NUV region and the lifetime of the LEDs is limited because of the degradation of these sulfide phosphors during LEDs operation [8].

$\text{Sm}^{3+}$  ion is widely used as activator of reddish orange emission due to its  $^4\text{G}_{5/2}-^6\text{H}_J$  ( $J = 5/2, 7/2, 9/2, 11/2$ ) transitions, which is the most suitable source for lighting and display from a practical viewpoint [10–12].  $\text{CaIn}_2\text{O}_4$  is a semiconductor with band gap ( $E_g$ ) as 3.9 eV, belonging to ordered  $\text{CaFe}_2\text{O}_4$  structures with the  $Pca21$  or  $Pbcm$  space group, and the lattice parameters  $a = 9.70 \text{ \AA}$ ,  $b = 11.30 \text{ \AA}$ , and  $c = 3.21 \text{ \AA}$  for  $Z = 4$  ( $Z$  is the number of formula units per unit cell)

[5, 13].  $\text{InO}_6$  octahedra connect to each other by sharing edges and corners to form a tunnel network structure and  $\text{Ca}^{2+}$  ions locate in the tunnels. The ionic radius of six-coordinated  $\text{Sm}^{3+}$  (0.958 Å) is similar to that of  $\text{Ca}^{2+}$  (1.14 Å) but larger than that of  $\text{In}^{3+}$  (0.94 Å), so  $\text{Sm}^{3+}$  ions more easily occupy  $\text{Ca}^{2+}$  sites in the tunnel of  $\text{InO}_6$  octahedra. So far the luminescence properties of  $\text{CaIn}_2\text{O}_4:\text{Tb}^{3+}$ ,  $\text{CaIn}_2\text{O}_4:\text{Pr}^{3+}$ ,  $\text{CaIn}_2\text{O}_4:\text{Dy}^{3+}$ , and  $\text{CaIn}_2\text{O}_4:\text{Eu}^{3+}$  under UV and VUV (vacuum ultraviolet) excitation have been investigated for the application on field emission displays (FEDs), cathode ray tube display (CRTs), and WLEDs [14–16]. To the best of our knowledge, there are few reports about the luminescence properties of  $\text{CaIn}_2\text{O}_4:\text{Sm}^{3+}$  for WLEDs application. Yan et al. reported the photoluminescence of  $\text{CaIn}_2\text{O}_4:\text{Eu}^{3+}, \text{Sm}^{3+}$ . The doped  $\text{Sm}^{3+}$  can sensitize the emission of  $\text{Eu}^{3+}$  and be effective to extend and strengthen the absorption of near-UV light with wavelength of 400–405 nm. The temperature quenching effect proved that  $\text{CaIn}_2\text{O}_4$  has good stability. And doping amount variation of  $\text{Sm}^{3+}$  can tune the CIE chromaticity coordinates of  $\text{CaIn}_2\text{O}_4:\text{Eu}^{3+}, \text{Sm}^{3+}$  better than conventional red phosphor  $\text{Y}_2\text{O}_2\text{S}:0.05\text{Eu}^{3+}$  under the excitation of NUV light [17]. Thus the research about the luminescence properties of  $\text{CaIn}_2\text{O}_4:\text{Sm}^{3+}$  under NUV excitation is very significant. So, in our paper, the luminescence properties of  $\text{CaIn}_2\text{O}_4:0.6\%\text{Sm}^{3+}$  codoped with  $\text{Zn}^{2+}$  or  $\text{Al}^{3+}$  ions were investigated in detail for basic research and potential application in WLEDs.

## 2. Experimental Details

The powder samples  $\text{CaIn}_2\text{O}_4:x\text{Sm}^{3+}$ ,  $\text{CaIn}_2\text{O}_4:0.6\%\text{Sm}^{3+}, y\text{Zn}^{2+}$ , and  $\text{CaIn}_2\text{O}_4:0.6\%\text{Sm}^{3+}, y\text{Al}^{3+}$  were prepared by solid state reactions [14–16]. The purity of  $\text{CaCO}_3$  and  $\text{In}_2\text{O}_3$  are A.R., while  $\text{Sm}_2\text{O}_3$ ,  $\text{ZnO}$  and  $\text{Al}_2\text{O}_3$  are better than 99.99%. Stoichiometric amounts of the starting reagents were thoroughly mixed and ground together. Then the mixture was heated at 1150°C for 12 h. Finally the samples were naturally cooled to room temperature in the furnace.

The normal crystal structure was characterized using  $\text{Cu K}\alpha$  radiation (DX-2700 powder X-ray diffractometer) over the angular range  $10^\circ \leq \theta \leq 80^\circ$ . The UV photoluminescence (PL) and photoluminescence excitation (PLE) spectra were recorded by F-7000 fluorescence spectrophotometer with Xe lamp as the light source. The quantum efficiencies were measured by FLS920 Fluorescence Spectrometer. All above spectra were recorded at room temperature.

## 3. Results and Discussion

$\text{CaIn}_2\text{O}_4:0.6\%\text{Sm}^{3+}$  was characterized by the powder X-ray diffractometer and corresponding powder X-ray diffraction (XRD) patterns are demonstrated in Figure 1 as a sample. It is obvious that most diffraction peaks can be indexed with the Joint Committee on Powder Diffraction Standards (JCPDS) card number 17-0643 indicating that it is almost single-phase structure. That also corresponds to XRDs reported in [13–16]. While there is a little different peak located at  $30.6^\circ$ , which is attributed to the diffraction peak of  $\text{In}_2\text{O}_3$ , the little

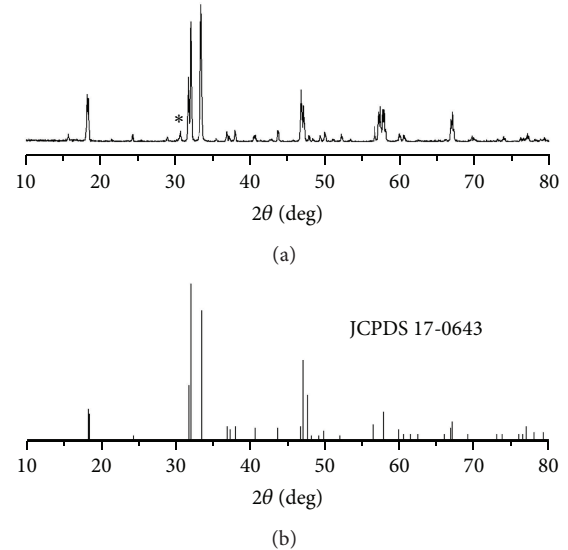


FIGURE 1: XRD patterns of  $\text{CaIn}_2\text{O}_4:0.6\%\text{Sm}^{3+}$  and the JCPDS card number 17-0643.

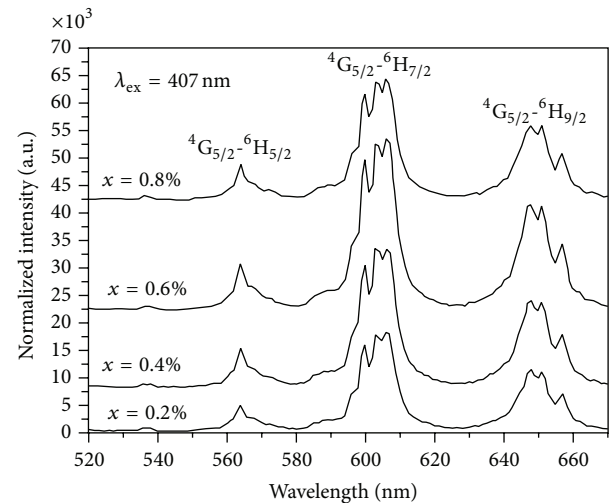


FIGURE 2: The PL spectra of  $\text{CaIn}_2\text{O}_4:x\text{Sm}^{3+}$  ( $0.2\% \leq x \leq 0.8\%$ ) ( $\lambda_{\text{ex}} = 407 \text{ nm}$ ).

impurity cannot play an important role in their luminescence properties.

PL spectra of  $\text{CaIn}_2\text{O}_4:x\text{Sm}^{3+}$  phosphors with different  $\text{Sm}^{3+}$  concentrations are shown in Figure 2. As can be seen from these figures, the emission intensity initially increases with  $\text{Sm}^{3+}$  concentration increasing and reaches a maximum at 0.6 mol%  $\text{Sm}^{3+}$  and then decreases which resulted from concentration quenching, because nonradiative energy transfer from one  $\text{Sm}^{3+}$  ion to another takes place. According to [18, 19], the probability of energy transfer among  $\text{Sm}^{3+}$  ions increases when the  $\text{Sm}^{3+}$  concentration increases. Nonradiative energy transfer from one  $\text{Sm}^{3+}$  ion to another usually may occur by exchange interaction, radiation reabsorption, or

multipole-multipole interaction. For  $\text{CaIn}_2\text{O}_4:\text{Sm}^{3+}$ , the concentration quenching is caused by the electric multipole-multipole interaction. We can roughly estimate the critical distance of energy transfer ( $R_c$ ). The distance at which the probability of transfer is equal to the probability of radiative emission can be made using the relation by Blasse to calculate  $R_c$  between activator ions of the kind doped in a host lattice:

$$R_c \approx 2 \left[ \frac{3V}{4\pi x_c Z} \right]^{1/3}, \quad (1)$$

where  $V$  is the volume of the unit cell,  $x_c$  the critical concentration of activator ion, and  $Z$  the number of formula units per unit cell [20]. For  $\text{CaIn}_2\text{O}_4$  host, using  $Z = 4$ ,  $x_c = 0.6 \text{ mol\%}$ , and  $V = 351.85 \text{ \AA}^3$ , the obtained  $R_c$  value is  $30.37 \text{ \AA}$ . Therefore, the energy transfer in the present case also occurs by electric multipole-multipole interaction.

The PLE and PL spectra of  $\text{CaIn}_2\text{O}_4:0.6\%\text{Sm}^{3+}$ ,  $\text{CaIn}_2\text{O}_4:0.6\%\text{Sm}^{3+},0.2\%\text{Zn}^{2+}$ , and  $\text{CaIn}_2\text{O}_4:0.6\%\text{Sm}^{3+},0.2\%\text{Al}^{3+}$  are compared in Figures 3 and 4, respectively. The PLE spectra are monitored by 606 nm. In PLE spectra, the excitation bands from 200 nm to 275 nm with a maximum at 225 nm belong to charge-transfer absorption band (CTB) of  $\text{O}^{2-}$  ions to  $\text{Sm}^{3+}$  ions. In the longer wavelength region, the  $f-f$  transitions within the  $\text{Sm}^{3+} 4f^5$  configuration can be detected, which is assigned as transition from the  ${}^6\text{H}_{5/2}$  ground state to the corresponding excited state of  $\text{Sm}^{3+}$ . Among these sharp lines, the strongest peak centered at 407 nm is assigned to  ${}^6\text{H}_{5/2} - {}^4\text{K}_{11/2}$ . It is obviously shown that  $0.2\%\text{Zn}^{2+}$  codoping can increase the characteristic transitions and CTB of  $\text{Sm}^{3+}$  ions. In  $\text{CaIn}_2\text{O}_4$  matrix, the ionic radius of  $\text{Zn}^{2+}$  ion is  $0.88 \text{ \AA}$ , similar to that of  $\text{In}^{3+}$  ion ( $0.94 \text{ \AA}$ ), so  $\text{Zn}^{2+}$  ion mainly occupies the  $\text{In}^{3+}$  ion sites. When  $\text{Sm}^{3+}$  ions replace  $\text{Ca}^{2+}$  ions in  $\text{CaIn}_2\text{O}_4$ , it causes the defects  $V_{\text{Ca}}''$  and  $\text{Sm}_{\text{Ca}}\cdot$  defects occur, which is to the disadvantage of photoluminescence. The introduction of small amount of  $\text{Zn}^{2+}$  ions can favor the charge balance in  $\text{CaIn}_2\text{O}_4:\text{Sm}^{3+}$  and further facilitate its photoluminescence. The enhanced  $\text{Sm}^{3+}$  emission comes mainly from radiative recombination of the large amount of trapped carriers excited from the  $\text{CaIn}_2\text{O}_4$  host. Upon photoexcitation, more oxygen holes can be trapped at the  $\text{Zn}_{\text{In}}'$  defects in  $\text{CaIn}_2\text{O}_4:\text{Sm}^{3+},\text{Zn}^{2+}$ . The increased recombination probability of electrons and trapped holes would cause the highly enhanced emission intensity of  $\text{Sm}^{3+}$  ions by the resultant energy transfer to the  $\text{Sm}^{3+}$  ions nearby. It also could be assumed that the incorporation of  $\text{Zn}^{2+}$  ions creates the oxygen vacancies, which might act as the sensitizer for the energy transfer to the rare earth ion due to the strong mixing of charge transfer states resulting in the highly enhanced luminescence. However, there is one different PLE spectrum with  $0.2\%\text{Al}^{3+}$  ions codoping. When the intensities of characteristic transitions of  $\text{Sm}^{3+}$  ions increase by a little amount of  $\text{Al}^{3+}$  ions codoping, the CTB intensities decrease. In  $\text{ZnNb}_2\text{O}_4:\text{Dy}^{3+},\text{Al}^{3+}$  material, the fact that energy can be transferred from CTB to excitation states of  $\text{Dy}^{3+}$  ions by codoping with  $\text{Al}^{3+}$  ions has been reported [21]. Thus  $\text{Al}^{3+}$

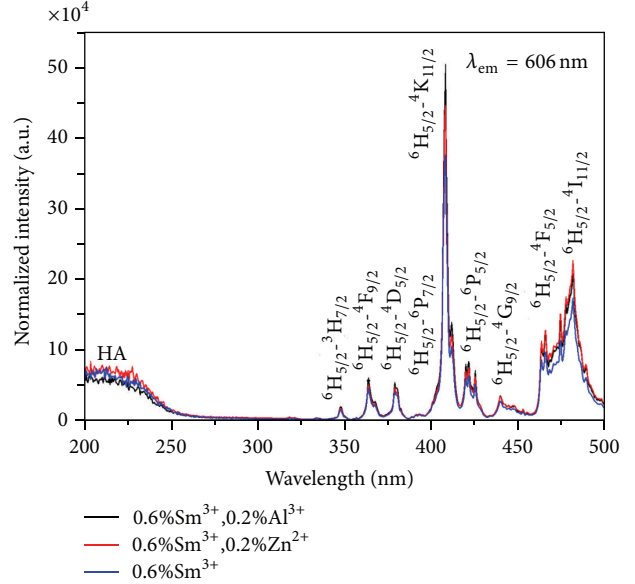


FIGURE 3: The PLE spectra of  $\text{CaIn}_2\text{O}_4:0.6\%\text{Sm}^{3+}$ ,  $\text{CaIn}_2\text{O}_4:0.6\%\text{Sm}^{3+},0.2\%\text{Zn}^{2+}$ , and  $\text{CaIn}_2\text{O}_4:0.6\%\text{Sm}^{3+},0.2\%\text{Al}^{3+}$  ( $\lambda_{\text{em}} = 606 \text{ nm}$ ).

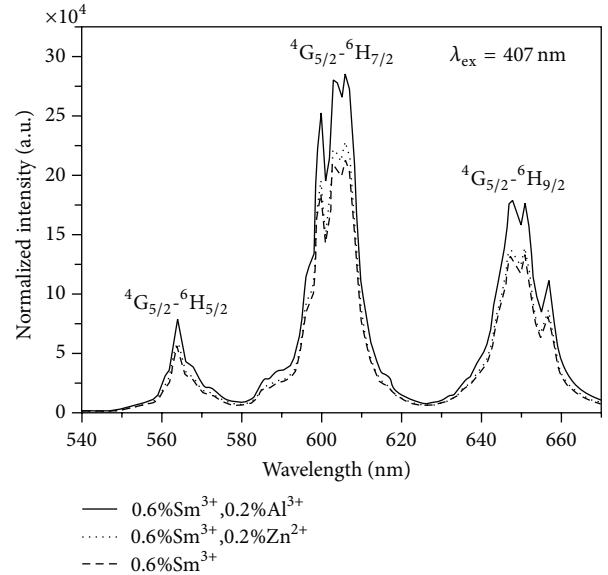


FIGURE 4: The PL spectra of  $\text{CaIn}_2\text{O}_4:0.6\%\text{Sm}^{3+}$ ,  $\text{CaIn}_2\text{O}_4:0.6\%\text{Sm}^{3+},0.2\%\text{Zn}^{2+}$ , and  $\text{CaIn}_2\text{O}_4:0.6\%\text{Sm}^{3+},0.2\%\text{Al}^{3+}$  ( $\lambda_{\text{ex}} = 407 \text{ nm}$ ).

ions also can help energy transfer from CTB to characteristic transitions of  $\text{Sm}^{3+}$  in  $\text{CaIn}_2\text{O}_4$  matrix.

In the corresponding PL spectra of  $\text{CaIn}_2\text{O}_4:0.6\%\text{Sm}^{3+}$ ,  $\text{CaIn}_2\text{O}_4:0.6\%\text{Sm}^{3+},0.2\%\text{Zn}^{2+}$ , and  $\text{CaIn}_2\text{O}_4:0.6\%\text{Sm}^{3+},0.2\%\text{Al}^{3+}$ , all emission peaks are obtained by 407 nm excitation and indexed in Figure 4. It is clearly shown that the little amount of  $\text{Zn}^{2+}$  or  $\text{Al}^{3+}$  ions codoping can enhance the intensity of photoluminescence, which corresponds to the PLE

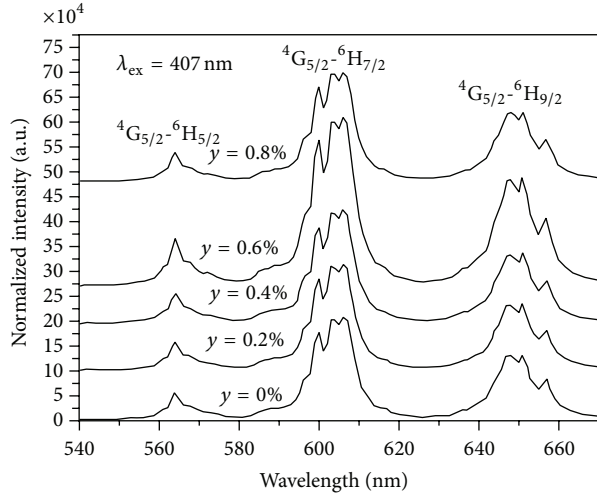


FIGURE 5: The PL spectra of  $\text{CaIn}_2\text{O}_4:0.6\%\text{Sm}^{3+}, y\text{Gd}^{3+}$  ( $0 \leq y \leq 0.8\%$ ) ( $\lambda_{\text{ex}} = 407 \text{ nm}$ ).

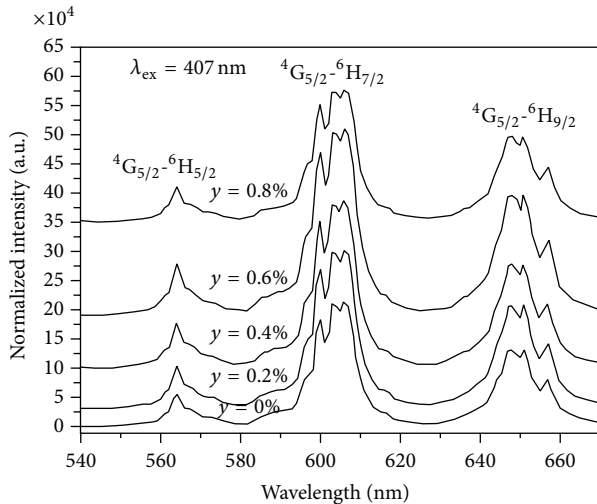


FIGURE 6: The PL spectra of  $\text{CaIn}_2\text{O}_4:0.6\%\text{Sm}^{3+}, y\text{Zn}^{2+}$  ( $0 \leq y \leq 0.8\%$ ) ( $\lambda_{\text{ex}} = 407 \text{ nm}$ ).

spectra in Figure 3. Therefore, the PL properties of the series  $\text{CaIn}_2\text{O}_4:0.6\%\text{Sm}^{3+}, y\text{Zn}^{2+}$  and  $\text{CaIn}_2\text{O}_4:0.6\%\text{Sm}^{3+}, y\text{Al}^{3+}$  were further investigated.

Figures 5 and 6 present the series of PL spectra of  $\text{CaIn}_2\text{O}_4:0.6\%\text{Sm}^{3+}, y\text{Zn}^{2+}$  and  $\text{CaIn}_2\text{O}_4:0.6\%\text{Sm}^{3+}, y\text{Al}^{3+}$  under 407 nm excitation, respectively. A little amount of  $\text{Zn}^{2+}$  and  $\text{Al}^{3+}$  codoping can facilitate the enhancement of luminescence intensity of  $\text{CaIn}_2\text{O}_4:0.6\%\text{Sm}^{3+}$ . When codoping amount of  $\text{Zn}^{2+}$  is 0.6%, the luminescence intensity of  $\text{CaIn}_2\text{O}_4:0.6\%\text{Sm}^{3+}$  can be enhanced to 1.59 times as  $\text{Zn}^{2+}$  free sample. On the same conditions, 0.6%  $\text{Al}^{3+}$  ions codoping can make 1.51 times luminescence intensity enhancement compared to  $\text{Zn}^{2+}$  free sample. The codoping amount of 0.6% is critical doping concentration of  $\text{Zn}^{2+}$  and  $\text{Al}^{3+}$  ions. When the codoping concentration  $y$  exceeded 0.6%, the PL intensity became decreasing; that was also caused by nonradiative

TABLE 1: The chromaticity coordinates for  $\text{CaIn}_2\text{O}_4:0.6\%\text{Sm}^{3+}$ ,  $\text{CaIn}_2\text{O}_4:0.6\%\text{Sm}^{3+}, 0.6\%\text{Zn}^{2+}$ , and  $\text{CaIn}_2\text{O}_4:0.6\%\text{Sm}^{3+}, 0.6\%\text{Al}^{3+}$  phosphors ( $\lambda_{\text{ex}} = 407 \text{ nm}$ ).

Samples	The chromaticity coordinates	
	$x$	$y$
$\text{CaIn}_2\text{O}_4:0.6\%\text{Sm}^{3+}$	0.616	0.383
$\text{CaIn}_2\text{O}_4:0.6\%\text{Sm}^{3+}, 0.6\%\text{Zn}^{2+}$	0.617	0.383
$\text{CaIn}_2\text{O}_4:0.6\%\text{Sm}^{3+}, 0.6\%\text{Al}^{3+}$	0.617	0.382

energy transfer among  $\text{Sm}^{3+}$  ions. The corresponding quantum efficiencies of  $\text{CaIn}_2\text{O}_4:0.6\%\text{Sm}^{3+}, 0.6\%\text{Zn}^{2+}$  and  $\text{CaIn}_2\text{O}_4:0.6\%\text{Sm}^{3+}, 0.6\%\text{Al}^{3+}$  were measured as 39.67 and 37.21 under 407 excitation, respectively. The values are higher than that of commercial red phosphor of  $\text{Y}_2\text{O}_3:\text{Eu}^{3+}$  (QE = 35%) under 317 nm excitation [22].

The chromaticity coordinates for  $\text{CaIn}_2\text{O}_4:0.6\%\text{Sm}^{3+}$ ,  $\text{CaIn}_2\text{O}_4:0.6\%\text{Sm}^{3+}, 0.6\%\text{Zn}^{2+}$ , and  $\text{CaIn}_2\text{O}_4:0.6\%\text{Sm}^{3+}, 0.6\%\text{Al}^{3+}$  phosphors with 407 nm excitation were simulated and listed in Table 1. With 0.6%  $\text{Zn}^{2+}$  or 0.6%  $\text{Al}^{3+}$  ions codoping, the chromaticity color coordinates of  $\text{CaIn}_2\text{O}_4:0.6\%\text{Sm}^{3+}$  have hardly any movements, which are all in reddish-orange region.

## 4. Conclusion

The series of phosphors  $\text{CaIn}_2\text{O}_4:\text{Sm}^{3+}$  codoped with  $\text{Zn}^{2+}$  or  $\text{Al}^{3+}$  ions were prepared by solid state reaction and their luminescence properties were investigated. Codoping  $\text{Zn}^{2+}$  or  $\text{Al}^{3+}$  ions can enhance the emissions of  $\text{CaIn}_2\text{O}_4:0.6\%\text{Sm}^{3+}$  excited by 407 nm, but the effects are different. The introduction of  $\text{Zn}^{2+}$  ions can favor the charge balance in  $\text{CaIn}_2\text{O}_4:\text{Sm}^{3+}$  to facilitate its photoluminescence, but  $\text{Al}^{3+}$  ions can effectively help energy transferred from CTB to characteristic transition of  $\text{Sm}^{3+}$  ions, utilizing more energy from host absorption to the photoluminescence of  $\text{Sm}^{3+}$  ions. All the chromaticity coordinates of  $\text{CaIn}_2\text{O}_4:0.6\%\text{Sm}^{3+}$ ,  $\text{CaIn}_2\text{O}_4:0.6\%\text{Sm}^{3+}, 0.6\%\text{Zn}^{2+}$ , and  $\text{CaIn}_2\text{O}_4:0.6\%\text{Sm}^{3+}, 0.6\%\text{Al}^{3+}$  are in reddish orange region and very close. The excellent luminescence properties of  $\text{CaIn}_2\text{O}_4:0.6\%\text{Sm}^{3+}, 0.6\%\text{Zn}^{2+}$  and  $\text{CaIn}_2\text{O}_4:0.6\%\text{Sm}^{3+}, 0.6\%\text{Al}^{3+}$  both present potential application value for WLEDs.

## Conflict of Interests

The authors declare that there is no conflict of interests regarding the publication of this paper.

## Acknowledgments

This research was supported by the Fundamental Research Funds for the Central Universities (GK201402015), National Natural Science Foundation of China (21302118), and Fundamental Doctoral Fund of Ministry of Education of China (20130202120015).

## References

- [1] H. A. Höpfe, "Recent developments in the field of inorganic phosphors," *Angewandte Chemie—International Edition*, vol. 48, no. 20, pp. 3572–3582, 2009.
- [2] S. Neeraj, N. Kijima, and A. K. Cheetham, "Novel red phosphors for solid-state lighting: the system  $\text{NaM}(\text{WO}_4)_{2-x}(\text{MoO}_4)_x$ :  $\text{Eu}^{3+}$  ( $\text{M}=\text{Gd}, \text{Y}, \text{Bi}$ )," *Chemical Physics Letters*, vol. 387, no. 1–3, pp. 2–6, 2004.
- [3] T. Nishida, T. Ban, and N. Kobayashi, "High-color-rendering light sources consisting of a 350-nm ultraviolet light-emitting diode and three-basal-color phosphors," *Applied Physics Letters*, vol. 82, no. 22, pp. 3817–3819, 2003.
- [4] J. S. Kim, P. E. Jeonny, J. C. Choi, H. L. Park, S. I. Mho, and G. C. Kim, "Warm-white-light emitting diode utilizing a single-phase full-color  $\text{Ba}_3\text{MgSi}_2\text{O}_8:\text{Eu}^{2+}, \text{Mn}^{2+}$  phosphor," *Applied Physics Letters*, vol. 84, no. 15, pp. 2931–2933, 2004.
- [5] L. Zhang, Z. Lu, P. Han, L. Wang, and Q. Zhang, "Effective red compensation of  $\text{Sr}_2\text{SiO}_4:\text{Dy}^{3+}$  phosphor by codoping  $\text{Mn}^{2+}$  ions and its energy transfer," *Journal of Nanomaterials*, vol. 2012, Article ID 848274, 7 pages, 2012.
- [6] S. Nakamura and G. Fasol, *The Blue Laser Diodes: GaN Based Blue Light Emitters and Lasers*, Springer, Berlin, Germany, 1997.
- [7] F. Lei and B. Yan, "Hydrothermal synthesis and luminescence of  $\text{CaMO}_4:\text{RE}^{3+}$  ( $\text{M}=\text{W}, \text{Mo}$ ;  $\text{RE}=\text{Eu}, \text{Tb}$ ) submicro-phosphors," *Journal of Solid State Chemistry*, vol. 181, no. 4, pp. 855–862, 2008.
- [8] C. F. Guo, D. X. Huang, and Q. Su, "Methods to improve the fluorescence intensity of  $\text{CaS}:\text{Eu}^{2+}$  red-emitting phosphor for white LED," *Materials Science and Engineering B: Solid-State Materials for Advanced Technology*, vol. 130, no. 1–3, pp. 189–193, 2006.
- [9] Y. Q. Li, G. de With, and H. T. Hintzen, "The effect of replacement of Sr by Ca on the structural and luminescence properties of the red-emitting  $\text{Sr}_2\text{Si}_5\text{N}_8:\text{Eu}^{2+}$  LED conversion phosphor," *Journal of Solid State Chemistry*, vol. 181, no. 3, pp. 515–524, 2008.
- [10] J. S. Liao, L. B. Liu, H. Y. You, H. P. Huang, and W. X. You, "Hydrothermal preparation and luminescence property of  $\text{MWO}_4:\text{Sm}^{3+}$  ( $\text{M} = \text{Ca}, \text{Sr}, \text{Ba}$ ) red phosphors," *Optik*, vol. 123, no. 10, pp. 901–905, 2012.
- [11] Y. Huang, W. Kai, Y. Cao et al., "Spectroscopic and structural studies of  $\text{Sm}^{2+}$  doped orthophosphate  $\text{K Sr PO}_4$  crystal," *Journal of Applied Physics*, vol. 103, no. 5, Article ID 053501, 2008.
- [12] Q. Wang, Z. Ci, G. Zhu et al., "Multicolor bright  $\text{Ln}^{3+}$  ( $\text{Ln} = \text{Eu}, \text{Dy}, \text{Sm}$ ) activated tungstate phosphor for multifunctional applications," *Optical Materials Express*, vol. 4, no. 1, pp. 142–154, 2014.
- [13] X. M. Liu, C. X. Li, Z. W. Quan, Z. Y. Cheng, and J. Lin, "Tunable luminescence properties of  $\text{CaIn}_2\text{O}_4:\text{Eu}^{3+}$  phosphors," *Journal of Physical Chemistry C*, vol. 111, no. 44, pp. 16601–16607, 2007.
- [14] X. M. Liu, R. Pang, Q. Li, and J. Lin, "Host-sensitized luminescence of  $\text{Dy}^{3+}, \text{Pr}^{3+}, \text{Tb}^{3+}$  in polycrystalline  $\text{CaIn}_2\text{O}_4$  for field emission displays," *Journal of Solid State Chemistry*, vol. 180, no. 4, pp. 1421–1430, 2007.
- [15] F. S. Kao and T.-M. Chen, "A study on the luminescent properties of new green-emitting terbium-activated  $\text{CaIn}_2\text{O}_4:\text{xTb}$  phosphors," *Journal of Luminescence*, vol. 96, no. 2–4, pp. 261–267, 2002.
- [16] F. S. Kao and T. M. Chen, "A study on the luminescent properties of praseodymium-activated  $\text{CaIn}_2\text{O}_4$  phosphors," *Journal of Solid State Chemistry*, vol. 155, no. 2, pp. 441–446, 2000.
- [17] X. Yan, W. Li, and K. Sun, "A novel red emitting phosphor  $\text{CaIn}_2\text{O}_4:\text{Eu}^{3+}, \text{Sm}^{3+}$  with a broadened near-ultraviolet absorption band for solid-state lighting," *Materials Research Bulletin*, vol. 46, no. 1, pp. 87–91, 2011.
- [18] D. L. Dexter, "A theory of sensitized luminescence in solids," *The Journal of Chemical Physics*, vol. 21, no. 5, pp. 836–850, 1953.
- [19] D. L. Dexter and J. H. Schulman, "Theory of concentration quenching in inorganic phosphors," *The Journal of Chemical Physics*, vol. 22, no. 6, pp. 1063–1070, 1954.
- [20] G. Blasse, "Energy transfer in oxidic phosphors," *Philips Research Report*, vol. 24, no. 2, pp. 131–144, 1969.
- [21] J. Gou, Y. H. Wang, and H. Z. Guo, "Energy transfer in  $\text{Dy}^{3+}$  and  $\text{Al}^{3+}$  co-doping  $\text{ZnNb}_2\text{O}_6$ ," *Journal of Physics: Conference Series*, vol. 152, no. 1, Article ID 012081, 6 pages, 2009.
- [22] Y. Huang, Y. Nakai, T. Tsuboi, and H. J. Seo, "The new red-emitting phosphor of oxyfluoride  $\text{Ca}_2\text{RF}_4\text{PO}_4:\text{Eu}^{3+}$  ( $\text{R}=\text{Gd}, \text{Y}$ ) for solid state lighting applications," *Optics Express*, vol. 19, no. 7, pp. 6303–6311, 2011.

## Research Article

# Synthesis and Electrochemical Performance of Graphene Wrapped $\text{Sn}_x\text{Ti}_{1-x}\text{O}_2$ Nanoparticles as an Anode Material for Li-Ion Batteries

Xing Xin, Xufeng Zhou, Tao Shen, and Zhaoping Liu

Ningbo Institute of Materials Technology & Engineering, Chinese Academy of Sciences, Zhejiang 315201, China

Correspondence should be addressed to Xufeng Zhou; [zhouxf@nimte.ac.cn](mailto:zhouxf@nimte.ac.cn) and Zhaoping Liu; [liuzp@nimte.ac.cn](mailto:liuzp@nimte.ac.cn)

Received 4 December 2014; Revised 9 January 2015; Accepted 9 January 2015

Academic Editor: Jiamin Wu

Copyright © 2015 Xing Xin et al. This is an open access article distributed under the Creative Commons Attribution License, which permits unrestricted use, distribution, and reproduction in any medium, provided the original work is properly cited.

Ever-growing development of Li-ion battery has urged the exploitation of new materials as electrodes. Here,  $\text{Sn}_x\text{Ti}_{1-x}\text{O}_2$  solid-solution nanomaterials were prepared by aqueous solution method. The morphology, structures, and electrochemical performance of  $\text{Sn}_x\text{Ti}_{1-x}\text{O}_2$  nanoparticles were systematically investigated. The results indicate that Ti atom can replace the Sn atom to enter the lattice of  $\text{SnO}_2$  to form substitutional solid-solution compounds. The capacity of the solid solution decreases while the stability is improved with the increasing of the Ti content. Solid solution with  $x$  of 0.7 exhibits the optimal electrochemical performance. The  $\text{Sn}_{0.7}\text{Ti}_{0.3}\text{O}_2$  was further modified by highly conductive graphene to enhance its relatively low electrical conductivity. The  $\text{Sn}_{0.7}\text{Ti}_{0.3}\text{O}_2$ /graphene composite exhibits much improved rate performance, indicating that the  $\text{Sn}_x\text{Ti}_{1-x}\text{O}_2$  solid solution can be used as a potential anode material for Li-ion batteries.

## 1. Introduction

$\text{SnO}_2$  has long been considered as a potential substitute for the conventional graphite anode in lithium ion batteries, since the theoretical capacity of  $\text{SnO}_2$  ( $783 \text{ mAh g}^{-1}$ ) is much higher than that of commercial graphite anode ( $372 \text{ mAh g}^{-1}$ ) [1]. However, large volume change for  $\text{SnO}_2$  occurs during the cycling process; thus it causes crumbling of the electrode and leads to destruction of the electrically conductive network. Therefore, the  $\text{SnO}_2$  based anode materials suffer from rapid fading of capacity [2, 3]. There have been many strategies to improve the cycle stability of the  $\text{SnO}_2$  based anode materials, including elaborate structure design and combination with conductive additives [3–7]. Unfortunately, the mitigation of the capacity fading is quite difficult because of the large volume change derived from alloying/dealloying reactions of Sn with Li, which is the fundamental electrochemical origin of the  $\text{SnO}_2$  electrode [8, 9].

The  $\text{SnO}_2$ /metal oxide hybrid electrode materials, such as  $\text{SnO}_2$ - $\text{SiO}_2$ ,  $\text{SnO}_2$ - $\text{Fe}_2\text{O}_3$ , and  $\text{SnO}_2$ - $\text{TiO}_2$  [10–13], have been reported to show improved electrochemical performance than pure  $\text{SnO}_2$  for lithium storage because metal oxide can

act as a buffering matrix to accommodate the large change in volume as well as the conductive additive to improve the electrical conductivity. Among these metal oxides,  $\text{TiO}_2$  itself has also attracted great attention as an alternative anode material owing to its low cost, low toxicity, stable cyclability, and good safety. However, the practical application of the  $\text{TiO}_2$  anode is challenging due to its low specific capacity and low intrinsic electrical conductivity which leads to limited rate capability [14–16]. There have been some reports on the  $\text{SnO}_2$ - $\text{TiO}_2$  mixed oxides as the anode material for Li-ion batteries. The studies involve a fundamental investigation of  $\text{SnO}_2$ - $\text{TiO}_2$  mixed oxides and aim to improve the cyclic performance by manipulating the morphology and content of  $\text{TiO}_2$ . Lin and coworkers [12] investigated the electrochemical performance of a  $\text{TiO}_2$ -supported  $\text{SnO}_2$  nanocomposite formed of equimolar amounts of  $\text{SnO}_2$  and  $\text{TiO}_2$ . The nanocomposite showed improved capacity and higher Coulombic efficiency. Du and coworkers [17] prepared three-dimensional  $\text{SnO}_2$ / $\text{TiO}_2$  composite by depositing  $\text{SnO}_2$  nanocrystals into  $\text{TiO}_2$  nanotube electrodes through solvothermal technique. The maximum reversible capacity of the composite could reach as high as  $\sim 300 \mu\text{Ah cm}^{-2}$ . Except the  $\text{SnO}_2$ - $\text{TiO}_2$

mixed oxides, Uchiyama and coworkers [18] first proposed that the  $\text{Sn}_x\text{Ti}_{1-x}\text{O}_2$  solid solution could be used as the potential anode material for Li-ion batteries. They found that there was not major collapse of the structure in the  $\text{Sn}_x\text{Ti}_{1-x}\text{O}_2$  solid solution during lithium insertion. However, the lithium insertion/extraction behavior of this rutile-type solid solution remains unclear, and the electrochemical performance such as cyclic performance, rate performance, and resistance of this solid solution should be further tested and improved.

In this paper, a series of  $\text{Sn}_x\text{Ti}_{1-x}\text{O}_2$  ( $0.3 \leq x \leq 0.9$ ) nanomaterials were successfully synthesized by an aqueous solution-based method. The morphology, structure, and the performance of  $\text{Sn}_x\text{Ti}_{1-x}\text{O}_2$  solid solutions as anode materials were examined in detail. The results proved that the electrochemical performance of  $\text{Sn}_x\text{Ti}_{1-x}\text{O}_2$  differed from either  $\text{SnO}_2$  or  $\text{TiO}_2$ . In order to further improve its electrochemical performance, the solid solution with a certain  $x$  value was modified by graphene. The improved electrochemical performance indicates that  $\text{Sn}_x\text{Ti}_{1-x}\text{O}_2/\text{graphene}$  composite can be used as a potential anode material for Li-ion battery.

## 2. Materials and Methods

**2.1. Materials.** All chemicals were of analytical grade and were purchased from Sinopharm Chemical Reagent Co., Ltd., China. Graphene oxide (GO) nanosheets were prepared by a chemical exfoliation process using natural graphite flakes of 300 mesh size according to the method we reported previously [19].

**2.2. Preparation of  $\text{Sn}_x\text{Ti}_{1-x}\text{O}_2$  Solid Solution.** Precursors of  $\text{Sn}_x\text{Ti}_{1-x}\text{O}_2$  solid solutions with different  $x$  values were obtained by dissolving tetrabutyl titanate (TBT) and  $\text{SnCl}_2 \cdot 2\text{H}_2\text{O}$  with a certain molar ratio into 50 mL of ethanol solution under stirring at room temperature. The total concentration of the metal ions (TBT +  $\text{SnCl}_2 \cdot 2\text{H}_2\text{O}$ ) was 0.1 M. The (TBT)/ $\text{SnCl}_2 \cdot 2\text{H}_2\text{O}$  molar ratio in the precursor solutions was adjusted to 8 : 2, 7 : 3, 6 : 4, 5 : 5, 4 : 6, 3 : 7, and 2 : 8. After 30 min, 50 mL of deionized water was added into the solution. The resulting white slurry was stirred for another 1 h and additionally aged for 8 h. The precipitate was collected by centrifuge and repeatedly washed with ethanol and then air-dried at 80 °C for 10 h. Different from the  $\text{Ti}_x\text{Sn}_{1-x}\text{O}_2$  reported by Uchiyama et al. under the same calcination temperature [18], the obtained sample was further calcinated at 500 °C–900 °C for 5 h, resulting in the final solid solutions. In order to compare, we prepared  $\text{TiO}_2$  and  $\text{SnO}_2$  particles with the precursor solutions only containing TBT or  $\text{SnCl}_2 \cdot 2\text{H}_2\text{O}$ , respectively.

**2.3. Preparation of  $\text{Sn}_x\text{Ti}_{1-x}\text{O}_2/\text{Graphene}$  Composite.**  $\text{Sn}_{0.7}\text{Ti}_{0.3}\text{O}_2$  was mixed with the GO solution to form a slurry with the weight ratio of  $\text{Sn}_{0.7}\text{Ti}_{0.3}\text{O}_2:\text{GO} = 4:1$ . The solid content of the slurry was adjusted to 10% by adding deionized water. After being ultrasonically exposed for 10 min, the slurry was spray-dried with an inlet air temperature of 200 °C to form solid powders. The composite

was then annealed at 500 °C under Ar to form  $\text{Sn}_{0.7}\text{Ti}_{0.3}\text{O}_2/\text{G}$  composite.

**2.4. Structural Characterization.** Powder X-ray diffraction (XRD) measurements were performed using AXS D8 Advance diffractometer (Cu  $K\alpha$  radiation; receiving slit, 0.2 mm; scintillation counter, 40 mA; 40 kV) from Bruker Inc. The morphology and structure were analyzed by a Hitachi S-4800 field emission scanning-electron microscope (SEM) and FEI Tecnai G<sup>2</sup> F20 transmission-electron microscope (TEM) at an accelerating voltage of 200 kV.

**2.5. Electrochemical Tests.** The evaluation of electrochemical performance was carried out using CR2032-type coin cells. The working electrode contained 80 wt % of active materials, 10 wt% of Super P, and 10 wt % of polyvinylidene fluoride (PVDF). The Li metal foil served as the counter electrode. The electrolyte was composed of 1 M  $\text{LiPF}_6$  solution in ethylene carbonate (EC)/dimethyl carbonate (DMC) (1 : 1 by volume). The coin cells were activated at a current density of 50 mA  $\text{g}^{-1}$  for the first cycle and then cycled under different current densities within the voltage range of 0.01–2 V using a LAND-CT2001A battery test system (Jinnuo Wuhan Corp., China). Cyclic voltammogram analysis was performed using Autolab 83710. Specific resistance of  $\text{Sn}_x\text{Ti}_{1-x}\text{O}_2$  electrode materials was measured by four-point resistivity test system (NAPSON CRESBOX) after coating the anode slurry on an insulating substrate.

## 3. Results and Discussion

The XRD patterns of  $\text{Sn}_x\text{Ti}_{1-x}\text{O}_2$  solid solutions with different  $x$  were collected to determine the crystal structures, as shown in Figure 1. All samples exhibit similar XRD patterns as that of pure rutile  $\text{SnO}_2$  and no peaks of other crystal phase are detected, indicating that Ti does not present in the form of  $\text{TiO}_2$  in the solid solution. When the  $x$  value of  $\text{Sn}_x\text{Ti}_{1-x}\text{O}_2$  decreases, all the peaks shift towards higher diffraction angles, demonstrating that the crystal structures remain the same whereas the lattice parameters of the solid solutions shrink gradually. It should be pointed out that the calcination temperature needs to be lowered to keep the pure solid solution structure at high Ti content. Though rutile  $\text{TiO}_2$  and rutile  $\text{SnO}_2$  both belong to tetragonal systems and the lattice parameters of two oxides are close, phase separation of  $\text{TiO}_2$  along with solid solutions may occur especially at high Ti content. For example, at the calcination temperature of 650 °C,  $\text{TiO}_2$  are detectable when the Ti content is above 0.5. Consequently, lower calcination temperatures were adopted in our experiments to prevent the formation of  $\text{TiO}_2$ . Specifically,  $\text{Sn}_{0.9}\text{Ti}_{0.1}\text{O}_2$ ,  $\text{Sn}_{0.8}\text{Ti}_{0.2}\text{O}_2$ ,  $\text{Sn}_{0.7}\text{Ti}_{0.3}\text{O}_2$ ,  $\text{Sn}_{0.6}\text{Ti}_{0.4}\text{O}_2$ ,  $\text{Sn}_{0.5}\text{Ti}_{0.5}\text{O}_2$ ,  $\text{Sn}_{0.4}\text{Ti}_{0.6}\text{O}_2$ , and  $\text{Sn}_{0.3}\text{Ti}_{0.7}\text{O}_2$  were obtained at 900 °C, 900 °C, 800 °C, 700 °C, 600 °C, 600 °C, and 500 °C, respectively. As a result of lower calcination temperature, the width of the peaks in the XRD pattern decreases with increasing Ti content, indicating that the particle size or the crystallinity of the solid solution decreases.

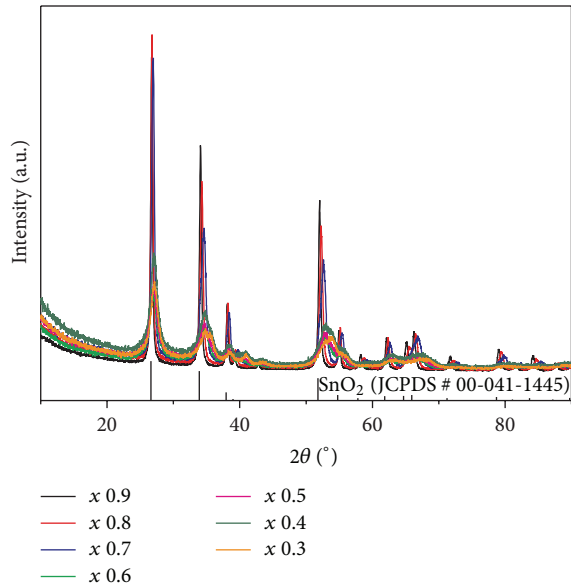


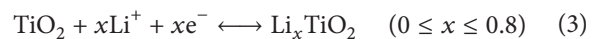
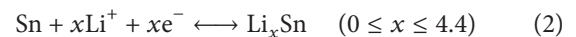
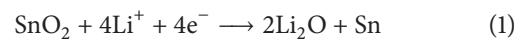
FIGURE 1: XRD patterns of  $\text{Sn}_x\text{Ti}_{1-x}\text{O}_2$  solid solutions with different  $x$  values.

The morphology of the precursors (before calcination) and the corresponding solid solutions were analyzed by SEM and TEM. As shown in Figures 2(a) and 2(b), both precursors of  $\text{Sn}_{0.9}\text{Ti}_{0.1}\text{O}_2$  and  $\text{Sn}_{0.4}\text{Ti}_{0.6}\text{O}_2$  present irregular sphere-like morphology. The particles of  $\text{Sn}_{0.4}\text{Ti}_{0.6}\text{O}_2$  precursor are more significantly aggregated than that of  $\text{Sn}_{0.9}\text{Ti}_{0.1}\text{O}_2$ . After calcination at different temperatures, as shown in Figures 2(c) and 2(d), both  $\text{Sn}_{0.9}\text{Ti}_{0.1}\text{O}_2$  and  $\text{Sn}_{0.4}\text{Ti}_{0.6}\text{O}_2$  still maintain the irregular particulate morphology. The particle size of  $\text{Sn}_{0.4}\text{Ti}_{0.6}\text{O}_2$  is about 10–20 nm, which is much smaller than that of  $\text{Sn}_{0.9}\text{Ti}_{0.1}\text{O}_2$  (30–50 nm) (Figures 2(e) and 2(f)). The clearly visible set of lattice fringes observed in TEM images (Figures 2(g) and 2(h)) with a period of 0.334 nm and 0.328 nm is characteristic of the (101) lattice planes of rutile  $\text{Sn}_x\text{Ti}_{1-x}\text{O}_2$  with  $x$  of 0.9 and 0.4, respectively. The decrease of the particle size along with the increase of the Ti content is consistent with the XRD results, which is probably due to the lower calcination temperature. However, the aggregation of  $\text{Sn}_x\text{Ti}_{1-x}\text{O}_2$  nanoparticles becomes more severe when the Ti content increases.

X-ray photoelectron spectroscopy (XPS) analysis of the  $\text{Sn}_{0.4}\text{Ti}_{0.6}\text{O}_2$  solid solution was performed in the range of 0–1200 eV, as shown in Figure 3(a). There are two symmetrical peaks at 487.15 eV and 495.60 eV in the Sn 3d spectrum (Figure 3(b)), which can be attributed to Sn 3d<sub>5/2</sub> and Sn 3d<sub>3/2</sub>, respectively. The separation between these two peaks is 8.45 eV, slightly larger than the energy splitting reported for  $\text{SnO}_2$  [11]. Similarly, the Ti 2p spectrum (Figure 3(c)) is also composed of two symmetrical peaks with binding energies of 459.5 eV and 465.15 eV, which are derived from Ti 2p<sub>3/2</sub> and Ti 2p<sub>1/2</sub>, respectively. The separation of 5.65 eV between these two signals indicates a normal state of  $\text{Ti}^{4+}$  in the rutile  $\text{Sn}_{0.4}\text{Ti}_{0.6}\text{O}_2$  solid solution [20]. As for the O 1s spectrum shown in Figure 3(d), the O 1s peak can be deconvoluted

into two peaks at 530.70 eV and 531.95 eV, corresponding to Ti–O–Ti and Sn–O–Ti bonds, respectively [21]. It should be noted that the Ti–O–Ti bonds should be attributed to the trace of  $\text{TiO}_2$  on the surface of solid solution especially when Ti content is high. From the Sn–O–Ti bonds it can be inferred that Ti has been successfully incorporated into the  $\text{SnO}_2$  matrix through Sn–O–Ti bonds.

Then the solid solutions were subjected to a systematic electrochemical analysis. Cyclic voltammetry (CV) was carried out at a scan rate of  $0.2\text{ mV s}^{-1}$  to identify the characteristics of the redox reactions during charge/discharge cycles. As can be seen from Figures 4(a), 4(b), and 4(c), all the solid solutions with different  $x$  present similar CV curves in the first cycle. The CV curves clearly indicate a reaction during the first discharge with a reduction peak around 1 V. The XRD results (Figure 4(d)) further confirm that, after the  $\text{Li}^+$  insertion, Sn as the only crystalline phase presents in both  $\text{Sn}_{0.9}\text{Ti}_{0.1}\text{O}_2$  and  $\text{Sn}_{0.7}\text{Ti}_{0.3}\text{O}_2$  anode material. Therefore, the peak around 1 V is speculated to represent the reaction of Li with  $\text{SnO}_2$  to form  $\text{Li}_2\text{O}$  and Sn, which is similar to the first discharge process of the  $\text{SnO}_2$  based anode material as the reaction (1). For the  $\text{SnO}_2$  based anode material, the reduction peak at 1 V disappears after the first discharge, indicating that the reaction of Li with  $\text{SnO}_2$  to form  $\text{Li}_2\text{O}$  and Sn is generally irreversible [5, 12, 22]. After the first cycle, electrochemically reduced Sn will react with  $\text{Li}^+$  to form a series of tin-lithium alloys during the following cycles as the reaction (2), which is reversible. On the other hand, it should be also mentioned that the insertion/extraction of  $\text{Li}^+$  in rutile  $\text{TiO}_2$  anode usually takes place in the potential range of 1.0–1.4 V in CV curves [23], and this process has a good reversibility as reaction (3):



For the  $\text{Sn}_x\text{Ti}_{1-x}\text{O}_2$ , there is no obvious redox peak at 1.0–1.4 V in the CV curves for the solid solution, suggesting that Ti in the solid solution does not undergo a similar electrochemical reaction as that in  $\text{TiO}_2$ . Basically, the charge-discharge process of the solid solution is similar to that of  $\text{SnO}_2$ .

The initial charge-discharge curves of  $\text{Sn}_{0.9}\text{Ti}_{0.1}\text{O}_2$ ,  $\text{Sn}_{0.7}\text{Ti}_{0.3}\text{O}_2$ , and  $\text{Sn}_{0.4}\text{Ti}_{0.6}\text{O}_2$  solid solutions at a current density of  $50\text{ mA g}^{-1}$  between 0.01 and 2 V are compared in Figure 5.  $\text{Sn}_{0.9}\text{Ti}_{0.1}\text{O}_2$  delivers a capacity of  $888\text{ mAh g}^{-1}$  in the first charge and  $1465\text{ mAh g}^{-1}$  in the first discharge, while  $\text{Sn}_{0.7}\text{Ti}_{0.3}\text{O}_2$  and  $\text{Sn}_{0.4}\text{Ti}_{0.6}\text{O}_2$  display 780, 1225, 600, and  $1125\text{ mAh g}^{-1}$  in the first charge and discharge, respectively. The increasing capacity of  $\text{Sn}_x\text{Ti}_{1-x}\text{O}_2$  with increasing  $x$  indicates that the increasing of Sn content can enhance the capacity of the solid solution. Moreover,  $\text{Sn}_{0.9}\text{Ti}_{0.1}\text{O}_2$  exhibits lower irreversible capacity loss in the first cycles comparing to that of  $\text{Sn}_{0.4}\text{Ti}_{0.6}\text{O}_2$ . Such phenomenon may be attributed to the smaller particle size of  $\text{Sn}_{0.4}\text{Ti}_{0.6}\text{O}_2$  and its lower crystallinity.

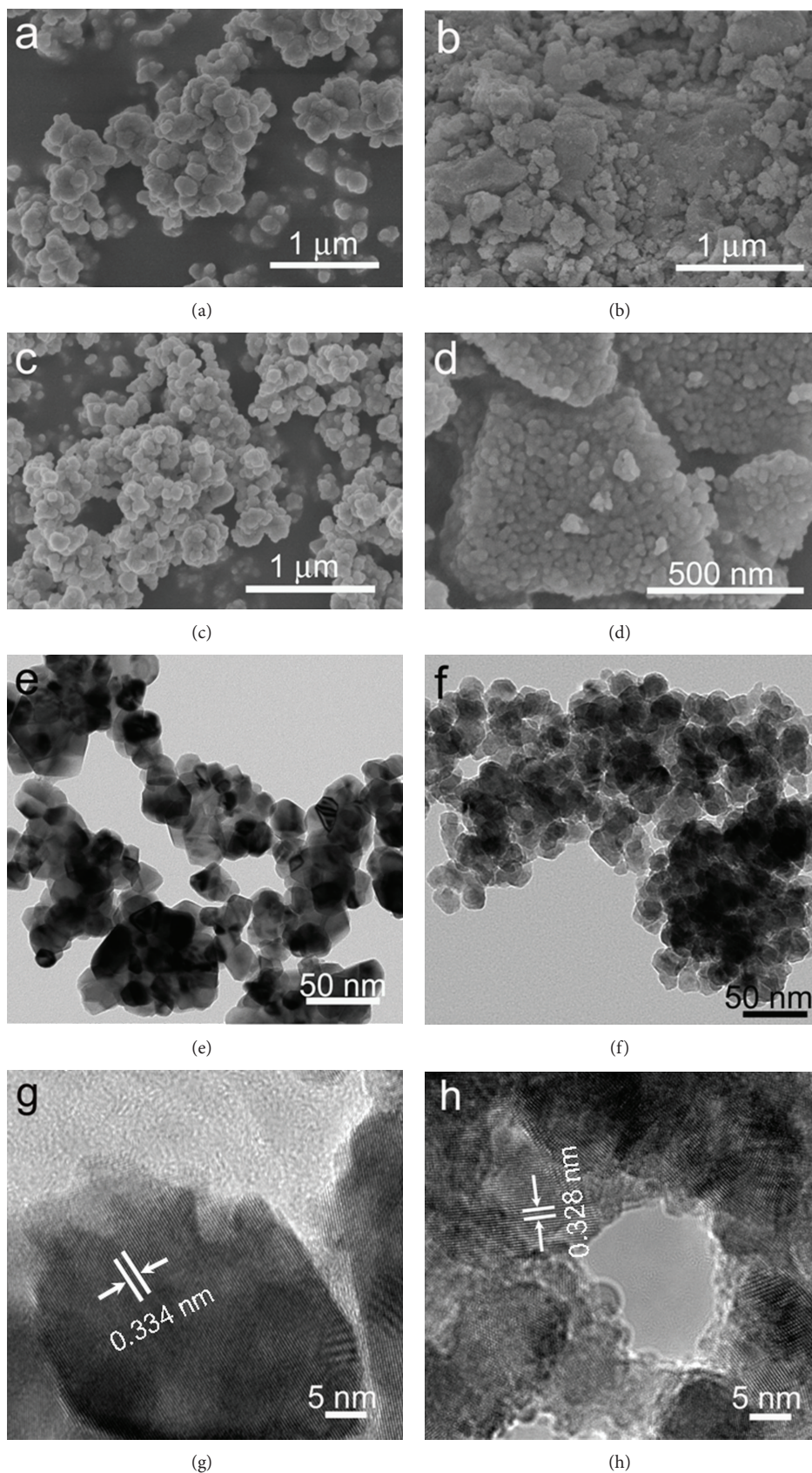


FIGURE 2: SEM images of the precursors of Sn<sub>0.9</sub>Ti<sub>0.1</sub>O<sub>2</sub> (a) and Sn<sub>0.4</sub>Ti<sub>0.6</sub>O<sub>2</sub> (b) solid solutions, and SEM images of Sn<sub>0.9</sub>Ti<sub>0.1</sub>O<sub>2</sub> (c) and Sn<sub>0.4</sub>Ti<sub>0.6</sub>O<sub>2</sub> (d) solid solutions. ((e), (f)) TEM images of Sn<sub>0.9</sub>Ti<sub>0.1</sub>O<sub>2</sub> (e) and Sn<sub>0.4</sub>Ti<sub>0.6</sub>O<sub>2</sub> (f) solid solutions. ((g), (h)) High-resolution TEM images of Sn<sub>0.9</sub>Ti<sub>0.1</sub>O<sub>2</sub> (g) and Sn<sub>0.4</sub>Ti<sub>0.6</sub>O<sub>2</sub> (h) solid solutions.

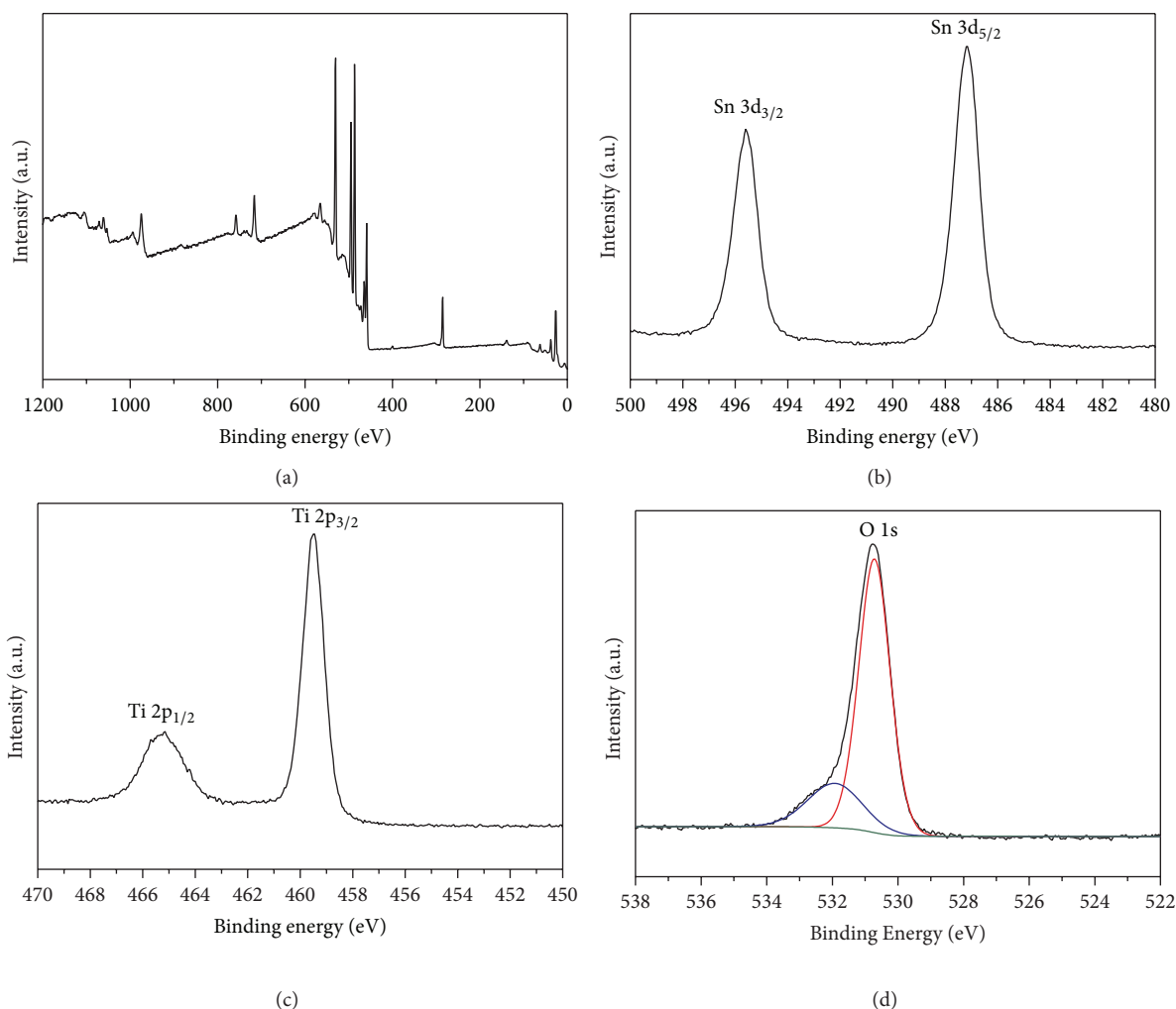


FIGURE 3: XPS spectra of the  $\text{Sn}_{0.4}\text{Ti}_{0.6}\text{O}_2$  solid solutions. Panel (a) shows the survey spectrum and panels (b), (c), and (d) show the high-resolution spectra of Sn, Ti, and O, respectively.

The cycling performance of bare  $\text{TiO}_2$ , bare  $\text{SnO}_2$ , and  $\text{Sn}_x\text{Ti}_{1-x}\text{O}_2$  solid solution with  $x$  of 0.9, 0.7, and 0.4 was evaluated at the current density of  $100 \text{ mA g}^{-1}$ , as shown in Figure 6. The bare- $\text{TiO}_2$  electrode presents a stable cyclability with the reversible capacity of  $200 \text{ mAh g}^{-1}$ . The excellent cycle stability of the  $\text{TiO}_2$  anode material should be attributed to its negligible volume change ( $<4\%$ ) during the charge/discharge processes. The bare- $\text{SnO}_2$  electrode delivers a high initial capacity of  $1100 \text{ mAh g}^{-1}$ , much higher than that of bare- $\text{TiO}_2$ . Unfortunately, there is a rapid fading of capacity due to the severe pulverization of  $\text{SnO}_2$  during cycling. After 30 cycles, only a low reversible capacity of  $94 \text{ mAh g}^{-1}$  is remained, which was about 10% retention of the initial reversible capacity. The  $\text{Sn}_{0.9}\text{Ti}_{0.1}\text{O}_2$ ,  $\text{Sn}_{0.7}\text{Ti}_{0.3}\text{O}_2$ , and  $\text{Sn}_{0.4}\text{Ti}_{0.6}\text{O}_2$  deliver the initial capacity of  $887 \text{ mAh g}^{-1}$ ,  $743 \text{ mAh g}^{-1}$ , and  $592 \text{ mAh g}^{-1}$ , respectively. It is obvious that the initial capacity of  $\text{Sn}_x\text{Ti}_{1-x}\text{O}_2$  declines with the increasing of the Ti content but is still much higher than that of pure  $\text{TiO}_2$ . As the content of Ti increases, the cycle stability is enhanced. After 30 cycles,  $\text{Sn}_{0.9}\text{Ti}_{0.1}\text{O}_2$  shows

$\sim 20\%$  retention ( $174 \text{ mAh g}^{-1}$ ) of the initial capacity, which is a little higher than that of pure  $\text{SnO}_2$  anode materials. The capacity retention can be further significantly raised to 47% and 60% when  $x$  is decreased to 0.7 ( $\text{Sn}_{0.7}\text{Ti}_{0.3}\text{O}_2$ ) and 0.4 ( $\text{Sn}_{0.4}\text{Ti}_{0.6}\text{O}_2$ ), respectively. With increasing Ti content, the resistivity of the solid solution also increases as displayed in Table 1. The above results thus demonstrate that the electrochemical performance of the solid solution found here is a combination of  $\text{TiO}_2$  and  $\text{SnO}_2$ . A gradual transition of the electrochemical performance from  $\text{SnO}_2$  to  $\text{TiO}_2$  can be observed along with the increase of Ti content in the solid solution, and the overall electrochemical performance of  $\text{Sn}_x\text{Ti}_{1-x}\text{O}_2$  is strongly affected by the ratio of Ti/Sn. Consequently, with an optimal  $x$  value, the characteristic high capacity of  $\text{SnO}_2$  anode material and superior cycle stability of  $\text{TiO}_2$  can be optimally balanced in one solid solution anode material. Based on the above results, the optimal  $x$  value is found to be 0.7.

Despite the fact that relative good electrochemical performance can be achieved, the solid solutions still suffer

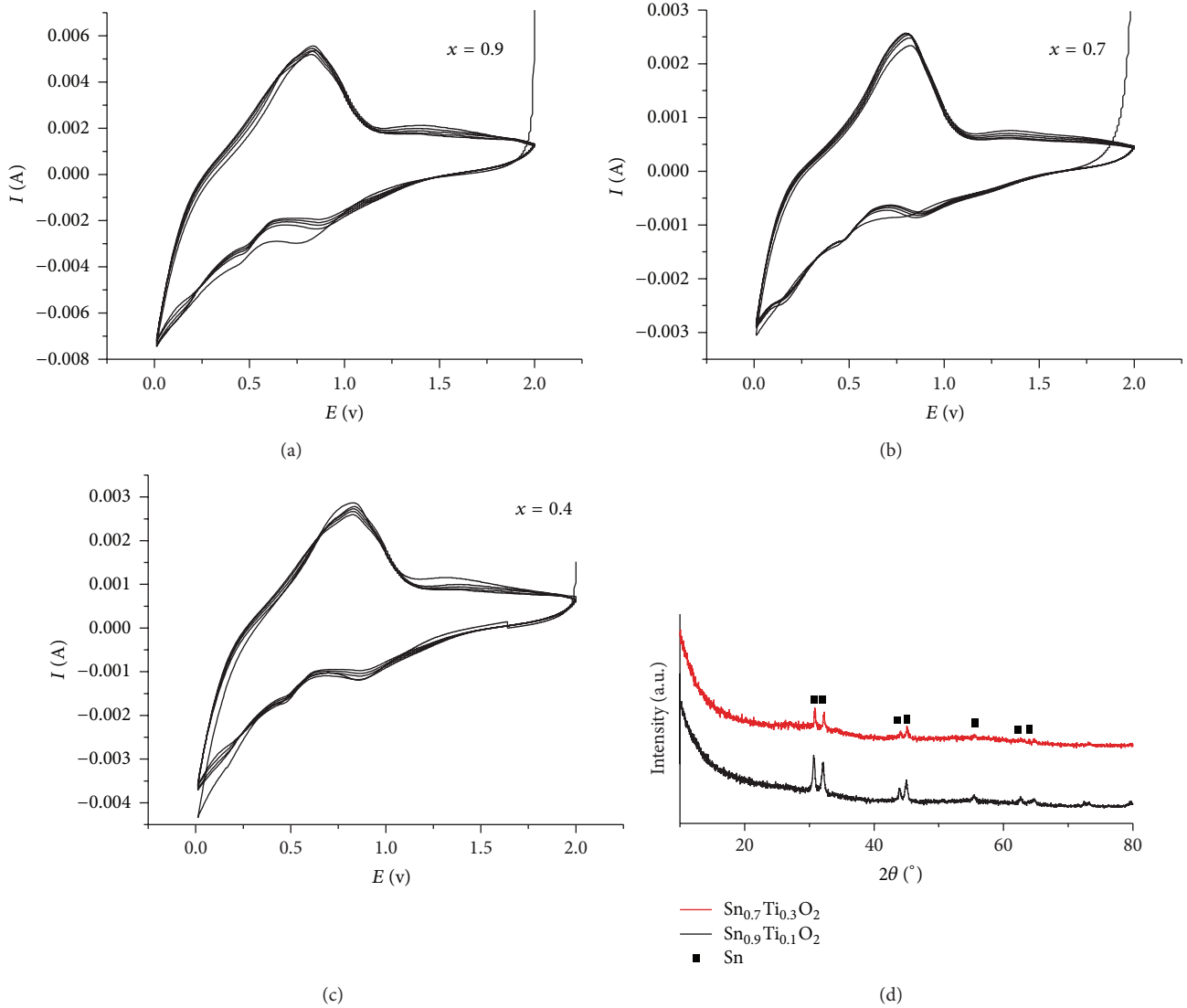


FIGURE 4: Cyclic voltammogram curves of  $\text{Sn}_x\text{Ti}_{1-x}\text{O}_2$  solid solution with  $x$  of 0.9 (a), 0.7 (b), and 0.4 (c) from the first cycle to the fifth cycle at a scan rate of  $0.2 \text{ mV s}^{-1}$  in the voltage range of 0.0–2.0 V. (d) XRD patterns of  $\text{Sn}_{0.9}\text{Ti}_{0.1}\text{O}_2$  and  $\text{Sn}_{0.7}\text{Ti}_{0.3}\text{O}_2$  after  $\text{Li}^+$  insertion.

TABLE 1: The resistance of  $\text{Sn}_x\text{Ti}_{1-x}\text{O}_2$  with different  $x$  tested by four probe tests.

$\text{Sn}_x\text{Ti}_{1-x}\text{O}_2$	$x = 0.9$	$x = 0.8$	$x = 0.7$	$x = 0.6$	$x = 0.5$	$x = 0.4$	$x = 0.3$
$R/\Omega\text{-cm}$	639.1	675.6	685.3	747.6	981.8	1508.3	1558.3

from low intrinsic conductivity (see Table 1). Therefore, modification of the solid solution with graphene by a spray drying method was carried out in our experiments in the case of  $\text{Sn}_{0.7}\text{Ti}_{0.3}\text{O}_2$  with the optimal performance. Graphene as the 2D carbon nanomaterial was recently widely used to improve the electrochemical performance of various electrode materials due to its superior electrical conductivity, large surface area, and excellent structural flexibility [24–29]. SEM image in Figure 7(a) shows an overview of the final  $\text{Sn}_{0.7}\text{Ti}_{0.3}\text{O}_2/\text{graphene}$  nanocomposite. The sample consists of secondary quasispherical microparticles with diameters of 2–5  $\mu\text{m}$ . SEM observation at a higher magnification

(Figure 7(b)) reveals that each microsphere is actually a random aggregation of primary  $\text{Sn}_{0.7}\text{Ti}_{0.3}\text{O}_2$  nanoparticles that are covered by soft graphene sheets. The TEM image further demonstrates that the  $\text{Sn}_{0.7}\text{Ti}_{0.3}\text{O}_2$  nanoparticles are loosely wrapped by a thin graphene layer as presented in Figure 7(c). The high resolution TEM image (Figure 7(d)) reveals that the  $\text{Sn}_{0.7}\text{Ti}_{0.3}\text{O}_2$  nanoparticles are coated with graphene shells whose thickness is less than 3 nm. In addition, the SEM and EDS mapping images show that Sn, Ti, O, and C are dispersed uniformly in the microspheres.

To further study the effects of graphene wrapping on the rate capability and cyclic stability of the solid solution,

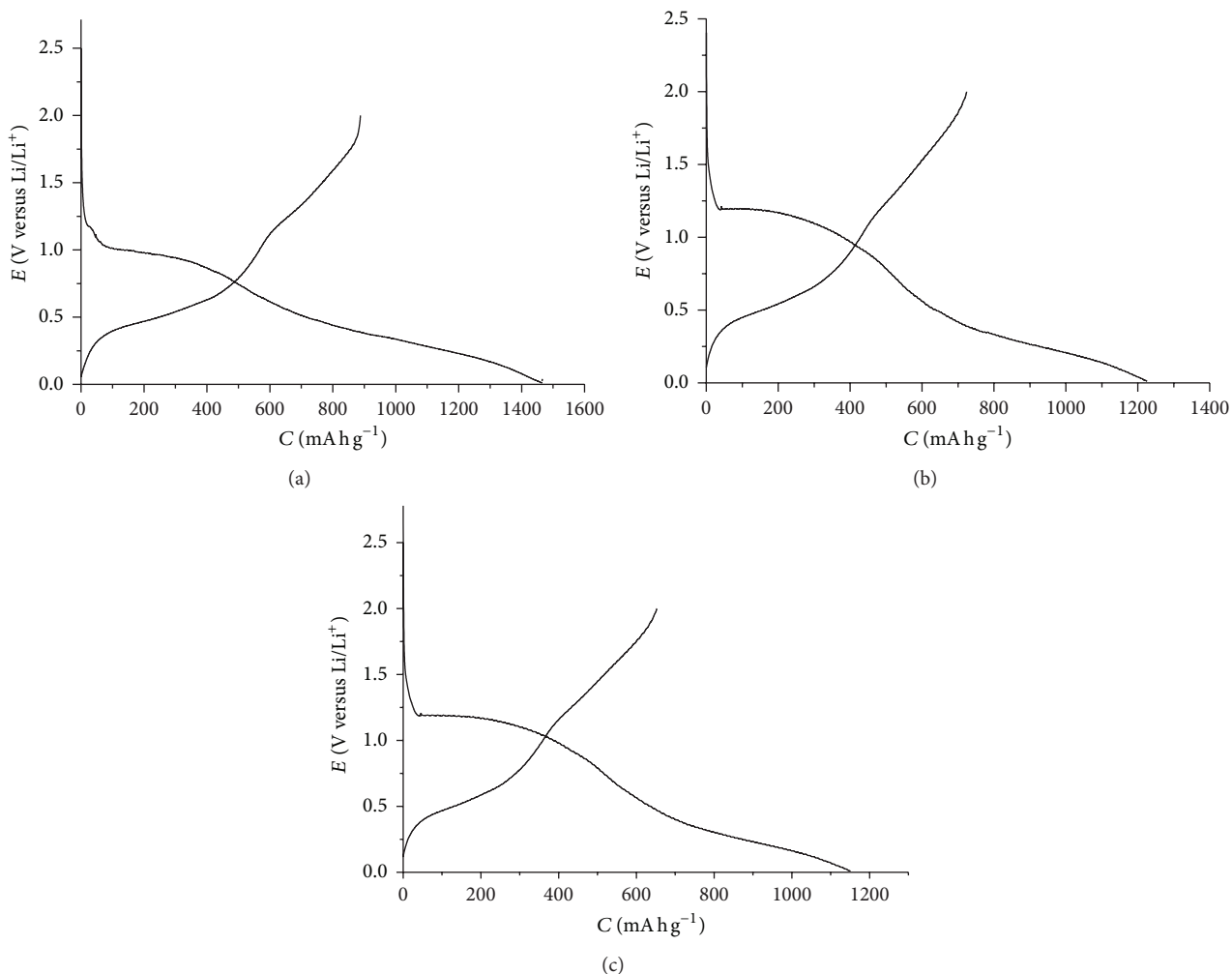


FIGURE 5: Initial charge-discharge curves of (a)  $\text{Sn}_{0.9}\text{Ti}_{0.1}\text{O}_2$ , (b)  $\text{Sn}_{0.7}\text{Ti}_{0.3}\text{O}_2$ , and (c)  $\text{Sn}_{0.4}\text{Ti}_{0.6}\text{O}_2$  solid solutions at the current density of  $50 \text{ mA g}^{-1}$  between 0.01 and 2 V.

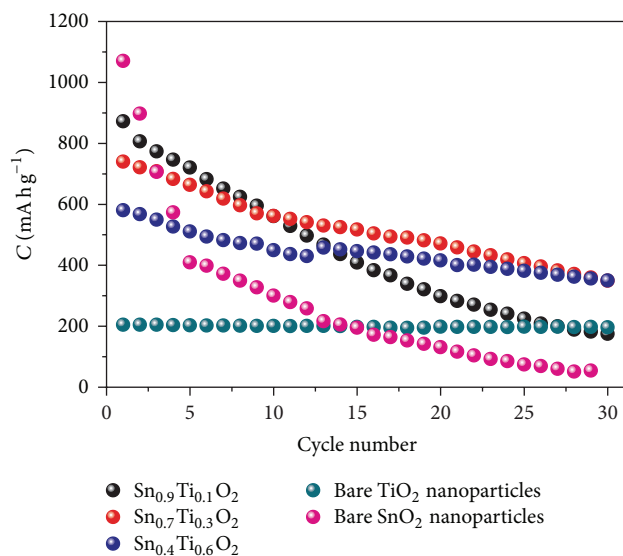


FIGURE 6: The capacity versus cycle number plots of  $\text{Sn}_{0.9}\text{Ti}_{0.1}\text{O}_2$ ,  $\text{Sn}_{0.7}\text{Ti}_{0.3}\text{O}_2$ , and  $\text{Sn}_{0.4}\text{Ti}_{0.6}\text{O}_2$  solid solutions at the current density of  $100 \text{ mA g}^{-1}$ .

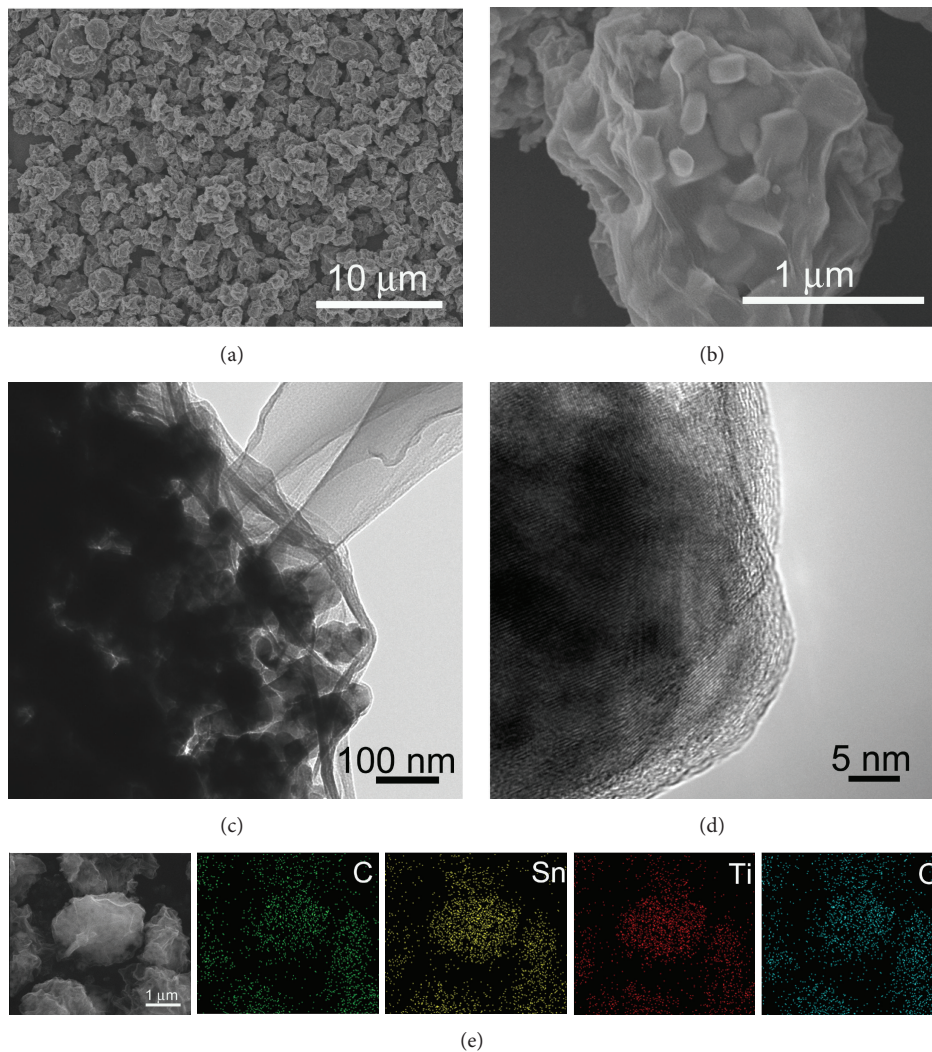


FIGURE 7: ((a), (b)) SEM images of  $\text{Sn}_{0.7}\text{Ti}_{0.3}\text{O}_2/\text{graphene}$  nanocomposite. (c) TEM image of  $\text{Sn}_{0.7}\text{Ti}_{0.3}\text{O}_2/\text{graphene}$  nanocomposite. (d) High-resolution TEM image of  $\text{Sn}_{0.7}\text{Ti}_{0.3}\text{O}_2/\text{graphene}$  nanocomposite. (e) SEM image and corresponding elemental map of  $\text{Sn}_{0.7}\text{Ti}_{0.3}\text{O}_2/\text{graphene}$  nanocomposite with green for C, red for Ti, yellow for Sn, and blue for O.

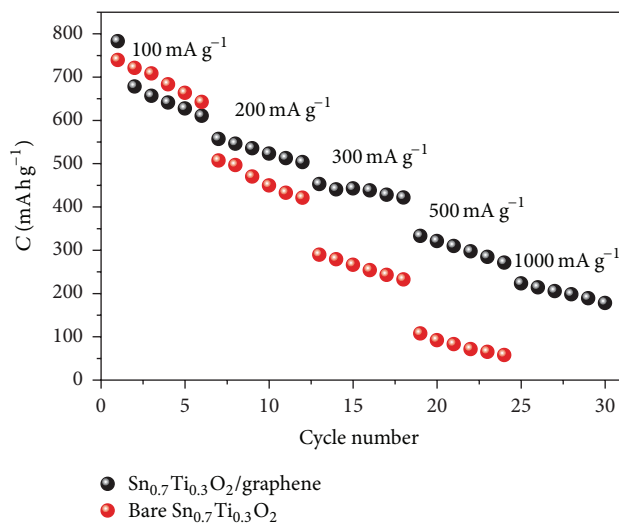


FIGURE 8: Rate capability of  $\text{Sn}_{0.7}\text{Ti}_{0.3}\text{O}_2/\text{graphene}$  nanocomposite and pure  $\text{Sn}_{0.7}\text{Ti}_{0.3}\text{O}_2$ . The charge and discharge rate was varied in the range from  $100 \text{ mA g}^{-1}$  to  $1000 \text{ mA g}^{-1}$ .

the reversible capacity of  $\text{Sn}_{0.7}\text{Ti}_{0.3}\text{O}_2/\text{graphene}$  nanocomposite and pure  $\text{Sn}_{0.7}\text{Ti}_{0.3}\text{O}_2$  were tested with variable current densities, as plotted in Figure 8. The reversible capacity of  $\text{Sn}_{0.7}\text{Ti}_{0.3}\text{O}_2/\text{graphene}$  maintains  $600 \text{ mAh g}^{-1}$  at a charge rate of  $100 \text{ mA g}^{-1}$ . Further increasing the charge rates to  $200 \text{ mA g}^{-1}$ ,  $300 \text{ mA g}^{-1}$ , and  $500 \text{ mA g}^{-1}$ , reversible capacities of  $550 \text{ mAh g}^{-1}$ ,  $470 \text{ mAh g}^{-1}$ , and  $330 \text{ mAh g}^{-1}$  can be obtained, respectively. Even at a high current density of  $1000 \text{ mA g}^{-1}$ , graphene modified solid solution can still deliver a reversible capacity of  $\sim 200 \text{ mAh g}^{-1}$ . In contrast to  $\text{Sn}_{0.7}\text{Ti}_{0.3}\text{O}_2/\text{graphene}$ ,  $\text{Sn}_{0.7}\text{Ti}_{0.3}\text{O}_2$  electrode shows much poorer rate-performance. At the initial six cycles under the current density of  $100 \text{ mA g}^{-1}$ , the charge capacity of  $\text{Sn}_{0.7}\text{Ti}_{0.3}\text{O}_2$  is slightly higher than that of  $\text{Sn}_{0.7}\text{Ti}_{0.3}\text{O}_2/\text{graphene}$ . However, as the current density increases, the capacity loss of the  $\text{Sn}_{0.7}\text{Ti}_{0.3}\text{O}_2$  was much larger than that of the  $\text{Sn}_{0.7}\text{Ti}_{0.3}\text{O}_2/\text{graphene}$ .  $\text{Sn}_{0.7}\text{Ti}_{0.3}\text{O}_2$  only delivers a capacity less than  $100 \text{ mAh g}^{-1}$  at a current density of  $500 \text{ mA g}^{-1}$ . The results strongly confirm that graphene conductive network can effectively improve the rate performance of the solid solution. Comparing to our previous works on the graphene modified  $\text{TiO}_2$  and  $\text{SnO}_2$  as anode materials for Li-ion battery, we could find that  $\text{Sn}_{0.7}\text{Ti}_{0.3}\text{O}_2/\text{graphene}$  presents much higher capacity than  $\text{TiO}_2/\text{graphene}$  [27, 30]. However, the cyclic life is not as high as  $\text{SnO}_2/\text{graphene}$ , which can be attributed to the large particle size of solid solution. Although more studies are required to further improve the coulombic efficiency and cyclic stability of  $\text{Sn}_{0.7}\text{Ti}_{0.3}\text{O}_2/\text{graphene}$  composite, we believe that it can be considered as a promising candidate for high-performance anode material in advanced LIBs.

#### 4. Conclusion

A series of  $\text{Sn}_x\text{Ti}_{1-x}\text{O}_2$  solid solutions were successfully prepared by sol-gel method. The electrochemical reaction of the  $\text{Sn}_x\text{Ti}_{1-x}\text{O}_2$  anode material is similar to that of  $\text{SnO}_2$ . The electrochemical performance of  $\text{Sn}_x\text{Ti}_{1-x}\text{O}_2$  is strongly affected by the ratio of Ti/Sn, which can be regarded as a gradual transition from that of  $\text{SnO}_2$  to  $\text{TiO}_2$  when the  $x$  value increases. At a suitable  $x$  value of 0.7, high specific capacity and good cycle stability can be achieved simultaneously, which make  $\text{Sn}_{0.7}\text{Ti}_{0.3}\text{O}_2$  a potential substitute anode material to  $\text{SnO}_2$  or  $\text{TiO}_2$ .  $\text{Sn}_{0.7}\text{Ti}_{0.3}\text{O}_2$  was further modified by graphene to enhance its electrical conductivity, which resulted in improved rate performance, indicating the potential application value of the solid solution as the anode material for Li-ion batteries.

#### Conflict of Interests

The authors declared that they have no conflict of interests to this work.

#### Acknowledgments

The authors are grateful for financial support from the Key Research Program of the Chinese Academy of Sciences

(Grant no. KGZD-EW-202-4), Projects 21201173 and 21371176 supported by the National Natural Science Foundation of China, Science and Technology Innovation Team of Ningbo (Grant no. 2012B82001), and the 973 Program (Grant no. 2011CB935900).

#### References

- [1] D. Deng and J. Y. Lee, "Hollow core-shell mesospheres of crystalline  $\text{SnO}_2$  nanoparticle aggregates for high capacity  $\text{Li}^+$  ion storage," *Chemistry of Materials*, vol. 20, no. 5, pp. 1841–1846, 2008.
- [2] J. Fan, T. Wang, C. Yu, B. Tu, Z. Jiang, and D. Zhao, "Ordered, nanostructured tin-based oxides/carbon composite as the negative-electrode material for lithium-ion batteries," *Advanced Materials*, vol. 16, no. 16, pp. 1387–1436, 2004.
- [3] Y. Wang, J. Y. Lee, and H. C. Zeng, "Polycrystalline  $\text{SnO}_2$  nanotubes prepared via infiltration casting of nanocrystallites and their electrochemical application," *Chemistry of Materials*, vol. 17, no. 15, pp. 3899–3903, 2005.
- [4] X. W. Lou, C. Yuan, and L. A. Archer, "Shell-by-shell synthesis of tin oxide hollow colloids with nanoarchitected walls: cavity size tuning and functionalization," *Small*, vol. 3, no. 2, pp. 261–265, 2007.
- [5] X. W. Lou, C. M. Li, and L. A. Archer, "Designed synthesis of coaxial  $\text{SnO}_2$ @carbon hollow nanospheres for highly reversible lithium storage," *Advanced Materials*, vol. 21, no. 24, pp. 2536–2539, 2009.
- [6] H. Kim and J. Cho, "Hard templating synthesis of mesoporous and nanowire  $\text{SnO}_2$  lithium battery anode materials," *Journal of Materials Chemistry*, vol. 18, no. 7, pp. 771–775, 2008.
- [7] Z. Wen, Q. Wang, Q. Zhang, and J. Li, "In situ growth of mesoporous  $\text{SnO}_2$  on multiwalled carbon nanotubes: a novel composite with porous-tube structure as anode for lithium batteries," *Advanced Functional Materials*, vol. 17, no. 15, pp. 2772–2778, 2007.
- [8] G. Derrien, J. Hassoun, S. Panero, and B. Scrosati, "Nanostructured Sn-C composite as an advanced anode material in high-performance lithium-ion batteries," *Advanced Materials*, vol. 19, no. 17, pp. 2336–2340, 2007.
- [9] M. S. Park, Y. M. Kang, J. H. Kim, G.-X. Wang, S.-X. Dou, and H.-K. Liu, "Effects of low-temperature carbon encapsulation on the electrochemical performance of  $\text{SnO}_2$  nanopowders," *Carbon*, vol. 46, no. 1, pp. 35–40, 2008.
- [10] F. Chen, Z. Shi, and M. Liu, "Preparation of mesoporous  $\text{SnO}_2$ - $\text{SiO}_2$  composite as electrodes for lithium batteries," *Chemical Communications*, vol. 21, pp. 2095–2096, 2000.
- [11] J. Zhu, Z. Lu, M. O. Oo et al., "Synergetic approach to achieve enhanced lithium ion storage performance in ternary phased  $\text{SnO}_2$ - $\text{Fe}_2\text{O}_3$ /rGO composite nanostructures," *Journal of Materials Chemistry*, vol. 21, no. 34, pp. 12770–12776, 2011.
- [12] Y. M. Lin, R. K. Nagarale, K. C. Klavetter, A. Heller, and C. B. Mullins, " $\text{SnO}_2$  and  $\text{TiO}_2$ -supported- $\text{SnO}_2$  lithium battery anodes with improved electrochemical performance," *Journal of Materials Chemistry*, vol. 22, no. 22, pp. 11134–11139, 2012.
- [13] Y.-Y. Wang, Y.-J. Hao, Q.-Y. Lai, J.-Z. Lu, Y.-D. Chen, and X.-Y. Ji, "A new composite material  $\text{Li}_4\text{Ti}_5\text{O}_{12}$ - $\text{SnO}_2$  for lithium-ion batteries," *Ionic*, vol. 14, no. 1, pp. 85–88, 2008.
- [14] D. Deng, M. G. Kim, J. Y. Lee, and J. Cho, "Green energy storage materials: nanostructured  $\text{TiO}_2$  and Sn-based anodes

- for lithium-ion batteries,” *Energy and Environmental Science*, vol. 2, no. 8, pp. 818–837, 2009.
- [15] J. Liu, J. S. Chen, X. Wei, X. W. Lou, and X.-W. Liu, “Sandwich-like, stacked ultrathin titanate nanosheets for ultrafast lithium storage,” *Advanced Materials*, vol. 23, no. 8, pp. 998–1002, 2011.
- [16] I. Moriguchi, R. Hidaka, H. Yamada, T. Kudo, H. Murakami, and N. Nakashima, “A mesoporous nanocomposite of  $\text{TiO}_2$  and carbon nanotubes as a high-rate Li-intercalation electrode material,” *Advanced Materials*, vol. 18, no. 1, pp. 69–73, 2006.
- [17] G. Du, Z. Guo, P. Zhang et al., “ $\text{SnO}_2$  nanocrystals on self-organized  $\text{TiO}_2$  nanotube array as three-dimensional electrode for lithium ion microbatteries,” *Journal of Materials Chemistry*, vol. 20, no. 27, pp. 5689–5694, 2010.
- [18] H. Uchiyama, E. Hosono, H. Zhou, and H. Imai, “Lithium insertion into nanometer-sized rutile-type  $\text{Ti}_x\text{Sn}_{1-x}\text{O}_2$  solid solutions,” *Solid State Ionics*, vol. 180, no. 14–16, pp. 956–960, 2009.
- [19] X. Zhou and Z. Liu, “A scalable, solution-phase processing route to graphene oxide and graphene ultralarge sheets,” *Chemical Communications*, vol. 46, no. 15, pp. 2611–2613, 2010.
- [20] Y. Luo, J. Luo, J. Jiang et al., “Seed-assisted synthesis of highly ordered  $\text{TiO}_2\alpha$ - $\text{Fe}_2\text{O}_3$  core/shell arrays on carbon textiles for lithium-ion battery applications,” *Energy and Environmental Science*, vol. 5, no. 4, pp. 6559–6566, 2012.
- [21] A. S. Sreekumaran Nair, Z. Peining, V. Jagadeesh Babu, Y. Shengyuan, P. Shengjie, and S. Ramakrishna, “Highly anisotropic titanates from electrospun  $\text{TiO}_2$ - $\text{SiO}_2$  composite nanofibers and rice grain-shaped nanostructures,” *RSC Advances*, vol. 2, no. 3, pp. 992–998, 2012.
- [22] S. Ding, D. Luan, F. Y. C. Boey, J. S. Chen, and X. W. Lou, “ $\text{SnO}_2$  nanosheets grown on graphene sheets with enhanced lithium storage properties,” *Chemical Communications*, vol. 47, no. 25, pp. 7155–7157, 2011.
- [23] Y.-S. Hu, L. Kienle, Y.-G. Guo, and J. Maier, “High lithium electroactivity of nanometer-sized rutile  $\text{TiO}_2$ ,” *Advanced Materials*, vol. 18, no. 11, pp. 1421–1426, 2006.
- [24] H. Bi, F. Huang, Y. Tang et al., “Study of  $\text{LiFePO}_4$  cathode modified by graphene sheets for high-performance lithium ion batteries,” *Electrochimica Acta*, vol. 88, pp. 414–420, 2013.
- [25] X. Zhou, F. Wang, Y. Zhu, and Z. Liu, “Graphene modified  $\text{LiFePO}_4$  cathode materials for high power lithium ion batteries,” *Journal of Materials Chemistry*, vol. 21, no. 10, pp. 3353–3358, 2011.
- [26] J. Yao, X. Shen, B. Wang, H. Liu, and G. Wang, “In situ chemical synthesis of  $\text{SnO}_2$ -graphene nanocomposite as anode materials for lithium-ion batteries,” *Electrochemistry Communications*, vol. 11, no. 10, pp. 1849–1852, 2009.
- [27] X. Wang, X. Zhou, K. Yao, J. Zhang, and Z. Liu, “A  $\text{SnO}_2$ /graphene composite as a high stability electrode for lithium ion batteries,” *Carbon*, vol. 49, no. 1, pp. 133–139, 2011.
- [28] P. Lian, X. Zhu, H. Xiang, Z. Li, W. Yang, and H. Wang, “Enhanced cycling performance of  $\text{Fe}_3\text{O}_4$ -graphene nanocomposite as an anode material for lithium-ion batteries,” *Electrochimica Acta*, vol. 56, no. 2, pp. 834–840, 2010.
- [29] W. Zhou, J. Zhu, C. Cheng et al., “A general strategy toward graphene@metal oxide core-shell nanostructures for high-performance lithium storage,” *Energy and Environmental Science*, vol. 4, no. 12, pp. 4954–4961, 2011.
- [30] X. Xin, X. Zhou, J. Wu, X. Yao, and Z. Liu, “Scalable synthesis of  $\text{TiO}_2$ /graphene nanostructured composite with high-rate performance for lithium ion batteries,” *ACS Nano*, vol. 6, no. 12, pp. 11035–11043, 2012.

## Research Article

# Superhydrophobic Polyimide via Ultraviolet Photooxidation: The Evolution of Surface Morphology and Hydrophobicity under Different Ultraviolet Intensities

Hongyu Gu,<sup>1,2</sup> Lixin Song,<sup>1</sup> Jinlin Zhang,<sup>1</sup> and Zhenyi Qi<sup>1</sup>

<sup>1</sup>Key Laboratory of Inorganic Coating Materials, Shanghai Institute of Ceramics, Chinese Academy of Sciences, 1295 Dingxi Road, Shanghai 200050, China

<sup>2</sup>University of Chinese Academy of Sciences, 19 Yuquan Road, Beijing 100049, China

Correspondence should be addressed to Lixin Song; [lxsong@mail.sic.ac.cn](mailto:lxsong@mail.sic.ac.cn) and Zhenyi Qi; [qzy@mail.sic.ac.cn](mailto:qzy@mail.sic.ac.cn)

Received 10 October 2014; Accepted 30 November 2014

Academic Editor: Yuanlie Yu

Copyright © 2015 Hongyu Gu et al. This is an open access article distributed under the Creative Commons Attribution License, which permits unrestricted use, distribution, and reproduction in any medium, provided the original work is properly cited.

Ultraviolet (UV) photooxidation has recently been developed to fabricate superhydrophobic polyimide (PI) films in combination with fluoroalkylsilane modification. However, it remains unclear whether the surface morphology and hydrophobicity are sensitive to technical parameters such as UV intensity and radiation environment. Herein, we focus on the effects of UV intensity on PI surface structure and wettability to gain comprehensive understanding and more effective control of this technology. Scanning electron microscopy (SEM) and atomic force microscopy (AFM) results showed that UV intensity governed the evolutionary pattern of surface morphology: lower UV intensity ( $5 \text{ mW/cm}^2$ ) facilitated in-plane expansion of dendritic protrusions while stronger UV ( $10$  and  $15 \text{ mW/cm}^2$ ) encouraged localized growth of protrusions in a piling-up manner. Surface roughness and hydrophobicity maximized at the intensity of  $10 \text{ mW/cm}^2$ , as a consequence of the slowed horizontal expansion and preferred vertical growth of the protrusions when UV intensity increased. Based on these results, the mechanism that surface micro/nanostructures developed in distinct ways when exposed to different UV intensities was proposed. Though superhydrophobicity (water contact angle larger than  $150^\circ$ ) can be achieved at UV intensity not less than  $10 \text{ mW/cm}^2$ , higher intensity decreased the effectiveness. Therefore, the UV photooxidation under  $10 \text{ mW/cm}^2$  for 72 h is recommended to fabricate superhydrophobic PI films.

## 1. Introduction

Superhydrophobic materials with water contact angle (WCA) above  $150^\circ$  have numerous potential applications such as in self-cleaning, antifrosting, anticorrosion, anti-icing, and drag reduction [1–3]. As a representative type, superhydrophobic polymers have attracted extensive interest in recent decades due to their low costs, light weight, flexibility, and ease of processing [4–6]. However, common polymers lack adequate stability against heat and tension, which seriously limits their applications in harsh environments [7]. Polyimide (PI), a widely used polymer, can avoid these drawbacks owing to its unique physical and chemical properties such as excellent thermal stability, high strength, and good chemical resistance [8–10]. Therefore, superhydrophobic PI would exhibit high

durability when applied in various extreme environments (e.g., space environment) [11, 12].

Superhydrophobic property is influenced by both surface energy and surface roughness [1]. Generally, WCA larger than  $120^\circ$  could only be obtained by altering the surface roughness [13]. However, PI surface is normally flat on the micron scale. Therefore, techniques including template [14–17], electrospinning [7, 18, 19], laser [11, 20], and plasma [21–23] are used to tailor surface morphology for superhydrophobic PI. Unfortunately, the complex operations, novel precursors, masks, or vacuum instruments involved usually limit the industrial fabrication. A facile strategy using ultraviolet (UV) photooxidation has been put forward by our group to fabricate micro/nanostructures on originally flat PI films. Then,

based on the proper surface morphology, superhydrophobic PI could be easily obtained by further 1H,1H,2H,2H-perfluorodecyltriethoxysilane (FAS) treatment. Being a dry process conducted under atmospheric environment, this UV photosensitized oxidation method possesses distinctive advantages compared with other techniques. The equipment investment and operating costs are relatively low, which would largely facilitate the large-scale production. In previous work [12], we have reported the preparation procedure and detailed characterization of the superhydrophobic PI films. UV photooxidation induced surface morphology was proven to be crucial to the wettability. However, it remains unclear whether the surface morphology and hydrophobicity are sensitive to technical parameters.

In this paper, the evolution of surface morphology and corresponding hydrophobicity under different UV intensities was studied to deeply understand the effects of UV intensity and better control the hydrophobicity of PI films.

## 2. Materials and Methods

**2.1. Materials.** Pyromellitic dianhydride-oxydianiline-type PI films (Kapton 100H,  $C_{22}H_{10}O_5N_2$ ) were obtained from Toray DuPont. 1H,1H,2H,2H-Perfluorodecyltriethoxysilane (FAS,  $C_{10}F_{17}H_4Si(OCH_2CH_3)_3$ , 97%) was supplied by Alfa Aesar. Ultrapure water was prepared using a Milli-Q-Plus system. Analytical grade ethanol (99.7%) was purchased from Sinopharm Chemical Reagent Co., Ltd. Prior to use, PI films were ultrasonically cleaned with purified water followed by ethanol and dried in an oven. Other chemicals were used as received.

**2.2. Fabrication of Hydrophobic PI.** In a typical process, the method was divided into two distinct procedures, that is, UV photooxidation and succedent fluoroalkylsilane modification (denoted by UV/FAS). UV photooxidation was conducted in air at ambient temperature in a cubic chamber ( $450 \times 450 \times 350 \text{ mm}^3$ ). The chamber was equipped with tubular mercury-quartz lamps ( $290 \text{ mm} \times 15 \text{ mm}$ , SunMonde) side-by-side emitting UV light at 254 and 185 nm. The output at 185 nm was equivalent to about 10% of that at 254 nm. During UV irradiation processes, rectangular PI films ( $30 \times 40 \text{ mm}^2$ ) were placed at different distances (ca. 8 mm, 25 mm, and 55 mm) from the lamps, where the intensities of the 254 nm UV light were measured to be 5, 10, and  $15 \text{ mW/cm}^2$ , respectively. The light at 185 nm attenuated quickly in air accompanied by dissociation of oxygen molecules into oxygen atoms. Here, we denoted the intensity of 254 nm UV light as the intensity of UV light for convenience. At each intensity, PI films were irradiated for 24, 48, 72, or 144 h in air at atmospheric environment. Fluoroalkylsilane modification was then carried out with FAS in heated reactors. Specifically, a few droplets (30–50  $\mu\text{L}$ ) of FAS were dispensed at the bottom of a Teflon container (200 mL) using a micro-adjustable pipette (720000, Dragon) while the UV-treated PI films were placed vertically in the Teflon container, which was further sealed in a stainless steel autoclave. The reactor was then annealed at  $120^\circ\text{C}$  for 2 h to enable the vapor of FAS to react with the modified PI films.

Finally, the samples were heated at  $150^\circ\text{C}$  for 3 h to volatilize unreacted FAS molecules.

**2.3. Characterization.** The morphology and element distribution were characterized by scanning electron microscopy (SEM) coupled with energy-dispersive X-ray spectroscopy (EDS) on an FEI Magellan 400 microscope. Before the examination, the surfaces of the samples were sputter-coated with a thin layer of Cd to prevent charging. For the EDS mappings, the colored spots corresponded to the presence of each element. The surface roughness was analyzed using an atomic force microscope (AFM) (Nanoscope V Multimode AFM System, Bruker) in tapping mode. The average AFM value was obtained at six different positions by measuring three samples. The static WCA was measured with 5  $\mu\text{L}$  water and the sliding angle was tested by 10  $\mu\text{L}$  water using a SL200B contact angle system (Solon Tech.) at ambient temperature. The average WCA value was obtained at six different positions by measuring three samples. The sliding angle was determined by slowly tilting the sample stage until the 10  $\mu\text{L}$  water droplet started moving. Meanwhile, a digital video camera was employed to take photographs at the rate of 1 frame/s.

## 3. Results and Discussion

**3.1. Surface Morphology.** The pristine PI films possessed a morphologically flat surface and could only be rendered slight hydrophobicity ( $\text{WCA} = 105.1^\circ$ ) after FAS modification. Further enhancement of hydrophobicity was proven to be feasible by constructing appropriate morphology through UV irradiation [12]. Therefore, investigations of the dependence of surface morphology and roughness on the UV treatment parameters would allow for rational control of the hydrophobicity. To this end, SEM in combination with AFM was used to study the evolution of surface morphology at different UV intensities (5, 10, and  $15 \text{ mW/cm}^2$ ). Note that samples with sequent UV exposure and FAS modification (denoted by UV/FAS-treated PI films hereafter) were used to analyze the morphological evolution, since the latter was proven to have no significant effect on the surface microstructure.

Figure 1 shows the surface microstructure of UV/FAS-treated PI when UV intensity was  $5 \text{ mW/cm}^2$  and irradiation period varied from 24 h to 144 h. As can be seen in Figure 1(a), 24 h of UV irradiation resulted in uniformly distributed nanoprotusions (in spherical or dendritic shape) and grooves on the PI surface. The protrusion areas gradually expanded and finally occupied most surface of the film as the exposure time prolonged (see Figures 1(a)–1(d)). This expansion, in fact, could be explained by the growth (in both width and length), interconnection, and final aggregation of the nanoprotusions, as clearly presented in the enlarged SEM images (Figures 1(e)–1(h)). Expansion of the dendritic protrusions along the in-plane directions can be regarded as a main characteristic of this type of growth mode. Consequently, the initial grooves (up to 200–300 nm in size) gradually diminished and were replaced by the narrow dendritic channels (less than 100 nm) in the end.

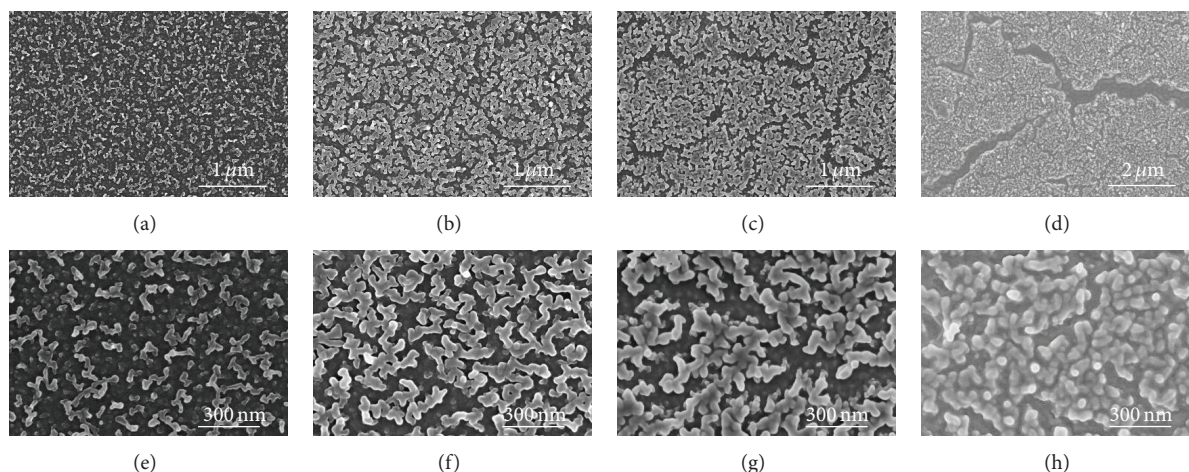


FIGURE 1: SEM images of the UV ( $5 \text{ mW/cm}^2$ )/FAS-treated PI films. The UV exposure periods are 24 h (a, e), 48 h (b, f), 72 h (c, g), and 144 h (d, h), respectively.

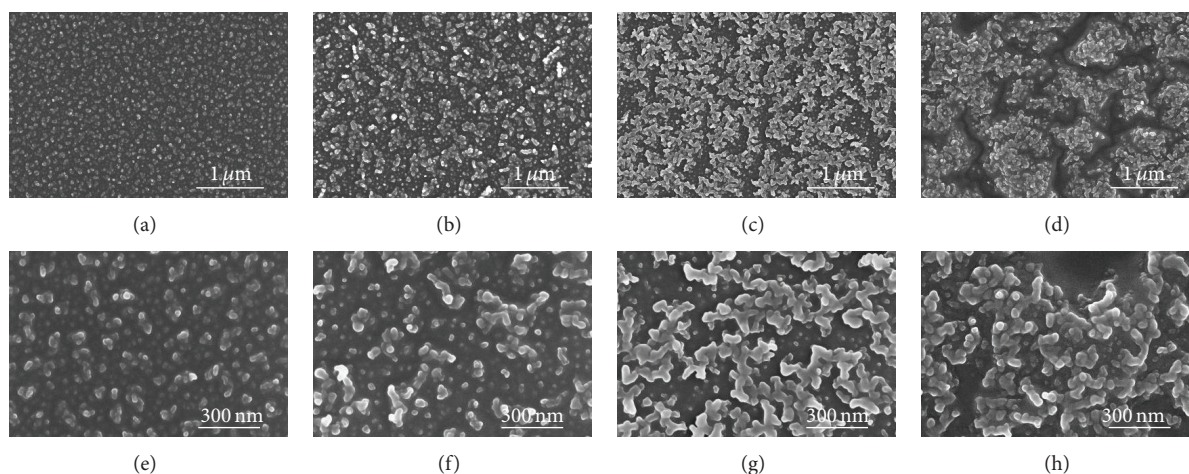


FIGURE 2: SEM images of UV ( $10 \text{ mW/cm}^2$ )/FAS-treated PI films. The UV treatment periods are 24 h (a, e), 48 h (b, f), 72 h (c, g), and 144 h (d, h), respectively.

It should be noted that many wide grooves (up to 900 nm) emerged (Figure 1(d)) on the 144 h irradiated films, separating the protrusion networks into micron-sized fragments. These wide grooves may be ascribed to the accumulated interfacial stress between the protrusions dominated surface and the underlying PI. In other words, the crack-like grooves formed as a manner to release the interfacial stress introduced by the newly formed micro/nanostructures. Overall,  $5 \text{ mW/cm}^2$  UV irradiation mainly benefits the in-plane expansion of nanoprotusions and tends to obtain PI films with protrusions densely distributing on the surface.

Figure 2 presents the SEM images of UV/FAS-treated PI films at the UV intensity of  $10 \text{ mW/cm}^2$ . The doubled UV intensity was supposed to significantly boost the evolution of the microstructure since higher concentration of active oxygen would be generated [24]. However, SEM images show that the growth of protrusions seemed to be suppressed from the very beginning compared with the  $5 \text{ mW/cm}^2$  irradiated

samples. During the first 24-hour irradiation, dense and uniform spherical nanoprotusions with dimension of ca. 50 nm in diameter formed on the surface and no dendritic protrusion was observed (Figure 2(e)). Instead of rapid growth and expansion in the horizontal direction, dendritic protrusions began to arise only after 48 h of exposure and became apparent until 72 h. The suppressed growth of protrusions (Figure 2(c)) resulted in larger area of channels compared to  $5 \text{ mW/cm}^2$  UV-treated films. As shown in Figures 2(d) and 2(h), further irradiation led to submicron or micron-sized islands that were piled up by the aggregated nanoprotusions and separated by evenly distributed channels (ca. 200–300 nm in width). Unlike in the case of  $5 \text{ mW/cm}^2$  UV exposure, wide grooves are not found on the surface, presumably due to the effective release of surface stress through the well-developed channels. In comparison, stronger UV irradiation tends to slow down the horizontal growth of the micro/nanostructures and form island-like nanoprotusion aggregates as well as well-developed channels in between.

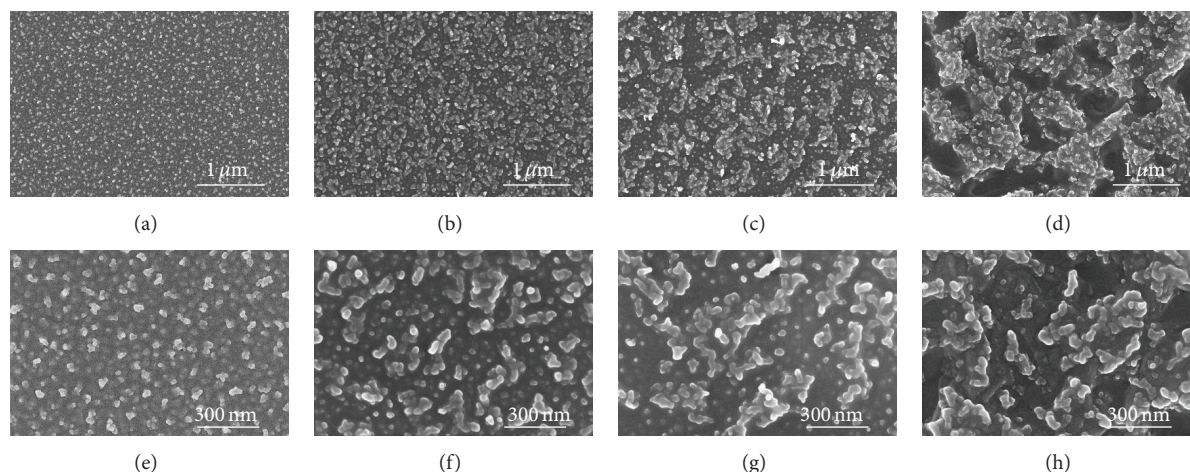


FIGURE 3: SEM images of UV ( $15 \text{ mW/cm}^2$ )/FAS-treated PI films. The UV treatment periods are 24 h (a, e), 48 h (b, f), 72 h (c, g), and 144 h (d, h), respectively.

To further confirm the effects of UV intensity on the evolution of the surface morphology, films treated under  $15 \text{ mW/cm}^2$  with various periods were investigated. As shown in Figure 3, the growth of protrusions, especially those in dendritic shape, became much slower when UV intensity increased from 10 to  $15 \text{ mW/cm}^2$ . Instead, localized growth of the spherical protrusions to the vertical direction of the surface dominated the whole evolution process, leading to the piling-up of the protrusions. The evolution of surface morphology at  $15 \text{ mW/cm}^2$  was similar to the polymer surface treated by Ar plasma with shorter exposure time to some extent [25]. In fact, this growth mode is also observed in the  $10 \text{ mW/cm}^2$  treated films but not as apparent. When the exposure time was extended to 144 h, interconnecting of the spherical and/or short protrusions also formed island-like aggregates owing to the vertical growth, but with much more and larger groove areas retained in between (Figures 3(d) and 3(h)) than those found in the 5 and  $10 \text{ mW/cm}^2$  UV-exposed films. Remarkably, grooves even possess an area nearly equal to that of the protrusion islands in this case.

Therefore, from the above discussion, it can be concluded that the evolution of micro/nanostructures on the surface was governed by distinct protrusion growth modes when UV intensity changed from 5 to  $15 \text{ mW/cm}^2$ . Increased UV irradiation suppressed the in-plane expansion of protrusions and facilitated the growth in the vertical direction, leading to different surface morphologies.

The evolution of protrusions in horizontal and vertical directions is expected to roughen the surface and thus affect the surface hydrophobicity. While SEM images allow visual assessment of the structural evolution mainly in the horizontal direction, quantified surface roughness values could reflect the growth of protrusions in both horizontal and vertical directions. Therefore, we measured surface roughness of the samples by means of AFM technique.

In Figure 4, root mean square surface roughness (RMS roughness) values at different UV intensities are plotted against the UV irradiation time. Overall, extended irradiation

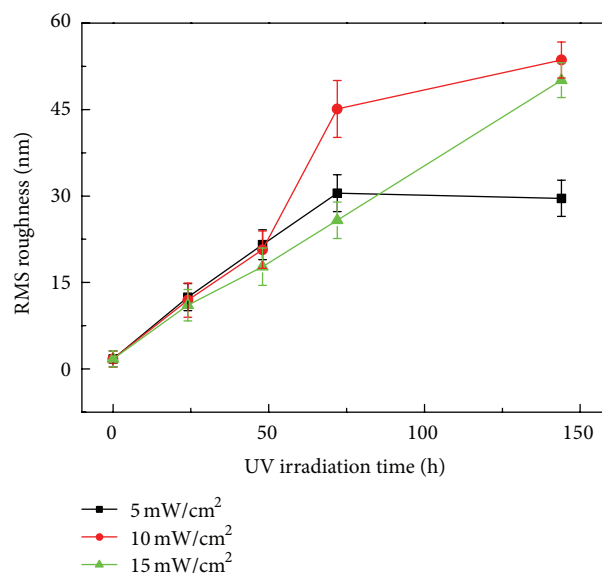


FIGURE 4: RMS roughness plotted against UV radiation time at different UV intensities.

under all UV intensities led to obviously rising trends of the RMS roughness. However, a turning point seemed to appear at 72 h for  $5 \text{ mW/cm}^2$  UV-treated samples. This turning point can be viewed as a result of the fast in-plane expansion of protrusions as described above. In other words, a proper proportion of grooves distributing among the protrusion networks were in favor of the surface roughening, but excessive in-plane expansion of the protrusion areas during the prolonged UV exposure would significantly diminish the groove areas and thus sacrifice the roughness. Then, combining the evolution of the protrusions and that of the grooves, we can speculate that the roughness at ca. 72 h (30.6 nm) was the maximum value that PI films could obtain under  $5 \text{ mW/cm}^2$  UV irradiation. However, this maximum

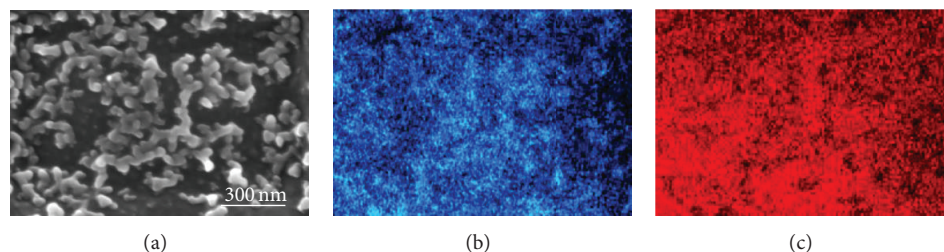


FIGURE 5: SEM image and corresponding EDS mappings of O (b) and C (c) of UV-treated PI (10 mW/cm<sup>2</sup>, 72 h). The images were taken at the same position of the sample at the same scale.

roughness was far surpassed by the samples with stronger UV irradiation. Obviously, this can hardly be explained by the suppressed expansion of protrusions in the horizontal directions. Considering the evolution of the microstructures under stronger UV (10 and 15 mW/cm<sup>2</sup>) irradiation described above, we assume that piling-up growth of protrusions in the vertical direction contributed to the surface roughening as well. The fact that roughness values of 10 mW/cm<sup>2</sup> UV-treated films were larger than those of any other samples also highlighted the combined effects of different protrusion growth modes.

To deepen the understanding of the protrusion evolution and the resultant surface roughness, we have tried to explain the effects of UV intensity from the perspectives of UV photooxidation. Figure 5 demonstrates a typical SEM image and corresponding EDS mappings showing the relation between elemental distributions and surface morphology after UV irradiation (10 mW/cm<sup>2</sup> for 72 h). As shown in Figure 5, protrusion areas are rich in O, yet poor in C. Given the fact that highly volatile and mobile low-molecular-weight (LMW) polymer chains would form as a result of the UV photooxidation induced chain scission [26], the protrusions are deemed to stem from the migration and redeposition of the oxidized polymer chains during UV irradiation [12]. Therefore, we think that UV intensity affected the protrusion evolution by changing the process of polymer chain scission and redeposition. Stronger UV irradiation would lead to higher photooxidation degree of polymer with shorter chains due to more concentrated active oxygen [24]. These oxidized polymers were more likely to volatilize and leave rather than redeposit on the surface, thus leading to the lower expansion rate of the protrusions. Another reason for the suppressed in-plane growth of the protrusions is the mismatch of interface energy between highly oxidized polymer chains and the newly formed PI surface, which was unfavorable for the redeposition on less oxidized areas, especially the groove areas. This can also explain why the protrusions preferred to grow in a piling-up mode when UV intensity increased.

**3.2. Hydrophobicity.** According to the Wenzel equation [27], surface roughening would further enhance the antiwetting capability if the smooth surface exhibits a hydrophobic nature. The hydrophobicity is strongly dependent on the RMS roughness of the surface. Therefore, it can be speculated that the hydrophobicity of the PI samples would change with the

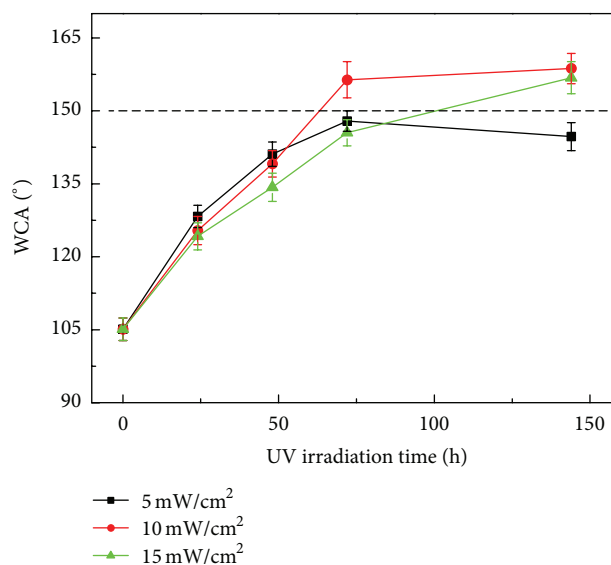


FIGURE 6: WCA plotted against UV radiation time at different UV intensities.

UV exposure period as well as UV intensity. To quantitatively confirm this relationship, WCA was used in this study to evaluate the hydrophobicity of the PI films.

The WCA against UV irradiation time at different UV intensities are plotted in Figure 6. The evolution of WCA is substantially consistent with the surface roughness in Figure 5. At the intensity of 5 mW/cm<sup>2</sup>, WCA increased from 105.1° to 148.1° with irradiation time extended from 0 h to 72 h and showed a relatively low hydrophobicity at 144 h with WCA of 144.7°. The WCA value of 5 mW/cm<sup>2</sup> at 144 h decreased as a result of the excessive in-plane expansion of the protrusion areas and the consequent surface roughness decrease as depicted in Figure 5. In contrast, the WCA increased continuously to 159.2° at the intensity of 10 mW/cm<sup>2</sup> and to 156.9° at 15 mW/cm<sup>2</sup> when UV exposure time was prolonged to 144 h. Eventually, superhydrophobic surfaces with WCA above 150° could be achieved after 72 h of irradiation at the intensity of 10 mW/cm<sup>2</sup> or after 144 h at 15 mW/cm<sup>2</sup>. As another important characteristic parameter, the sliding angle was further investigated for the superhydrophobic samples. As shown in Figure 7, water drops (10 μL) were found to readily roll off all the superhydrophobic PI

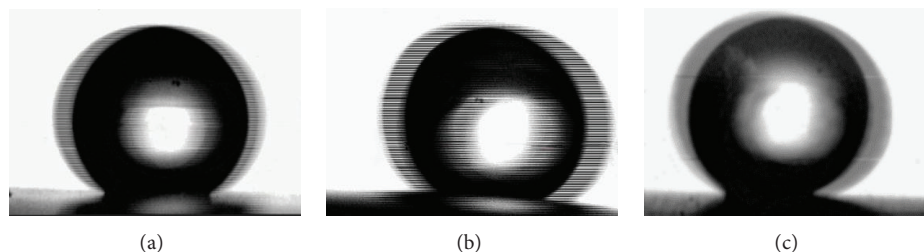


FIGURE 7: Water droplets ( $10\ \mu\text{L}$ ) sliding on slightly tilted surfaces. The UV treatment parameters are 72 h at  $10\ \text{mW}/\text{cm}^2$  (a), 144 h at  $10\ \text{mW}/\text{cm}^2$  (b), and 144 h at  $15\ \text{mW}/\text{cm}^2$  (c), respectively. These were critical images obtained by slowly tilting the sample stage until the  $10\ \mu\text{L}$  water droplet started moving using a digital video camera.

films with the tilted angle below  $5^\circ$ . These data strongly support that superhydrophobicity could be obtained by both  $10\ \text{mW}/\text{cm}^2$  and  $15\ \text{mW}/\text{cm}^2$  UV irradiation.

It should also be stressed that rational choosing of UV intensity is very important for the fabrication of superhydrophobic PI materials. Either too low or too high UV intensity is adverse to superhydrophobicity. In a relatively short period (72 h), a medium UV intensity of  $10\ \text{mW}/\text{cm}^2$  could afford the films WCA larger than  $150^\circ$  and sliding angle below  $5^\circ$ . In contrast,  $5\ \text{mW}/\text{cm}^2$  UV irradiation failed to achieve superhydrophobicity, and a longer time was proven to be required (up to 144 h) for  $15\ \text{mW}/\text{cm}^2$ . Considering the efficiency and costs, UV photooxidation under  $10\ \text{mW}/\text{cm}^2$  for 72 h is an optimized choice to obtain superhydrophobic PI films.

It is worth noting that the trend discussed above was different from the case in which laser ablation or plasma treatment was used to engineer the surface structures of polymers [20–22]. Generally, the surface roughness and hydrophobicity of PI surfaces treated by shaped laser increased when intensity or exposure time was enhanced [11, 20], which was quite different from the evolution modes of surface morphology and corresponding surface roughness when UV intensity increased in this work. The difference could be explained by different surface dynamics. Under UV irradiation of polymers in air, the polymer surfaces undergo chemical modification (photooxidation and induced hydrolysis) and induced degradation, crosslinking, and redeposition. Whereas for the laser ablation its energy is deposited in a short period, ablation dominated the morphological change while the crosslinking and redeposition could be neglected for laser-treated PI surfaces [28].

#### 4. Conclusions

In summary, we investigated the effects of UV intensity on the PI surface morphology and wetting performance, following the development of UV photooxidation as a method to prepare hydrophobic PI in combination with FAS modification. Surface morphology was found to present different evolutionary patterns against UV irradiation time when UV intensity varied.  $5\ \text{mW}/\text{cm}^2$  UV intensity facilitated in-plane expansion of dendritic protrusions while 10 and  $15\ \text{mW}/\text{cm}^2$  UV intensity encouraged localized growth of protrusions in

a piling-up manner. Surface roughness and hydrophobicity maximized at the intensity of  $10\ \text{mW}/\text{cm}^2$ . The mechanism that enhanced degree of photooxidation under stronger UV intensity suppressed the horizontal expansion and boosted the preferred vertical growth of protrusions was proposed to explain the changes in evolutionary patterns of surface structure. Though superhydrophobicity (WCA larger than  $150^\circ$ ) can be achieved at UV intensity not less than  $10\ \text{mW}/\text{cm}^2$ , a longer time was proven to be required (up to 144 h for  $15\ \text{mW}/\text{cm}^2$ ). Considering the efficiency and costs, UV photooxidation under  $10\ \text{mW}/\text{cm}^2$  for 72 h is an optimized choice to obtain superhydrophobic PI films. We expect that this work would further promote the application of UV method in hydrophobicity control of PI materials.

#### Conflict of Interests

The authors declare that there is no conflict of interests regarding the publication of this paper.

#### References

- [1] K. Liu, Y. Tian, and L. Jiang, “Bio-inspired superoleophobic and smart materials: design, fabrication, and application,” *Progress in Materials Science*, vol. 58, no. 4, pp. 503–564, 2013.
- [2] K. Liu and L. Jiang, “Bio-inspired self-cleaning surfaces,” *Annual Review of Materials Research*, vol. 42, pp. 231–263, 2012.
- [3] H. Li, M. Qu, Z. Sun, J. He, and A. Zhou, “Facile fabrication of a hierarchical superhydrophobic coating with aluminate coupling agent modified kaolin,” *Journal of Nanomaterials*, vol. 2013, Article ID 497216, 5 pages, 2013.
- [4] T. Darmanin, E. T. de Givenchy, S. Amigoni, and F. Guittard, “Superhydrophobic surfaces by electrochemical processes,” *Advanced Materials*, vol. 25, no. 10, pp. 1378–1394, 2013.
- [5] M. Wolfs, T. Darmanin, and F. Guittard, “Superhydrophobic fibrous polymers,” *Polymer Reviews*, vol. 53, no. 3, pp. 460–505, 2013.
- [6] N. Wang, F. Guo, J. Wu, Y. Zhao, and L. Jiang, “Variable responsive wettability films via electrospinning induced by solvents,” *Journal of Nanomaterials*, vol. 2014, Article ID 817418, 7 pages, 2014.
- [7] G. Gong, J. Wu, J. Liu, N. Sun, Y. Zhao, and L. Jiang, “Bio-inspired adhesive superhydrophobic polyimide mat with high thermal stability,” *Journal of Materials Chemistry*, vol. 22, no. 17, pp. 8257–8262, 2012.

- [8] M. K. Ghosh and K. L. Mittal, *Polyimides: Fundamentals and Applications*, CRC Press, 1996.
- [9] Y. Zhu, P. Zhao, X. Cai, W.-D. Meng, and F.-L. Qing, "Synthesis and characterization of novel fluorinated polyimides derived from bis[4-(4'-aminophenoxy)phenyl]-3,5-bis(trifluoromethyl)phenyl phosphine oxide," *Polymer*, vol. 48, no. 11, pp. 3116–3124, 2007.
- [10] S. Mu, D. Wu, S. Qi, and Z. Wu, "Preparation of polyimide/Zinc oxide nanocomposite films via an ion-exchange technique and their photoluminescence properties," *Journal of Nanomaterials*, vol. 2011, Article ID 950832, 10 pages, 2011.
- [11] C. J. Wohl, M. A. Belcher, L. Chen, and J. W. Connell, "Laser ablative patterning of copoly(imide siloxane)s generating superhydrophobic surfaces," *Langmuir*, vol. 26, no. 13, pp. 11469–11478, 2010.
- [12] H. Y. Gu, Z. Y. Qi, W. Wu, Y. Zeng, and L. X. Song, "Superhydrophobic polyimide films with high thermal endurance via UV photo-oxidation," *Express Polymer Letters*, vol. 8, no. 8, pp. 588–595, 2014.
- [13] T. Nishino, M. Meguro, K. Nakamae, M. Matsushita, and Y. Ueda, "The lowest surface free energy based on -CF<sub>3</sub> alignment," *Langmuir*, vol. 15, no. 13, pp. 4321–4323, 1999.
- [14] K.-C. Chang, H.-I. Lu, C.-W. Peng et al., "Nanocasting technique to prepare lotus-leaf-like superhydrophobic electroactive polyimide as advanced anticorrosive coatings," *ACS Applied Materials & Interfaces*, vol. 5, no. 4, pp. 1460–1467, 2013.
- [15] Y. Zhao, M. Li, Q. Lu, and Z. Shi, "Superhydrophobic polyimide films with a hierarchical topography: combined replica molding and layer-by-layer assembly," *Langmuir*, vol. 24, no. 21, pp. 12651–12657, 2008.
- [16] S. Zhu, Y. Li, J. Zhang et al., "Biomimetic polyimide nanotube arrays with slippery or sticky superhydrophobicity," *Journal of Colloid and Interface Science*, vol. 344, no. 2, pp. 541–546, 2010.
- [17] K. Liu, J. Du, J. Wu, and L. Jiang, "Superhydrophobic gecko feet with high adhesive forces towards water and their bio-inspired materials," *Nanoscale*, vol. 4, no. 3, pp. 768–772, 2012.
- [18] C.-J. Weng, Y.-S. Jhuo, C.-H. Chang et al., "A smart surface prepared using the switchable superhydrophobicity of neat electrospun intrinsically electroactive polyimide fiber mats," *Soft Matter*, vol. 7, no. 21, pp. 10313–10318, 2011.
- [19] J. Y. Park, K. O. Oh, J. C. Won, H. Han, H. M. Jung, and Y. S. Kim, "Facile fabrication of superhydrophobic coatings with polyimide particles using a reactive electro spraying process," *Journal of Materials Chemistry*, vol. 22, no. 31, pp. 16005–16010, 2012.
- [20] V. Oliveira, B. Nunes, and R. Vilar, "Wetting response of KrF laser ablated polyimide surfaces," *Nuclear Instruments and Methods in Physics Research, Section B: Beam Interactions with Materials and Atoms*, vol. 268, no. 10, pp. 1626–1630, 2010.
- [21] G. Scheen, K. Ziouche, Z. Bougrioua, P. Godts, D. Leclercq, and T. Lasri, "Simultaneous fabrication of superhydrophobic and superhydrophilic polyimide surfaces with low hysteresis," *Langmuir*, vol. 27, no. 10, pp. 6490–6495, 2011.
- [22] H. C. Barshilia, A. Ananth, N. Gupta, and C. Anandan, "Superhydrophobic nanostructured Kapton surfaces fabricated through Ar + O<sub>2</sub> plasma treatment: effects of different environments on wetting behaviour," *Applied Surface Science*, vol. 268, pp. 464–471, 2013.
- [23] C. J. Wohl, M. A. Belcher, S. Ghose, and J. W. Connell, "Modification of the surface properties of polyimide films using polyhedral oligomeric silsesquioxane deposition and oxygen plasma exposure," *Applied Surface Science*, vol. 255, no. 18, pp. 8135–8144, 2009.
- [24] M. L. Sham, J. Li, P. C. Ma, and J.-K. Kim, "Cleaning and functionalization of polymer surfaces and nanoscale carbon fillers by uv/ozone treatment: a review," *Journal of Composite Materials*, vol. 43, no. 14, pp. 1537–1564, 2009.
- [25] J. Yun, T.-S. Bae, J.-D. Kwon, S. Lee, and G.-H. Lee, "Antireflective silica nanoparticle array directly deposited on flexible polymer substrates by chemical vapor deposition," *Nanoscale*, vol. 4, no. 22, pp. 7221–7230, 2012.
- [26] U. Sener, B. Parekh, A. Entenberg, T. Debies, and G. A. Takacs, "Surface modification of poly(biphenyl dianhydride-para-phenylene diamine) (BPDA-PDA) polyimide by UV photo-oxidation," *Journal of Adhesion Science and Technology*, vol. 20, no. 4, pp. 319–334, 2006.
- [27] R. N. Wenzel, "Resistance of solid surfaces to wetting by water," *Industrial & Engineering Chemistry*, vol. 28, no. 8, pp. 988–994, 1936.
- [28] H. Hiraoka and S. Lazare, "Surface modifications of Kapton and cured polyimide films by ArF excimer laser: applications to imagewise wetting and metallization," *Applied Surface Science*, vol. 46, no. 1–4, pp. 264–271, 1990.

## Research Article

# Surface Morphology and Growth of Anodic Titania Nanotubes Films: Photoelectrochemical Water Splitting Studies

**Chin Wei Lai**

*Nanotechnology & Catalysis Research Centre (NANOCAT), Institute of Postgraduate Studies (IPS), University of Malaya, 3rd Floor, Block A, 50603 Kuala Lumpur, Malaysia*

Correspondence should be addressed to Chin Wei Lai; [cwlai@um.edu.my](mailto:cwlai@um.edu.my)

Received 29 September 2014; Revised 23 November 2014; Accepted 19 June 2015

Academic Editor: Jinmei He

Copyright © 2015 Chin Wei Lai. This is an open access article distributed under the Creative Commons Attribution License, which permits unrestricted use, distribution, and reproduction in any medium, provided the original work is properly cited.

Design and development of one-dimensional nanoarchitecture titania (TiO) assemblies have gained significant scientific interest, which have become the most studied material as they exhibit promising functional properties. In the present study, anodic TiO<sub>2</sub> films with different surface morphologies can be synthesized in an organic electrolyte of ethylene glycol (EG) by controlling an optimum content of ammonium fluoride (NH<sub>4</sub>F) using electrochemical anodization technique. Based on the results obtained, well-aligned and bundle-free TiO<sub>2</sub> nanotube arrays with diameter of 100 nm and length of 8 μm were successfully synthesized in EG electrolyte containing ≈5 wt% of NH<sub>4</sub>F for 1 h at 60 V. However, formation of nanoporous structure and compact oxide layer would be favored if the content of NH<sub>4</sub>F was less than 5 wt%. In the photoelectrochemical (PEC) water splitting studies, well-aligned TiO<sub>2</sub> nanotubular structure exhibited higher photocurrent density of ≈1 mA/cm<sup>2</sup> with photoconversion efficiency of ≈2% as compared to the nanoporous and compact oxide layer due to the higher active surface area for the photon absorption to generate more photo-induced electrons during photoexcitation stage.

## 1. Introduction

At present, one of the crucial steps taken by many countries to aid our mother earth [1–3] and minimizing environmental problems is applying sustainable development [4–8]. It seems that sustainable development to create an alternative clean and renewable energy [3, 5] to sustain the present level of population and economic development is a strategic goal of modern society reflecting contemporary demand for economic, social, political, and environmental development [9, 10]. To date, hydrogen (H<sub>2</sub>) has been established as a potential future energy carrier [7–9] and possibly the best substitute for fossil fuel to secure the future supply of a clean and sustainable energy [11–14]. This probable supply of energy in the future is by trapping the solar energy to split the water into hydrogen and oxygen gases within a PEC water splitting cell [10–16]. The controlled reaction of hydrogen and oxygen gases within a fuel cell will generate electricity [17–19]. However, the cost effective generation of H<sub>2</sub> with sunlight via water splitting process is a critical breakthrough needed

to transition to a renewable energy based hydrogen economy [14–16].

In fact, a suitable candidate as a photoelectrode for H<sub>2</sub> production via water splitting process must have three basic criteria as shown below [7, 8].

(i) *Stability*. The semiconductor must be photochemically stable in aqueous solution, in which it will not be photocorroded during the water splitting process.

(ii) *Band Gap*. The semiconductor must have a band gap of about 1.7–2.0 eV considering the overpotential losses and energy required for water splitting process.

(iii) *Energy Level*. For spontaneous water splitting process, the oxidation and reduction potential must lie between the valence and conduction band edges of the semiconductor.

Since 1972, PEC water splitting using TiO<sub>2</sub> as photoelectrode was successfully reported by Fujishima and Honda [4, 5]. Since then, TiO<sub>2</sub> has been extensively used as an efficient

photoelectrode in PEC water splitting system for  $H_2$  generation [11–16] because of its unique characteristics, such as high active surface area, strong oxidation ability, active at room temperature, outstanding charge transport property, and high stability against corrosion [20, 21]. This breakthrough has triggered the subsequent interests in photocatalysis research by scientists and researchers from all over the world on  $TiO_2$  and made  $TiO_2$  an important component in photocatalysis field [6, 7]. However, bundling problem (disorder arrangement of nanotube arrays) and weak adherence of the nanotubes on Ti substrate remains as a great challenge for synthesizing high quality of one-dimensional (1D)  $TiO_2$  nanotubes film [12–16]. Thus, considerable efforts have been conducted to the development of more efficient photoanode materials, especially well-aligned and ordered arrangement of 1D  $TiO_2$  nanotubes [20–22]. Nowadays, synthesis of  $TiO_2$  nanostructures can be achieved by various approaches, such as sol-gel methods [23–25], hydrothermal synthesis [26–28], and anodization technique [22, 29, 30]. Among all of these methods, electrochemical anodization technique has been seen as an effective and economical way in the formation of well-aligned  $TiO_2$  nanotubes [31–34]. Moreover, anodization technique is relatively simple and can be adopted for large-scale industrial production for creating self-organized anodic oxides in the form of nanotubular structures with almost perfect vertical alignment.

In order to obtain the right dimensions and morphologies, a controlled synthesis procedure for the production of well-aligned and ordered arrangement of 1D  $TiO_2$  nanotubes must be investigated and optimized [35–37]. In principles, three different morphologies of Ti anodic oxide layer could be achieved via anodization technique, which are compact oxide layer, nanoporous structure, and self-organized nanotube arrays [38, 39]. The most important point ought to be mentioned is that anodization technique is a versatile technique to form self-organized nanotubular thin film with controllable dimension, such as tubular's diameter, length, and wall thickness [35–40]. Therefore, well understanding regarding the formation of highly ordered and bundle-free nanotubular structure on anodized Ti surface is important in order to obtain the right dimensions and morphologies in PEC water splitting studies. In this work, a study has been performed to evaluate the morphology of the anodized Ti foil in different contents of  $NH_4F$  and determine the best morphology for high efficient PEC water splitting performance.

## 2. Experimental Procedure

Ti foil (99.7% purity) with a thickness of 127  $\mu m$  from STREM Chemicals, USA, was selected in this experimental work. Before the anodization process was conducted, Ti foils were degreased by sonication in ethanol for 30 minutes. Then, Ti foils were rinsed in deionised water and dried in a nitrogen stream. Next, anodization process was conducted in a two-electrode configuration bath, where Ti foil served as anode and the platinum foil served as counter electrode. The anodic oxidation was conducted in EG electrolyte containing 5 wt% of  $H_2O_2$  with different amounts of  $NH_4F$  (1 wt%, 3 wt%, and

5 wt%) for 1 hour at a constant potential of 60 V. In the present study,  $H_2O_2$  was maintained at 5 wt% and applied potential was fixed at 60 V because smooth and highly ordered nanotubes arrays could be synthesized when they are maintained around this value according to our preliminary study [29, 41]. The current density transient was recorded using a computerized Keithley DC Power Supply. The sweep rate was maintained at 1 V/min. After the anodization process, the anodic samples were cleaned using acetone and dried in nitrogen stream. The as-prepared anodic samples were then annealed for 4 h at 400°C in argon atmosphere. It was anticipated that the formation of the single crystalline anatase phase would result in enhanced PEC performance [37, 42].

The morphologies of the  $TiO_2$  nanotubes were characterized through field emission scanning electron microscopy (FESEM) using a Zeiss SUPRA 35 VP at working distances down to 10 mm. To obtain the thickness of the nanotube layer, cross-sectional measurements were carried out on mechanically bent samples. The actual length of the nanotube arrays was fixed on a 45° sample stage to view the cross-sectional morphologies. Then, actual length was determined by dividing the observed length by  $\cos 45^\circ$ . The PEC water splitting properties of the samples were characterized using a three-electrode PEC water splitting cell with  $TiO_2$  nanotube arrays as the working photoelectrode, platinum rod as the counter electrode, and saturated calomel electrode (SCE) as the reference electrode. A solution of 1 M KOH with addition of 1 wt% of EG was used as the electrolyte in the PEC cell. In this study, ethylene glycol was used as sacrificial agent to reduce electron-hole recombination losses, which could improve the photocurrent density [7]. All three electrodes were connected to a potentiostat ( $\mu$ Autolab III). A 150 W xenon lamp (Zolix LSP-X150) with an intensity of 800  $W/m^2$  was used to produce a largely continuous and uniform spectrum. The light was transmitted by the quartz glass as the xenon lamp shone on the working electrode (photoanode). The xenon lamp was switched on after the three electrodes were connected to the potentiostat and the photocurrent was measured during the voltage sweeping (5 mV/s).

## 3. Results and Discussion

An optimum content of  $NH_4F$  has significant influence on the morphology of anodic  $TiO_2$  nanotubes film. Figure 1 shows FESEM images of the surface of the anodized Ti foils formed in EG electrolyte containing 5 wt% of  $H_2O_2$  with different contents of  $NH_4F$  from 1 wt% to 5 wt%. The insets are the cross-sectional morphology of the oxide layers. From those FESEM images, the morphology of the Ti anodic oxides was dependent on the contents of  $NH_4F$  in the electrolyte. Anodization of Ti foil in a bath containing 1 wt%  $NH_4F$  resulted in a thin  $TiO_2$  compact oxide layer with small random pits on the surface of Ti foil as shown in Figure 1(a). The overall thickness of the oxide is approximately 500 nm. This result indicates that a low fluoride ( $F^-$ ) concentration can only form small pits over the  $TiO_2$  foil. The reason is attributed to the inactive chemical dissolution reaction, which is induced by the low content of  $F^-$  ions.

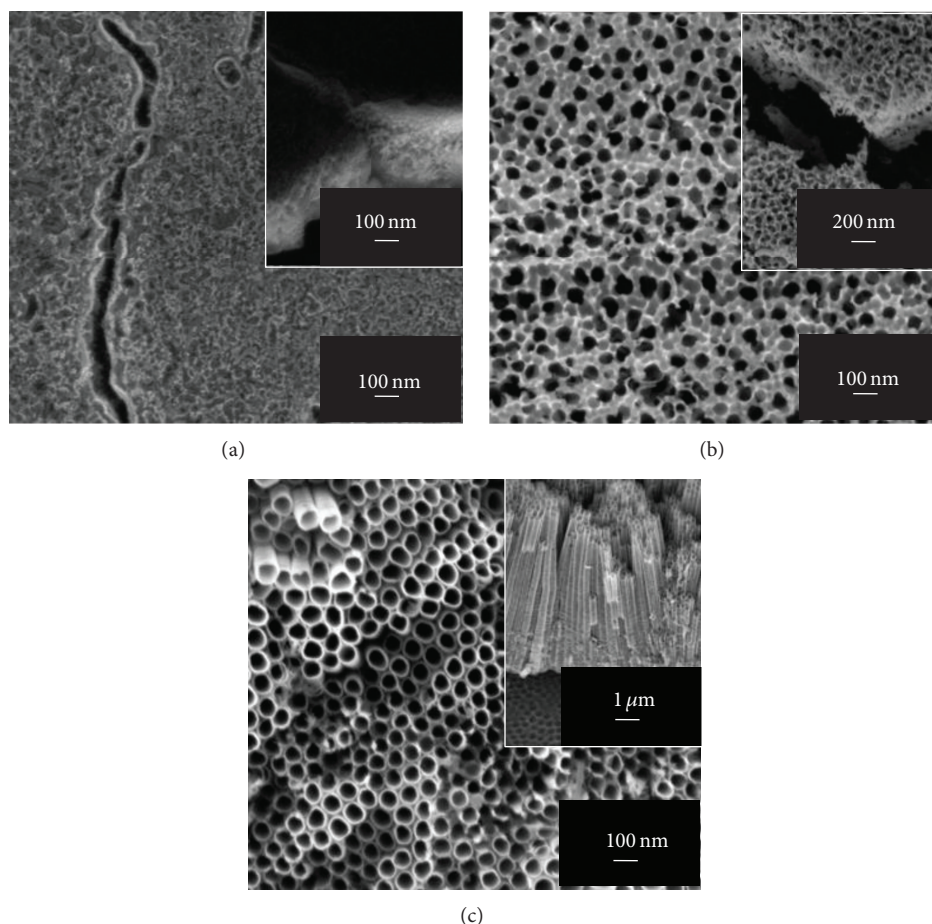
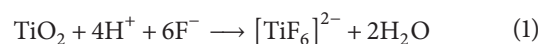


FIGURE 1: FESEM images of the  $\text{TiO}_2$  anodic oxide film anodized at 60 V for 1 h in EG electrolyte containing 5 wt% of  $\text{H}_2\text{O}_2$  and different contents of  $\text{NH}_4\text{F}$ , (a) 1 wt%, (b) 3 wt%, and (c) 5 wt%.

When the amount of  $\text{NH}_4\text{F}$  in the electrolyte was increased to 3 wt%, Ti surface contained irregular features and a porous oxide instead of ordered nanopores was observed (Figure 1(b)). The irregular pore sizes are in the range of 25 nm–100 nm and the thickness of this porous oxide layer is approximately 800 nm. The insufficient  $\text{F}^-$  content in the electrolyte probably caused incomplete chemical dissolution and oxidation at the interface between Ti and the barrier layer. Thus, the irregular features and nanoporous oxide layer formed. For the 5 wt%  $\text{NH}_4\text{F}$ , self-organized and well-aligned  $\text{TiO}_2$  nanotube arrays were successfully synthesized. This indicates that sufficient  $\text{F}^-$  content is able to increase the chemical dissolution reaction during electrochemical anodization process. This led to further acidification to develop a nanotube structure, as shown in Figure 1(c). The  $\text{TiO}_2$  nanotube arrays with diameters of approximately 100 nm and lengths of 8  $\mu\text{m}$  were formed when the  $\text{F}^-$  concentration was increased up to 5 wt%. Based on the results obtained,  $\text{NH}_4\text{F}$  plays an important role in the formation of the nanotubular structure of Ti anodic oxide films and an optimum  $\text{F}^-$  content was identified as  $\approx 5$  wt% in the EG electrolyte in order to synthesize well-aligned nanotube arrays.

A simple schematic illustration explaining the  $\text{TiO}_2$  nanotube arrays formation is exhibited in Figure 2. First of all, an oxide layer was formed on Ti surface and then turned into  $\text{TiO}_2$  due to the electrochemical oxidation process [43, 44]. In the presence of  $\text{F}^-$  ions, the oxide layer dissolves locally and small pits are formed on the oxide layer (Figure 2(a)). These random pits react with the  $\text{F}^-$  ions to produce  $[\text{TiF}_6]^{2-}$  complex ions as shown in the following [43–45]:



The porous structure is formed as a result of the localized chemical dissolution of the oxide by  $[\text{TiF}_6]^{2-}$  complex ions during electrochemical anodization process (Figure 2(b)) [34]. The chemical dissolution reduces the thickness of the oxide layers and allows electrochemical etching process to continue at the bottom of the pits [44, 46]. Meanwhile, the high applied potential during anodization process will lead to the field-assisted dissolution, where Ti metal ions ( $\text{Ti}^{4+}$ ) dissolve into electrolyte. The growth of pores is due to the competition between electrochemical oxide formation and chemical dissolution by sufficient content of  $\text{F}^-$  ions [43–47]. Finally, the nanotube structure will grow inwards

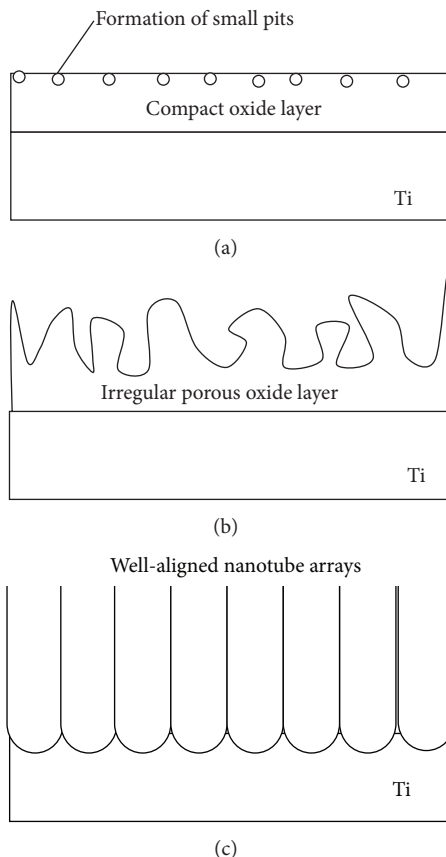


FIGURE 2: Schematic illustration explaining the  $\text{TiO}_2$  nanotube arrays formation: (a) growth of compact oxide layer and small pits formation; (b) growth of irregular porous oxide layer; and (c) well-aligned nanotube arrays.

(Figure 2(c)). In summary, formation of  $\text{TiO}_2$  nanotube arrays in fluorinated electrolyte was the result of three simultaneously occurring processes: (1) field-assisted oxidation of Ti metal to form  $\text{TiO}_2$ , (2) field-assisted dissolution of  $\text{Ti}^{4+}$  ions into electrolyte, and (3) chemical dissolution of Ti and  $\text{TiO}_2$  in the presence of  $\text{F}^-$  ions [38, 39]. From the results obtained, it could be concluded that optimum amount of  $\text{NH}_4\text{F}$  is one of the important factors for the formation of well-aligned  $\text{TiO}_2$  nanotubes.

The difference in morphology of the  $\text{TiO}_2$  nanotube arrays under different amounts of  $\text{NH}_4\text{F}$  can be explained by referring to the current density profile, as shown in Figure 3. It was found that current density increased up to  $7.8 \text{ mA/cm}^2$  when increasing the  $\text{NH}_4\text{F}$  up to 5 wt% (Figure 3(c)). The reason is attributed to the high diffusivity of the  $\text{F}^-$  ions concentration in the electrolyte, which led to enhanced conductivity of the solution [48, 49]. The higher current density in the electrolyte indicates that the higher chemical etching process induces by the  $[\text{TiF}_6]^{2-}$  complex ions [50].

In order to evaluate the effect of the various morphologies of anodic  $\text{TiO}_2$  layer on the PEC water splitting performance, the above-discussed samples were used as photoelectrode in

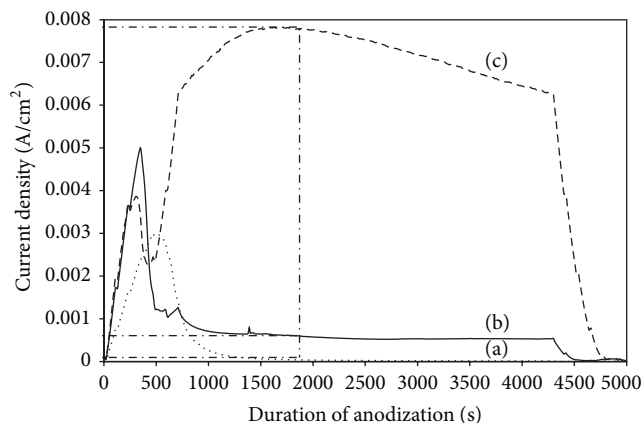


FIGURE 3: The current density-time behavior during the anodization of Ti foils at 60 V in EG electrolyte containing 5 wt%  $\text{H}_2\text{O}_2$  and different amounts of  $\text{NH}_4\text{F}$ , (a) 1 wt%, (b) 3 wt%, and (c) 5 wt%.

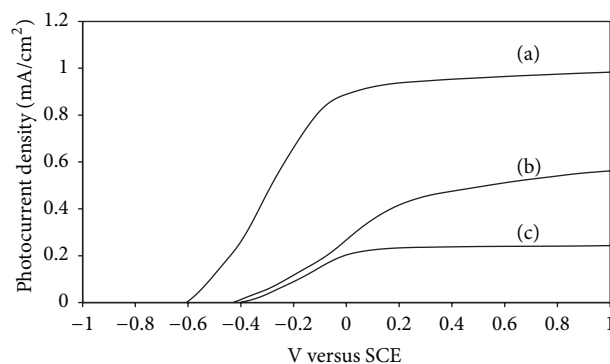


FIGURE 4: The  $I$ - $V$  characteristics of different surface morphologies of anodic  $\text{TiO}_2$  photoanode in 1 M KOH solution with 1 wt% of EG, (a) nanotubes, (b) nanoporous, and (c) compact oxide layer.

the PEC water splitting cell. The  $I$ - $V$  characteristics of the samples were recorded under illumination by a 150 W xenon lamp, with a light intensity of approximately  $800 \text{ W/m}^2$ . Based on the  $I$ - $V$  characteristic curves, the photocurrent density was increased when the voltage was increased from  $-1 \text{ V}$  to  $1 \text{ V}$  under solar illumination. A maximum photocurrent density of approximately  $1 \text{ mA/cm}^2$  was observed from the anodic  $\text{TiO}_2$  nanotube arrays as compared to the nanoporous and compact oxide layer as exhibited in Figure 4(a). Meanwhile, the  $\text{TiO}_2$  nanoporous structure and  $\text{TiO}_2$  compact oxide layer exhibited decrease of photocurrent densities, which are approximately  $0.55 \text{ mA/cm}^2$  (Figure 4(b)) and  $0.25 \text{ mA/cm}^2$  (Figure 4(c)), respectively.

$\text{TiO}_2$  nanotube arrays exhibited higher photocurrent density among the samples. The reason is mainly attributed to the larger specific surface area. It is noteworthy to point out that larger specific surface area of well-aligned nanotube arrays can greatly increase the density of active sites available for the photon absorption to generate more photo-induced electrons. The highly ordered, vertically oriented tubular structure is suitable for a high degree of electrons mobility along the tube axis and perpendicular to the Ti

substrate, which will greatly reduce interface recombination. As a matter of fact, nanotubular structure offers a preferred dimensionally to the TiO<sub>2</sub> back contact, which can improve the transportation of charge carriers due to the less grain boundaries in the one-dimensional nanotube arrays system [16, 35, 36, 38, 39, 42]. In addition, both sides of the nanotube walls and the entire tube sidewalls can act as large number of reaction sites for chemical reactions to occur and allow more photo-induced electrons generated for the hydrogen reduction process during illumination. The larger active surface area proximal to the electrolyte solution enhances the generation of photo-induced electrons from nanotube arrays towards to the back contact of the TiO<sub>2</sub> and eventually these photo-induced electrons move to counter electrode (platinum electrode) through the external circuit where they reduce H<sup>+</sup> ions creating H<sub>2</sub> molecules ( $2\text{H}^+ + 2\text{e}^- \rightarrow \text{H}_2$ ) under external bias [51, 52]. This statement was further confirmed by the more negative values of photopotential for the TiO<sub>2</sub> nanotube arrays (−0.65 V) compared to TiO<sub>2</sub> nanoporous structure (−0.45 V) and TiO<sub>2</sub> oxide layer (−0.4 V) as shown in Figure 4. The more negative values of photopotential or open circuit potential indicated that more photo-induced electrons were generated from valence band to the conduction band when the terminal was left open (no bias voltage was applied).

The drawback of the used irregular nanoporous TiO<sub>2</sub> structure in PEC studies is most probably due to the numerous defect sites and trapping sites, which results in more recombination losses of charge carriers and reduces the photo-induced collection at the TiO<sub>2</sub> back contact [53]. Thus, the photocurrent density was decreasing significantly. On the other hand, the use of TiO<sub>2</sub> compact oxide layer showed the lowest photocurrent density among the samples. The compact oxide layer generally will have less specific surface area compared to the nanotubular and nanoporous structure. Thus, the number of photo-induced electrons generated from the photoelectrode will significantly reduce. Based on the results obtained, it is crucial to maximize the specific surface area of TiO<sub>2</sub> photoelectrode in the PEC water splitting studies.

Next, the TiO<sub>2</sub> response with different surface morphologies towards the interruption of light was studied with a potentiostatic (photocurrent density versus time) at a fix bias voltage of 0.6 V. The photocurrent density of the samples was measured and plotted in Figure 5. All samples showed good photoresponses under light pulse illumination. The photo-induced electrons can effectively transfer from TiO<sub>2</sub> photoelectrode to counter electrode and eventually generate the photocurrent response during illumination. The photocurrent drastically dropped to approximately 0 mA under dark conditions. This indicates that TiO<sub>2</sub> is a good photo-response semiconductor for the transfer and decay of the photo-induced electrons [13, 42]. It is noteworthy to point out that the photocurrent reverted back to the original state within a couple of seconds under illumination. This photocurrent pattern was highly reproducible for several on-off cycles. The results from the potentiostatic curves are in good agreement with the results in photocurrent density curves.

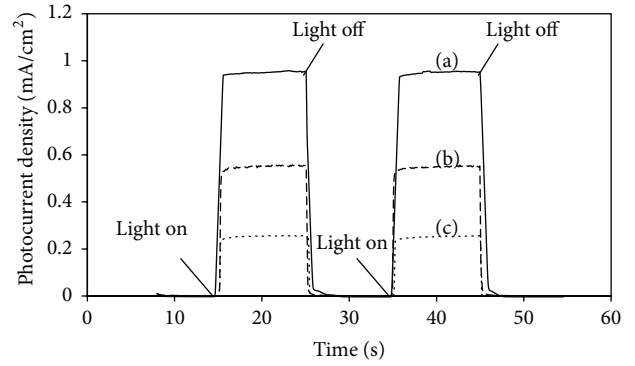


FIGURE 5: Potentiostatic plot of photocurrent density for different surface morphologies of anodic TiO<sub>2</sub> photoanode in 1M KOH solution with 1wt% of EG under interrupted illumination, (a) nanotubes, (b) nanoporous, and (c) compact oxide layer.

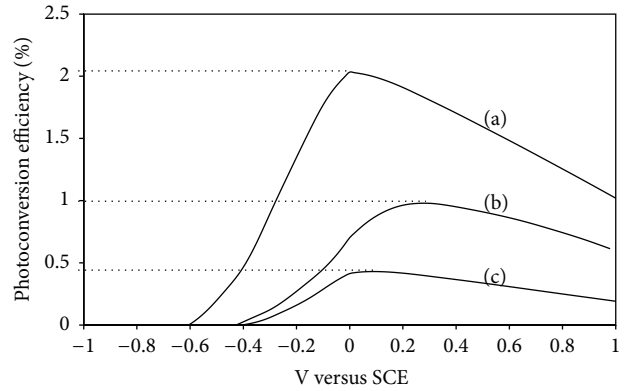


FIGURE 6: Photoconversion efficiency versus potential applied to the different surface morphologies of anodic TiO<sub>2</sub> photoanode (a) nanotubes, (b) nanoporous, and (c) compact oxide layer.

The photoconversion efficiency ( $\eta$ ) for the water splitting reaction was calculated based on the following equation:

$$\eta (\%) = \left[ \frac{\text{total power output} - \text{electrical power output}}{\text{light power input}} \right] \times 100 = j_p \left[ \frac{E_{\text{rev}}^0 - |E_{\text{app}}|}{I_0} \right] \times 100, \quad (2)$$

where  $j_p$  is the photocurrent density (mA/cm<sup>2</sup>);  $j_p E_{\text{rev}}^0$  is the total power output;  $j_p |E_{\text{app}}|$  is the electrical power input;  $I_0$  is the power density of the incident light (mW/cm<sup>2</sup>);  $E_{\text{rev}}^0$  is the standard reversible potential (1.23 V/SHE);  $E_{\text{app}} = E_{\text{mean}} - E_{\text{aoc}}$ ;  $E_{\text{mean}}$  is the electrode potential (versus SCE) of the working electrode where the photocurrent was measured under illumination; and  $E_{\text{aoc}}$  is the potential (versus SCE) of the working electrode at open circuit condition.

The highest visible spectrum efficiency (about 2%) was obtained from TiO<sub>2</sub> nanotube arrays from the photoconversion efficiency curves shown in Figure 6. The decrease in

photocurrent efficiency was as follows: 1% and 0.5%, which correspond to nanoporous and compact oxide structure, respectively. These results clearly indicate that the PEC performance is dependent on the specific surface area of the TiO<sub>2</sub> anodic film.

#### 4. Conclusion

The formation mechanism of self-organized and well-aligned TiO<sub>2</sub> nanotube arrays in the fluorinated-based electrolyte was investigated and discussed. The present study demonstrated that bundle-free TiO<sub>2</sub> nanotube arrays film was successfully synthesized in EG electrolyte containing ≈5 wt% of H<sub>2</sub>O<sub>2</sub> and ≈5 wt% of NH<sub>4</sub>F. It is shown that anodic TiO<sub>2</sub> synthesized in EG electrolyte containing less than 5 wt% of NH<sub>4</sub>F will result in the formation of nanoporous structure and compact oxide layer. The high specific surface area of anodic TiO<sub>2</sub> nanotubes generated a good photocurrent response of 1 mA/cm<sup>2</sup> with photoconversion efficiency of 2%. The main reason could be attributed to the better light absorption for the PEC water splitting reaction sites by generating more photo-induced electrons under illumination. In summary, it is crucial to maximize the specific surface area of TiO<sub>2</sub> anodic films in order to achieve maximum photocurrent generation and photoconversion efficiency.

#### Conflict of Interests

The author declares that there is no conflict of interests regarding the publication of this paper.

#### Acknowledgments

This research is supported by High Impact Research Chancellor Grant UM.C/625/1/HIR/228 (J55001-73873) from the University of Malaya. In addition, the author would like to thank University of Malaya for sponsoring this work under MOSTI-ScienceFund (SF003-2015). Lastly, financial supports from PPP grant (PG052-2013 and PG058-2014B) are gratefully acknowledged.

#### References

- [1] J. A. Turner, "A realizable renewable energy future," *Science*, vol. 285, no. 5428, pp. 687–689, 1999.
- [2] S. E. Gledhill, B. Scott, and B. A. Gregg, "Reviews—energy and the environment special section," *Journal of Materials Research*, vol. 20, no. 12, pp. 3167–3179, 2005.
- [3] M. Jefferson, "Sustainable energy development: performance and prospects," *Renewable Energy*, vol. 31, no. 5, pp. 571–582, 2006.
- [4] M. Kitano, M. Matsuoka, M. Ueshima, and M. Anpo, "Recent developments in titanium oxide-based photocatalysts," *Applied Catalysis A: General*, vol. 325, no. 1, pp. 1–14, 2007.
- [5] A. Fujishima, X. T. Zhang, and D. A. Tryk, "TiO<sub>2</sub> photocatalysis and related surface phenomena," *Surface Science Reports*, vol. 63, no. 12, pp. 515–582, 2008.
- [6] K. Yu and J. Chen, "Enhancing solar cell efficiencies through 1-D nanostructures," *Nanoscale Research Letters*, vol. 4, no. 1, pp. 1–10, 2009.
- [7] M. Ni, M. K. H. Leung, D. Y. C. Leung, and K. Sumathy, "A review and recent developments in photocatalytic water-splitting using TiO<sub>2</sub> for hydrogen production," *Renewable and Sustainable Energy Reviews*, vol. 11, no. 3, pp. 401–425, 2007.
- [8] V. M. Aroutiounian, V. M. Arakelyan, and G. E. Shahnazaryan, "Metal oxide photoelectrodes for hydrogen generation using solar radiation-driven water splitting," *Solar Energy*, vol. 78, no. 5, pp. 581–590, 2005.
- [9] T. K. Tromp, R.-L. Shia, M. Allen, J. M. Eiler, and Y. L. Yung, "Potential environmental impact of a hydrogen economy on the stratosphere," *Science*, vol. 300, no. 5626, pp. 1740–1742, 2003.
- [10] D. A. Tryk, A. Fujishima, and K. Honda, "Recent topics in photoelectrochemistry: achievements and future prospects," *Electrochimica Acta*, vol. 45, no. 15–16, pp. 2363–2376, 2000.
- [11] R. Dholam, N. Patel, M. Adami, and A. Miotello, "Hydrogen production by photocatalytic water-splitting using Cr- or Fe-doped TiO<sub>2</sub> composite thin films photocatalyst," *International Journal of Hydrogen Energy*, vol. 34, no. 13, pp. 5337–5346, 2009.
- [12] Z. Zhang, M. F. Hossain, and T. Takahashi, "Photoelectrochemical water splitting on highly smooth and ordered TiO<sub>2</sub> nanotube arrays for hydrogen generation," *International Journal of Hydrogen Energy*, vol. 35, no. 16, pp. 8528–8535, 2010.
- [13] C. W. Lai and S. Sreekantan, "Effect of applied potential on the formation of self-organized TiO<sub>2</sub> nanotube arrays and its photoelectrochemical response," *Journal of Nanomaterials*, vol. 2011, Article ID 142463, 7 pages, 2011.
- [14] V. K. Mahajan, S. K. Mohapatra, and M. Misra, "Stability of TiO<sub>2</sub> nanotube arrays in photoelectrochemical studies," *International Journal of Hydrogen Energy*, vol. 33, no. 20, pp. 5369–5374, 2008.
- [15] S. K. Mohapatra, K. S. Raja, V. K. Mahajan, and M. Misra, "Efficient photoelectrolysis of water using TiO<sub>2</sub> nanotube arrays by minimizing recombination losses with organic additives," *Journal of Physical Chemistry C*, vol. 112, no. 29, pp. 11007–11012, 2008.
- [16] Y. Xie, L. Zhou, and J. Lu, "Photoelectrochemical behavior of titania nanotube array grown on nanocrystalline titanium," *Journal of Materials Science*, vol. 44, no. 11, pp. 2907–2915, 2009.
- [17] M. Grätzel, "Photoelectrochemical cells," *Nature*, vol. 414, no. 6861, pp. 338–344, 2001.
- [18] J. Nowotny, T. Bak, M. K. Nowotny, and L. R. Sheppard, "Titanium dioxide for solar-hydrogen II. Defect chemistry," *International Journal of Hydrogen Energy*, vol. 32, no. 14, pp. 2630–2643, 2007.
- [19] A. Currao, "Photoelectrochemical water splitting," *Chimia*, vol. 61, no. 12, pp. 815–819, 2007.
- [20] W. H. Ryu, C. J. Park, and H. S. Kwon, "A special section on nanocomposites and nanoporous materials," *Journal of Nanoscience and Nanotechnology*, vol. 10, no. 1, pp. 1–2, 2010.
- [21] V. V. Kislyuk and O. P. Dimitriev, "Nanorods and nanotubes for solar cells," *Journal of Nanoscience and Nanotechnology*, vol. 8, no. 1, pp. 131–148, 2008.
- [22] W. Zhu, X. Liu, H. Liu, D. Tong, J. Yang, and J. Peng, "An efficient approach to control the morphology and the adhesion properties of anodized TiO<sub>2</sub> nanotube arrays for improved photoconversion efficiency," *Electrochimica Acta*, vol. 56, no. 6, pp. 2618–2626, 2011.
- [23] D.-S. Seo, J.-K. Lee, and H. Kim, "Preparation of nanotube-shaped TiO<sub>2</sub> powder," *Journal of Crystal Growth*, vol. 229, no. 1–4, pp. 428–432, 2001.

- [24] Z.-Y. Yuan and B.-L. Su, "Titanium oxide nanotubes, nanofibers and nanowires," *Colloids and Surfaces A: Physicochemical and Engineering Aspects*, vol. 241, no. 1–3, pp. 173–183, 2004.
- [25] P. Hoyer, K. Nishio, and H. Masuda, "Preparation of regularly structured porous metal membranes with two different hole diameters at the two sides," *Thin Solid Films*, vol. 286, no. 1–2, pp. 88–91, 1996.
- [26] S. Sreekantan and L. C. Wei, "Study on the formation and photocatalytic activity of titanate nanotubes synthesized via hydrothermal method," *Journal of Alloys and Compounds*, vol. 490, no. 1–2, pp. 436–442, 2010.
- [27] M. Zhang, Z. S. Jin, J. W. Zhang et al., "Effect of annealing temperature on morphology, structure and photocatalytic behavior of nanotubed  $\text{H}_2\text{Ti}_2\text{O}_4(\text{OH})_2$ ," *Journal of Molecular Catalysis A: Chemical*, vol. 217, no. 1–2, pp. 203–210, 2004.
- [28] T. Kasuga, M. Hiramatsu, A. Hoson, T. Sekino, and K. Niihara, "Titania nanotubes prepared by chemical processing," *Advanced Materials*, vol. 11, no. 15, pp. 1307–1311, 1999.
- [29] S. Sreekantan, L. C. Wei, and Z. Lockman, "Extremely fast growth rate of  $\text{TiO}_2$  nanotube arrays in electrochemical bath containing  $\text{H}_2\text{O}_2$ ," *Journal of the Electrochemical Society*, vol. 158, no. 12, pp. C397–C402, 2011.
- [30] Y.-C. Hsiao and Y.-H. Tseng, "Preparation of Pd-containing  $\text{TiO}_2$  film and its photocatalytic properties," *Micro & Nano Letters*, vol. 5, no. 5, pp. 317–320, 2010.
- [31] M. Paulose, H. E. Prakasham, O. K. Varghese et al., " $\text{TiO}_2$  nanotube arrays of 1000  $\mu\text{m}$  length by anodization of titanium foil: Phenol red diffusion," *Journal of Physical Chemistry C*, vol. 111, no. 41, pp. 14992–14997, 2007.
- [32] G. K. Mor, O. K. Varghese, M. Paulose, K. Shankar, and C. A. Grimes, "A review on highly ordered, vertically oriented  $\text{TiO}_2$  nanotube arrays: fabrication, material properties, and solar energy applications," *Solar Energy Materials and Solar Cells*, vol. 90, no. 14, pp. 2011–2075, 2006.
- [33] J. M. Macak and P. Schmuki, "Anodic growth of self-organized anodic  $\text{TiO}_2$  nanotubes in viscous electrolytes," *Electrochimica Acta*, vol. 52, no. 3, pp. 1258–1264, 2006.
- [34] J. M. Macak, H. Hildebrand, U. Marten-Jahns, and P. Schmuki, "Mechanistic aspects and growth of large diameter self-organized  $\text{TiO}_2$  nanotubes," *Journal of Electroanalytical Chemistry*, vol. 621, no. 2, pp. 254–266, 2008.
- [35] J. Yan and F. Zhou, " $\text{TiO}_2$  nanotubes: structure optimization for solar cells," *Journal of Materials Chemistry*, vol. 21, no. 26, pp. 9406–9418, 2011.
- [36] A. Ghicov and P. Schmuki, "Self-ordering electrochemistry: a review on growth and functionality of  $\text{TiO}_2$  nanotubes and other self-aligned  $\text{MO}_x$  structures," *Chemical Communications*, no. 20, pp. 2791–2808, 2009.
- [37] S. Sreekantan, R. Hazan, and Z. Lockman, "Photoactivity of anatase-rutile  $\text{TiO}_2$  nanotubes formed by anodization method," *Thin Solid Films*, vol. 518, no. 1, pp. 16–21, 2009.
- [38] C. A. Grimes, "Synthesis and application of highly ordered arrays of  $\text{TiO}_2$  nanotubes," *Journal of Materials Chemistry*, vol. 17, no. 15, pp. 1451–1457, 2007.
- [39] P. Roy, S. Berger, and P. Schmuki, " $\text{TiO}_2$  nanotubes: synthesis and applications," *Angewandte Chemie*, vol. 50, no. 13, pp. 2904–2939, 2011.
- [40] K. S. Raja, M. Misra, and K. Paramguru, "Formation of self-ordered nano-tubular structure of anodic oxide layer on titanium," *Electrochimica Acta*, vol. 51, no. 1, pp. 154–165, 2005.
- [41] C. W. Lai and S. Sreekantan, "Comparison of photocatalytic and photoelectrochemical behavior of  $\text{TiO}_2$  nanotubes prepared by different organic electrolyte," *Optoelectronics and Advanced Materials: Rapid Communications*, vol. 6, no. 1–2, pp. 82–86, 2012.
- [42] V. K. Mahajan, M. Misra, K. S. Raja, and S. K. Mohapatra, "Self-organized  $\text{TiO}_2$  nanotubular arrays for photoelectrochemical hydrogen generation: effect of crystallization and defect structures," *Journal of Physics D: Applied Physics*, vol. 41, no. 12, Article ID 125307, 2008.
- [43] H.-J. Kim and K.-H. Lee, "Dependence of the morphology of nanostructured titanium oxide on fluoride ion content," *Electrochemical and Solid-State Letters*, vol. 12, no. 3, pp. C10–C12, 2009.
- [44] C. W. Lai and S. Sreekantan, "Photoelectrochemical performance of smooth  $\text{TiO}_2$  nanotube arrays: effect of anodization temperature and cleaning methods," *International Journal of Photoenergy*, vol. 2012, Article ID 356943, 11 pages, 2012.
- [45] H. Yang and C. Pan, "Diameter-controlled growth of  $\text{TiO}_2$  nanotube arrays by anodization and its photoelectric property," *Journal of Alloys and Compounds*, vol. 492, no. 1–2, pp. L33–L35, 2010.
- [46] P.-C. Chen, S.-J. Hsieh, C.-C. Chen, and J. Zou, "Fabrication and characterization of chemically sensitive needle tips with aluminum oxide nanopores for pH indication," *Ceramics International*, vol. 39, no. 3, pp. 2597–2600, 2013.
- [47] K. Yasuda, J. M. Macak, S. Berger, A. Ghicov, and P. Schmuki, "Mechanistic aspects of the self-organization process for oxide nanotube formation on valve metals," *Journal of the Electrochemical Society*, vol. 154, no. 9, pp. C472–C478, 2007.
- [48] L. V. Taveira, J. M. Macák, H. Tsuchiya, L. F. P. Dick, and P. Schmuki, "Initiation and growth of self-organized  $\text{TiO}_2$  nanotubes anodically formed in  $\text{NH}_4\text{F}/(\text{NH}_4)_2\text{SO}_4$  electrolytes," *Journal of the Electrochemical Society*, vol. 152, no. 10, pp. B405–B410, 2005.
- [49] A. Elsanousi, J. Zhang, H. M. H. Fadlalla et al., "Self-organized  $\text{TiO}_2$  nanotubes with controlled dimensions by anodic oxidation," *Journal of Materials Science*, vol. 43, no. 22, pp. 7219–7224, 2008.
- [50] B. G. Lee, J. W. Choi, S. E. Lee, Y. S. Jeong, H. J. Oh, and C. S. Chi, "Formation behavior of anodic  $\text{TiO}_2$  nanotubes in fluoride containing electrolytes," *Transactions of Nonferrous Metals Society of China*, vol. 19, no. 4, pp. 842–845, 2009.
- [51] L. Sun, S. Zhang, X. Sun, and X. He, "Effect of the geometry of the anodized titania nanotube array on the performance of dye-sensitized solar cells," *Journal of Nanoscience and Nanotechnology*, vol. 10, no. 7, pp. 4551–4561, 2010.
- [52] Y. B. Liu, J. H. Li, B. X. Zhou et al., "Comparison of photoelectrochemical properties of  $\text{TiO}_2$ -nanotube-array photoanode prepared by anodization in different electrolyte," *Environmental Chemistry Letters*, vol. 7, no. 4, pp. 363–368, 2009.
- [53] L. Yang, Y. Xiao, S. Liu, Y. Li, Q. Cai, and S. Luo, "Photocatalytic reduction of  $\text{Cr}(\text{VI})$  on  $\text{WO}_3$  doped long  $\text{TiO}_2$  nanotube arrays in the presence of citric acid," *Applied Catalysis B: Environmental*, vol. 94, p. 142, 2010.

## Research Article

# Electrodeposition and Characterization of CuTe and Cu<sub>2</sub>Te Thin Films

Wenya He,<sup>1,2</sup> Hanzhi Zhang,<sup>2</sup> Ye Zhang,<sup>2</sup> Mengdi Liu,<sup>2</sup> Xin Zhang,<sup>1,2</sup> and Fengchun Yang<sup>2</sup>

<sup>1</sup>Shaanxi Provincial Key Laboratory of Electroanalytical Chemistry, Institute of Analytical Science, Northwest University, Xi'an, Shaanxi 710069, China

<sup>2</sup>Key Laboratory of Synthetic and Natural Functional Molecule Chemistry of Ministry of Education, College of Chemistry and Materials Science, Northwest University, Xi'an, Shaanxi 710127, China

Correspondence should be addressed to Xin Zhang; zhangxin@nwu.edu.cn and Fengchun Yang; fyang@nwu.edu.cn

Received 22 November 2014; Revised 25 December 2014; Accepted 25 December 2014

Academic Editor: Jiamin Wu

Copyright © 2015 Wenya He et al. This is an open access article distributed under the Creative Commons Attribution License, which permits unrestricted use, distribution, and reproduction in any medium, provided the original work is properly cited.

An electrodeposition method for fabrication of CuTe and Cu<sub>2</sub>Te thin films is presented. The films' growth is based on the epitaxial electrodeposition of Cu and Te alternately with different electrochemical parameter, respectively. The deposited thin films were characterized by X-ray diffraction (XRD), field emission scanning electronic microscopy (FE-SEM) with an energy dispersive X-ray (EDX) analyzer, and FTIR studies. The results suggest that the epitaxial electrodeposition is an ideal method for deposition of compound semiconductor films for photoelectric applications.

## 1. Introduction

Semiconducting compounds such as I–VI copper chalcogenides are widely used in the fabrication of photoconductive and photovoltaic devices [1]. Copper based chalcogenides exhibited the characteristics of a p-type semiconductor for the vacancies of copper and are potential materials for wide applications. Thin films of copper chalcogenides especially have been a subject of interest for many years mainly because of their wide range of applications in solar cells [2], superionic conductors [3], photodetectors, photothermal [4] converters [5], electroconductive electrodes [6], and so forth.

Of these copper chalcogenides, copper telluride compounds have gained great interest owing to its superionic conductivity [7], direct band gap between 1.1 and 1.5 eV [8], and large thermoelectric power. In the literature, a number of methods for preparation of Cu<sub>x</sub>Se [9] and Cu<sub>x</sub>S [10, 11] thin films have been reported. However, fabrication of CuTe thin films is much less studied to date. Copper telluride compounds (Cu<sub>x</sub>Te, where  $x = 1, 2$  or between 1 and 2) were known to exist in a wide range of compositions and phases whose properties are controlled by the Cu:Te ratio [12] and can be grown by chemical bath deposition, coevaporation, and fusion method [13].

Electrochemical atomic layer deposition is considered as a controllable and simple deposition technique [14] for homogeneous compound semiconductors on conductive substrates without annealing [15]. The electrochemical atomic layer deposition was based on the alternated underpotential deposition which was a phenomenon of surface limited [16] so that the resulting deposit was generally limited to one atomic layer [17]. Thus, each deposition cycle formed a single layer of the compound [18, 19], and the number of deposition cycles controls the thickness of deposits [20]. In this paper, an epitaxial electrodeposition method for preparation of CuTe and Cu<sub>2</sub>Te thin films on ITO substrates by controlling the solution conditions in contact with the deposit and the potential of the electrode is reported. The crystallographic structures of the obtained films are discussed on the basis of X-ray diffraction data. Field emission scanning electronic microscopy (FE-SEM) with an energy dispersive X-ray (EDX) analyzer shows investigation of morphology. Optical characteristics of the films are studied by FTIR.

## 2. Experimental

Electrochemical experiments were carried out using a CHI 660A electrochemical workstation (CH Instrument, USA).

The deposition was performed in a three-electrode cell with a platinum wire as counter electrode and Ag/AgCl/sat. KCl as reference electrode. Indium doped tin oxide (ITO) glass slide ( $\approx 20 \Omega/\text{cm}$ ) was used as a working electrode. Prior to electrodeposition, the ITO substrate was ultrasonic cleaned with acetone, ethanol, and water sequentially.

All solutions were prepared with nanopure water purified by the Milli-Q system (Millipore Inc., nominal resistivity  $18.2 \text{ M}\Omega \text{ cm}$ ), and all chemicals were of analytical reagent grade. The oxygen was removed by blowing purified  $\text{N}_2$  before each measurement, and the whole experiments were conducted at room temperature.

The crystallographic structures of the thin films obtained were determined by XRD (Rigaku D/max-2400). The morphology is investigated by FE-SEM (Kevex JSM-6701F, Japan) equipped with an EDX analyzer. Glancing angle absorption measurements were performed using an FTIR spectrophotometer (Nicolet Nexus 670, USA).

### 3. Results and Discussion

#### 3.1. Thin Film Deposition

**3.1.1. CuTe Thin Film Deposition.** Figure 1 shows the cyclic voltammograms of ITO electrode in blank and Cu solution, respectively. For CuTe film growth,  $\text{H}_2\text{SO}_4$  was used as supporting electrolyte. From Figure 1(b), only one pair of redox peaks was observed at  $-0.34 \text{ V}$  (C1) and  $0.30 \text{ V}$  (A1), corresponding to  $\text{Cu}^{2+}$  reduction to Cu, as reaction (1) shows

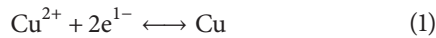
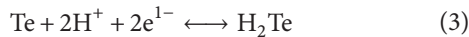
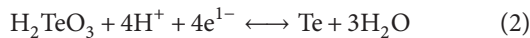


Figure 2 shows the cyclic voltammograms of Cu-covered ITO electrode in  $0.1 \text{ M H}_2\text{SO}_4$  and in  $5 \text{ mM H}_2\text{TeO}_3 + 0.1 \text{ M H}_2\text{SO}_4$  solutions. In these experiments, the potential scanning was started at  $0 \text{ V}$  to avoid the oxidative stripping of Cu. Similar to most literatures, two reduction peaks are seen: peak C2 at about  $-0.21 \text{ V}$  based upon the four-electron process for Te reduction shown in reaction (1) and peak C3 at about  $-0.46 \text{ V}$ , which should be corresponded to bulk Te (0) reduction to  $\text{Te}^{2-}$ , as reaction (2) shows



Therefore, we applied  $-0.30 \text{ V}$  as the electrodeposition potentials for Cu and  $-0.20 \text{ V}$  for Te. Repeat electrodepositing Cu at  $-0.30 \text{ V}$  and Te at  $-0.20 \text{ V}$  for  $15 \text{ s}$  alternately as many times as desired to grow epitaxial nanofilms of CuTe on ITO substrate.

**3.1.2.  $\text{Cu}_2\text{Te}$  Thin Film Deposition.** For  $\text{Cu}_2\text{Te}$  film growth,  $\text{KNO}_3$  was used as supporting electrolyte because  $\text{Cu}^+$  ions cannot exist in a strong acid solution like  $0.1 \text{ M H}_2\text{SO}_4$ . Figure 3 shows the cyclic voltammograms of ITO electrode in blank  $\text{KNO}_3$  and Cu solution, respectively. In Figure 3(b), two well-defined cathodic peaks are located at  $-0.23 \text{ V}$  (C4) and  $-0.51 \text{ V}$  (C5), which are related to the formation of  $\text{Cu}_2\text{O}$

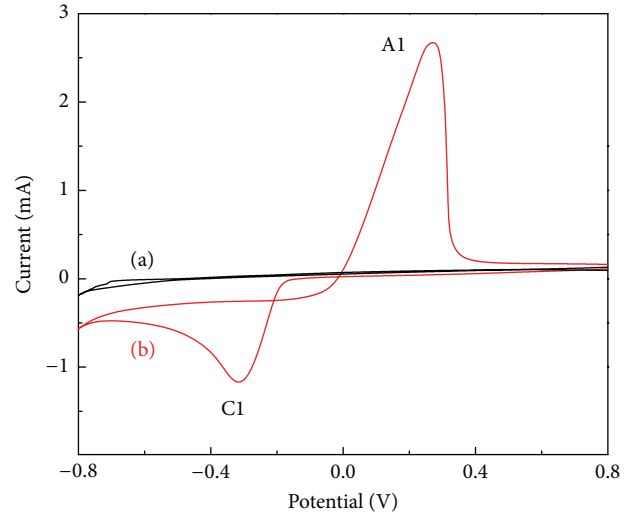


FIGURE 1: Cyclic voltammograms of ITO electrode in (a)  $0.1 \text{ M H}_2\text{SO}_4$ ; (b)  $0.1 \text{ M H}_2\text{SO}_4$  with  $5 \text{ mM CuSO}_4$  (scan rate:  $10 \text{ mV/s}$ ).

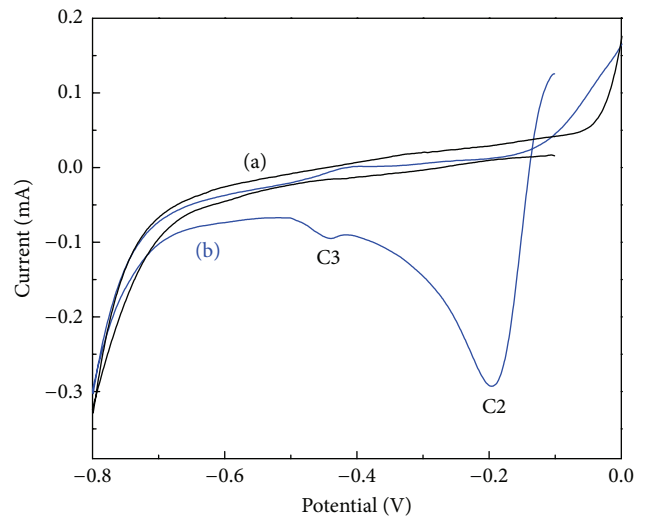


FIGURE 2: Cyclic voltammograms of Cu-covered ITO electrode in (a)  $0.1 \text{ M H}_2\text{SO}_4$ ; (b)  $0.1 \text{ M H}_2\text{SO}_4$  with  $5 \text{ mM TeO}_2$  (scan rate:  $10 \text{ mV/s}$ ).

and reduction of Cu on the ITO substrate, as reaction (4) and (1) show [14]:

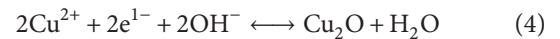
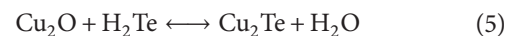


Figure 4 shows the cyclic voltammograms of  $\text{Cu}_2\text{O}$ -covered ITO electrode in  $0.1 \text{ M KNO}_3$  and in  $5 \text{ mM H}_2\text{TeO}_3 + 0.1 \text{ M KNO}_3$  solutions. From Figure 4(b), two reduction peaks are also seen: peak C6 at about  $-0.35 \text{ V}$  based upon the  $\text{H}_2\text{TeO}_3$  reduction to Te and peak C7 at about  $-0.60 \text{ V}$  corresponding to Te reduction to  $\text{H}_2\text{Te}$ , which immediately react with the underlying  $\text{Cu}_2\text{O}$  layer to form  $\text{Cu}_2\text{Te}$ , as reaction (5) shows



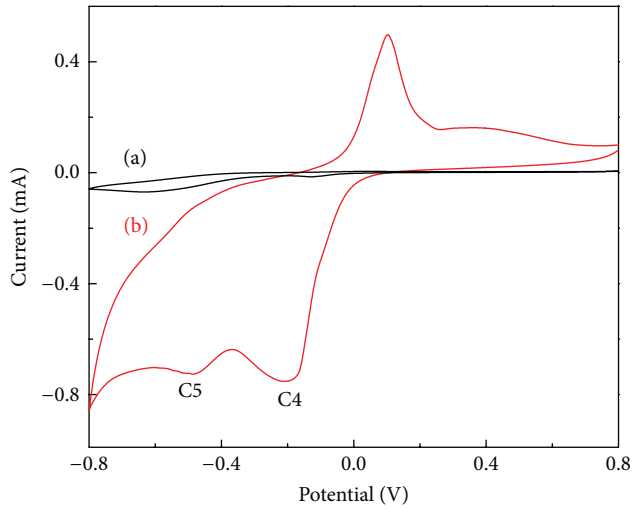


FIGURE 3: Cyclic voltammograms of ITO electrode in (a) 0.1 M  $\text{KNO}_3$ ; (b) 0.1 M  $\text{KNO}_3$  with 5 mM  $\text{CuSO}_4$  (scan rate: 10 mV/s).

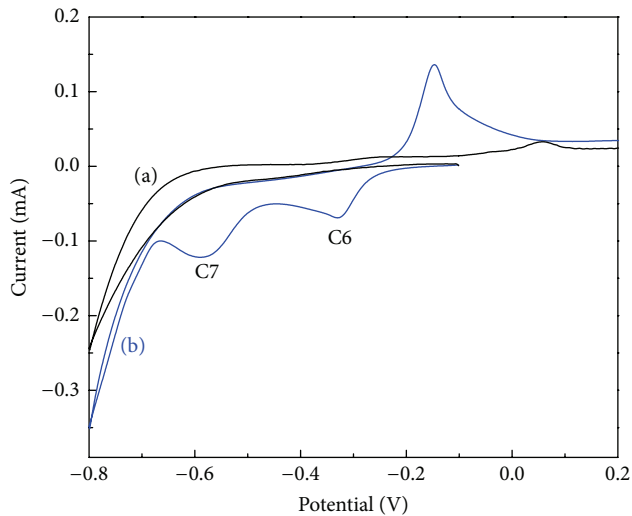


FIGURE 4: Cyclic voltammograms of  $\text{Cu}_2\text{O}$ -covered ITO electrode in (a) 0.1 M  $\text{KNO}_3$ ; (b) 0.1 M  $\text{KNO}_3$  with 5 mM  $\text{TeO}_2$  (scan rate: 10 mV/s).

Therefore, we applied  $-0.20$  V as the electrodeposition potentials for Cu and  $-0.60$  V for Te. Repeat electrodepositing Cu at  $-0.20$  V and Te at  $-0.60$  V for 15 s alternately as many times as desired to grow epitaxial nanofilms of  $\text{Cu}_2\text{Te}$  on ITO substrate.

### 3.2. Thin Film Characterization

**3.2.1. X-Ray Investigations.** Identification of the obtained thin films was carried out using the X-ray diffraction method. The recorded XRD patterns of deposited CuTe and  $\text{Cu}_2\text{Te}$  are presented in Figure 5. Figure 5(a) shows the XRD patterns of deposited CuTe film. The observed peak positions of the deposited CuTe film are in well agreement with those due to reflection from (0 1 1), (1 0 1), and (1 1 2) planes of the reported CuTe data with an orthorhombic structure

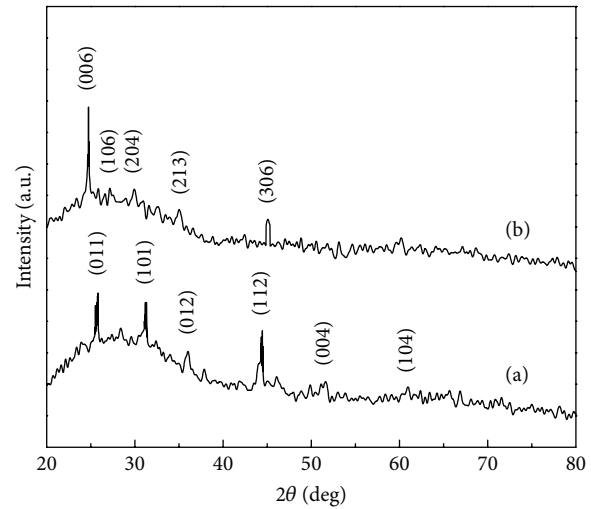


FIGURE 5: XRD patterns of deposited CuTe (a) and  $\text{Cu}_2\text{Te}$  (b) films.

(JCPDS 22-0252). The XRD pattern of deposited  $\text{Cu}_2\text{Te}$  film is presented in Figure 5(b). As can be seen, the analysis indicates that the deposited  $\text{Cu}_2\text{Te}$  film is in hexagonal structure, with the preferential orientation of (0 0 6) plane (JCPDS 49-1411).

The average crystal size was estimated using the well-known Debye-Scherrer relationship:

$$d = \frac{0.9 \cdot \lambda}{\beta \cdot \cos \theta}, \quad (6)$$

where  $\theta$  is the Bragg angle,  $\lambda$  is the X-ray wavelength, and  $\beta$  is the full width at half-maximum. It was found that the average crystal size of the deposited CuTe film is 92.11 nm and  $\text{Cu}_2\text{Te}$  film was found to be about 36.84 nm, which are consistent with the SEM observation.

**3.2.2. SEM Observations.** The SEM micrographs of deposited CuTe and  $\text{Cu}_2\text{Te}$  films are shown in Figures 6(a) and 6(b), respectively, at 30,000x magnification. In deposited CuTe film (Figure 3(a)), the grains are more distinct and of bigger size, while, in  $\text{Cu}_2\text{Te}$  film (Figure 3(b)), the grains are of smaller size, more compact with densely packed microcrystals. The EDX analysis was carried out only for Cu and Te. The average atomic percentage of Cu:Te in deposited CuTe film was 50.4 : 49.6. It is close to 1 : 1 stoichiometry. Similar results for  $\text{Cu}_2\text{Te}$  were 67.3 : 32.7, close to 2 : 1 stoichiometry.

**3.2.3. Optical Measurements.** For optical characterization, FTIR spectra of deposited CuTe and  $\text{Cu}_2\text{Te}$  thin films were recorded. The optical band gap ( $E_g$ ) for deposited CuTe and  $\text{Cu}_2\text{Te}$  thin films was calculated on the basis of the FTIR spectra, using the well-known relation

$$\alpha h\nu = A (h\nu - E_g)^{1/2}, \quad (7)$$

where  $A$  is the constant,  $E_g$  is the band gap, and  $h\nu$  is the photon energy. Figure 7 shows the variation of  $(\alpha h\nu)^2$  with  $h\nu$  for deposited CuTe and  $\text{Cu}_2\text{Te}$ . By extrapolating straight line portion of  $(\alpha h\nu)^2$  against  $h\nu$  plot to  $\alpha = 0$ , the optical

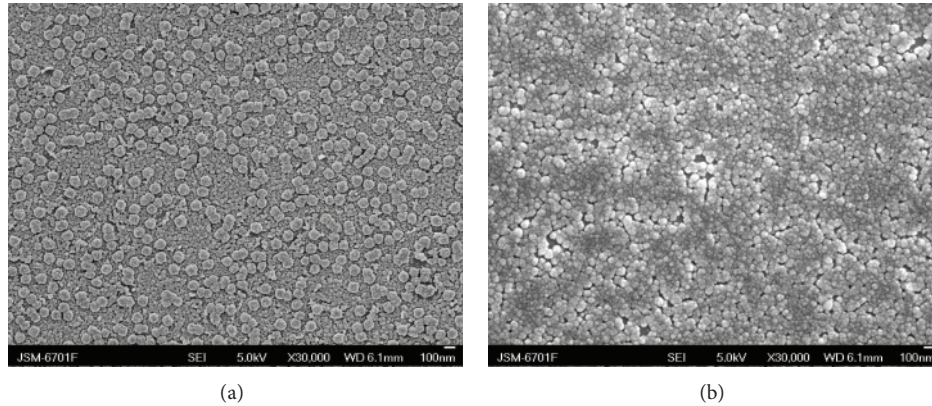


FIGURE 6: SEM micrograph of deposited CuTe (a) and Cu<sub>2</sub>Te (b) films.

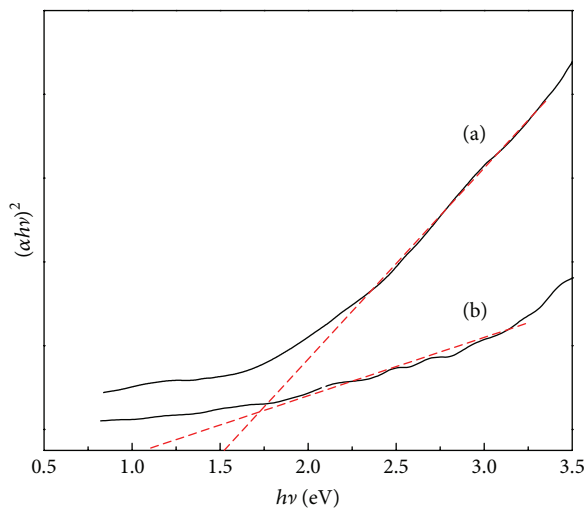


FIGURE 7: The dependence of  $(\alpha h\nu)^2$  on  $h\nu$  for deposited CuTe (a) and Cu<sub>2</sub>Te (b) films.

band gap energy was found to be 1.51 eV for CuTe and 1.12 eV for Cu<sub>2</sub>Te films, comparable with the value reported earlier for CuTe and Cu<sub>2</sub>Te thin film [1, 15].

#### 4. Conclusion

In this work, the Cu/Te ratio has been successfully controlled to prepare crystalline CuTe and Cu<sub>2</sub>Te thin films on the ITO electrode via electrodeposition. The copper-tellurium films were epitaxial electrodeposited under layer-by-layer, potentiostatic conditions. XRD, SEM, and IR studies of the deposited CuTe and Cu<sub>2</sub>Te thin films confirm the high quality of the deposits and demonstrate that the epitaxial electrodeposition is applicable to the deposition of stoichiometric nanofilms of copper-tellurium films of good quality.

#### Conflict of Interests

The authors declare that there is no conflict of interests regarding the publication of this paper.

#### Acknowledgments

The authors gratefully acknowledge the supports from the National Natural Scientific Foundation of China (nos. 21301137 and 21405120), the Shaanxi Provincial Science and Technology Development Funds (nos. 2014KW08-02 and 2014JQ2050), the Undergraduate Innovation and Entrepreneurship Training Program (no. 2015103), and NFFTBS (nos. J1103311 and J1210057).

#### References

- [1] K. Neyvasagam, N. Soundararajan, G. S. Okram, and V. Ganesan, "Low-temperature electrical resistivity of cupric telluride (CuTe) thin films," *Physica Status Solidi (B)*, vol. 245, no. 1, pp. 77–81, 2008.
- [2] O. Mahammad Hussain, B. S. Naidu, and P. J. Reddy, "Photovoltaic properties of n-CdS/p-Cu<sub>2</sub>Te thin film heterojunctions," *Thin Solid Films*, vol. 193–194, no. 2, pp. 777–781, 1990.
- [3] M. A. Korzhuev, "Dufour effect in superionic copper selenide," *Physics of the Solid State*, vol. 40, no. 2, pp. 217–219, 1998.
- [4] S. R. Gosavi, N. G. Deshpande, Y. G. Gudage, and R. Sharma, "Physical, optical and electrical properties of copper selenide (CuSe) thin films deposited by solution growth technique at room temperature," *Journal of Alloys and Compounds*, vol. 448, no. 1–2, pp. 344–348, 2008.
- [5] C. Naşcu, I. Pop, V. Ionescu, E. Indrea, and I. Bratu, "Spray pyrolysis deposition of CuS thin films," *Materials Letters*, vol. 32, no. 2–3, pp. 73–77, 1997.
- [6] W. Wei, S. Zhang, C. Fang et al., "Electrochemical behavior and electrogenerated chemiluminescence of crystalline CuSe nanotubes," *Solid State Sciences*, vol. 10, no. 5, pp. 622–628, 2008.
- [7] J. Zhou, X. Wu, A. Duda, G. Teeter, and S. H. Demtsu, "The formation of different phases of Cu<sub>x</sub>Te and their effects on CdTe/CdS solar cells," *Thin Solid Films*, vol. 515, no. 18, pp. 7364–7369, 2007.
- [8] S. Kashida, W. Shimosaka, M. Mori, and D. Yoshimura, "Valence band photoemission study of the copper chalcogenide compounds, Cu<sub>2</sub>S, Cu<sub>2</sub>Se and Cu<sub>2</sub>Te," *Journal of Physics and Chemistry of Solids*, vol. 64, no. 12, pp. 2357–2363, 2003.
- [9] M. Dhanam, P. K. Manoj, and R. R. Prabhu, "High-temperature conductivity in chemical bath deposited copper selenide thin

- films," *Journal of Crystal Growth*, vol. 280, no. 3-4, pp. 425–435, 2005.
- [10] R. Córdova, H. Gómez, R. Schrebler et al., "Electrosynthesis and electrochemical characterization of a thin phase of  $\text{Cu}_x\text{S}$  ( $x \rightarrow 2$ ) on ITO electrode," *Langmuir*, vol. 18, no. 22, pp. 8647–8654, 2002.
- [11] S. Lindroos, A. Arnold, and M. Leskelä, "Growth of CuS thin films by the successive ionic layer adsorption and reaction method," *Applied Surface Science*, vol. 158, no. 1-2, pp. 75–80, 2000.
- [12] K. Sridhar and K. Chattopadhyay, "Synthesis by mechanical alloying and thermoelectric properties of  $\text{Cu}_2\text{Te}$ ," *Journal of Alloys and Compounds*, vol. 264, no. 1-2, pp. 293–298, 1998.
- [13] F. Pertlik, "Vulcanite, CuTe: hydrothermal synthesis and crystal structure refinement," *Mineralogy and Petrology*, vol. 71, no. 3-4, pp. 149–154, 2001.
- [14] X. Zhang, X. Shi, and C. Wang, "Optimization of electrochemical aspects for epitaxial depositing nanoscale ZnSe thin films," *Journal of Solid State Electrochemistry*, vol. 13, no. 3, pp. 469–475, 2009.
- [15] W. Zhu, X. Liu, H. Liu, D. Tong, J. Yang, and J. Peng, "Coaxial heterogeneous structure of  $\text{TiO}_2$  nanotube arrays with CdS as a superthin coating synthesized via modified electrochemical atomic layer deposition," *Journal of the American Chemical Society*, vol. 132, no. 36, pp. 12619–12626, 2010.
- [16] H. Kou, X. Zhang, Y. Jiang et al., "Electrochemical atomic layer deposition of a  $\text{CuInSe}_2$  thin film on flexible multi-walled carbon nanotubes/polyimide nanocomposite membrane: structural and photoelectrical characterizations," *Electrochimica Acta*, vol. 56, no. 16, pp. 5575–5581, 2011.
- [17] X. Liang, N. Jayaraju, C. Thambidurai, Q. Zhang, and J. L. Stickney, "Controlled electrochemical formation of  $\text{GexSbyTez}$  using atomic layer deposition (ALD)," *Chemistry of Materials*, vol. 23, no. 7, pp. 1742–1752, 2011.
- [18] D. M. Kolb, R. Kötz, and K. Yamamoto, "Copper monolayer formation on platinum single crystal surfaces: optical and electrochemical studies," *Surface Science*, vol. 87, no. 1, pp. 20–30, 1979.
- [19] U. Demir and C. Shannon, "Reconstruction of cadmium sulfide monolayers on Au(100)," *Langmuir*, vol. 12, no. 2, pp. 594–596, 1996.
- [20] W. Shang, X. Shi, X. Zhang, C. Ma, and C. Wang, "Growth and characterization of electro-deposited  $\text{Cu}_2\text{O}$  and Cu thin films by amperometric  $I$ - $T$  method on ITO/glass substrate," *Applied Physics A: Materials Science and Processing*, vol. 87, no. 1, pp. 129–135, 2007.

## Research Article

# Fabrication of Mechanical Durable Polysiloxane Superhydrophobic Materials

Mengnan Qu, Jinmei He, Sun Zhe, Kanshe Li, Xiangrong Liu, and Chunxia Yu

*College of Chemistry and Chemical Engineering, Xi'an University of Science and Technology, Xi'an 710054, China*

Correspondence should be addressed to Jinmei He; [jinmhe@xust.edu.cn](mailto:jinmhe@xust.edu.cn)

Received 23 November 2014; Accepted 13 March 2015

Academic Editor: Ion Tiginyanu

Copyright © 2015 Mengnan Qu et al. This is an open access article distributed under the Creative Commons Attribution License, which permits unrestricted use, distribution, and reproduction in any medium, provided the original work is properly cited.

A mechanical durable polysiloxane superhydrophobic surface was successfully prepared by means of polymerization of silanes blending with particles. The as-prepared polysiloxane surface showed stable superhydrophobicity even after the surface underwent a long distance friction. The superhydrophobicity of the polysiloxane materials can be even slightly enhanced by the surface abrasion. The scanning electron microscopy demonstrated that the micro- and nanometer structures distributed through the whole materials thickness are responsible for the mechanical durable superhydrophobicity.

## 1. Introduction

The wettability of solid surface is one of the most important aspects in both theoretical and industrial applications [1]. One of the extreme cases of wettability, superhydrophobicity, has aroused considerable interests for many researchers inspired by the water-repellent nature of lotus leaves in recent years [2]. Heretofore, numerous methods were presented to fabricate the superhydrophobic surfaces with various materials by mimicking the surface of lotus leaves [3–10]. Due to its novel and important properties, the superhydrophobic surfaces were greatly anticipated to be used in applications such as self-cleaning coatings [11], anti-icing and fogging surfaces [12–14], nonwetting fabrics [15, 16], and buoyancy and flow enhancement [17, 18]. However, there are still quite few real applications with superhydrophobic materials so far.

Durability is of great importance in many applications of superhydrophobic surface. The micro- and nanoscale surface topography, which is essential for superhydrophobicity, can be very easily destroyed by even a slight friction on the surface. Up to date, studies have begun to address the mechanical durability and methods were developed to enhance the durability of superhydrophobic surface [19], such as fabricating self-healing surfaces, enhancing the robustness

of the hierarchical structure, and fabricating with hydrophobic materials. Li et al. demonstrated a self-healing superhydrophobic coating fabricated by preserving healing agents of reacted fluoroalkylsilane in layered polymeric coatings [20]. When the top layer of fluoroalkyl chains decomposes or the coatings are scratched, the healing agents migrate to the surface to restore the superhydrophobicity. In this case, it takes special conditions and hours time to restore the superhydrophobicity and the fluoroalkylsilane reagent is still required. It still remains a great challenge to fabricate superhydrophobic materials with excellent antiwear property.

In the current study, we presented a facile and cheap method to fabricate wear-durable superhydrophobic materials. Inspired by the ability that the lotus leaf can regenerate its microstructures, we have presented a strategy to fabricate the materials which are made up of the microstructures through the whole thickness of the materials to resist the surface abrasion. When the initial surface suffered abrasion, a new surface with new hierarchical roughness will appear. Herein, the micro- and nanoparticles were used to shape the hierarchical roughness and the organic silanes were used to fix these particles. The as-prepared polysiloxane superhydrophobic materials showed good antiwear property. From both theoretical and practical aspects, the present results and the fabrication strategy are of great significance

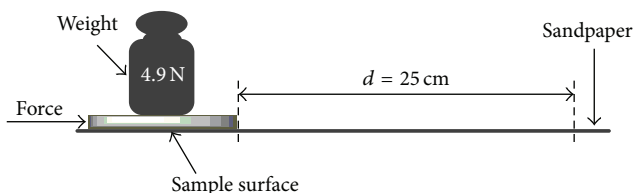


FIGURE 1: Schematic representation of abrasion measurement employed to evaluate wearability of the as-prepared material surface.

to fabricate superhydrophobic materials with stable antiwear property.

## 2. Experimental Section

**2.1. Materials.** The nanoscale silicon dioxide particles (50 nm) were purchased from Ross Technology Corporation. The microscale silicon dioxide particles (0.5–10  $\mu\text{m}$ , approximately 80% between 1 and 5  $\mu\text{m}$ ), the triethoxymethylsilane, and the diethoxydimethylsilane were all purchased from Sigma-Aldrich. Hydrochloric acid (HCl, 37%), the isopropanol, acetone, and methanol were analytical and used as received without any purification. In all the process, deionized water was used.

**2.2. Fabrication of the Antiwear Superhydrophobic Materials.** The 0.12 g nanoscale silicon dioxide particles and 0.6 g microscale silicon dioxide particles were added to 8 mL mixed solution of isopropanol and water (V:V = 2:1). The mixture was ultrasonic and dispersed for 30 min. Then 0.4 mL hydrochloric acid, 3.0 mL triethoxymethylsilane (0.015 mmol), and 0.90 mL diethoxydimethylsilane (0.005 mmol) were added to the mixed solution. The reaction mixture was stirred for 3 hours at 60°C. After the mixture was cooled to room temperature, the mixture was then dropped onto the glass slide (2.5 cm  $\times$  2.5 cm) surface until it spread all over the glass surface. A Petri dish cover was placed above the glass in order that the solvent evaporates slowly. After the mixture was dried overnight the samples were heat-treated at 160°C for 2 hours.

**2.3. Characterization.** The methodology illustrated in Figure 1 was invoked to evaluate the antiwear property. The grade of sandpapers adopted here is 180. The sample surfaces were blown by the  $\text{N}_2$  and washed by large amounts of water to remove the abrasion dust after each abrasion test. Contact angles were measured at ambient temperature. The advancing contact angles were measured by advancing a small volume of water onto the surface using a syringe. The receding contact angle was measured by slowly removing water from a drop already on the surface. The water droplets were 5  $\mu\text{L}$  for the contact angle measurement and 10  $\mu\text{L}$  for the sliding angle for measurement. For each sample, a minimum of four different readings was recorded and the typical error in measurements was 1°. The thickness of the material was measured with an optical microscope by observing the sample's cross section, and three different

readings were recorded. The surfaces were observed by the scanning electron microscopy (SEM, XL-30, Philips) to characterize their morphology.

## 3. Results and Discussion

The applications of superhydrophobic surfaces have been greatly hampered by the poor mechanical durability of the microscopic surface topography. Furthermore, most of the artificial superhydrophobic surfaces fabricated with hydrophilic materials required a hydrophobic surface coating and it is obvious that the original hydrophilic materials would be exposed when the surface was mechanically damaged. Herein we adopted the strategy to fabricate the superhydrophobic materials which consist of the micro- and nanometer scale structures through the whole thickness of materials to resist the abrasion. Two kinds of particles were used for fabricating the micro- and nanometer scale structures which are essential for superhydrophobicity. The triethoxymethylsilane was adopted to polymerize to embed and fix the microparticles. The diethoxydimethylsilane was added to control the polymer with appropriate rigidity, flexibility, and hydrophobicity. After the polymers were cured in oven, the as-prepared particles combined polysiloxane surface has a static water contact angle (CA) of 133°, as shown in Figure 2(a), while the water CA can be greatly increased from 133° to 160° after the polysiloxane surface bore a 25 cm slide on the sandpaper surface.

Although there is no standardized test method to evaluate the mechanical durability of a superhydrophobic surface [19], the apparatus by rubbing the sample against the sandpaper illustrated in Figure 1 was adopted here. Figure 3(a) showed the relationship between the static water CA and the length of the sample surface sliding on sandpaper. The initial water CA of the as-prepared particles combined polysiloxane surface is only 133°, which shows hydrophobicity not superhydrophobicity. After a 25 cm length rubbing against the sandpaper with a 500 g weight on the back of the sample, the water contact angle has increased greatly to 160° and presented the good superhydrophobicity. After one more 25 cm length slide, there is 2° increment of water CA. After this the water CA shows little fluctuation and changed from about 162° to 163° when the surface bore 75 cm to 200 cm length slide abrasion. Figure 2(b) showed the water droplets have a static water CA of 163° on the polysiloxane surface which bore a 200 cm slide on the sandpaper surface. A superhydrophobic steel surface, which is prepared according to Zhang's procedure [21], also underwent the same abrasion test. The result showed that the superhydrophobic steel surface, which is fabricated with hydrophilic material and hydrophobic coatings, has a poor antiwear property. The water CA decreased dramatically from 159° to 72° after the superhydrophobic surface endured a 25 cm length rubbing against the sandpaper with a 500 g weight on the back of the sample, as shown in Figure 3(a). After one more 25 cm length slide, the initial superhydrophobic steel surface lost completely its superhydrophobicity and switched to a hydrophilic surface with a water CA of 15°. The thickness

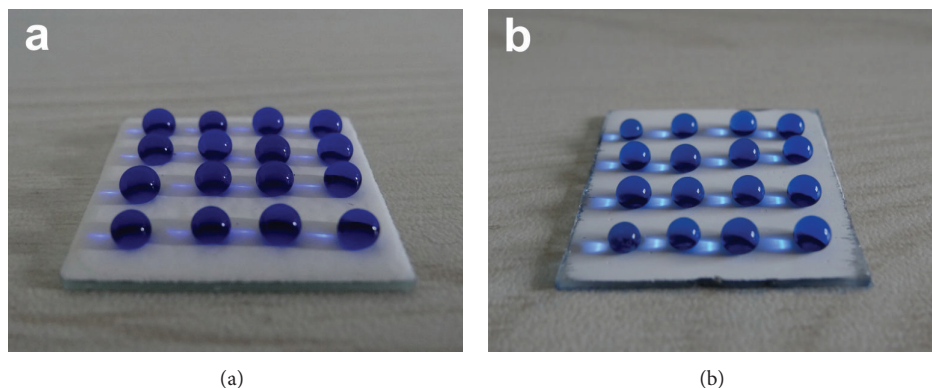


FIGURE 2: Images of water droplets dyed by methylene blue with different sizes on the particles combined polysiloxane surfaces of the same sample before (a) and after (b) the surface abrasion. The contact angles of the water droplets on the corresponding surfaces are  $133^\circ$  (a) and  $163^\circ$  (b), respectively.

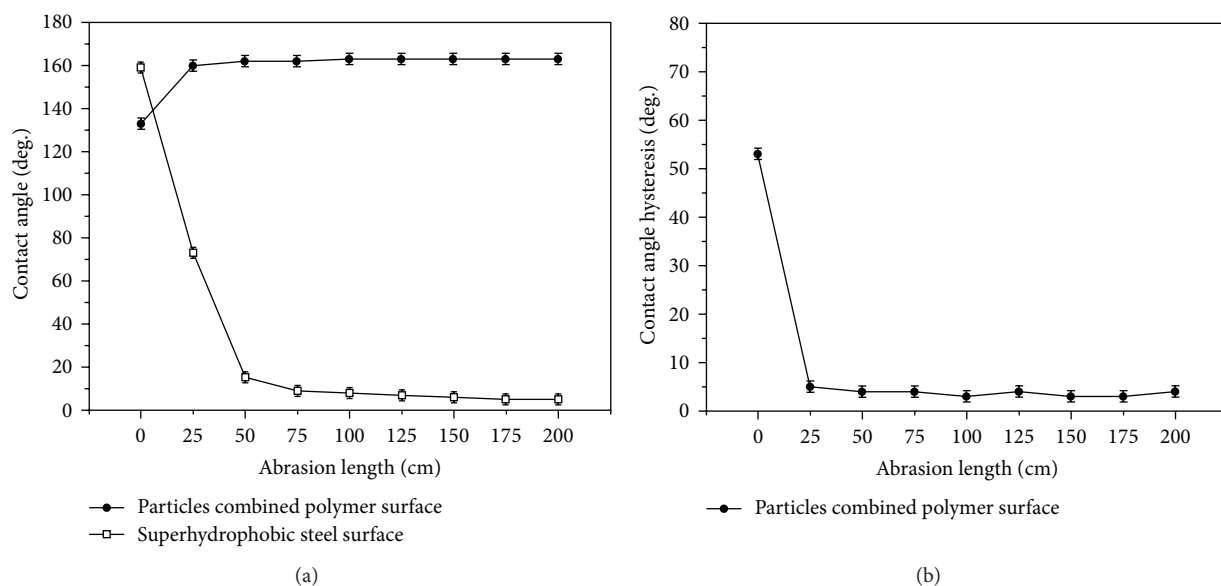


FIGURE 3: (a) The relationship between the static water contact angle and the lengths of the as-prepared polysiloxane surface (superhydrophobic steel surface) sliding on the sandpaper. (b) The relationship between the contact angle hysteresis and the lengths of the as-prepared polysiloxane surface sliding on the sandpaper.

measurements have also been carried out with an optical microscope before and after the abrasion test to investigate the thickness change of the polysiloxane film. It showed that the polysiloxane film of the as-prepared sample is 0.89  $\mu\text{m}$ , while the thickness of the film decreased to 0.22  $\mu\text{m}$  after the surface bore the 200 cm length slide abrasion. These results clearly revealed that the water repellency of the particles combined polysiloxane film not only has the mechanical durability but also can be enhanced with the increase of surface roughness by the surface abrasion.

In addition to a high static contact angle, a small contact angle hysteresis is also vital for a surface to be truly superhydrophobic because a small hysteresis leads to a water droplet being able to roll off of a surface easily. Thus, the contact angle hysteresis after the sample rubbed against the sandpaper should also be measured. Figure 3(b) showed

the CA hysteresis of the as-prepared particles combined polymers after each slide. Before the surface abrasion, the initial combined polysiloxane surface has a CA hysteresis of  $53^\circ$ , which is relatively high and implying a high roll-off angle. After a 25 cm slide against the sandpaper, the CA hysteresis has decreased greatly to  $5^\circ$  and the falling water droplet already can bounce from the surfaces and eventually roll off without ever coming to rest on the surface. The CA hysteresis shows little fluctuation when the surface bore 75 cm to 200 cm length slide abrasion. These results clearly proved that the as-prepared particles combined polymers have remained of the true superhydrophobicity even after a severe surface abrasion.

The initial as-prepared polysiloxane surface has a water CA of  $133^\circ$ , while the water CA is increased greatly to  $162^\circ$  after the surface abrasion. The great changes of the surfaces morphology before and after the surface abrasion have been

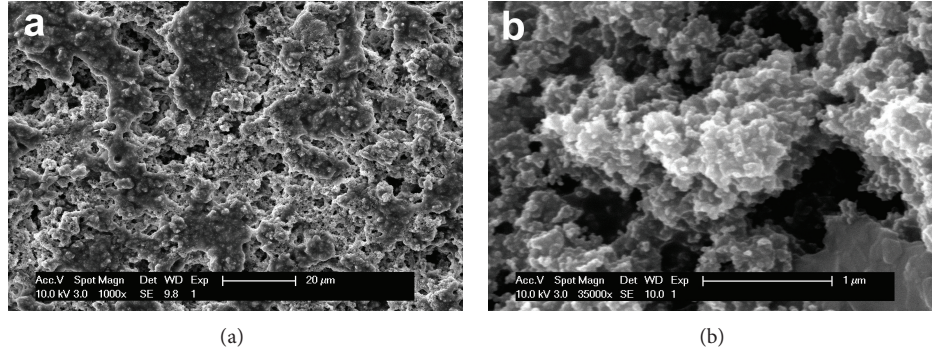


FIGURE 4: (a) SEM images of the as-prepared particles combined polysiloxane surface before the abrasion. (b) The porous and rough structures with micro- and nanometer scale exist below the outmost surface. The scale bars represent  $20\ \mu\text{m}$  (a) and  $1\ \mu\text{m}$  (b), respectively.

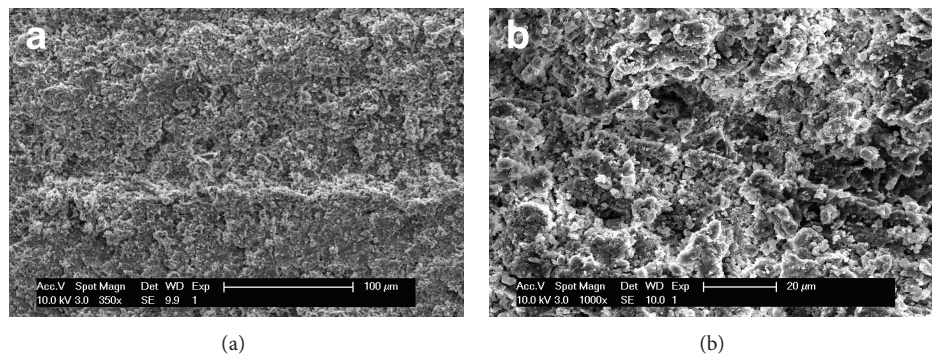


FIGURE 5: SEM images at different magnifications of the particles combined polysiloxane surface after the abrasion. The scale bars represent  $100\ \mu\text{m}$  (a) and  $20\ \mu\text{m}$  (b), respectively.

observed carefully by the scanning electron microscopy. Figure 4 is the SEM images before the surface abrasion test. There is a porous and rough structure which made up the materials. However, many-large-island structure with diameters of about  $20\text{--}50\ \mu\text{m}$  is distributed randomly across the upper surface, as shown in Figure 4(a). Figure 4(a) also revealed that the top of the island structure is relatively flat and there is no porous structure on the island surfaces. This relative flat surface probably formed during the process of the solvent evaporate process has decreased the surface roughness to a certain extent and lowered the water CA as a result. According to the Cassie equation [22],

$$\cos \theta_r = f_1 \cos \theta - f_2, \quad (1)$$

which is generally valid for heterogeneous surfaces, composed of air and a solid with superhydrophobicity. Here,  $\theta_r$  ( $132^\circ$ ) is the CA of the initial particles combined polysiloxane surface.  $\theta$  ( $107^\circ$ ) is the CA of the smooth polysiloxane surface without particles and  $f_1$  and  $f_2$  are the fractional interfacial areas of the microstructures and of the air in the interspaces among the microstructures, respectively (i.e.,  $f_1 + f_2 = 1$ ). According to the equation, the  $f_2$  value of the rough surface with the microstructures is estimated to be 0.53. This means that air occupies only 53% of contact area between the water droplet and the microstructures. Figure 4(b) is a magnified image of the porous and rough

structures with micrometer scale existing below this flat island. Figure 4(b) showed that the nanoscale particles are distributed across the rough structure surface. These micro- and nanometer scale structures inside the surface have the certain superhydrophobicity and it was exposed after the top flat islands were gotten rid of.

Figure 5(a) is the low-magnification image of the new surface produced by the surface abrasion. Compared with Figure 4(a), the main difference is that there are no more island structures on the top of surface and the remarkable scratches appeared across the surface. Figure 5(b) showed that a furrow-like structure with width of  $20\text{--}50\ \mu\text{m}$  micrometer was parallel distributed on the surface. These scratches which are produced by the sandpaper during sample sliding on sandpaper surface are vital to the superhydrophobicity since this behavior has gotten rid of the flat-top island and greatly increased the surface roughness. These images clearly revealed that a new surface appeared after the surface abrasion just like the natural superhydrophobic plant leaves regenerating their hydrophobic wax coating. The existence of the nanometer particles is also important to the superhydrophobicity for forming the nanometer scale structure and bestowing the synergistic binary geometric structures on the surfaces. These images demonstrated that the particles combined polymers surface after the surface abrasion has the structures at the micro- and nanometer scale, and such synergistic binary geometric structures made the surface

roughness increase and the air fraction of the interfacial areas high enough. The binary micro- and nanometer scale structures have already trapped enough amount of air to prevent the penetration of the water droplet into the holes, which bestowed the superhydrophobicity on the surfaces. According to the Cassie equation, the  $f_2$  value of the rough surface with the hierarchical rough structures is estimated to be 0.93. This means that air already occupies 93% of contact area, which is responsible for the enhancement of superhydrophobicity after the surface abrasion.

#### 4. Conclusions

In summary, we fabricated the mechanically durable superhydrophobic surfaces with organic silane and particles by polymerizing silane and embedding the particles. The as-prepared particles combined polysiloxane surface showed stable superhydrophobicity even after the surface underwent a long distance friction. Furthermore, the superhydrophobicity of the polymer materials can be enhanced or restored. These properties will greatly accelerate and broaden the applications of superhydrophobic surfaces. We expect this strategy will open a new avenue in the preparation of mechanically durable superhydrophobic surface.

#### Conflict of Interests

The authors declare that there is no conflict of interests regarding the publication of this paper.

#### Acknowledgments

The authors thank the National Natural Science Foundation of China (Grants no. 21473132 and no. 21102113), the Natural Science Foundation of Shaanxi Province, China (Grant no. 2014JM2047), and the Natural Science Research Project of Science and Technology Agency of Shaanxi Province, China (Grant no. 2013KJXX-41), for continuing financial support.

#### References

- [1] T. Sun, L. Feng, X. Gao, and L. Jiang, "Bioinspired surfaces with special wettability," *Accounts of Chemical Research*, vol. 38, pp. 644–652, 2005.
- [2] W. Barthlott and C. Neinhuis, "Purity of the sacred lotus, or escape from contamination in biological surfaces," *Planta*, vol. 202, no. 1, pp. 1–8, 1997.
- [3] L. Passoni, G. Bonvini, A. Luzio, A. Facibeni, C. E. Bottani, and F. Di Fonzo, "Multiscale effect of hierarchical self-assembled nanostructures on superhydrophobic surface," *Langmuir*, vol. 30, no. 45, pp. 13581–13587, 2014.
- [4] J. C. Tuberquia, N. Nizamidin, R. R. Harl et al., "Surface-initiated polymerization of superhydrophobic polymethylene," *Journal of the American Chemical Society*, vol. 132, no. 16, pp. 5725–5734, 2010.
- [5] S. Huang, "Mussel-inspired one-step copolymerization to engineer hierarchically structured surface with superhydrophobic properties for removing oil from water," *ACS Applied Materials & Interfaces*, vol. 6, no. 19, pp. 17144–17150, 2014.
- [6] N. Verplanck, E. Galopin, J.-C. Camart, V. Thomy, Y. Coffinier, and R. Boukherroub, "Reversible electrowetting on superhydrophobic silicon nanowires," *Nano Letters*, vol. 7, no. 3, pp. 813–817, 2007.
- [7] T. Sun, G. Wang, H. Liu, L. Feng, L. Jiang, and D. Zhu, "Control over the wettability of an aligned carbon nanotube film," *Journal of the American Chemical Society*, vol. 125, no. 49, pp. 14996–14997, 2003.
- [8] J. Bravo, L. Zhai, Z. Wu, R. E. Cohen, and M. F. Rubner, "Transparent superhydrophobic films based on silica nanoparticles," *Langmuir*, vol. 23, no. 13, pp. 7293–7298, 2007.
- [9] K. Tadanaga, J. Morinaga, A. Matsuda, and T. Minami, "Superhydrophobic—superhydrophilic micropatterning on flowerlike alumina coating film by the sol–gel method," *Chemistry of Materials*, vol. 12, no. 3, pp. 590–592, 2000.
- [10] Y. Li, X. J. Huang, S. H. Heo et al., "Superhydrophobic bionic surfaces with hierarchical microsphere/SWCNT composite arrays," *Langmuir*, vol. 23, no. 4, pp. 2169–2174, 2007.
- [11] I. P. Parkin and R. G. Palgrave, "Self-cleaning coatings," *Journal of Materials Chemistry*, vol. 15, no. 17, pp. 1689–1695, 2005.
- [12] L. Cao, A. K. Jones, V. K. Sikka, J. Wu, and D. Gao, "Anticing superhydrophobic coatings," *Langmuir*, vol. 25, no. 21, pp. 12444–12448, 2009.
- [13] J. A. Howarter and J. P. Youngblood, "Self-cleaning and antifog surfaces via stimuli-responsive polymer brushes," *Advanced Materials*, vol. 19, no. 22, pp. 3838–3843, 2007.
- [14] X. Gao, X. Yan, X. Yao et al., "The dry-style antifogging properties of mosquito compound eyes and artificial analogues prepared by soft lithography," *Advanced Materials*, vol. 19, no. 17, pp. 2213–2217, 2007.
- [15] L. Gao and T. J. McCarthy, "'Artificial lotus leaf' prepared using a 1945 patent and a commercial textile," *Langmuir*, vol. 22, no. 14, pp. 5998–6000, 2006.
- [16] W. Choi, A. Tuteja, S. Chhatre, J. M. Mabry, R. E. Cohen, and G. H. McKinley, "Fabrics with tunable oleophobicity," *Advanced Materials*, vol. 21, no. 21, pp. 2190–2195, 2009.
- [17] Q. Pan and M. Wang, "Miniature boats with striking loading capacity fabricated from superhydrophobic copper meshes," *ACS Applied Materials & Interfaces*, vol. 1, no. 2, pp. 420–423, 2009.
- [18] J. Ou, B. Perot, and J. P. Rothstein, "Laminar drag reduction in microchannels using ultrahydrophobic surfaces," *Physics of Fluids*, vol. 16, no. 12, pp. 4635–4643, 2004.
- [19] T. Verho, C. Bower, P. Andrew, S. Franssila, O. Ikkala, and R. H. A. Ras, "Mechanically durable superhydrophobic surfaces," *Advanced Materials*, vol. 23, no. 5, pp. 673–678, 2011.
- [20] Y. Li, L. Li, and J. Sun, "Bioinspired self-healing superhydrophobic coatings," *Angewandte Chemie*, vol. 49, no. 35, pp. 6129–6133, 2010.
- [21] M. Qu, B. Zhang, S. Song, L. Chen, J. Zhang, and X. Cao, "Fabrication of superhydrophobic surfaces on engineering materials by a solution-immersion process," *Advanced Functional Materials*, vol. 17, no. 4, pp. 593–596, 2007.
- [22] A. B. D. Cassie and S. Baxter, "Wettability of porous surfaces," *Transactions of the Faraday Society*, vol. 40, pp. 546–551, 1944.

## Research Article

# A Facile Strategy for the Functionalization of Boron Nitride Nanotubes with Pd Nanoparticles

Yuanlie Yu,<sup>1</sup> Hua Chen,<sup>1</sup> and Yun Liu<sup>2</sup>

<sup>1</sup>Centre for Advanced Microscopy, Australian National University, Canberra, ACT 0200, Australia

<sup>2</sup>Research School of Chemistry, Australian National University, Canberra, ACT 0200, Australia

Correspondence should be addressed to Hua Chen; [hua.chen@anu.edu.au](mailto:hua.chen@anu.edu.au)

Received 7 October 2014; Accepted 17 November 2014

Academic Editor: Mengnan Qu

Copyright © 2015 Yuanlie Yu et al. This is an open access article distributed under the Creative Commons Attribution License, which permits unrestricted use, distribution, and reproduction in any medium, provided the original work is properly cited.

A facile *in situ* fabrication of palladium nanoparticles decorated boron nitride nanotubes (Pd-BNNTs) is described. The decoration of BNNTs was carried out by the self-regulated reduction of palladium chloride (PdCl<sub>2</sub>) with the aid of sodium dodecyl sulfate (SDS). During the preparation process, the surfactant SDS plays a dual role: it aids the dispersibility of BNNTs and produces the reductant of CH<sub>3</sub>(CH<sub>2</sub>)<sub>10</sub>CH<sub>2</sub>OH. Then the CH<sub>3</sub>(CH<sub>2</sub>)<sub>10</sub>CH<sub>2</sub>OH can reduce Pd<sup>2+</sup> to form Pd nanoparticles on the surface of BNNTs. The as-prepared Pd-BNNTs were characterized by field emission scanning electron microscopy, transmission electron microscopy, X-ray energy dispersive spectroscopy, and Fourier transform infrared spectroscopy. The results show that the Pd nanocrystalline particles can be deposited onto the BNNTs surface *via* this simple route. This approach constitutes a basis for the assembly and integration of nanoscale materials onto BNNTs and puts a light on the potential application of the BNNTs in electronic, catalysis, and hydrogen storage fields.

## 1. Introduction

Boron nitride nanotubes (BNNTs) have recently attracted increased attention due to their various potential applications in electronic, mechanical, and optical devices. Structurally similar to carbon nanotubes (CNTs), BNNTs exhibit excellent mechanical [1–3] and thermal [4–6] properties. Despite these similarities, BNNTs exhibit excellent chemical stability and high resistance to oxidation at high temperature [7]. BNNTs are uniform semiconductors with a bandgap of 5.5 eV, basically independent of tube chirality and diameters [8], while CNTs exhibit variable metallic and semiconducting characteristics. In addition, recent research has also demonstrated that BNNTs can be used as room temperature hydrogen storage media [9], humidity sensor devices [10], and oil/water separation materials [11]. Considering the above-mentioned properties, BNNTs have become very attractive for innovative applications in various fields of science and technology, especially in hazardous and high temperature environments. However, the insolubility in common solvents and good insulating property also limit their applications. Further modification of BNNTs is therefore necessary for

the utilization of BNNT-based materials for novel sensory, electronic, catalytic, and biomedical applications. For example, the multiwalled BNNTs modified with long alkyl chains are soluble in many organic solvents [12]. And subsequent cathodoluminescence and UV-Vis absorption tests show that long alkyl chains can induce drastic changes in the band structure of BNNTs [12]. The Au decoration on the surface of BNNTs significantly enhanced their field emission current densities [13]. Additionally, the introduction of rare-earth element into the walls of BNNTs can result in broad and tunable light emission [14, 15], making them a potential candidate in nanosized lighting sources and nanospectroscopy. Yet it is difficult to directly decorate the BNNTs with metal nanoparticles by chemical route due to the good chemical inertness of the BNNTs. At present, the synthesis of metal nanoparticles decorated BNNTs is mainly realized by physical vapour deposition (PVD) [13] or a complicated chemical route [16]. Although metal nanoparticles with uniform size can be obtained by PVD, the deposition only occurs on the top surface of bulk BNNTs samples facing the metal target. And, for previous chemical route, the surface of the BNNTs and metal nanoparticles needs to be functionalized with

organic molecules, which is fairly complicated. Therefore, simpler and effective methods are required to prepare these metal nanoparticles decorated BNNTs.

In this work, a facile *in situ* preparation of Pd-BNNTs is developed. The process was carried out by self-regulated reduction of PdCl<sub>2</sub> with the aid of SDS. The method provides a basis for the assembly and integration of nanoscale materials onto the BNNTs. In addition, Pd is an important transition metal in catalysis due to their high hydrogen solubility, diffusivity, and corrosion resistance [17, 18] and it can also be used as hydrogen storage media [19] for its high affinity for hydrogen. That is, the introduction of Pd may improve the catalytic activity and hydrogen adsorption property of the BNNTs, making them potential candidate in these fields.

## 2. Experimental Procedure

The BNNTs were synthesized by a ball milling and subsequent high temperature annealing process [13–15]. Typically, the amorphous boron powder was first milled in a planetary mill with a stainless steel bowl and several balls for 50 h at a rotation speed of 300 rpm. The weight ratio of the milling balls to the boron powder was 50 : 1. Then, the milled boron powder was annealed in a tube furnace at 1100°C for 2 h under a H<sub>2</sub>/N<sub>2</sub> (15% H<sub>2</sub>) gas flow (100 mL/min). Then, 0.5 mg of as-synthesized BNNTs was suspended in 2 mL of 0.05 M aqueous SDS solution and ultrasonicated for 30 min. Subsequently, 1 mL of PdCl<sub>2</sub> saturated solution (20°C) was added to the BNNTs/SDS dispersion and the mixture was refluxed for 6 h at 130 ± 1°C. After cooling down to room temperature naturally, the reaction mixture was filtered with 0.45 μm membrane filter, washed several times with distilled water to remove the excess surfactant, and then redissolved in ethanol.

Zeiss UltraPlus analytical field emission scanning electron microscopy (FESEM) was used for morphology investigation. X-ray energy dispersive spectroscopy (EDS) attached to the Zeiss UltraPlus analytical FESEM was used to examine the components. Philips CM300 high-resolution transmission electron microscopy (HRTEM) was employed to probe the interior construction of the as-prepared BNNTs and Pd-BNNTs. The X-ray diffraction spectrum was collected with BRUKER-AXS X-ray diffractometer (XRD) with monochromatic Cu Kα radiation. The bonding information of BNNTs was identified with PerkinElmer Fourier transform infrared spectroscopy (FTIR).

## 3. Results and Discussion

As shown in Figure 1(a), the typical XRD pattern of the as-prepared BNNTs shows three peaks (marked with black rhombus “◆”) at the d-spacing of 3.36, 2.15, and 2.06 which can be assigned to (002), (100), and (101) planes of hexagonal boron nitride structure (JCPDF card number 73-2095) [20]. The rest peak marked with hollow rhombus (◇) can be identified as (110) plane of α-Fe, which was introduced in the ball milling process and used as catalyst in the BNNTs growth process. In addition, two IR absorption regions can

be obviously distinguished at 805 cm<sup>-1</sup> and 1385 cm<sup>-1</sup> in the FTIR spectrum (Figure 1(b)), corresponding to the out-of-plane radial buckling (R) mode where boron and nitrogen atoms are moving radially inward or outward and transverse optical (TO) mode of h-BN sheets that vibrate along the longitudinal or tube axis of BNNTs, respectively [21, 22]. Figures 1(c) and 1(d) show the typical FESEM and TEM images and EDS spectrum of the as-prepared BNNTs. The FESEM image (Figure 1(c)) reveals that pure products were formed on the sample surfaces, which possess a high density of one-dimensional structures with relatively uniform diameters in the range of 100–300 nm. The inset EDS spectrum confirms that the main components composed of the nanotubes are boron and nitride. Further examination carried out by TEM analysis (Figure 1(d)) indicates that the BNNTs are formed by repeated cup-like structures with void interior. The intrinsic plane spacing of the walls is determined to be 0.34 nm in terms of the HRTEM images (inset in Figure 1(d)), which is well matched with that of h-BN (002) plane.

As described in Figure 2, the *in situ* decoration of BNNTs with Pd nanoparticles is realized by refluxing a dispersion of BNNTs in an aqueous solution of SDS/PdCl<sub>2</sub> for 6 h (details can be seen in Experimental Procedure section). During the whole preparation process, the surfactant SDS plays a dual role. Firstly, as the surfactant, a great deal of SDS molecules will be absorbed on the surface of the BNNTs thus aiding the dispersion of BNNTs in water as shown in Figure 2. Secondly, SDS acts as a reactant to participate in the oxidation-reduction reaction. During the reflux process, CH<sub>3</sub>(CH<sub>2</sub>)<sub>10</sub>CH<sub>2</sub>OH was generated by the reaction of SDS with H<sub>2</sub>O (reaction (1) in Figure 3), and then the Pd<sup>2+</sup> ions that had diffused into the core of the micelle were reduced by the CH<sub>3</sub>(CH<sub>2</sub>)<sub>10</sub>CH<sub>2</sub>OH to form Pd atoms (reaction (2) in Figure 3) [23]. With the increase in the reduced Pd atoms, they agglomerated together on the BNNTs' surface to form Pd nanoparticles. After separating and carefully rinsing, the residual organic was removed and Pd-BNNTs were achieved. Figure 4(a) shows a typical SEM image of the Pd nanoparticles decorated BNNT, where Pd nanoparticles can be clearly seen attached on the surface of BNNT. EDS analysis (inset in Figure 4(a)) confirmed that the attached nanoparticles are indeed palladium. Figures 4(b) and 4(c) present the TEM micrographs of pristine and Pd nanoparticles decorated BNNTs, respectively. Comparing Figure 4(c) with Figure 4(b), the dark spots particles can be clearly seen on the surface of Pd nanoparticles decorated BNNT. Inset in Figure 4(c) is a typical HRTEM image of the Pd nanoparticles attached on the surface of BNNTs. The lattice constant of the nanoparticles is calculated to be 0.197 nm, which is the same as the (200) plane distance of the cubic Pd crystal structure [24], demonstrating that the Pd nanoparticles are successfully deposited on the surface of the BNNTs.

## 4. Conclusions

It has been demonstrated that Pd-BNNTs can be prepared by the self-regulated reduction of PdCl<sub>2</sub> with the aid of SDS.

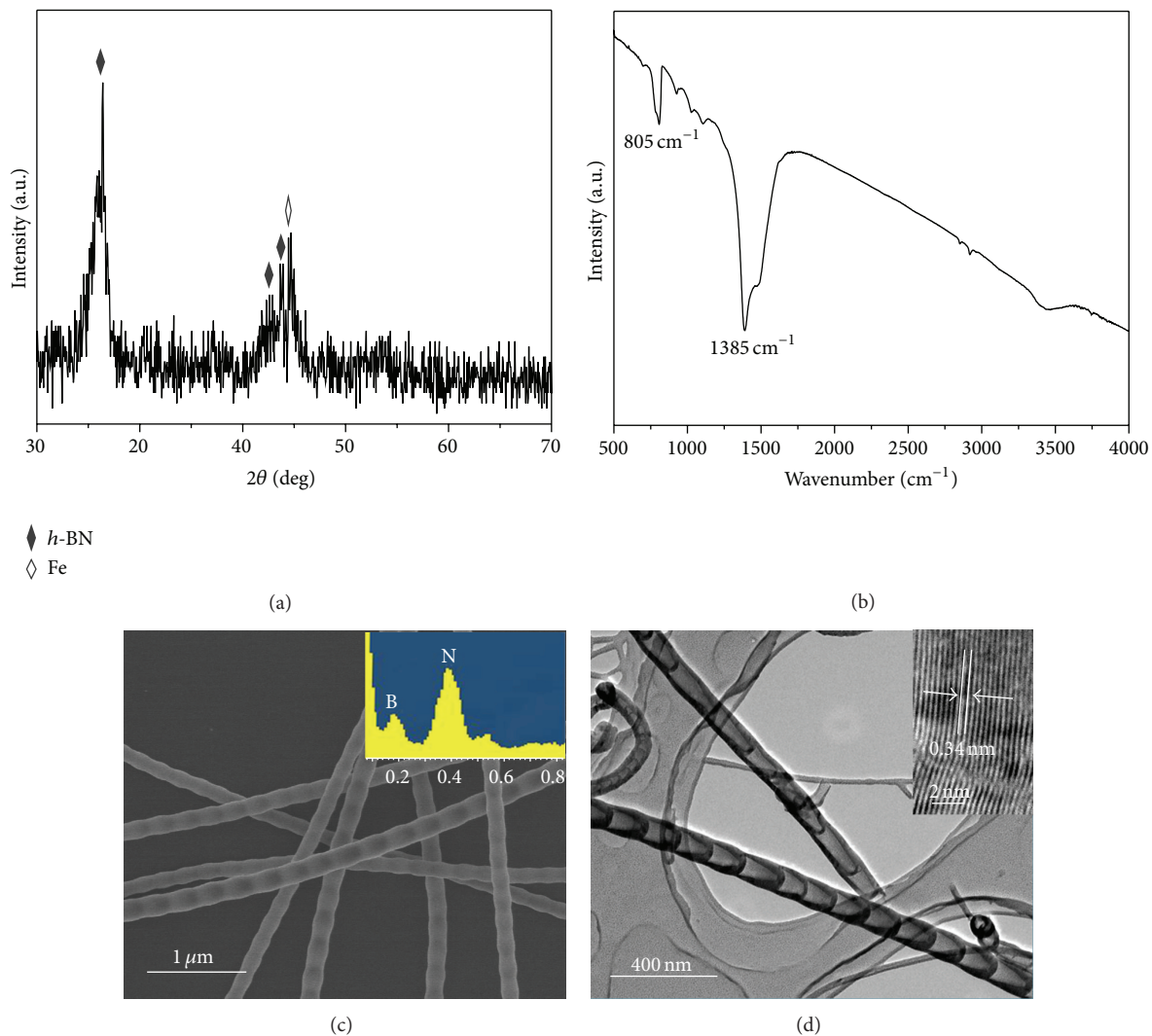


FIGURE 1: (a) The XRD pattern and (b) the FTIR spectrum of the BNNTs; (c) and (d) the FESEM image (inset is the EDS spectrum) and the TEM image (inset is the HRTEM image) of the as-synthesized BNNTs.

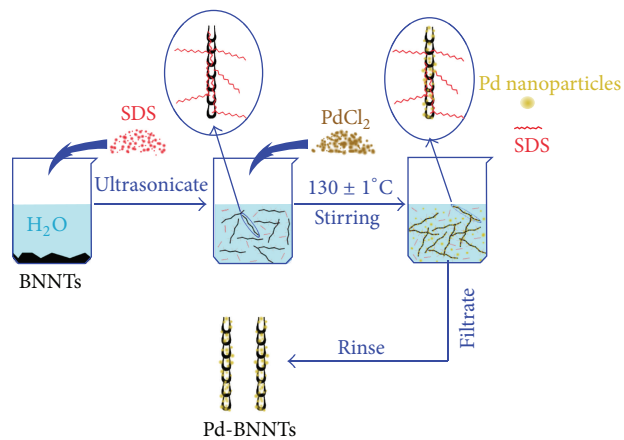


FIGURE 2: The process for the decoration of BNNTs with Pd nanoparticles.

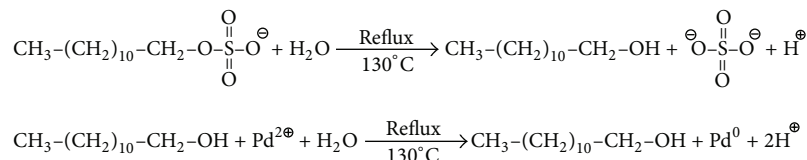


FIGURE 3: The reactions during the reflux process.

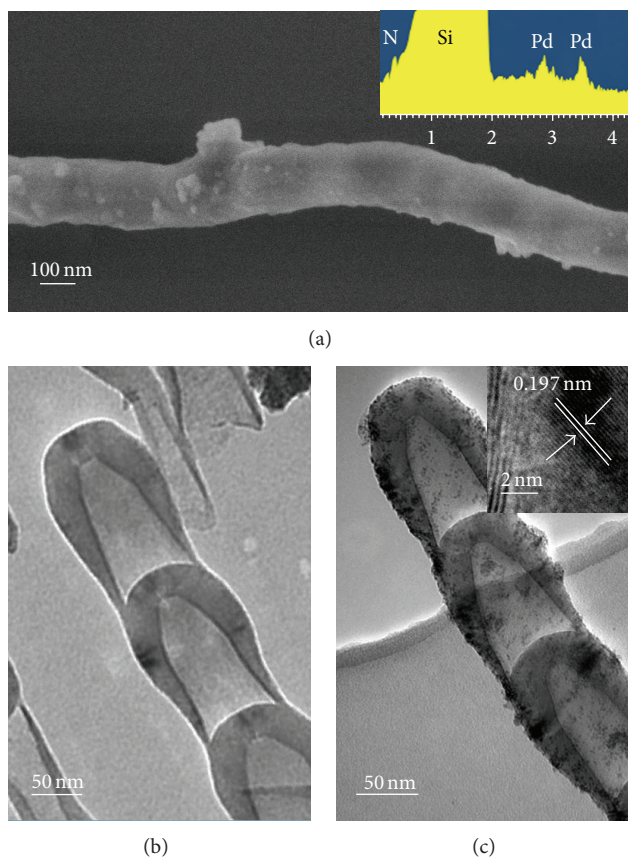


FIGURE 4: (a) FESEM image of the Pd-BNNTs (inset is the corresponding EDS spectrum); (b) and (c) the typical TEM images of pristine BNNTs and BNNTs with Pd nanoparticles (inset is the HRTEM image).

During the preparation process, the surfactant SDS plays a very important role in the dispersibility of BNNTs and reduction of  $\text{Pd}^{2+}$  to form Pd nanoparticles. The characterization results indicate that Pd nanocrystalline particles can be successfully deposited on the BNNTs surface *via* this simple wet chemical route, which constitutes a basis for the assembly and integration of nanoscale materials onto the BNNTs. The good activity catalysis of Pd combined with the excellent properties of BNNTs may make the Pd-BNNTs be potential candidate in the application of electronic and catalysis fields.

### Conflict of Interests

The authors declare that there is no conflict of interests regarding the publication of this paper.

### Acknowledgments

The authors acknowledge the financial support from the Australian Microscopy and Microanalysis Research Facility (AMMRF) and from the Australian Research Council in the form of the Discovery Projects.

### References

- [1] N. G. Chopra and A. Zettl, "Measurement of the elastic modulus of a multi-wall boron nitride nanotube," *Solid State Communications*, vol. 105, no. 5, pp. 297–300, 1998.
- [2] A. P. Suryavanshi, M.-F. Yu, J. Wen, C. Tang, and Y. Bando, "Elastic modulus and resonance behavior of boron nitride nanotubes," *Applied Physics Letters*, vol. 84, no. 14, pp. 2527–2529, 2004.

- [3] D. Golberg, P. M. F. J. Costa, O. Lourie et al., "Direct force measurements and kinking under elastic deformation of individual multiwalled boron nitride nanotubes," *Nano Letters*, vol. 7, no. 7, pp. 2146–2151, 2007.
- [4] L. Wirtz and A. Rubio, "Ab initio calculations of the lattice dynamics of boron nitride nanotubes," *Physical Review B*, vol. 68, no. 4, Article ID 045425, 2003.
- [5] D. Sanchez-Portal and E. Hernandez, "Vibrational properties of single-wall nanotubes and monolayers of hexagonal BN," *Physical Review B*, vol. 66, no. 23, Article ID 235415, pp. 1–12, 2002.
- [6] V. N. Popov, "Lattice dynamics of single-walled boron nitride nanotubes," *Physical Review B*, vol. 67, no. 8, Article ID 085408, 6 pages, 2003.
- [7] Y. Xiao, X. H. Yan, J. X. Cao, J. W. Ding, Y. L. Mao, and J. Xiang, "Specific heat and quantized thermal conductance of single-walled boron nitride nanotubes," *Physical Review B*, vol. 69, no. 20, Article ID 205415, 2004.
- [8] A. Rubio, J. L. Corkill, and M. L. Cohen, "Theory of graphitic boron nitride nanotubes," *Physical Review B*, vol. 49, no. 7, pp. 5081–5084, 1994.
- [9] R. Z. Ma, Y. Bando, H. W. Zhu, T. Sato, C. L. Xu, and D. H. Wu, "Hydrogen uptake in boron nitride nanotubes at room temperature," *Journal of the American Chemical Society*, vol. 124, no. 26, pp. 7672–7673, 2002.
- [10] Y. Yu, H. Chen, Y. Liu, L. H. Li, and Y. Chen, "Humidity sensing properties of single Au-decorated boron nitride nanotubes," *Electrochemistry Communications*, vol. 30, pp. 29–33, 2013.
- [11] Y. L. Yu, H. Chen, Y. Liu, V. Craig, L. H. Li, and Y. Chen, "Superhydrophobic and superoleophilic boron nitride nanotube-coated stainless steel meshes for oil and water separation," *Advanced Materials Interfaces*, vol. 1, no. 1, Article ID 1300002, pp. 1–5, 2014.
- [12] C. Zhi, Y. Bando, C. Tang et al., "Covalent functionalization: towards soluble multiwalled boron nitride nanotubes," *Angewandte Chemie International Edition*, vol. 44, no. 48, pp. 7932–7935, 2005.
- [13] H. Chen, H. Zhang, L. Fu et al., "Nano Au-decorated boron nitride nanotubes: conductance modification and field-emission enhancement," *Applied Physics Letters*, vol. 92, no. 24, Article ID 243105, 2008.
- [14] H. Chen, Y. Chen, C. P. Li et al., "Eu-doped boron nitride nanotubes as a nanometer-sized visible-light source," *Advanced Materials*, vol. 19, no. 14, pp. 1845–1848, 2007.
- [15] H. Chen, Y. Chen, and Y. Liu, "Cathodoluminescence of boron nitride nanotubes doped by ytterbium," *Journal of Alloys and Compounds*, vol. 504, supplement 1, pp. S353–S355, 2010.
- [16] H. Chen, Y. Chen, Y. Liu et al., "Rare-earth doped boron nitride nanotubes," *Materials Science and Engineering: B*, vol. 39, no. 40, pp. 189–192, 2008.
- [17] T. Sainsbury, T. Ikuno, D. Okawa, D. Pacilé, J. M. J. Fréchet, and A. Zettl, "Self-assembly of gold nanoparticles at the surface of amine- and thiol-functionalized boron nitride nanotubes," *Journal of Physical Chemistry C*, vol. 111, no. 35, pp. 12992–12999, 2007.
- [18] B. M. Trost, J. Xu, and T. Schmidt, "Palladium-catalyzed decarboxylative asymmetric allylic alkylation of enol carbonates," *Journal of the American Chemical Society*, vol. 131, no. 51, pp. 18343–18357, 2009.
- [19] S. Yu, U. Welp, L. Z. Hua, A. Rydh, W. K. Kwok, and H. H. Wang, "Fabrication of palladium nanotubes and their application in hydrogen sensing," *Chemistry of Materials*, vol. 17, no. 13, pp. 3445–3450, 2005.
- [20] Q. Qian, J. Wang, Y. Gu et al., "Convenient synthesis of Fe-filled boron nitride nanotubes by SHS method," *Materials Letters*, vol. 65, no. 5, pp. 866–868, 2011.
- [21] E. Borowiak-Palen, T. Pichler, G. G. Fuentes et al., "Infrared response of multiwalled boron nitride nanotubes," *Chemical Communications*, vol. 9, no. 1, pp. 82–83, 2003.
- [22] J. L. Wang, C. H. Lee, Y. Bando, D. Golberg, and Y. K. Yap, "B-C-N nanotubes and related nanostructures," in *Multiwalled Boron Nitride Nanotubes: Growth, Properties, and Applications*, vol. 6 of *Lecture Notes in Nanoscale Science and Technology*, chapter 2, pp. 23–44, Springer, New York, NY, USA, 2009.
- [23] C. L. Lee, C. C. Wan, and Y. Y. Wang, "Synthesis of metal nanoparticles via self-regulated reduction by an alcohol surfactant," *Advanced Functional Materials*, vol. 11, no. 5, pp. 344–347, 2011.
- [24] F. Ksar, G. Surendran, L. Ramos et al., "Palladium nanowires synthesized in hexagonal mesophases: application in ethanol electrooxidation," *Chemistry of Materials*, vol. 21, no. 8, pp. 1612–1617, 2009.

## Research Article

# Fabrication and Evaluation of Polycaprolactone/Gelatin-Based Electrospun Nanofibers with Antibacterial Properties

Lor Huai Chong,<sup>1</sup> Mim Mim Lim,<sup>1</sup> and Naznin Sultana<sup>1,2</sup>

<sup>1</sup>Faculty of Biosciences and Medical Engineering, Universiti Teknologi Malaysia, 81310 Johor, Malaysia

<sup>2</sup>Advanced Membrane Technology Research Centre, Universiti Teknologi Malaysia, 81310 Johor, Malaysia

Correspondence should be addressed to Naznin Sultana; naznin@biomedical.utm.my

Received 8 September 2014; Accepted 27 November 2014

Academic Editor: Qi Wang

Copyright © 2015 Lor Huai Chong et al. This is an open access article distributed under the Creative Commons Attribution License, which permits unrestricted use, distribution, and reproduction in any medium, provided the original work is properly cited.

Nanofibrous scaffolds were fabricated through blending of a synthetic polymer, polycaprolactone (PCL), and a natural polymer, gelatin (GE), using an electrospinning technique. Processing and solution parameters were optimized to determine the suitable properties of PCL/GE-based nanofibers. Several characterizations were conducted to determine surface morphology by scanning electron microscopy (SEM), wettability using water contact angle measurement, and chemical bonding analysis using attenuated total reflectance (ATR) of PCL/GE-based nanofibers. Experimental results showed that 14% (w/v) PCL/GE with a flow rate of 0.5 mL/h and 18 kV demonstrated suitable properties. This nanofiber was then further investigated for its *in vitro* degradation, drug loading (using a model drug, tetracycline hydrochloride), and antibacterial testing (using zone inhibition method).

## 1. Introduction

In cases of full-thickness burns or deep ulcers, there are no remaining sources of cells for tissue regeneration and recovery [1]. These severely injured parts will deteriorate further if a patient has diabetes [2]. Hence, tissue engineering (TE) technology is crucial to solve this issue. TE provides an alternative pathway for tissue regeneration and recovery using polymeric biomaterials [3] to harvest tissues for transplantation [4] from the patient's own cells. In human skin, extracellular matrix (ECM) is a key element in monitoring cell behavior while scaffold design is the most important component in TE [5]. Biomaterials scaffolds play a pivotal role in providing a synthetic but suitable ECM environment for growing cells and drug delivery in severely injured skin [6].

Recently, the rapid growth of nanotechnology has spurred the development of nanofibrous scaffolds [7]. There are many fabrication techniques including phase separation, self-assembly, and electrospinning [8]. Among these, electrospinning is the most widely used [9]. The technique of electrospinning is dependent on several types of parameters, including solution parameters such as concentration, viscosity, and solution conductivity and processing parameters such as voltage applied, temperature, flow rate, and distance

between tip of syringe and collector [10–12]. Electrospinning technology has led to wide interest in scaffold fabrication, in the main because the biological and mechanical properties of nanofibers can be easily manipulated by altering the solution and processing parameters [13]. Electrospinning is a relatively simple technique for fabricating highly porous nanosize scaffolds from a wide variety of polymers including biopolymers such as gelatin, collagen, and fibrinogen [14] on a large scale. The large surface area to volume ratio of nanofibers enhances the diffusion efficiency of nutrient and gaseous exchange [15]. Porosity, air permeability, and surface wettability of nanofibers are important elements for regenerating skin tissue [16]. Also electrospinning is able to fabricate nanofibers with similar morphology and architectural features to the natural ECM in skin [13]. In addition, biodegradable scaffolds are able to degrade and thus change their structure over time to seeded cells in order to proliferate and produce their own ECM [17]. Using biodegradable polymer via electrospinning is important in skin to avoid the need for surgical removal [18].

Recent studies have shown that PCL/GE can be used for dermal reconstitution [13] and wound healing or wound dressing [19]. However, there is less research on the antibacterial testing of PCL/GE nanofibers for the application

of skin tissue regeneration. It is essential to apply antibiotic to the severely injured part of the skin via a drug delivery system to reduce inflammation caused by bacterial infection [20]. Therefore, it is important to fabricate an antibacterial test for PCL/GE-based nanofibers to avoid the interference of bacteria with cell activities during tissue regeneration and repair. Kenawy et al.'s research demonstrated the potential of electrospun nanofibers as effective carriers for drug delivery and tetracycline hydrochloride was used in the research [21]. According to Bhardwaj and Kundu's research, tetracycline has been found to prevent skin inflammation from bacterial infection [14]. However, there is still no report investigating the antibacterial activities of tetracycline hydrochloride in PCL/GE nanofibers for skin loss application.

In this paper, PCL/GE-based nanofibers were fabricated using the electrospinning technique by varying certain parameters. Characterizations and degradation tests were carried out to determine potential nanofibers for further investigation. Tetracycline hydrochloride was loaded into PCL/GE-based nanofibers and tested on their antibacterial activity against Gram-negative and Gram-positive bacteria.

## 2. Materials and Methods

**2.1. Materials.** Polymer of GE powder from porcine skin, PCL pellets (Mw = 70,000–90,000), and solvent of formic acid (density: 1.22 g/mL) were purchased from Sigma-Aldrich. The drug (antibiotic) used in this study was tetracycline hydrochloride, obtained from Calbiochem.

### 2.2. Methods

**2.2.1. Preparation of PCL/GE-Based Polymer Solutions.** Three different polymer blend solutions of PCL/GE, which were 12% (w/v) (PCL = 1.0 g; GE = 0.2 g), 14% (w/v) (PCL = 1.0 g; GE = 0.4 g), and 18% w/v (PCL = 1.0 g; GE = 0.8 g), were prepared by dissolving different amounts of PCL pellets and GE powder into 10 mL formic acid. Based on the solution properties, 14% w/v was found to be suitable for producing nanofibers. The PCL pellets and GE powder were dissolved completely in formic acid by stirring magnetically using a magnetic stirrer (LABMART HTS-1003) at 600 rpm at room temperature for up to three hours.

**2.2.2. Fabrication of PCL/GE-Based Electrospun Nanofibers.** An electrospinning unit (NaBond, China) was used in the fabrication of PCL/GE-based nanofibers. The prepared polymer solution (12% [w/v] PCL/GE-based) was transferred into a 5 mL syringe with the constant flow rate of 0.5 mL/h using an infusion pump (Veryark TCV-IV, China). Once high voltage at 18 kV was applied to the needles of the syringe, a fluid jet was ejected from the needles and accelerated towards a grounded collector (10 cm × 10 cm) aluminum sheet. The needle was placed at a distance of 10 cm away from the aluminum collector. The polymer solution was evaporated and the charged polymer fibers were deposited on the collector in the form of nanofibers. These steps

were repeated with 14% (w/v) and 18% (w/v) PCL/GE-based polymer solution.

### 2.2.3. Characterization of PCL/GE-Based Electrospun Nanofibers

**Morphology.** First, the electrospun nanofibers were coated with gold. Then, the surface morphology of the coated PCL/GE-based electrospun nanofibers was obtained by SEM (Hitachi TM 3000, Japan) at an accelerating voltage of 15 kV and a field emission scanning electron microscope (FESEM). The obtained images were further analyzed to examine fiber diameters and pore size diameters by *J-Image*. At least 30 fibers were measured for their fiber diameters and pore sizes and the average and standard deviations were plotted.

**Attenuated Total Reflectance (ATR): Fourier Transform Infrared Spectroscopy (FTIR).** Chemical bonding of PCL and PCL/GE was determined by ATR-FTIR (Perkin-Elmer 5 Series, USA) over a range of 400 to 4000 cm<sup>-1</sup>.

**Contact Angle.** Wettability of hydrophilicities of PCL/GE-based electrospun nanofibers was examined through a contact angle measuring system (VCA Optima, AST Products, Inc.) and further analyzed using VCA Optima software. The size of dropping deionized water was 3 μL.

**2.2.4. In Vitro Degradation Study.** The selected sample of nanofibers was cut into 1 cm<sup>2</sup> pieces and immersed in phosphate buffered saline (PBS, pH = 7.4) and incubated *in vitro* at 37°C for different periods of time (day 1 and day 14). After each degradation period, the nanofibers were washed and subsequently dried in room temperature for 24 hours. The morphologies of degraded nanofibers were observed with field emission scanning electron microscopy (FESEM) and the fiber diameters were calculated using *J-Image*.

**2.2.5. Drug Loading.** Tetracycline hydrochloride was used as the model drug (antibiotics) in this study. It had to be predissolved in methanol before being added to the spinning solution. Tetracycline 0.2 g was prepared to be predissolved in 10 mL methanol to load 2% (w/v) of tetracycline hydrochloride into the nanofibers. After all the tetracycline hydrochloride was completely predissolved into methanol, just 1 mL of tetracycline hydrochloride solution was taken out and added to the blended polymer solution selected. After mixing the 1 mL of 2% w/v tetracycline hydrochloride with the blended polymer solution, electrospinning was then carried out to fabricate PCL/GE-based nanofibers with tetracycline hydrochloride.

**2.2.6. Antibacterial Tests.** Antibacterial activity of tetracycline hydrochloride-loaded PCL/GE-based electrospun nanofibers was investigated by zone inhibition method. Tetracycline hydrochloride-incorporated PCL/GE nanofibers were cut into 14 mm diameter circular discs. *Escherichia coli* (Gram-negative bacteria) and *Bacillus cereus* (Gram-positive bacteria) were chosen as model microorganisms in this study.

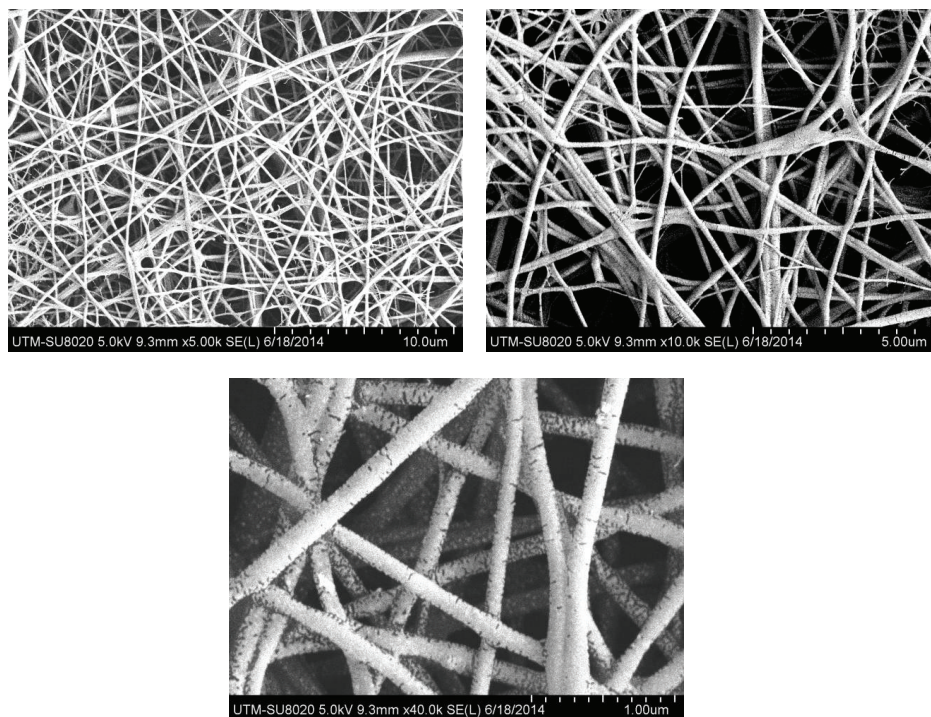


FIGURE 1: FESEM micrographs of 14% w/v PCL/GE-based nanofibers at different magnification.

The spread plate method was used as nutrient agar plates were inoculated with 1 mL of bacterial suspension which contained around  $10^8$  cfu/mL for each type of bacteria. Nanofibers were gradually placed on the inoculated plates and incubated for 24 hours at  $37^\circ\text{C}$ . Zones of inhibition were determined by calculating the diameter of clear area formed around each of the nanofibers.

**2.2.7. Statistical Analysis.** Three to five samples were tested and the average and standard deviations were plotted and analyzed.

### 3. Results and Discussion

**3.1. Morphology of PCL/GE-Based Nanofibers.** Figure 1 shows the microstructures of PCL/GE-based nanofibers fabricated from 14% w/v PCL/GE-based solution. Electrospun PCL/GE-based nanofibers produced from lower concentrations had unwanted beads because of low polymer concentration. The fibers were in wet form when reaching the collector during the electrospinning process. Thus unwanted bead formation occurred. Fewer beads were observed with the increase of solution concentration. However, if the blended polymer solution was too concentrated, it was difficult to eject the fluid jet from the needles and to accelerate it toward a grounded collector. In some cases, the droplet of overconcentrated polymer solution might dry out at the tip and halt the electrospinning process.

The diameter and pore sizes of electrospun nanofibers are presented in Figure 2. According to Figure 2(a), the average fiber diameter increased with the increasing concentration

of the polymer solution. Concentrations of 12%, 14%, and 18% w/v PCL/GE-based nanofibers attained fiber diameters of 15.9 nm, 87.7 nm, and 547.6 nm, respectively. Higher viscosity resistance as a result of higher concentration of the blended solution fails to maintain its flow at the tip of needles. Hence, a large size of nanofibers formation is obtained. Basically, a small fiber diameter is much preferred over a larger size due to its high surface area to volume ratio which is able to enhance its nutrient and gaseous delivery efficiency as well as drug loading and drug release via the diffusion process. On the other hand, the pore size of the nanofibers was also examined for the polymer concentration of 12% w/v, 14% w/v, and 18% w/v (Figure 2(b)). It was found that 14% w/v had the highest pore size, which was around 178.42 nm. Larger pore size improves cell activities such as cell migration and cell proliferation. From the surface morphology characterization, the average fiber diameters and pore size of 14% w/v displayed the optimum characteristic which is needed for skin tissue regeneration.

**3.2. ATR-FTIR.** ATR-FTIR analysis was done to identify the intermolecular interaction between PCL- and PCL/GE-based electrospun nanofibers. According to the spectrum shown in Figure 3, PCL and PCL/GE have the same infrared spectra showing that they have similar chemical bonding. The common band included  $2,949\text{ cm}^{-1}$  (asymmetric  $\text{CH}_2$  stretching),  $2,865\text{ cm}^{-1}$  (symmetric  $\text{CH}_2$  stretching),  $1,727\text{ cm}^{-1}$  (carbonyl stretching),  $1,293\text{ cm}^{-1}$  (C–O and C–C stretching), and  $1,240\text{ cm}^{-1}$  (asymmetric COC stretching).

The only difference in bands between PCL and PCL/GE was the presence of an amide group ( $\text{NH}_2$ ) in PCL/GE.

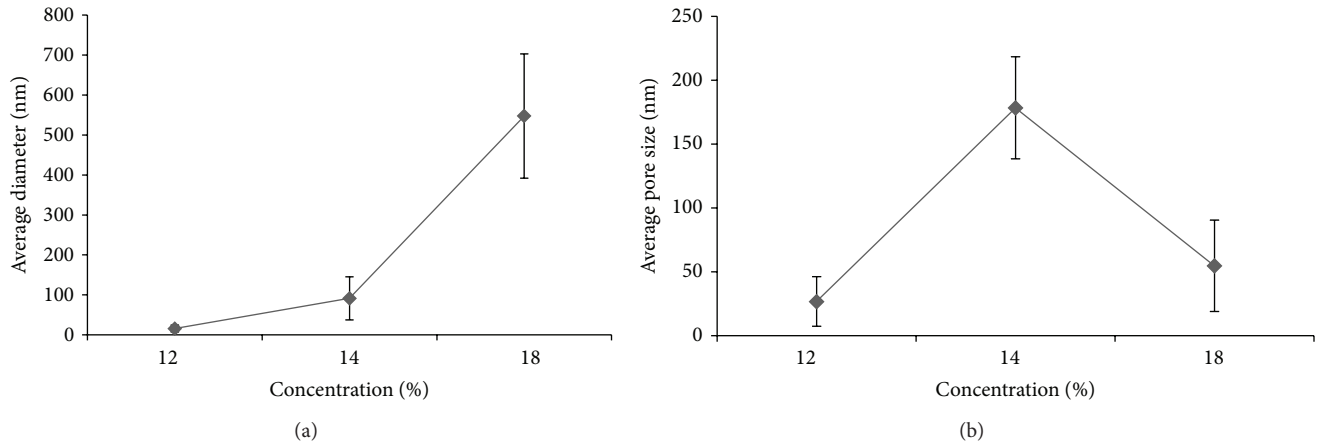


FIGURE 2: Average fiber diameters (a) and average pores sizes (b) of PCL/GE-based electrospun nanofibers fabricated from 12% w/v, 14% w/v, and 18% w/v PCL/GE-based polymer solution.

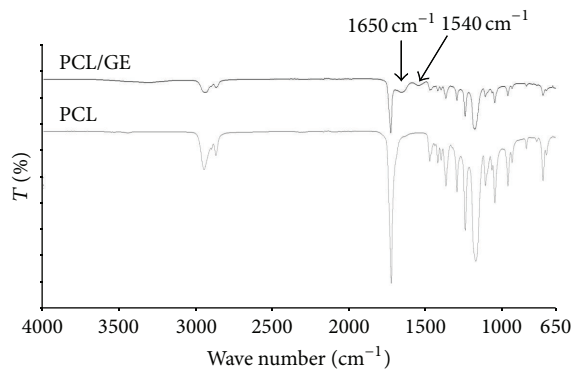


FIGURE 3: ATR- FTIR spectra of PCL- and PCL/GE-based nanofibers.

The bands of GE appeared at approximately  $1,650\text{ cm}^{-1}$  (amide I) and  $1,540\text{ cm}^{-1}$  (amide II). The presence of an amide group confirms the presence of GE in nanofibers after polymer blending and electrospinning. Amide groups in gelatin are able to form hydrogen bonds with water molecules. Thus gelatin has the ability to increase the hydrophilicity of PCL-based nanofibers.

**3.3. Water Contact Angle.** Since the PCL/GE-based nanofibers that we fabricated are intended to be used in skin tissue regeneration, contact with water, blood, and other bodily fluids is frequent. Thus it is essential to characterize the PCL/GE-based nanofibers for their wettability. The wettability of the fiber was measured using water contact angle. Table 1 demonstrates the contact angle of water on the surface of nanofibers produced at different concentrations.

It was observed that the nanofibers of 12% (w/v) showed the highest contact angle of  $98^\circ \pm 2.0^\circ$  compared to those of 14% (w/v) which were  $49.5^\circ \pm 3.2^\circ$ . When the amount of GE increased to 0.8 g, the contact angle decreased significantly and it was absorbed completely on the surface as GE is highly hydrophilic in nature. The contact angle of nanofibers showed

TABLE 1: Contact angle of PCL/GE-based electrospun nanofibers produced from different polymer concentrations.

Concentration of PCL/GE solution (w/v)	Contact angles ( $^\circ$ )
12%	$98 \pm 2.0$ Angles: $[98.10^\circ, 98.10^\circ]$
14%	$49.5 \pm 3.2$ Angles: $[49.50^\circ, 49.50^\circ]$
18%	(Image showing complete absorption of water droplet)

hydrophilic property with less than  $90^\circ$  value. Since 14% w/v PCL/GE-based nanofibers exhibit the most optimum characteristics such as smaller fiber diameters, largest pore size, and good hydrophilicity, they were thus chosen for further analysis and characterization.

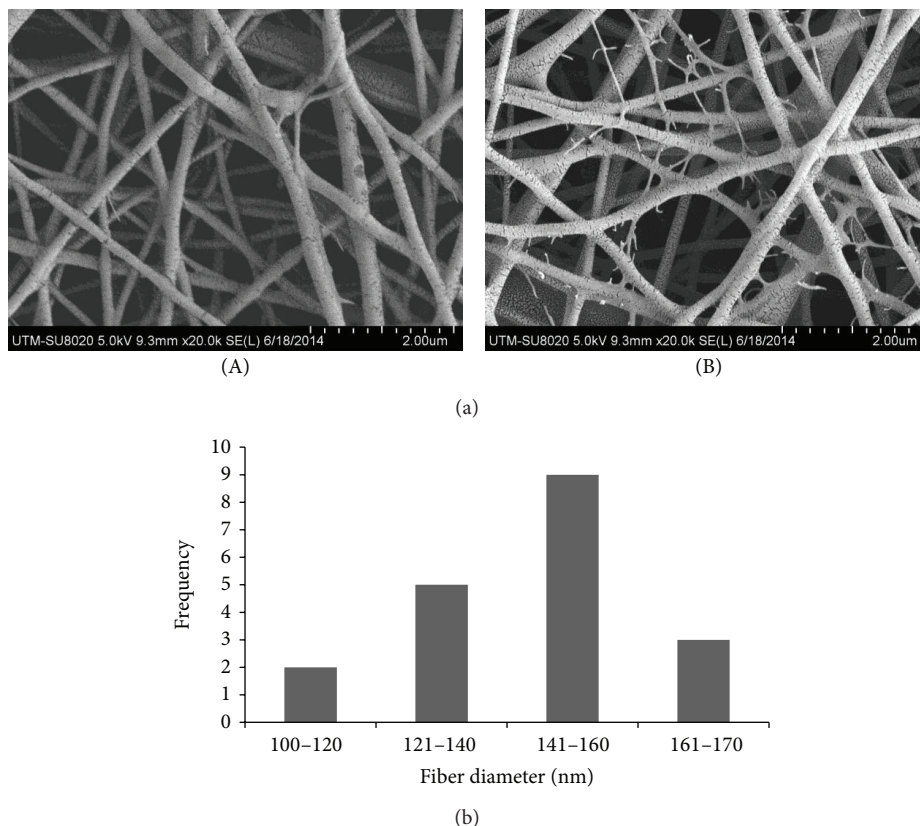


FIGURE 4: FESEM micrographs of (a) 14% w/v PCL/GE-based nanofibers: as-fabricated (A) and degraded (B); (b) distribution of fiber diameters in 14% w/v PCL/GE-based nanofibers after degradation.

The GE component in PCL/GE nanofibers is expected to be gradually dissolved when it comes into contact with water (or bodily fluid); hence, it is able to create more space for cell growth and cell migration. Similarly, the good deformation properties of GE provide easier opening of space to harvest the skin tissue and cells. It is not easy to fabricate desired pore sizes through electrospinning due to the random deposited fibers. However, the overall network architecture structure fabricated is similar and able to mimic the natural ECM, providing the advantage in the process of skin tissue regeneration and repair.

**3.4. In Vitro Degradation.** The ability of nanofibers to degrade was evaluated through soaking them in PBS solution for 14 days using a sample of 14% (w/v). The morphology of as-fabricated and degraded PCL/GE nanofibers was studied by FESEM. The FESEM images are shown in Figure 4(a). At day 14, it was observed that many fibers were broken down. The diameter range of degraded nanofibers was in the range of 26.7 nm–206 nm, with average diameters of 127.29 nm. Figure 4(b) shows the distribution of nanofiber diameters. The broken fibers and the percentages of weight loss (Table 2 and Figure 5) from 3.3% (day 7) to 15.5% (day 14) indicated that the blended nanofibers were successfully degraded due to the presence of GE, which has a faster degradation rate than PCL (0% for both day 7 and day 14). Consisting of an amide group, GE was able to form a hydrogen bond with water

TABLE 2: The percentages of weight loss for 14% PCL-based nanofibers and 14% PCL/GE-based nanofibers.

Days	PCL (%)	PCL/GE (%)
0	0.0	0.0
7	0.0	3.3 ± 1.1
14	0.0	15.5 ± 2.0

molecule. These biodegradable and hydrophilic properties of 14% w/v PCL/GE-based nanofibers are beneficial to skin tissue regeneration.

**3.5. Drug Loading.** It is important to load antibiotics into PCL/GE-based nanofibers to reduce inflammation caused by bacterial infection during the process of recovery activities, since the injured part of skin is an ideal environment for microbial growth. The 14% PCL/GE-based nanofibers incorporated with tetracycline hydrochloride were examined using EDX and FESEM (Figure 6(a)). Meanwhile, smooth fibers with no bead formation and decrement in average fiber diameter were observed in the FESEM image, as shown in Figure 6(b).

**3.6. Antibacterial Tests.** It is essential to carry out antibacterial tests on tetracycline hydrochloride-loaded PCL/GE-based nanofibers to investigate the potential of nanofibers

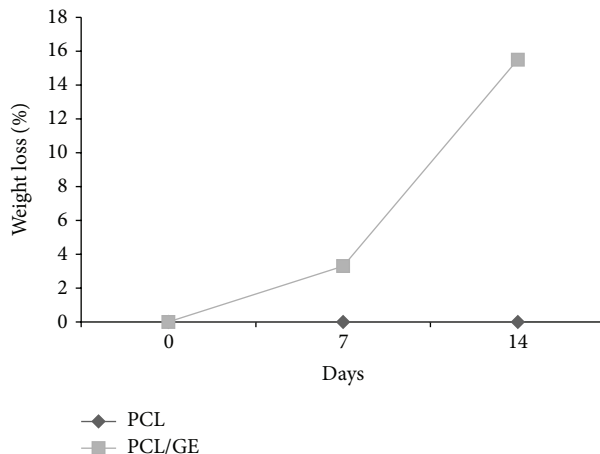


FIGURE 5: The percentages of weight loss of PCL- and PCL/GE-based nanofibers in day 7 and day 14.

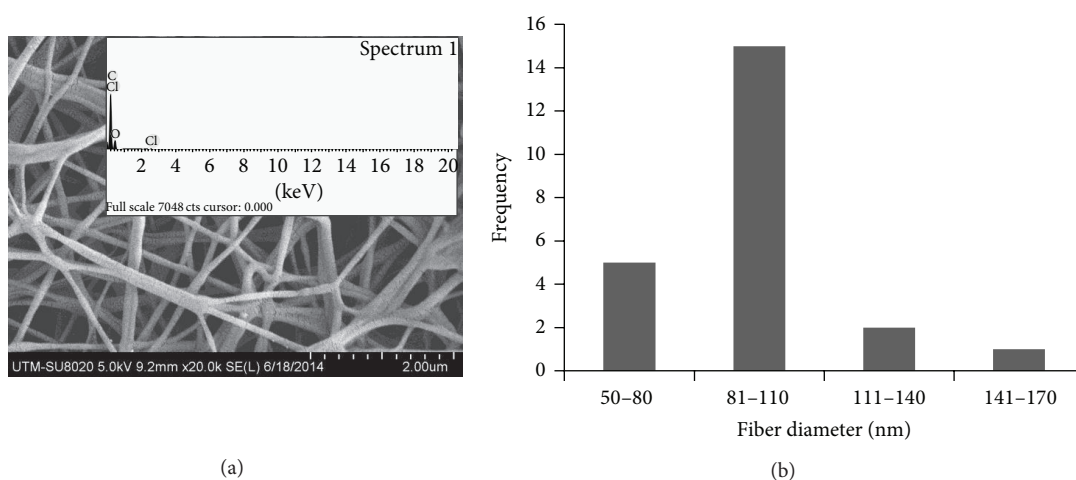


FIGURE 6: FESEM micrograph and EDX spectrums of 14% w/v PCL/GE-based electrospun nanofibers with tetracycline hydrochloride (a) and its fiber diameter distribution (b).

in the inhibition of bacterial growth. The antibacterial tests were performed using the zone inhibition method by examining the antibacterial activities against two types of bacteria, *Bacillus cereus* (Gram-positive bacteria) and *Escherichia coli* (Gram-negative bacteria). Figure 7 displays the inhibition zone of the nanofibers while Table 3 shows the diameters of the inhibition zone. Based on the result observed, the drug-loaded nanofibers showed a large area of zone inhibition toward the two bacteria. The initial diameter of nanofibers was 14 mm. The diameters of clear inhibition were at least double the initial diameter. This result indicates that tetracycline hydrochloride possesses efficient antibacterial property and a small amount of tetracycline hydrochloride (2%) is enough to inhibit a large area of bacterial growth. The drug-loaded nanofibers fabricated should be able to prevent the growth of bacteria responsible for severe harm to skin tissue, thus aiding the tissue regeneration process and effectively avoiding exogenous infections.

TABLE 3: Antibacterial activity of tetracycline hydrochloride-loaded PCL/GE-based nanofibers (14% w/v) against *Bacillus cereus* and *Escherichia coli*.

Bacteria	The diameter of inhibition zone (mm)
<i>Bacillus cereus</i>	$34 \pm 0.5$
<i>Escherichia coli</i>	$30 \pm 1.2$

#### 4. Conclusions

PCL/GE-based electrospun nanofibers were successfully fabricated using the electrospinning technique. Suitable fibers with suitable properties were fabricated with 14% w/v of PCL/GE with flow rate 0.5 mL/h and 18 kV. Results from these experiments confirmed that 14% w/v PCL/GE was in the range of ideal porosity and was able to degrade with time. It was possible to incorporate drugs into the nanofibers. The 14% PCL/GE-based nanofibers with tetracycline hydrochloride showed clear inhibition zones against Gram-positive and

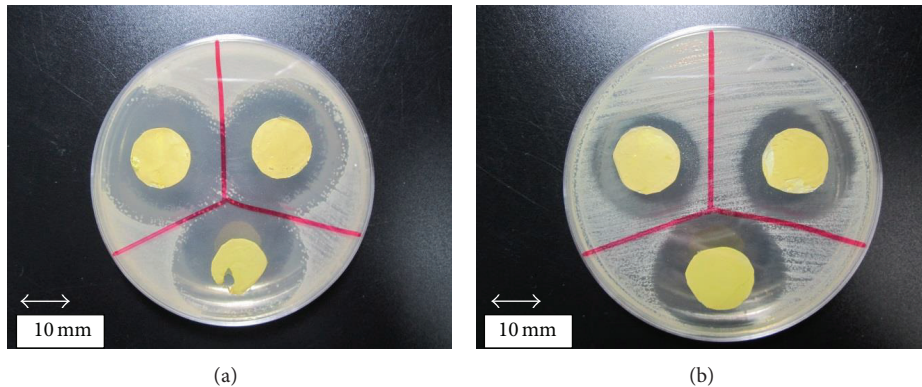


FIGURE 7: Antibacterial activity of 14% w/v PCL/GE-based nanofiber: (a) *Bacillus cereus* and (b) *Escherichia coli*.

Gram-negative bacteria. The nanofibers are suitable for use in inhibiting bacterial infections and protect the injured part of both skin and tissues from contamination during skin tissue engineering.

### Conflict of Interests

The authors do not have any conflict of interests.

### Acknowledgments

The authors acknowledge MOHE, GUP Tier 1 Grants (Vot: 05H07, 06H84), FRGS (Vot: 4F507), MOHE, UTM, and RMC for financial support. Lab facilities of FBME are also acknowledged.

### References

- [1] J. J. Marler, J. Upton, R. Langer, and J. P. Vacanti, "Transplantation of cells in matrices for tissue regeneration," *Advanced Drug Delivery Reviews*, vol. 33, no. 1-2, pp. 165–182, 1998.
- [2] S. Sriputtirat, W. Boonkong, S. Pengprecha, A. Petsom, and N. Thongchul, "Low molecular weight poly(lactide-co-caprolactone) for tissue adhesion and tetracycline hydrochloride controlled release in wound management," *Advances in Chemical Engineering and Science*, vol. 2, no. 1, pp. 15–27, 2012.
- [3] L. Ghasemi-Mobarakeh, M. P. Prabhakaran, M. Morshed, M. Nasr-Esfahani, and S. Ramakrishna, "Electrospun poly( $\epsilon$ -caprolactone)/gelatin nanofibrous scaffolds for nerve tissue engineering," *Biomaterials*, vol. 29, no. 34, pp. 4532–4539, 2008.
- [4] P. X. Ma, "Biomimetic materials for tissue engineering," *Advanced Drug Delivery Reviews*, vol. 60, no. 2, pp. 184–198, 2008.
- [5] C. Y. Xu, R. Inai, M. Kotaki, and S. Ramakrishna, "Aligned biodegradable nanofibrous structure: a potential scaffold for blood vessel engineering," *Biomaterials*, vol. 25, no. 5, pp. 877–886, 2004.
- [6] L. H. Chong, M. M. Lim, and N. Sultana, "Polycaprolactone(PCL)/gelatin(Ge)-based electrospun nanofibers for tissue engineering and drug delivery application," *Applied Mechanics and Materials*, vol. 554, pp. 57–61, 2014.
- [7] N. Ashammakhi, A. Ndreu, Y. Yang, H. Ylikauppila, and L. Nikkola, "Nanofiber-based scaffolds for tissue engineering," *European Journal of Plastic Surgery*, vol. 35, no. 2, pp. 135–149, 2012.
- [8] M. C. Beilke, J. W. Zewe, J. E. Clark, and S. V. Olesik, "Aligned electrospun nanofibers for ultra-thin layer chromatography," *Analytica Chimica Acta*, vol. 761, pp. 201–208, 2013.
- [9] J. Miao, M. Miyauchi, T. J. Simmons, J. S. Dordick, and R. J. Linhardt, "Electrospinning of nanomaterials and applications in electronic components and devices," *Journal of Nanoscience and Nanotechnology*, vol. 10, no. 9, pp. 5507–5519, 2010.
- [10] K. L. Ou, C. S. Chen, L. H. Lin et al., "Membranes of epitaxial-like packed, super aligned electrospun micron hollow poly(l-lactic acid) (PLLA) fibers," *European Polymer Journal*, vol. 47, no. 5, pp. 882–892, 2011.
- [11] F. Roozbahani, N. Sultana, A. F. Ismail, and H. Noupavar, "Effects of chitosan alkali pretreatment on the preparation of electrospun PCL/chitosan blend nanofibrous scaffolds for tissue engineering application," *Journal of Nanomaterials*, vol. 2013, Article ID 641502, 6 pages, 2013.
- [12] J. Doshi and D. H. Reneker, "Electrospinning process and applications of electrospun fibers," *Journal of Electrostatics*, vol. 35, no. 2-3, pp. 151–160, 1995.
- [13] E. J. Chong, T. T. Phan, I. J. Lim et al., "Evaluation of electrospun PCL/gelatin nanofibrous scaffold for wound healing and layered dermal reconstitution," *Acta Biomaterialia*, vol. 3, no. 3, pp. 321–330, 2007.
- [14] N. Bhardwaj and S. C. Kundu, "Electrospinning: a fascinating fiber fabrication technique," *Biotechnology Advances*, vol. 28, no. 3, pp. 325–347, 2010.
- [15] T. J. Sill and H. A. von Recum, "Electrospinning: applications in drug delivery and tissue engineering," *Biomaterials*, vol. 29, no. 13, pp. 1989–2006, 2008.
- [16] X. Liu, T. Lin, J. Fang et al., "In vivo wound healing and antibacterial performances of electrospun nanofibre membranes," *Journal of Biomedical Materials Research—Part A*, vol. 94, no. 2, pp. 499–508, 2010.
- [17] W.-J. Li, C. T. Laurencin, E. J. Caterson, R. S. Tuan, and F. K. Ko, "Electrospun nanofibrous structure: a novel scaffold for tissue engineering," *Journal of Biomedical Materials Research*, vol. 60, no. 4, pp. 613–621, 2002.
- [18] I. Armentano, M. Dottori, E. Fortunati, S. Mattioli, and J. M. Kenny, "Biodegradable polymer matrix nanocomposites for tissue engineering: a review," *Polymer Degradation and Stability*, vol. 95, no. 11, pp. 2126–2146, 2010.

- [19] T. D. J. Heunis and L. M. T. Dicks, "Nanofibers offer alternative ways to the treatment of skin infections," *Journal of Biomedicine and Biotechnology*, vol. 2010, Article ID 510682, 10 pages, 2010.
- [20] S. Sriputtirat, W. Boonkong, S. Pengprecha, A. Petsom, and N. Thongchul, "Low molecular weight poly(lactide-co-caprolactone) for tissue adhesion and tetracycline hydrochloride controlled release in wound management," *Advances in Chemical Engineering and Science*, vol. 2, pp. 15–27, 2012.
- [21] E.-R. Kenawy, G. L. Bowlin, K. Mansfield et al., "Release of tetracycline hydrochloride from electrospun poly(ethylene-co-vinylacetate), poly(lactic acid), and a blend," *Journal of Controlled Release*, vol. 81, no. 1-2, pp. 57–64, 2002.